A Search for Pulsation in Young Brown Dwarfs and Very Low Mass Stars

Thesis by

Ann Marie Cody

In Partial Fulfillment of the Requirements
for the Degree of
Doctor of Philosophy

California Institute of Technology
Pasadena, California

2012

(Defended December 15, 2011)

ii

Acknowledgements

This thesis represents the fruit of five years of work, including many long nights spent at far off telescopes, even longer days spent massaging the data, and a host of insights about young stars, brown dwarfs, and the nature of their flickerings. I want to first and foremost express sincere appreciation to my PhD advisor, Lynne Hillenbrand, for her commitment to the success of my project. You patiently gave me the independence that I needed, but also made sure to infuse me with valuable knowledge, from how to deal with data (the good, the bad, and the ugly!) to how to write a winning proposal. I thank you for the myriad opportunities you provided to enhance and expand my research.

My astronomy roots go back years to many dark nights spent as a high school student at Oak Ridge Observatory in Massachusetts. Although the facility is sadly now closed, I want to acknowledge astronomers Joe Caruso and Bob Stefanik for being among the first to show me that one can enjoy gazing up at the stars and make a career of it too. You have inspired me to continue showing young people the wonders of the night sky. In later years, my research and career path were guided by influential advisors including Dimitar Sasselov and Douglas Gough. Along the way, my thesis committee also kept their doors open for me, expressing interest in my work well beyond the standard exams; I thank them all for helpful advice over the course of my student career.

When it came to observing opportunities, I owe credit to the the Caltech Optical Observatories and the SMARTS consortium for their investment in small telescopes, which provided the backbone for this work. Much of this research also would not have been possible without the help of dedicated staff at the Palomar, Keck, and Cerro Tololo observatories. They made sure to keep the dewars filled, the domes rotating, and much more– particularly when I observed remotely. Agradezco especialmente a mis amigos Mauricio, Claudio y José: gracias por cuidarme en el cerro, entretenerme, y hacerme parte de la familia Tololo.

Vital data reduction advice and contributions to this research came from a handful of fellow students and collaborators, including Justin Steinfadt, Joanna Robaszewski, Kryzsztof Findeisen, Mansi Kasliwal, and Adam Kraus. Adam also trained me in the art of how not to botch observations with a very large telescope; my appreciation for your continued advice. In addition, I received numerous helpful tips from local postdocs, including Greg Herczeg, Kelle Cruz, Jane Rigby, Jessica Lu, and Nairn Baliber.

Thanks to wonderful classmates and officemates who over the years not only provided wise advice about scientific problems, but were also happy to engage in semi-illicit stress-relieving activities involving "window washing" at the crack of dawn (you know who you are). I have many fond memories of late nights and horrible jokes in the basement of Robinson. Tucker and Mansi, you are each special role models. Ryan and Swarnima, I continue to benefit from your sense of humor. Laura y Walter, gracias por todo! I want to congratulate the entire student body of the Caltech astronomy department for maintaining such a close-knit and warm atmosphere, all the while producing top-notch research.

Additional appreciation goes to the countless other folks who worked behind the scenes over the past few years to keep me healthy, wealthy, and wise. And finally, to my family near and far– thanks for your caring phone calls, your perpetual questions about brown dwarfs, and most of all for your love and support. Tommy, takk for din tålmodighet, kjærlighet... og selvfølgelig din dyptgående kunnskap om måneost.

Abstract

In 2005, Palla & Baraffe proposed that brown dwarfs and very low mass stars (<0.1 solar masses) may be unstable to radial oscillations during the pre-main-sequence deuterium burning phase. With associated oscillation periods of 1–4 hours, this potentially new class of pulsation offers unprecedented opportunities to probe the interiors and evolution of low-mass objects in the 1–15 million year age range. Furthermore, several previous reports of short-period variability have suggested that deuterium-burning pulsation is in fact at work in young clusters.

For my dissertation, I developed a photometric monitoring campaign to search for low-amplitude periodic variability in young brown dwarfs and very low mass stars using meter-class telescopes from both the ground and space. The resulting high-precision, high-cadence timeseries photometry targeted four young clusters and achieved sensitivity to periodic oscillations with photometric amplitudes down to several millimagnitudes. This unprecedented variability census probed timescales ranging from minutes to weeks in a sample of 200 young, low-mass cluster members of IC 348, Sigma Orionis, Chamaeleon I, and Upper Scorpius. While I find a dearth of photometric periods under 10 hours, the campaign's high time resolution and precision have enabled detailed study of diverse light curve behavior in the clusters: rotational spot modulation, accretion signatures, and occultations by surrounding disk material. Analysis of the data has led to the establishment of a lower limit for the timescale of periodic photometric variability in young low-mass and substellar objects, an extension of the rotation period distribution to the brown dwarf regime, as well as insights into the connection between variability and circumstellar disks in the Sigma Orionis and Chamaeleon I clusters.

Contents

List of Figures

List of Tables

Chapter 1

Introduction

Stars and brown dwarfs in the $\sim$1–10 million year (Myr) age range occupy a pivotal position in the stellar evolution sequence, characterized by emergence from molecular cloud birthplaces, ongoing dissipation of primordial circumstellar disks, and assembly of planet systems. The evolutionary stage also involves dramatic changes in internal structure as well as radius and angular momentum. Stellar and circumstellar phenomena during this epoch are interconnected, through deposition of accreting material onto the central object, as well as transfer of angular momentum to the surrounding disk. How do these processes operate together to determine the eventual structures and distributions of (sub)stellar objects? The holy grail of brown dwarf (BD) and star formation studies is a unified model incorporating the physics of gravitational collapse, outflow, gas accretion, disk structure and chemistry, magnetic field configuration, and angular momentum transfer, all coupled with stellar evolution. Today, many components of this model exist, but the linkages remain weak and the details scarce.

Theoretical understanding of young, low-mass objects and their environments has long progressed hand in hand with observation. Our current picture of the first few Myr of the stellar or substellar life cycle has been established in large part through dedicated surveys of young clusters. Extensive, unbiased studies of known members are crucial for assessment of the initial mass function, angular momentum, and spatial aggregation that are thought to bear the imprint of the formation process. With a number of young stellar associations now identified at ages of 1–10 Myr, comprehensive censuses provide statistically meaningful data on the characteristics of low-mass populations, including hundreds of brown dwarfs. Although the physics governing their early evolution remains difficult to probe directly,

both the global observational properties as well as accompanying variability offer valuable tracers of the various underlying phenomena at work.

Data derived from temporal variability studies complement single-epoch surveys of stellar populations spanning a range of spectral types and ages in nearby young clusters by contributing information on changes occurring much faster than the evolutionary timescale. A major aim of this thesis work is to show how high-precision, high-cadence optical and infrared photometric monitoring can open up new avenues of research into young, very low mass stars (VLMSs; $\lesssim$0.1 $M_\odot$) and brown dwarfs. In the coming sections we will review the present understanding of these objects and their environments, open questions, and how time series observations can illuminate some of these problems.

1.1   State of the knowledge on young brown dwarfs and very low mass stars

1.1.1   Interior and evolution models

Much of the modeling efforts to date on young BDs and VLMSs has focused on predicting their interior and overall properties, such as mass and radius, as a function of age. The main theoretical difficulty is that the physics relevant to these objects is far from that of a simple gas or solid. With a combination of cool, dense outer layers and hot, degenerate centers, brown dwarfs have non-trivial equations of state (Saumon et al. 1994) and low-temperature opacities. The treatment of convection adds additional complications.

Despite numerous challenges, the science of low-mass stellar and substellar evolution has come a long way since the first structure models were produced decades ago by Hayashi & Nakano (1963) and Kumar (1963). On the pre-main sequence, gravitational contraction is a primary source of energy. Ultimately, the core either becomes hot enough to fuse hydrogen (stars with $M \gtrsim 0.075 M_\odot$) or dense enough for electron degeneracy to dominate pressure support ($M \lesssim 0.075 M_\odot$). The value of 0.075 $M_\odot$ is referred to as the hydrogen-burning minimum mass and sets the boundary between stars and brown dwarfs, the latter of which Kumar (1963) originally designated "black dwarfs."

While the BDs may not burn significant hydrogen, they nevertheless have much in common with their stellar cousins. All objects on the pre-main sequence are fully convective,

and those with spectral types M0 and later ($M \lesssim 0.5$ $M_\odot$) exhibit significant optical and infrared absorption due to the formation of molecules such as H_2O, TiO, VO, and other metal oxides in their atmospheres. At even cooler temperatures and older ages, grain formation becomes another important source of opacity. The accuracy of atmospheric models has increased greatly over the past 15 years (Allard et al. 1997; Burrows et al. 1997), with the inclusion of frequency-dependent absorption due to these molecular species as well as dust grain formation below $\sim$2800 K. As a result, self-consistent models of the radiative properties of low-mass objects are now available and routinely output color-magnitude and color-color data in line with observations (Baraffe & Chabrier 2000; Burrows et al. 2001).

Deuterium burning, whereby ^{3}He is produced from ^{2}D, is another important piece of input physics at low mass and young ages. This process is more rapid than the p-p chain, and hence ignition can take place at lower temperatures, down to 4×10^5 K (Chabrier et al. 2000). When burning commences, it dominates the luminosity and temporarily halts gravitational contraction. Grossman & Graboske (1973) were among the first to determine that the minimum mass for this process is $\sim$0.012 $M_\odot$, although their estimates for the duration of burning were too large by an order of magnitude. Burrows et al. (1997) and Chabrier et al. (2000) later confirmed the mass limit, finding that 99% of deuterium is depleted within $\sim$2 Myr for the 0.1 $M_\odot$ stars and within $\sim$30 Myr for the 0.015 $M_\odot$ BDs. Objects with masses above 0.065 $M_\odot$ also have high enough interior temperatures ($> 2.5 \times 10^6$ K) to burn lithium as well (Chabrier et al. 1996).

Dantona & Mazzitelli (1985) were one of the earliest groups to present detailed pre-main sequence evolutionary models down to 0.04 $M_\odot$, incorporating appropriate equations of state, opacities, boundary conditions, and deuterium abundances. Current-generation models (e.g., D'Antona & Mazzitelli 1997; Baraffe et al. 1998; Siess et al. 2000; Burrows et al. 2003; Tognelli et al. 2011) have further refined equations of state along with non-grey atmospheres, and they now match observed temperature/luminosity data reasonably well (e.g., Luhman 1999). Young BDs and VLMSs have effective temperatures ranging from $\sim$2400 to 3200 K, and estimated radii of $\sim$0.5–0.8 $R_\odot$, although independent observational confirmation of this latter parameter is difficult. At ages of a few Myr, objects at the substellar boundary have luminosities of $\sim$0.05 $L_\odot$, over 1.5 orders of magnitude larger than field objects of similar spectral type. After the exhaustion of deuterium, they eventually cool by a factor of 100–100,000, making detection more challenging.

1.1.2 Inventory of young BDs and VLMSs

The discovery and characterization of substellar objects in star-forming regions preceded that of the cooler field brown dwarfs, whose faintness precludes detection for all but the closest (i.e., within $\sim$50 pc). The first field brown dwarf, Gliese 229B, was discovered in 1995 by Nakajima et al. via coronographic imaging. BDs in young clusters, on the other hand, were long understood to exist as a natural extension of the initial mass function (IMF). It is in these molecular cloud regions that they are thought to form en masse, along with the higher mass stars. Prior to the advent of dedicated spectroscopic follow-up, many faint cluster objects were suspected to be substellar because of their red colors (e.g., Hillenbrand 1997; Luhman et al. 1997). Nevertheless, the first young BDs with confirmed spectral types of M6 and later were not identified until nearly two decades ago (e.g., Strom & Strom 1994, 's study of the Taurus-Auriga region).

Since then, surveys have uncovered over 500 substellar objects in young clusters and star-forming regions (see §2.1 and §2.2 for a discussion of the census), through wide-field optical and infrared imaging, detection of x-ray emission, proper motion measurements, and spectroscopic surveys for emission and youth-related features. Most of the discovered substellar objects lie in nearby low-mass star-forming regions, such as the Orion Nebula Cluster, ρ Ophiuchus, the Taurus-Auriga and Upper Scorpius associations, and IC 348. A variety of methods are at our disposal for confirming an object's cluster membership, most notably the identification of spectral lines consistent with youth (Li, Na, broad Hα emission) and the detection of infrared excess associated with a circumstellar disk. Particularly comprehensive surveys have typically involved initial photometric criteria for selection of young candidates, along with follow-up spectroscopy (e.g., Luhman 2007; Slesnick et al. 2008). Thanks to these surveys, data ranging from spectral types to accretion measures is widely available, and comparison of the observed effective temperatures and luminosities with theoretical structure and formation models is now feasible in many young clusters.

1.2 Open questions

The recent onslaught of data on young, low-mass cluster members has provided valuable feedback for modeling efforts. While the basic physics of convection, degeneracy, and pre-main-sequence contraction have been confirmed, there nonetheless remain substantial uncer-

tainties related to the structure of young, very low mass objects and their immediate environments. Comparisons of parameters output by different low-mass evolution codes reveals significant discrepancies in the predicted Hertzsprung-Russell ("H-R") diagram positions (Gennaro et al. 2012). Yet with the relatively recent detection of hundreds of extrasolar planets around other stars, much of the detailed modeling has increasingly focused on much lower masses (i.e., M_{Jup}–the mass of Jupiter–and below). The somewhat higher masses of brown dwarfs, along with the relatively youthful ages of star-forming clusters represent a different parameter space than those of planetary companions to field stars. Consequently, there are also different challenges to generating accurate models and determining the relevant input physics. We highlight here some of the primary–and often interrelated–questions surrounding young BDs and VLMSs that await explanation in the coming years.

1.2.1   Origins of brown dwarfs

Although the existence of brown dwarfs has been acknowledged for nearly two decades, how exactly they form remains a serious problem to explain. The standard picture of low-mass star formation entails gravitational collapse of unstable Jeans-mass (Jeans 1902) regions of molecular cloud where densities exceed a critical value. With typical Jeans masses of order 1 $M_{\odot}$, most star-forming clusters would not be expected to produce low-mass stars and brown dwarfs with masses an order of magnitude less that this value. It is nevertheless possible to extend the formation process well into the substellar regime by taking into account areas of much higher density, where the minimum mass for gravitational fragmentation can theoretically drop below 0.01 $M_{\odot}$ (Kumar 2003). However, the opacity of very low mass cores typically increases prohibitively during the collapse process, such that the resulting heating raises the Jeans mass and counteracts fragmentation. Compounding the issue of low-mass core formation is the accretion process. Hydrodynamic star formation simulations indicate that it is rare for a nascent BD to stop accreting material before it has reached stellar mass (Bate et al. 2003). Thus it is a challenge to contrive scenarios in which brown dwarfs could form directly from cloud fragmentation.

Three hypotheses have been proposed to explain this conundrum. First, the Jeans mass could lie well below 1.0 $M_{\odot}$. The theory used to estimate this value assumes spherical symmetry, whereas if objects form in elongated sheets or filaments of material, then they could potentially conglomerate at lower masses. This is the basis of the turbulent fragmen-

tation theory (Padoan & Nordlund 2002; Hennebelle & Chabrier 2008), in which colliding flows of turbulent gas are entrained by magnetic fields to produce regions of high density necessary to form small cores. Reipurth & Clarke (2001), on the other hand, argued that cores destined to become stars may have their mass assembly cut off prematurely if they are dynamically ejected from a multi-body system. This process would halt accretion before an object has gathered enough gas to cross the substellar boundary. Whitworth & Zinnecker (2004) proposed a similar idea to produce brown dwarfs as a byproduct of star formation, through photoevaporation of massive cores.

An additional possibility for producing brown dwarfs is a planet-like formation scenario (Pickett et al. 2000). Whitworth & Stamatellos (2006) have successfully simulated the formation of BDs via gravitational fragmentation in the disks surrounding higher mass stars. The conditions for formation via this gravitational instability are a relatively massive disk and a cooling time comparable to the disk orbital timescale. Their radiative hydrodynamics code produces objects with typical masses $\sim$20–30 M_{Jup}, many of which are subsequently ejected into the field to become isolated BDs.

It may in fact be the case that all three formation mechanisms are at work in star and BD-forming regions (Stamatellos & Whitworth 2011). Whichever modes are dominant has implications for the initial mass function (IMF) and multiplicity properties of brown dwarfs. Likewise, the observed properties of brown dwarfs–such as presence of disks, companions, accretion and outflows–provide opportunities to evaluate some of these theories.

1.2.2 Disks and accretion around brown dwarfs

Tied to the formation of brown dwarfs is the presence of disks of dust and gas encircling them. Since launch of the *Spitzer Space Telescope* in 2003 (Werner et al. 2004), mid-infrared photometry has been possible to the sensitivity level required for unambiguously detecting emission from warm dust around very low mass objects. Indeed, some of the first surveys with the *Spitzer* Infrared Array Camera (IRAC) Multiband Imaging Photometer (MIPS) and instrument revealed infrared excesses associated with a substantial fraction (40–50%) of substellar members of the young clusters IC 348 and Cha I (Luhman et al. 2005a). These data were interpreted to suggest that the disks fractions of young BDs are similar to those of the higher mass stars at the same age. Subsequent studies have detected such circumsubstellar disks in a number of other clusters, including σ Orionis, Taurus, Upper

Scorpius, and the TW Hydrae association (Scholz et al. 2007; Muench et al. 2007; Damjanov et al. 2007; Riaz & Gizis 2008; Luhman et al. 2008b,a; Riaz et al. 2009; Luhman et al. 2010) .

Not only do young brown dwarfs possess disks, but many also display signatures of active accretion from them, whether through strong emission lines, photometric variability, or even spectroscopic jets and outflows (Whelan et al. 2005, 2009). This evidence can be used to argue that BDs arise from the same formation processes as higher mass stars. But while the prevalence and phenomenology of disks may be similar above and below the substellar boundary, there is evidence for substantial variation of chemistry–and even planet-forming potential–with central object mass. Mass accretion rates decrease into the substellar regime, according to an approximate empirical correlation $M \propto M_*^2$ (Muzerolle et al. 2003; Mohanty et al. 2005). Recent theoretical work has furthermore suggested that this relation may be bimodal, and substantially steeper at very low mass (Vorobyov & Basu 2009). Observations of bulk disk properties also confirm that dust around BDs displays the grain growth and settling required for planet formation (Apai 2005), although the disks appear to be significantly flatter (i.e., more settled) than those in disks around higher mass stars (Szűcs et al. 2010). Further details on the distinct properties of circumsubstellar disks await discovery.

1.2.3   Interior and atmospheric physics

In addition to the difficulties in explaining the origins of BDs and surrounding disks, there are many gaps to fill in our knowledge of the early stages of their evolution. Theoretical models (Burrows et al. 1997; Baraffe et al. 2003) are moderately successful in reproducing the observed properties of BDs and VLMSs, at least at intermediate and old ages Burrows et al. (2001). Such models can be used to estimate fundamental parameters, namely mass and age. However, they have not been extensively tested by independent measurements of these parameters, nor do they account in detail for more complex realities such as magnetic fields and rotation which can have significant effects as illustrated for very low mass stars by D'Antona et al. (2000). Furthermore, below ages of 5 Myr and masses of 0.5 $M_\odot$, substantial uncertainties in the initial radii and accretion history as well as the convection efficiency, low-temperature opacity, and equation of state of these objects hamper theoretical modeling efforts (Baraffe et al. 2002).

From an observational point of view, there are currently few ways to independently verify physical assumptions and measure fundamental parameters of very low mass cluster members. The positions of objects on the H-R diagram provides useful comparison of data with theoretical isochrones. However, this exercise is typically complicated by the presence of significant extinction and accretion, which can skew the magnitudes, colors and spectral types used to derive temperature and luminosity. Eclipsing binaries offer a convenient method to robustly measure masses and radii for comparison with models, but there are currently only six published young, low-mass systems. Analysis of a larger sample of eclipsing binary systems, including those in later evolutionary stages, indicates that the models underpredict radii at the 10% level for masses less than ~1.0 $M_\odot$ (e.g., Ribas et al. 2008; Jackson et al. 2009). The disagreement worsens below ~0.5 $M_\odot$, and effective temperatures also appear to be underestimated, although to a lesser extent ($\sim5\%$). At the very low mass end, one young BD eclipsing binary system has been discovered thus far (Stassun et al. 2006), and the radii of the components do not agree well with the theoretical models. Surprisingly, the inferred temperature ratio is also the reverse of predictions. Chabrier et al. (2007) proposed that the discrepancies seen in this system and others could arise from spotted surfaces and reduced convective efficiency, as a consequence of rapid rotation and strong magnetic fields in relatively close binary systems. Further observations have lent some support to this idea, since it appears that there is less disagreement between observed and theoretical radii for more widely separated systems (Kraus et al. 2011) and for single stars (Demory et al. 2009).

Additional uncertainties surrounding the model-derived parameters of low-mass stars and BDs arise when one considers the age ranges implied by young cluster object positions on the H-R diagram. A significant spread in luminosity among objects in the same cluster (e.g., Hillenbrand 2009) suggests that either the observational errors are substantial, that the objects formed at different times, or that some factor not included in the models induces an apparent age spread. The latter two possibilities have important consequences for our understanding of low-mass star and BD evolution. It has recently been suggested that accretion could be the sought-after additional model parameter that influences stellar properties. Although steady accretion (or no accretion at all!) is often assumed for theoretical simplicity, the luminosity distribution of young, embedded stars (Kenyon & Hartmann 1990) suggests that the process is more likely to take place in bursts (Vorobyov & Basu

2009; Dunham et al. 2008). Baraffe et al. (2009) showed that the introduction of episodic accretion into their low-mass models could account for the apparent age spread in young clusters, and Littlefair et al. (2011) support for the idea through an observational correlation of H-R diagram position and rotation, which is influenced by accretion. Later work by Hosokawa et al. (2011), on the other hand, has argued that the effect of accretion history on low-mass star (i.e., those with effective temperatures less than 4000 K) properties is negligible when more self-consistent initial conditions are incorporated into the models.

Clearly, much work remains to be done in characterizing the properties of young, low-mass objects with respect to accretion, magnetic activity, and equilibrium size. Filling in these gaps will not only provide feedback for theoretical structure and evolution models, but it will also illuminate the initial conditions associated with their formation.

1.2.4 Angular momentum evolution

Low-mass eclipsing binary systems supply crucial data points for the calibration of theoretical evolutionary models. While multi-epoch observations enable determinations of radius, mass, and other global stellar properties, further insights can be gleaned through photometric studies of non-eclipsing young objects. Among the most appreciated stellar parameters accessed through time series monitoring is the rotational angular momentum. For objects with periodic brightness changes that can be attributed to the passage of cool surface spots, photometric variability analyses yield rotation rates. Recent work has established the overall angular momentum trends from the pre-main-sequence (PMS) through ages of 500 Myr, as reviewed by Herbst et al. (2007), Bouvier (2007), and Scholz (2009). Of particular interest is the 1–10 Myr regime, which is the first opportunity to measure the cumulative effect of the formation process on rotation rates after the embedded phases of protostellar development. During these early stages, a large portion of the initial angular momentum is carried off by outflows and jets, and additional amounts subsequently may be deposited into surrounding disks via magnetic interaction with the central star. The growing census of young stars and brown dwarfs has allowed recent studies to probe rotation rates in a number of 1–10 Myr old clusters, including Chamaeleon I (Joergens et al. 2003), IC 348 (Cohen et al. 2004; Littlefair et al. 2005; Cieza & Baliber 2006), Taurus (Nguyen et al. 2009), the Orion Nebula Cluster (Stassun et al. 1999; Herbst et al. 2002), σ Orionis (Scholz & Eislöffel 2004), ϵ Orionis (Scholz & Eislöffel 2005), NGC 2363 (Irwin et al. 2008), and

NGC 2264 (Lamm et al. 2005).

Observations to date find that the majority of rotation rates at ages of a few Myr correspond to periods between 1 and 10 days, with a smaller population of slower rotators extending to periods of $\sim$25 days. In addition, the distribution appears to be highly mass-dependent: earlier than spectral type M2.5 (or $\sim$0.3–0.4 $M_\odot$, depending on the theoretical model used), typical rotation periods lie between $\sim$2 and 10 days, and in some cases display a bimodal distribution (Herbst et al. 2002; Lamm et al. 2005) However, where data are available at lower mass, the distribution peaks near 1–3 days and steadily declines toward longer periods (e.g., Cieza & Baliber 2007). At first glance the slow rotation rates are somewhat surprising, given that these stars are recently accreting material and still undergoing pre-main-sequence contraction. Stellar evolution theory alone predicts approximately an order of magnitude increase in angular velocity during the PMS phase, whereas rotation rate distributions in clusters of different age remain roughly constant out to $\sim$30 Myr (Irwin & Bouvier 2009). Current evidence suggests that at least among the higher mass objects, rotation rates are strongly linked to the presence or lack of a disk, as indicated by long-wavelength infrared excesses (Rebull et al. 2006; Cieza & Baliber 2007).

Despite the wealth of data, many open questions remain, which we will address in this work. The mechanism for removal of angular momentum during the protostar stages is not well understood, and the role of circumstellar disks in rotation rate regulation remains controversial among the low-mass stars at spectral type M2.5 and later (Stassun et al. 1999; Rebull 2001). Furthermore, the lower limit to rotation periods in young clusters is not well established. Photometric derivations of rotation rate or pulsation period are complicated by the variety of variable phenomena operating in young stars. Notably, aperiodic variability due to stochastic accretion can appear as a semi-periodic phenomenon when sampling is sparse or when hot spots produced by columns of accreting material produce transient signals at the period of rotation (Bouvier & Bertout 1989; Fernandez & Eiroa 1996; Herbst et al. 2007). A number of authors claim evidence for a pattern of faster rotation as masses decrease into the brown dwarf regime (Bailer-Jones & Mundt 2001; Herbst et al. 2001; Zapatero Osorio et al. 2003; Scholz & Eislöffel 2005; Rodríguez-Ledesma et al. 2009). In some cases, periods as short as a few hours are inferred for brown dwarfs (BDs) and very low mass stars (VLMSs), implying that they may be spinning at close to break-up velocity. Palla & Baraffe (2005) suggested that variability in these particular short-period objects

may represent a completely different effect–pulsation powered by deuterium burning. As we explain in §1.3, detection of this phenomenon is the main motivation for our work.

1.2.5 Variability mechanisms

Variability studies of young stars have been a fixture of astronomical photometry for decades. Since the seminal work of Joy (1949), it has been known that the light curves of T Tauri stars with masses near solar exhibit variability on levels of ~1–50%. At visible and near-infrared wavelengths, prominent phenomena causing photometric variability are thought to include modulations of the stellar brightness by rotation of cool magnetic surface spots, sporadic flux variations due to accretion, extinction fluctuations due to clumpy circumstellar material, and eclipses by companions. Data derived from temporal variability studies complement single-epoch surveys of stellar populations spanning a range of spectral types and ages in nearby young clusters by contributing information on changes occurring much faster than the evolutionary timescale. Photometric monitoring campaigns have thus become an integral part of our toolbox in the investigation of young cluster members.

With the recent discovery of hundreds of brown dwarfs (BDs) in young (i.e., 1–10 Myr) clusters has come the revelation that many display evidence of accretion from surrounding disks, just like their higher mass counterparts. Some of these substellar objects also exhibit non-periodic brightness changes similar to those seen in T Tauri light curves. What are the mechanisms behind this variability, and how does it relate to physical conditions, particularly in the BD regime? While disk-related phenomena are suspected to play a role, these questions have proven surprisingly difficult to answer in detail.

Initial attempts to match the optical and near-infrared time-domain properties of young stars to models (e.g., Herbst et al. 1994; Carpenter et al. 2001, 2002; Scholz et al. 2009a) have noted photometric behavior that is largely consistent with either variable accretion, hot and cool photospheric spots, or variable obscuration by circumstellar material. Yet with limited wavelength coverage or temporally sparse data, these scenarios could not be distinguished unambiguously. Further work on class II sources by Eiroa et al. (2002) revealed optical and near-IR flux changes suggestive of disk structural changes on 1–2 day timescales. While they speculated that changes in disk structure could produce disk emission or scattered light variations, the rapidity is difficult to explain. At longer wavelengths, instruments aboard the *Spitzer Space Telescope* enabled Muzerolle et al. (2009), Espaillat et al. (2011),

and Morales-Calderón et al. (2011) to uncover mid-IR brightness fluctuations in disk-bearing young stars. Variable accretion and extinction, as well as disk warps and shadowing, are cited as plausible variability mechanisms. Complementary modeling efforts such as those by Dullemond et al. (2003), Flaherty & Muzerolle (2010), and Romanova et al. (2011) have begun to offer detailed descriptions of inner disk dynamics and star-disk interaction but nevertheless require more extensive input from observations on more varied timescales and wavelengths.

Another important hole in our knowledge of young object variability properties their underlying mechanisms is how they change at very low mass. As mentioned above, brown dwarfs may rotate significantly faster in the BD regime, but the existing sample size is small. In addition, time series observations of a handful of young BDs have provided significant evidence for variability at optical through infrared bands (Caballero et al. 2004; Luhman et al. 2008a; Scholz et al. 2009b; Luhman et al. 2009), but in most cases time sampling was too sparse for detailed study. It remains unknown as to whether the spot properties, accretion fluctuation timescales, and disk geometries applicable to BDs substantially affect their variability characteristics. Conversely, study of their light curves may lead to new insights into the different physical conditions relevant to this mass regime.

1.3 Pulsation as a window into very low mass young cluster members

1.3.1 The promise of asteroseismology

With so many uncertainties surrounding very low mass young cluster members, new observational methods are direly needed to investigate their origin and structure. We highlight here the great potential that asteroseismology offers in illuminating the interior properties and evolution of these objects. This tool has proven very useful in the study of many classes of higher mass stars. Underlying it is the basic premise that small displacements of material within a star can lead to global instabilities if there is an energy source to amplify them and a restoring force to maintain oscillations. Stellar pulsation modes are typically supported by pressure ("p modes") or gravity ("g modes"), and may take on the form of a purely radial displacement or a more complex mixture of radial and angular oscillations.

This generates both radial velocity variations as the surface expands and shrinks, and also brightness changes due to the corresponding effective temperature and luminosity fluctuations. Depending on the amplitude, pulsation may be observed by identifying periodic variability in a photometric time series or a set of spectroscopic velocity measurements.

The past two decades have witnessed an explosion in both observational data and modeling of the pulsation features of main sequence and pre-main sequence intermediate-mass stars (γ Doradus and δ Scuti pulsators; Breger 2000; Bouabid et al. 2011), white dwarfs (Córsico et al. 2011), Sun-like stars (Kjeldsen et al. 2008), and now red giants as well (Gilliland et al. 2010; Christensen-Dalsgaard 2011). The fact that observable oscillation modes appear in the Sun and other stars implies that the physics of vibrations may be used to probe the otherwise inaccessible interiors of these objects. Their global characteristics, such as mass, radius, and age are potentially inferable by comparison of oscillation frequencies with detailed stellar structure models. In addition, when multiple modes are excited, many more parameters, such as heavy-element abundance (e.g., Houdek & Gough 2011) and convection zone depth (e.g., van Saders & Pinsonneault 2012), may be derived.

1.3.2 The possibility of pulsation in young brown dwarfs and very low mass stars

Although pulsation is well known in stars with masses of the Sun and larger, it is unclear as to whether the phenomenon might appear in lower mass objects. If discovered, then the application of asteroseismology to BDs and VLMSs could open up entirely new avenues of study. Incidentally, the idea of pulsation in brown dwarfs and very low mass stars on the pre-main sequence is not a particularly new one. Gabriel (1964, 1967) and Toma (1972) were the first to suggest that M dwarfs with masses of $\sim$0.2 $M_\odot$ may be destabilized to radial pulsation by either convection or deuterium burning ("D burning"). Gahm et al. (1989) examined the D-burning instability in polytropic star models with masses of 0.2– 3.0 $M_\odot$, finding periods ranging from $\sim$2.5 days to 10 hours, respectively. Their estimate of the deuterium burning onset and its duration provided guidelines for a preliminary pulsation instability strip on the H-R diagram. Marconi & Palla (2003) further suggested that deuterium burning can drive oscillations even in brown dwarfs, and they extended the instability strip of Gahm et al. (1989) to lower mass (0.04 $M_\odot$) using polytropic models. While all of these analyses were in rough agreement regarding pulsation periods, many

uncertainties concerning the initial abundance of deuterium and its burning timescale hindered the accuracy of the calculations. The potential of nuclear burning to drive pulsation depends crucially on its duration, as compared to the *e*-folding growth timescale of oscillation modes. If the latter is longer, then the modes will not have enough time to grow to observable amplitudes before their energy source is quenched. Hence the initial models could not confidently confirm the age and mass range over which D-burning pulsation might operate.

Despite somewhat promising theoretical predictions, as of 2005 there was still little observational evidence for pulsation in low-mass objects at ages of a few million years. Palla & Baraffe (2005, hereafter PB05) renewed interest in the subject by combining state-of-the-art low-mass interior models with a non-adiabatic, linear stability analysis. Incorporating for the first time accurate deuterium abundances and ignition times as a function of mass, they concluded that deuterium burning could indeed excite radial mode oscillations, but only in BDs and VLMSs within the interval 0.02–0.1 $M_{\odot}$, at ages of $\sim$1–10 Myr. The expected periods range from $\sim$1–4 hours, with the shortest timescales corresponding to the lowest masses. As PB05 pointed out, several young BDs have been reported to display periodic light curve variations on these timescales (Osorio et al. 2003; Bailer-Jones & Mundt 2001), and modulation of surface spots is an unlikely explanation since this would require rotation at or above the break-up speed.

To illuminate the results of PB05, we now outline the general approach to evaluating pulsation in young stars and BDs. Two steps are necessary to predict mode properties: First, a linear, adiabatic stability analysis determines the possible values of oscillation frequencies, *if* they are excited. Second, a non-adiabatic or quasi-non-adiabatic analysis indicates whether a selected driving mechanism can amplify small perturbations in the interior to potentially observable levels, and if so, at which preferential frequencies. We explain both of these procedures for the D-burning instability below.

1.3.2.1   Linear adiabatic stability analysis

The input for an adiabatic analysis is an equilibrium structure model that satisfies the standard hydrodynamic equations:

$$\frac{\partial \rho}{\partial t} + \nabla \cdot (\rho \mathbf{v}) = 0, \tag{1.1}$$

$$\rho \frac{\partial \mathbf{v}}{\partial t} + \rho(\mathbf{v} \cdot \nabla)\mathbf{v} + \nabla P + \rho \nabla \Phi = 0, \tag{1.2}$$

$$\nabla^2 \Phi = 4\pi G \rho, \tag{1.3}$$

$$\frac{\mathrm{d}E}{\mathrm{d}t} - \frac{P}{\rho^2}\frac{d\rho}{dt} = \epsilon - \frac{1}{\rho}\nabla \cdot (F_R + F_C), \tag{1.4}$$

$$F_R = -\left(\frac{4ac}{3\kappa\rho}\right)T^3\nabla T, \tag{1.5}$$

where ρ is density, p is pressure, $\mathbf{v}$ is velocity, G is the gravitational constant, E is internal energy, ϵ is the thermonuclear energy generation rate per unit mass, F_R and F_C are the radiative and convective fluxes, c is the speed of light, T is temperatures, κ is opacity, a is a constant, and Φ is the gravitational potential, such that the gravitational force $\mathbf{g}$ equals $-\nabla\Phi$. These equations correspond to continuity (1.1), conservations of momentum (1.2), Poisson's equation (1.3), energy conservation (1.4), and radiative diffusion (1.5). Next, small linear perturbations are incorporated in temperature, pressure, density, and flux. Denoting a change in radius r from its initial position r_0 as ξ and the change in any other parameter f along the fluid flow as δf, we have

$$\xi \equiv r - r_0 \tag{1.6}$$

$$\delta f \equiv f(r_0 + \xi). \tag{1.7}$$

Similarly, the perturbation f' corresponding to a parameter f at fixed position is

$$f' \equiv f(r) - f_0(r) = \delta f - \xi \cdot \nabla f_0. \tag{1.8}$$

Allowing the temporal component of all perturbed quantities to vary in time as $e^{i\sigma t}$, the hydrodynamic equations can then be linearized in small quantities and reduced to:

$$\rho' + \nabla \cdot (\rho\xi) = 0 \tag{1.9}$$

$$\sigma^2\xi = -\frac{\nabla P'}{\rho} + \left(\frac{\rho'}{rho^2}\right)\nabla P \tag{1.10}$$

$$\nabla^2\Phi' = 4\pi G\rho' \tag{1.11}$$

$$F_R' = F_R \left(3\frac{T'}{T} - \frac{\kappa'}{\kappa} - \frac{\rho'}{\rho} \right) - \left(\frac{4ac}{3\kappa} \right) T^3 \nabla T'. \tag{1.12}$$

These may be further simplified to an eigenvalue equation of form $\sigma^2 \xi = \mathcal{L}(\xi)$, for which the solutions are a set of oscillation frequencies, σ. Each value corresponds to an eigenmode, which can be described by its number of radial nodes, n, and angular degree l. To evaluate pulsation in BDs and VLMSs, PB05 used "NextGen" models (Baraffe et al. 1998) as input for the equilibrium structure values to derive fundamental radial mode (i.e., $n = 0$, $l = 0$) periods of 1–4 hours. We have obtained very similar results using the BD equilibrium models of Burrows et al. (1997, 2007, private communication) along with the Aarhus adiabatic pulsation code ADIPLS (Christensen-Dalsgaard 2008). We note that neither the amplitude nor the color dependence of pulsation can be determined from this analysis, since these are non-linear quantities.

1.3.2.2 Quasi-non-adiabatic analysis

The set of oscillation frequencies, $\{\sigma\}$, is infinite, but in reality only modes that are tied to an excitation mechanism will grow from minute perturbations to coherent, observable oscillations. Evaluation of the mode selection may be carried out with a three-dimensional non-linear, non-adiabatic analysis, but this approach is infeasible with the current one-dimensional brown dwarf structure codes. Instead, PB05 and others adopted a simpler approach, using the initial linear, adiabatic oscillation solution to estimate an exponential growth timescale applicable to the excitation of deuterium-burning modes.

While the interiors of stars and BDs are more complicated than a simple harmonic oscillator, the analogy is nonetheless useful for illustrating how the growth timescale is related to energy exchange within a system. When an oscillator is damped or driven, its deviation ξ from the equilibrium position can be described by the following equation:

$$\xi(t) = A \sin(\sigma t) e^{-\eta t}, \tag{1.13}$$

where A is the initial amplitude, σ is the oscillation frequency, and η^{-1} is the growth or decay timescale (all specified by the properties of the material). The instantaneous total energy

(kinetic and potential), $E(t)$, associated with these oscillations can also be calculated:

$$E_{\text{tot}}(t) = \frac{1}{2}A^2\sigma^2 e^{-2\eta t}. \tag{1.14}$$

Thus η^{-1} can be viewed as the e-folding timescale for growth or decay of a mode; when negative, this parameter provides a rough estimate of how long it would take for a small perturbation to grow to observable amplitudes. Relating it to the work done on the oscillating material, we find

$$\frac{W}{E_{\text{tot}}} = \frac{4\pi\eta}{\sigma} = 2\eta P. \tag{1.15}$$

Since $\langle\frac{dW}{dt}\rangle$ is approximately equal to $\frac{W}{P}$, we can relate the parameter η to the average rate of work done during an oscillation period:

$$\eta \sim -\frac{1}{2E_{\text{tot}}}\langle\frac{dW}{dt}\rangle. \tag{1.16}$$

Therefore, if $\langle\frac{dW}{dt}\rangle$ is negative, the amplitude can grow exponentially.

Returning now to the (sub)stellar interior, it is the work done by gravity and pressure on all mass elements within the star or BD that determines the growth rate. If the total work over a period is positive, then kinetic energy increases and the oscillation mode is said to be driven. Likewise, driving regions within the interior gain heat while under greatest compression. An expression for the rate of work associated with a sinusoidal oscillation (i.e., the linear solution described in §1.3.2.1) can be derived by relating it to the heat (Q) gained over the mass of the entire star, which is in turn related to the perturbations in temperature and entropy (S):

$$\frac{dW}{dt} = \int^M \frac{dQ}{dt}dM(r) = \int^M \delta T\left(\frac{d\delta S}{dt}\right). \tag{1.17}$$

We can rewrite this expression in terms of the temperature and energy perturbations:

$$\frac{dW}{dt} = \int^M \frac{\delta T}{T}\delta\left(\epsilon - \frac{1}{\rho}\nabla\cdot(F_R + F_C)\right)dM(r), \tag{1.18}$$

where ϵ is the nuclear energy generation rate and F_R and F_C are the radiative and convective fluxes. We next separate the perturbation into spatial and temporal components, averaging

over one oscillation period (P) to obtain the mean rate of work:

$$\delta \epsilon \sim \epsilon_r e^{i\sigma t}; \delta T \sim T_r e^{i\sigma t}, \tag{1.19}$$

$$\langle \frac{dW}{dt} \rangle \sim \frac{1}{P} \oint \frac{dW}{dt} dt = \frac{1}{2} \int^M \frac{\delta T_r}{T} \delta[\epsilon_r - \frac{1}{\rho} \nabla \cdot (F_R + F_C)] dM(r). \tag{1.20}$$

Ignoring the contributions of flux for the moment, we can isolate the effect of nuclear burning has on driving oscillations:

$$\langle \frac{dW}{dt} \rangle \sim \frac{1}{2} \int^M \frac{\delta T_r}{T} \delta \epsilon_r dM(r). \tag{1.21}$$

The nuclear burning rate is traditionally written as an exponential function of density and temperature, $\rho^{\epsilon_\rho} T^{\epsilon_T}$ such that we can define the following partial derivatives:

$$\epsilon_T \equiv \left(\frac{\partial \ln \epsilon}{\partial \ln T} \right)_\rho, \epsilon_\rho \equiv \left(\frac{\partial \ln \epsilon}{\partial \ln \rho} \right)_T, \tag{1.22}$$

and the nuclear burning perturbation can be rewritten in terms of the temperature perturbation:

$$\frac{\delta \epsilon}{\epsilon} = \epsilon_\rho \frac{\delta \rho}{\rho} + \epsilon_T \frac{\delta T}{T} = \frac{\delta T}{T} \left(\frac{\epsilon_\rho}{\Gamma_3 - 1} + \epsilon_T \right), \tag{1.23}$$

where

$$\Gamma_3 - 1 = \left(\frac{\partial \ln T}{\partial \ln \rho} \right)_S, \tag{1.24}$$

for fixed entropy S. Incorporating these expressions into Eq. 1.21, we find

$$\langle \frac{dW}{dt} \rangle \sim \frac{1}{2} \int^M \left(\frac{\delta T_r}{T} \right)^2 \epsilon_r \left(\epsilon_T + \frac{\epsilon_\rho}{\Gamma_3 - 1} \right) dM(r). \tag{1.25}$$

In brown dwarfs and very low mass stars at ages of a few Myr, the interior temperature typically reaches $\sim 10^6$ K, and for deuterium burning $\epsilon_\rho \sim$1–2, whereas $\epsilon_T \sim$12–14. The relatively large temperature exponent as compared to hydrogen burning via the p-p chain ($\epsilon_T \sim 2$) gives rise to the possibility that the quantity in Eq. 1.25–known as the work integral–will be positive, and hence the amplitude of any instability will grow with time. This method for driving oscillations is referred to as the "epsilon mechanism," and while it has been predicted for more massive CNO-burning stars (whose nuclear burning also depends strongly on temperature), a detection in young BDs and VLMSs would be its first

observational confirmation.

PB05 have numerically calculated the work integral for a set of realistic young, very low mass models pulsating in the fundamental radial mode or an overtone. Their computations confirm that not only is its value large and positive during the deuterium phase, but the growth timescale η^{-1} is generally shorter than the D-burning timescale for the fundamental mode only. Consequently, perturbations at thus frequency should have time to grow before the supply of deuterium runs out. The work integral for a 0.03 $M_\odot$ BD from PB05 is presented in Fig. 1.1, illustrating the strongly positive contribution of nuclear burning. Since young objects are not particularly centrally concentrated, this energy input occurs throughout a significant portion of their interior, raising the chance that oscillations will persist out to the surface. It is nevertheless possible that energy exchange between modes and the fully convective interior causes damping that is not accounted for by the models. PB05 have neglected convection in their calculations, on the premise that the overturn timescale in young BDs and VLMSs (on the order of weeks) is much longer than the pulsation periods (a few hours). However, we caution that this "frozen-in" approximation may not be valid near the surface where convection becomes much more vigorous. Since the dynamics of pulsation-convection interaction are too complicated to model accurately, confirmation of global oscillations in young, very low mass objects is thus relegated to observation.

1.3.3 Observational predictions for D-burning pulsation

As noted above, the main observational prediction for young BDs and VLMSs is that they undergo fundamental mode pulsation with periods of 1–4 hours, depending on mass. The lowest mass objects, at $M \sim 0.02\ M_\odot$, should have the shortest periods (∼1 hour) and the longest duration of deuterium burning (15-20 Myr). Very low mass stars, on the other hand, may pulsate with ∼5-hour periods, and both their pulsation growth and D-burning timescales are much shorter, at ∼2–3 Myr. Rodríguez-López et al. (2012) have recently confirmed the excitation of the fundamental mode with roughly these timescales, using a non-adiabatic oscillation code. At masses higher than $\sim 0.1\ M_\odot$, deuterium is predicted to exhaust too quickly for pulsations to be excited at all (PB05).

The most crucial feedback for observational efforts is the D-burning instability strip, which PB05 have generated based on a grid of young, very low mass models. The subset for which the growth timescale η^{-1} is comparable to or larger than the deuterium-burning
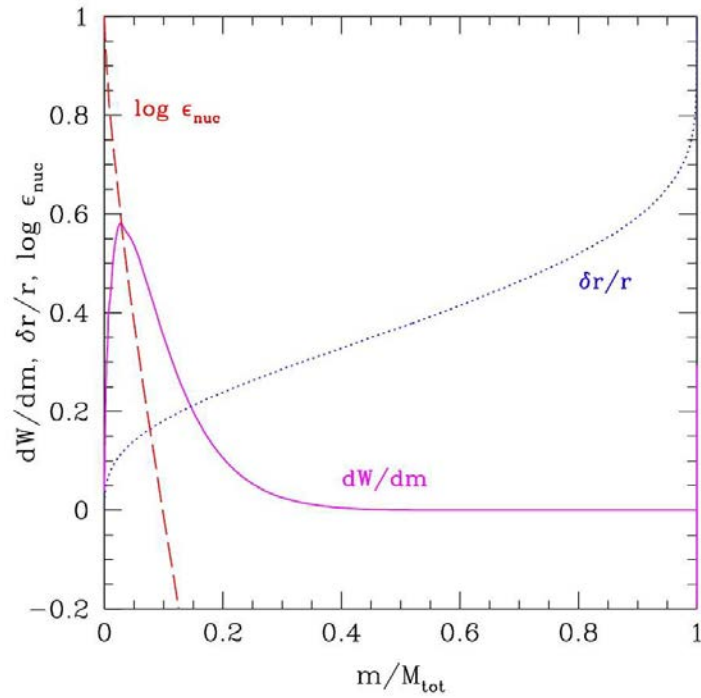
Figure 1.1 The derivative of the work integral as a function of mass (dW/dm; magenta curve), for an 0.03 $M_\odot$ brown dwarf at 2.4 Myr. This figure is reproduced from Palla & Baraffe (2005). It is clear that its total value will be positive when integrated over the mass of the entire star. PB05 have also displayed the nuclear energy generation rate (erg/g/s) and the amplitude of the fundamental radial pulsation, scaled to 1.0 at the surface.
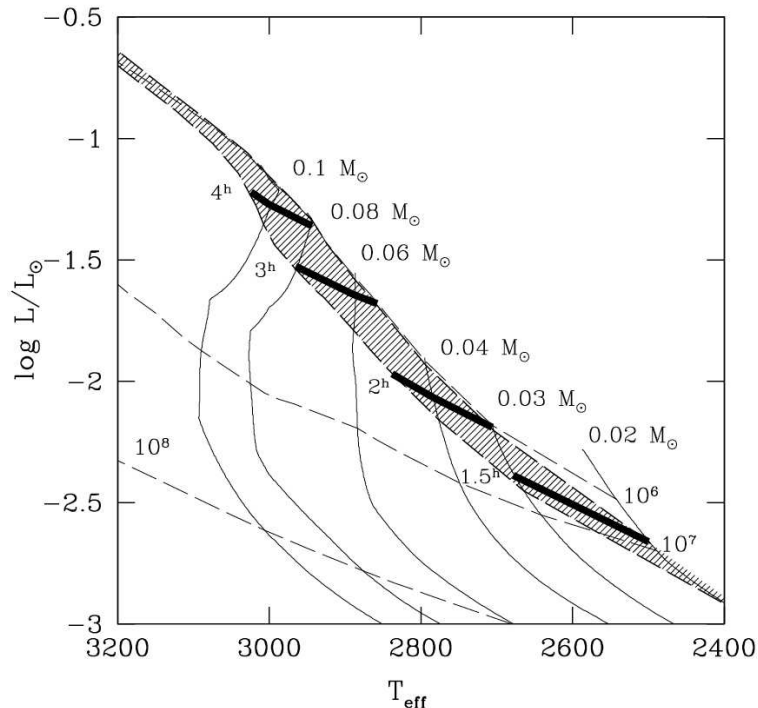
Figure 1.2 The deuterium-burning instability strip (dashed lines) on the H-R diagram, reproduced from Palla & Baraffe (2005). Their isochrones and evolutionary tracks based on NextGen models are labeled with masses and ages. The black lines mark loci of constant pulsation period, from 1.5 to 4 hours.

timescale translates into a narrow region on the H-R diagram where pulsators are expected to lie. We reproduce PB05's instability strip in Fig. 1.2 along with their overplotted NextGen isochrones and evolutionary tracks. While there may be systematic errors in the computation of the strip (i.e., the neglect of convection), it currently offers the best guidance for the selection of candidate pulsators for observational scrutiny.

Given the strong predictions for this new type of instability, we have set out to search for it in young BDs and VLMS, in hopes of opening a new window into their interiors and evolution. With the recent discoveries of hundreds of low-mass objects in few-Myr-old clusters, we will assess the available sample of candidates and use them to confront the theory in the coming chapters.

1.4 Overview of the thesis

The primary goal of this work is to search for deuterium-burning pulsation in a large sample of young very low mass stars and brown dwarfs. To this end, we have designed a time series monitoring campaign on four young star-forming regions in the 1–5-Myr age range: IC 348, σ Orionis, Chamaeleon I, and Upper Scorpius. We have employed a number of ground and space-based telescopes, including the Palomar 60-inch telescope, the Cerro Tololo Interamerican Observatory (CTIO) 1.0 meter telescope, the *Hubble Space Telescope*, and the *Spitzer Space Telescope*. The details of the survey design and execution are provided in Chapter 2, whereas the collected data and search results are presented in Chapter 4.

For many of our observed fields, we obtained photometry on not only VLMSs and BDs, but also numerous other cluster members in the 0.1–0.5 $M_\odot$ range. This rich dataset has enabled a more comprehensive study of the variability phenomena among young low-mass stars, which include rotationally modulated spot features, accretion signatures, stellar flares, eclipses, and occultations by disk material. Through the detailed study of the additional light curves, we address many of the questions posed in §1.2. Our assessment of the resulting relationships between variability, angular momentum, accretion, and disks, including the extension of these properties into the relatively uncharted very low mass regime, are highlighted in Chapter 5.

This thesis is intended to not only explore the science behind variability and pulsation in young, very-low-mass objects, but also to provide a primer on the techniques of high-precision photometry under different observational setups. The goal of discovering or placing stringent limits on the amplitude of deuterium pulsation entailed much fine tuning of the photometric extraction procedures. It led to exquisite high-cadence light curves, particularly from observations on the CTIO 1.0 m telescope. In Chapter 3 we present the lesson learned and strategies developed for obtaining photometric precisions down to several millimagnitudes.

Auxiliary data, such as spectral types, extinction, and luminosities, are crucial for placing objects on the H-R diagram and assessing their cluster membership properties. For a subset of targets in σ Orionis, spectroscopy was limited and membership was uncertain. Therefore, we conducted low-resolution spectroscopic follow-up observations of selected objects in our σ Orionis fields that displayed variability. Several of these appear to be new

cluster members, and we present the collected data from the Palomar 200-inch telescope Double Spectrograph in Chapter 6.

Finally, in Chapter 7, we summarize the main findings of the photometric monitoring campaign and discuss the prospects for observing deuterium-burning pulsation in young BDs and VLMSs.

Chapter 2

Survey Framework

2.1 The cluster sample

The prospect of detecting pulsation in young BDs and VLMSs is exciting and yet highly dependent on the existence of a suitable observational sample. Because the pulsation instability strip is fairly narrow compared to the characteristic range of luminosities observed in 1–10 Myr clusters, most very low mass members of a typical young, roughly coeval population will not be candidate pulsators. The success of our survey therefore relies in part on a large sample size. To select suitable clusters for the campaign, we also required that the known population extend into the substellar regime where pulsation is predicted to occur, and that the members be bright enough for high-precision photometry with telescope apertures of up to a few meters. Consequently, we limited the cluster distance to 500 pc. The level of extinction in some of the star-forming regions further restricts the feasibility of photometrically monitoring candidates for pulsation.

Our campaign relied heavily on previous work establishing the presence and locations of very low mass deuterium-burning objects. Fortunately the study of young star clusters, and in particular, characterization of their low-mass stellar and substellar members, has received increasing attention with the advent of near-infrared photometric surveys and focused spectroscopic techniques. These regions are an important arena for testing scenarios for the formation and subsequent evolution of stars, brown dwarfs, and planets. Most cluster surveys to date have selected candidates based on proper motions or colors, and confirmed membership by identifying features of youth (e.g., strong Hα emission or low-gravity lines) in follow-up spectra. However, the rich variety of phenomena in these regions, as traced by

x-ray activity, photometric variability, accretion, and circumstellar disk signatures, provides alternative methods for uncovering young stellar and substellar objects.

In recent years, substantial populations of very low mass stars (VLMSs) and brown dwarfs (BDs) have been identified in open clusters and star forming regions (e.g., Hillenbrand & Carpenter 2000; Slesnick et al. 2006a; Luhman et al. 2003b; Eiroa et al. 2006; Luhman 2007). We compiled a list of the young clusters in the 1–10 Myr range whose known populations (as of the 2007 campaign inception) extend into the substellar regime. As a starting point, we investigated the catalog of nearby (e.g., within 1 kpc) young clusters and groups presented by Porras et al. (2003). Notably missing from this list are diffuse star-forming regions such as Taurus-Auriga and Upper Scorpius, whose members are spread over many degrees of sky and do not cluster around a single molecular cloud. We added them to the compilation since they harbor numerous spectroscopically confirmed young objects, some of which are low enough in mass to still be burning deuterium.

The resulting list of 16 low-mass star-forming clusters considered is assembled in Table 2.1. Since there were too many regions to cover during the $\sim$3 year duration of the photometric campaign, we narrowed down the target list by considering additional properties, including number of known BDs, distance, and extinction. Areas containing a large number of very low mass members within small areas of sky (i.e., $< 1°$) were given priority. Only a few clusters in the 1–10 Myr range contain enough catalogued, unobscured, very low mass members to enable monitoring of more than one or two BDs simultaneously in the optical band. Among these are IC 348 and σ Orionis. The latter provided particularly promising targets for our pulsation search, since the objects S Ori 31, S Ori 45 had already been claimed as short-term variables (Bailer-Jones & Mundt 2001; Zapatero Osorio et al. 2003). We focused further on objects with previously established spectral types, as these result in better estimates of effective temperatures than do colors alone. The combination of effective temperature and luminosity (reliant on accurate estimates of distance, extinction, and magnitude) enable placement on the H-R diagram and comparison with the location of the deuterium-burning pulsation instability strip. Finally, we strived to select clusters comprising a range of evolutionary statuses, since the instability can be more prominent at a particular ages, depending on object mass.

The regions ultimately chosen for study included Chamaeleon I, Upper Scorpius, IC 348, σ Orionis, and Taurus. As such, the monitoring program covers a significant fraction of

the spectroscopically confirmed very low-mass objects in young star-forming areas. The 1-5 Myr range of these clusters enables testing the effect of not only mass, but also age, on our results, ultimately allowing a comparison of observed trends with pulsation theory predictions. In §2.2 we present the assembled census (as of 2007) of young objects in these regions with masses less than 0.1 $M_\odot$. Their properties and locations shaped the observing strategy and determined the specific pointings subsequently chosen for the photometric campaign.

2.2 Preliminary census of potential targets

Many very low mass young cluster members are now catalogued and thus available for time series monitoring. Nevertheless, there is a wide range in both the quality and quantity of data available on them. In some cases, only basic photometry or tentative x-ray identifications exist, whereas in others there is complete confirmation of membership, including spectra with youth-specific lines, spectral types, and infrared excesses indicative of disks. To choose BDs and VLMSs suitable for the photometric monitoring campaign, we needed not only to be confident that the selected targets were young, but also that they had a high probability of exhibiting pulsation, based on luminosity and temperature consistent with PB05's predicted position of the pulsation instability strip. For most of the clusters, observations of one or two fields would only cover a fraction of the known members. Therefore it was crucial to optimize the field positions to include as many pulsation candidates as possible. This task was initiated by searching the literature relevant to each of the five chosen clusters and noting which objects had spectral types later than M4 (corresponding to $\lesssim 0.2$ $M_\odot$, and a high likelihood that they are still burning deuterium) as well as established membership, to rule out status as a field dwarf. The collected data was then used to produce H-R diagrams and ultimately compare the positions of known BDs and VLMSs with the deuterium-burning instability strip, so that the best pulsation candidates could prioritized for observation. We now provide an overview of this data for each of the chosen clusters, as was available during the campaign planning stage in 2007.

Table 2.1.   Nearby young clusters and star-forming regions with spectroscopically confirmed and likely candidate brown dwarfs

Region	Age (Myr)	Number of BDs[1]	Distance (pc)	Sky area	Extinction (A_V)	References
Taurus	1–3 Myr	55	145±15	$200^{\circ\,2}$	0–2	1
Chamaeleon I	1–3 Myr	14	160–170	$3^{\circ\,2}$	0–5	2
Upper Scorpius	5 Myr	91	145±2	$250^{\circ\,2}$	0–1	3
IC 348	2–3 Myr	22	315	$1000'^{\,2}$	0–6	4
ρ Ophiuchus	0–2 Myr	27[a]	120±5	$1000'^{\,2}$	5–50	5
σ Orionis	5 Myr	37	440±30	$1^{\circ\,2}$	0–1	6
ϵ Orionis	8–10 Myr	11[a]	440	$1^{\circ\,2}$	0–1	7
Lupus 3	1 Myr	10	200	$5^{\circ\,2}$	5–15	8
Serpens	4 Myr	45	230±20	$10^{\circ\,2}$	5–10	9
R Coronae Australis	3 Myr	6	150	$600'^{\,2}$	5–50	10
NGC 2024	0.5 Myr	23	415	$150'^{\,2}$	1–15	11
NGC 1333	0.5 Myr	22[a]	300	$200'^{\,2}$	0–15	12
Chamaeleon II	4 Myr	7	178	$2^{\circ\,2}$	1–20	13
25 Orionis	7–10 Myr	8	330	$1^{\circ\,2}$	0–1	14
λ Orionis	4–6 Myr	14	450±50	$15^{\circ\,2}$	0-1	15
Orion Nebula Cluster	1–3 Myr	∼150	414±7	$800'^{\,2}$	1–50	16

Note. — a refers to clusters lack of spectroscopically confirmed brown dwarfs. [1]The number of BDs quoted refers to the known population as of 2007 when campaign planning was underway. References are as follows: (1) Briceño et al. (1998), Martín et al. (2001), Briceño et al. (2002), Luhman et al. (2003a), Luhman (2004b), Guieu et al. (2005), Luhman (2006), Kraus & Hillenbrand (2007); (2) Whittet et al. (1997), Bertout et al. (1999), Luhman (2004a), Comerón et al. (2004); (3) de Zeeuw et al. (1999), Ardila et al. (2000), Preibisch et al. (2002), Martín et al. (2004), Slesnick et al. (2006a), Lodieu et al. (2006); (4) Luhman (1999), Luhman et al. (2003b), Luhman et al. (2005b), Muench et al. (2007); (5) Wilking et al. (1999), Cushing et al. (2000), Torres-Lopez et al. (2007); (6) Barrado y Navascués et al. (2003), Béjar et al. (2004); (7) Scholz & Eislöffel (2005), citetBriceno:2005p6877; (8) Comerón et al. (2003), Martí et al. (2005), Allen et al. (2007), Comerón (2008); (9) Lodieu et al. (2002), Klotz et al. (2004), Eiroa et al. (2006); (10) Wilking et al. (1997), Fernández & Comerón (2001); (11) Anthony-Twarog (1982), Levine et al. (2006); (12) Wilking et al. (2004), Greissl et al. (2007); (13) Whittet et al. (1997), Spezzi et al. (2007), Spezzi et al. (2008); (14) Briceño et al. (2007); (15) Dolan & Mathieu (2001), Barrado y Navascués et al. (2004), Barrado y Navascués et al. (2007), Mathieu (2008); (16) Hillenbrand (1997), Slesnick et al. (2004), Menten et al. (2007), Rio et al. (2009), Rodríguez-Ledesma et al. (2009), Reggiani et al. (2011),

2.2.1 Sigma Orionis

The σ Orionis cluster was first identified by Wolk (1996) and Walter et al. (1997) via clustered sources of x-ray emission in ROSAT observations. Possibly associated with the Orion OB1b subgroup, the cluster of low-mass stars surrounds the O9.5V binary star σ Ori AB. At a distance of 440 pc (Sherry et al. 2008), angular extent of ~1 square degree, [Fe/H] of -0.02 (González Hernández et al. 2008), and low extinction ($E(B\text{-}V) = 0.05$; Lee 1968), the cluster is a convenient target for photometric and spectroscopic studies. Indeed, prior surveys have revealed a rich population of 338 confirmed members (Caballero 2008, and references therein), along with some ~300 additional candidates from photometry, proper motions, and x-ray detections (e.g., Lodieu et al. 2009; Sherry et al. 2004; Franciosini et al. 2006). Béjar et al. (1999) and Zapatero Osorio et al. (2000) presented an initial sample of candidate low-mass cluster members, for most of which spectral types were later determined by Barrado y Navascués et al. (2003). Subsequent surveys (e.g., Sherry et al. 2004; Burningham et al. 2005; Kenyon et al. 2005) have augmented the list of low-mass candidate members via photometric selection in the near-IR, spectroscopic analysis of Hα, Na I, and Li lines, as well as characterization of mid-IR excesses indicative of disks (e.g., Hernández et al. 2007). While most of these methods do not rule out the presence of foreground and background sources, the contamination rate from photometry alone is expected to be relatively low (~15% based on the color-magnitude distribution of a non-cluster field; Lodieu et al. 2009).

2.2.1.1 Very low mass members

We compiled a list of likely and candidate σ Orionis cluster members from Béjar et al. (1999), Béjar et al. (2001), Barrado y Navascués et al. (2001), Barrado y Navascués et al. (2003), Béjar et al. (2004), Caballero et al. (2004), Sherry et al. (2004), Scholz & Eislöffel (2004), Burningham et al. (2005), Kenyon et al. (2005), Franciosini et al. (2006), Caballero et al. (2007), Hernández et al. (2007), Caballero (2008), Luhman et al. (2008b), and Lodieu et al. (2009), including available signatures of youth and kinematic measurements. Of these sources, only a few provide spectral types derived from low-resolution spectra (as opposed to estimated from color relations, as is done in Sacco et al. 2008). To carry out a preliminary assessment of the number of pulsation candidates, we assembled a list of objects with masses

estimated to be less than 0.2 $M_\odot$ (or spectral type equal to or later than $\sim$M4) and optical or near-infrared photometry available for the derivation of luminosities (as of 2007). We provide this list below in Table 2.2. We note that although we have derived spectral types for many additional σ Orionis objects (Chapter 6), these were not available at the time of the campaign start, so we do not include them here.

2.2.1.2 H-R diagram

Placement of objects on the H-R diagram requires accurate values for their temperatures and luminosities. Temperatures were estimated from spectral types via the intermediate gravity temperature scale derived by Luhman et al. (2003b), which accounts for the lower gravity of young objects compared to field dwarfs and is appropriate for the young objects studied here. In addition, they have been calibrated for consistency with the Baraffe et al. (1998) low-mass evolutionary models, on which the pulsation instability strip from PB05 is based.

Luminosities of σ Ori members are dependent upon the estimated distance to the cluster. This value has often been taken to be 350^{+120}_{-90} pc, based on the Hipparcos parallax of σ Ori AB itself. However, Sherry et al. (2008) showed that a distance of 440^{+30}_{-30} is more consistent with main sequence fitting to observations of cluster A stars. Jeffries et al. (2006) pointed out that what has traditionally been considered the σ Ori cluster is in fact likely a superposition of two kinematically distinct groups with different radial velocities, ages, and distances. They propose that one of the populations corresponds to the Orion OB1a and OB1b association subgroups, while the other is associated with the star σ Ori itself. With these considerations in mind, we adopt the Sherry et al. (2008) distance but for completeness we also explore (in §7.1) the effect of the smaller value on our computed luminosities and positions on the H-R diagram. The resulting distance moduli, m-M, are 8.21$\pm$0.15 and 7.72 $\pm$0.65 magnitudes. Extinction toward σ Ori is relatively low, and we adopted A$_J$ = 0.044 (Barrado y Navascués et al. 2003).

Final luminosities were determined with J-band magnitudes from Barrado y Navascués et al. (2003), Caballero (2008), and Béjar et al. (1999). Both the J and I bands are generally favored for their relative lack of contamination from accretion and disk excess. However, bolometric corrections in J have the additional advantage of being less sensitive to color and surface gravity age (e.g., Luhman 1999). We adopted the bolometric corrections used

Table 2.2. σ Orionis: Candidates with spectral type M4–M9, known as of 2007

Object	R.A.	decl.	I	SpT	Membership	Refs
SOri-J053949.3-022346	05:39:49.4	-02:23:46	15.14	M4	Li,Hα	d
SOri-J054001.8-022133	05:40:02.0	-02:21:33	14.32	M4	IR,Li,Hα	d
SOri-J053715.1-024202	05:37:15.2	-02:42:02	15.07	M4	Li	d
SOri-J053820.1-023802	05:38:20.2	-02:38:02	14.41	M4	Li	d
SOri-J053911.4-023333	05:39:11.4	-02:33:33	16.731	M5	low g, VR, Hα	g
SOri-J053826.1-024041	05:38:26.1	-02:40:41	16.96	M6,M8	low g, Li	g,c
SOri-J053829.0-024847	05:38:29.0	-02:48:47	17.040	M6	IR	a,h
SOri-J054005.1-023052	05:40:05.1	-02:30:52	15.9	M5	Li	d
SOri-J053847.5-022711	05:38:47.5	-02:27:11	14.46	M5	Li	d
SOri-J053951.6-022248	05:39:51.6	-02:22:48	14.59	M5.5	Li,Hα	d
SOri-J053825.4-024241	05:38:25.4	-02:42:41	16.86	M6	nIR	c
SOri-J053838.6-024157	05:38:38.6	-02:41:57	16.38	M5.5	low g,VR,Li	a,c
SOri-J053954.3-023719	05:39:54.3	-02:37:19	16.79	M6	IR	a,b,c
2M J05390756-0212145	05:39:07.8	-02:12:13	17.06	M5	Hα	e
2M J05384928-0223575	05:38:49.4	-02:23:58	15.83	M4	Hα	e
2M J05381279-0212266	05:38:12.9	-02:12:28	16.62	M5.5	Hα	e
r053820-0234	05:38:20.4	-02:34:09	14.58	M4	Li,Hα	d
SOri15	05:38:48.0	-02:28:54	16.789	M5.5	low g, VR, Hα	a,g
SOri17	05:39:04.4	-02:38:35	16.945	M6	log g, Li,Hα	b
SOri22	05:38:35.2	-02:25:24	17.109	M6	low g, VR, Hα	g
SOri25	05:39:08.8	-02:39:58	17.163	M7.5	Hα	b
SOri27	05:38:17.3	-02:40:24	17.08	M7	low g, VR,Li,Hα	d,g
SOri28	05:39:23.1	-02:46:56	17.11	M5	low g, VR	f,g
SOri29	05:38:29.5	-02:25:17	17.230	M6.5	low g, VR	g
SOri30	05:39:13.0	-02:37:51	17.438	M6	IR,Hα	d,h
SOri38	05:39:15.1	-02:21:52	17.640	M7	IR,Hα	d,h
SOri39	05:38:32.4	-02:29:58	17.922	M6.5	low g, VR	g
SOri40	05:37:36.4	-02:41:57	17.93	M7	nIR,low g, VR	b,g
SOri42	05:39:23.3	-02:40:57	19.01	M7.5	nIR,Hα	d
SOri45	05:38:25.6	-02:48:36	19.724	M8.5	Li,Hα	d
SOri55	05:37:25.9	-02:34:32	21.32	M9	low g, Hα	i

Note. — Membership criteria includes spectral lines indicative of low gravity and hence youth ("low g"), lithium absorption ("Li"), a radial velocity consistent with the cluster ("VR"), broad Hα emission, and infrared or near-infrared excess indicative of a disk ("IR," "nIR"). References: [a]Caballero et al. (2007), [b]Muzerolle et al. (2003), [c]Caballero et al. (2006), [d]Barrado y Navascués et al. (2003), [e]Scholz & Eislöffel (2004), [f]Franciosini et al. (2006), [g]Kenyon et al. (2005), [h]Hernández et al. (2007), [i]Zapatero Osorio et al. (2002)
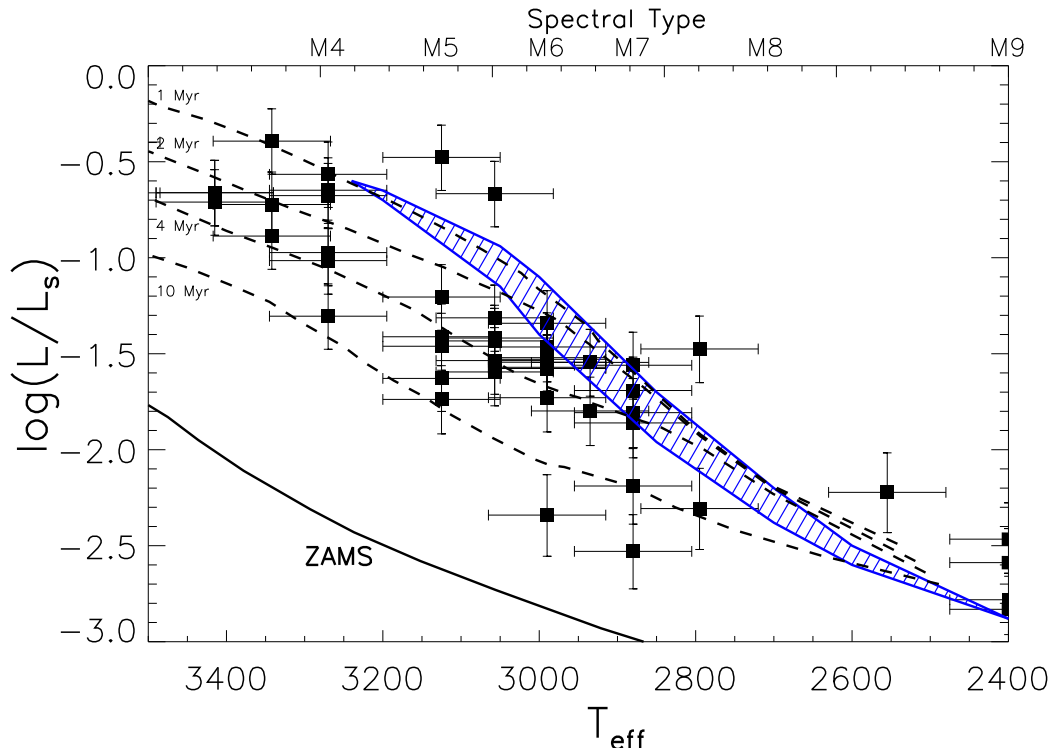
Figure 2.1 All known low-mass σ Orionis members with spectral types are plotted on the H-R diagram, along with the deuterium-burning instability strip from PB05 (blue dashed region). Effective temperature (T_{eff}) is in Kelvins, and luminosity is in solar units (L_{S}). We have overplotted isochrones from Baraffe et al. (1998). With typical errors of 75 K in temperature and 0.15–0.2 dex in log luminosity, many of the data points are on or near the instability strip, suggesting that they might exhibit pulsation.

in Kraus & Hillenbrand (2007), and also used those of Caballero et al. (2007) to check that the results were relatively insensitive to the form of the corrections as a function of color and spectral type; we adopt their value of 0.15 magnitudes as a typical uncertainty.

We show the computed locations of all late-type objects with available spectral types on the H-R diagram with respect to the theoretical pulsation instability strip in Fig. 2.1, for both possible distance modulus values. Uncertainties in luminosity include photometric and bolometric correction errors. However, the true errors are dominated by the systematic uncertainty in the distance to the cluster.

Additional systematics may be introduced by the choice of band used to calculate the luminosity. We performed a comparison test of luminosities derived from the I band for a representative subset of objects with available I-band photometry. There is an approx-

imately uniform discrepancy of ~ 0.35 dex between luminosities derived from the J-band magnitudes, versus the I-band magnitudes. One might conclude that the J-band magnitudes include contributions from circumstellar disks, but in fact the J-band luminosities are *fainter*. Such a discrepancy may be caused by the unknown difference between the dwarf-like bolometric corrections adopted here and those that account for the lower surface gravities of young objects. We have retained the luminosities as derived from the J band but caution that the for computations relying on H-R diagram position (e.g., 7.1) there may be a systematic error in the results.

2.2.2   Chamaeleon I

The Chamaeleon I region is a collection of young stars and brown dwarfs associated with a dense, dark cloud visible from the southern hemisphere at Dec. $= -77°$, located at relatively high Galactic latitude ($b \sim -15°$). While some of its members remain embedded at ~ 3 Myr, it nevertheless has many more visible YSOs than its neighboring clouds, Cha II and Cha III. At a distance of ~ 160 pc (Whittet et al. 1997; Bertout et al. 1999), this region is particularly amenable to the characterization and study of a young population down through the substellar limit. Some of its T Tauri stars were initially discovered in the 1960s through slit spectrum surveys, and variability searches also suggested a large population of PMS objects (Bertout et al. 1999; Hoffmeister 1963; Henize 1963; Mendoza 1972). A population of emission line stars was later identified via objective prism spectroscopy (Henize & v 1973). Subsequent infrared imaging (Glass 1979; Hyland et al. 1982; Baud et al. 1984) uncovered further members of Cha I. These studies paved the way for more extensive investigations of the young population and its properties (Gauvin & Strom 1992, and references therein).

2.2.2.1   Very low mass members

The first confirmed brown dwarfs in Chamaeleon I were discovered by (Neuhauser & Comeron 1998), (Comerón et al. 1999), and (Comerón et al. 2000). Further identification of substellar candidates followed with near-infrared variability studies (Carpenter et al. 2002), wide-field optical and Hα imaging (Martí et al. 2004), and low-resolution optical and near-infrared spectroscopy (Gómez & Mardones 2003; Comerón et al. 2004; Luhman 2004a). The most definitive census of Cha I members down through the substellar limit was put forth by Luhman (2007) and includes 226 confirmed young objects, a number of whom were

presented in the previous surveys. Since this compilation subsumes all previous surveys and contains spectroscopically derived spectral types, we used it as the sole input for our own list of very low mass Cha I members. A total of 121 confirmed Cha I members with spectral types equal to or later than M4 were known as of 2007.

2.2.2.2   H-R diagram

J-band photometry is available for most sources from the 2MASS point source catalog, but the bolometric luminosities computed by Luhman (2007) are already suitable for our purposes. He incorporated extinctions primarily from measurements of color excesses between 6000 and 9000 Åin optical spectra. Where spectra were not available, the extinctions were determined from near-infrared colors. Likewise, the adopted bolometric corrections and distance modulus (6.05) are detailed in Luhman (2007). Since individual uncertainties are not available, we have used the quoted typical error of 0.08 on all luminosities.

The second component required for placement on the H-R diagram is effective temperature. As with luminosity, we directly adopted the values provided by Luhman (2007). His spectral type uncertainty of 0.25 subclass is roughly equivalent to an error of ∼50 K in temperature; in case of systematics, we increase this to 75 K (roughly half a subclass). The resulting H-R diagram for very low mass Cha I members is shown in Fig. 2.2 along with PB05's deuterium-burning instability strip. The positions of a number of objects overlap the strip and are therefore promising pulsation candidates; these were prioritized for the selection of the photometric field.

2.2.3   IC 348

The IC 348 cluster is coincident with a nebula at the eastern edge of the Perseus Molecular Cloud. At an age of 2–3 Myr (Luhman et al. 2003b), it harbors a population of several hundred young T Tauri stars, brown dwarfs, and protostars (Muench et al. 2007) within an area of $\sim 0.2^{2\circ}$. The cluster distance is either 316±22 pc based on main sequence fitting (Herbig 1998) or 260±25 pc as suggested by Hipparcos parallaxes (Scholz et al. 1999).

Herbig (1954) conducted the first survey for cluster members with a slitless grism Hα study. The membership census grew subsequently with a number of infrared surveys (Strom et al. 1974), later x-ray (Preibisch & Zinnecker 2001, 2004), optical, and infrared imaging (Lada & Lada 1995; Trullols & Jordi 1997; Herbig 1998; Luhman et al. 1998; Muench et al.
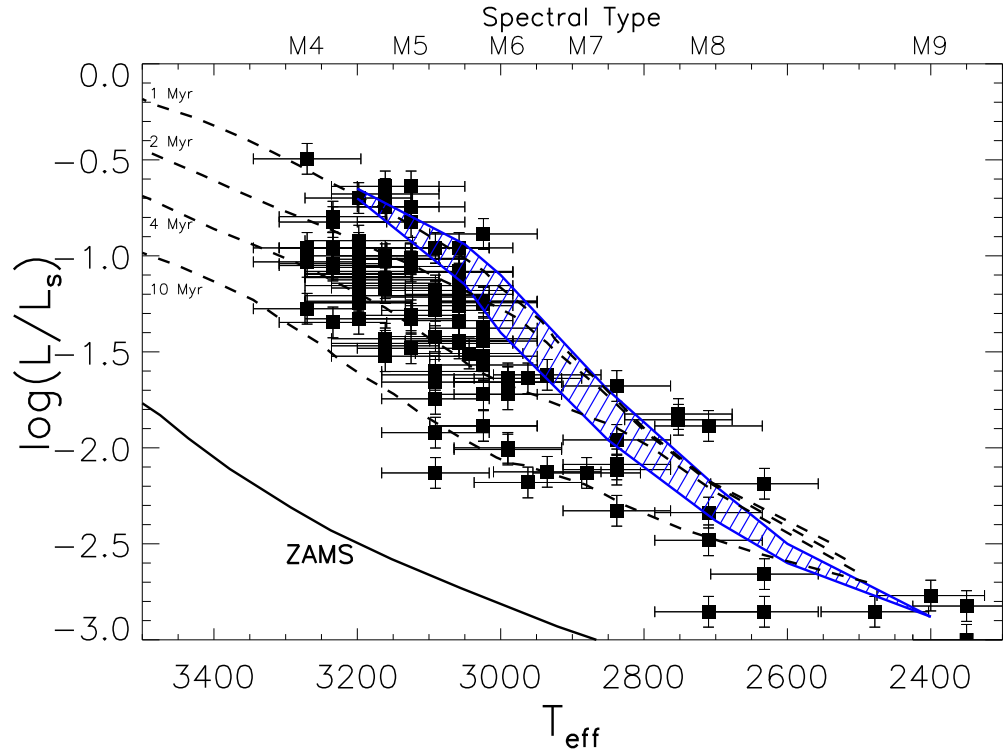
Figure 2.2 Known low-mass Cha I members with spectral types M4 and later are plotted on the H-R diagram, along with the deuterium-burning instability strip from PB05 (blue dashed region). Effective temperature (T_{eff}) is in Kelvins, and luminosity is in solar units (L_{S}). We have overplotted isochrones from Baraffe et al. (1998). With typical errors of 75 K in temperature and 0.1 dex in log luminosity, many of the data points are on or near the instability strip, suggesting that they might exhibit pulsation.

2003; Lada et al. 2006; Muench et al. 2007), and follow-up spectroscopy (Luhman 1999; Luhman et al. 2003b, 2005b). Most of the currently known IC 348 members are located near the center of the nebula, but several studies extending to up to half a degree ($\sim$1 pc) outside of the cluster core have suggested that further young objects are to be found in these regions (Cieza & Baliber 2006; Muench et al. 2007).

2.2.3.1 Very low mass members

While T Tauri members of IC 348 have been known for decades, the first $\sim$20 brown dwarfs in IC 348 were discovered more recently by Luhman (1999) and Najita et al. (2000). Eighteen additional sources consistent with L and T spectral types were uncovered by Mainzer & McLean (2003) with deep, narrowband photometry. The most up-to-date compilation of confirmed IC 348 members down through the substellar limit is available from Luhman et al. (2003b). His work provides both photometry in R through K bands, as well as low-resolution spectroscopic follow-up to confirm membership and derive spectral types for 288 IC 348 members, including 23 BDs. A later paper (Luhman et al. 2005b) presented an additional 14 M-type IC 348 objects, most of which are probably just above the substellar limit. Muench et al. (2007) found additional members based on the Spitzer survey of Lada et al. (2006), including 8 presumed substellar objects (based on a spectral type boundary of M6). Using these three sources, we have compiled a list of the known very low mass cluster members with available spectral types that are M4 and later.

2.2.3.2 H-R diagram

To compare the observed positions of IC 348 members with the predictions of deuterium-burning pulsation and select targets for our photometric campaign, we placed all low-mass objects on an H-R diagram. Fortunately luminosities and temperatures for all sources are available from Luhman et al. (2003b) and Muench et al. (2007). Luminosities were derived via J-band bolometric corrections, assuming a distance modulus of 7.5. Luhman et al. (2003b) argues for this distance derived from main sequence fitting, as opposed to the lower value suggested by Hipparcos data, based in part on the detection of δ Scuti pulsations in one of the stars by (Ripepi et al. 2002). Muench et al. (2007) provide uncertainties on the bolometric luminosities, which we have also adopted. These do not include systematic errors in distance modulus, but in our later pulsation analysis, we explore the effect of
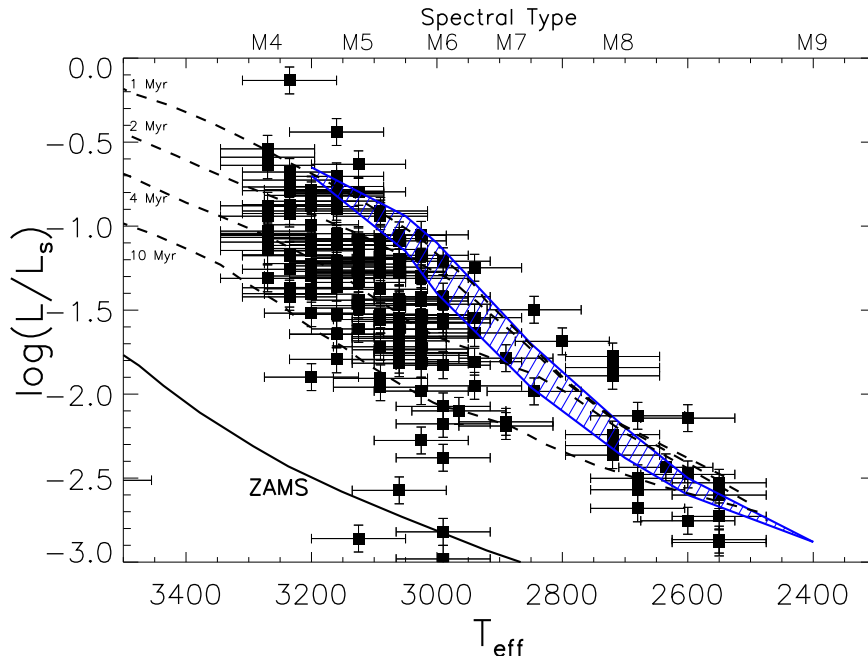
Figure 2.3 Known low-mass IC 348 members with spectral types M4 and later are plotted on the H-R diagram, along with the deuterium-burning instability strip from PB05 (blue dashed region). Effective temperature (T_{eff}) is in Kelvins, and luminosity is in solar units (L_{S}). We have overplotted isochrones from Baraffe et al. (1998). With typical errors of 75 K in temperature and 0.15–0.2 dex in log luminosity, many of the data points are on or near the instability strip, suggesting that they might exhibit pulsation.

both possible distances on the H-R diagram and position of objects with respect to the deuterium-burning instability strip.

Temperatures were also estimated by both Luhman (2003) and Muench et al. (2007) from a spectral type scale that is between that of field dwarfs and giants, to incorporate the lower surface gravities characteristic of young objects. However, Muench et al. (2007) used an older version of this scale that was presented by Luhman (1999), differing only for spectral types M7 and later. We have adjusted the effective temperatures of Muench et al. (2007) for consistency with the more up-to-date scale. With 75 K error bars (roughly half a subclass) in T_{eff}, we illustrate the collection of 192 VLMSs and BDs in IC 348 on the H-R diagram in Fig. 2.3.

2.2.4 Upper Scorpius

Part of Scorpius Centaurus OB Association, Upper Scorpius ("USco") is 145 pc distant (de Zeeuw et al. 1999) and covers many degrees on the sky. While widely dispersed, many candidate members were first uncovered as part of x-ray surveys (Walter et al. 2; Preibisch et al. 1998; Kunkel 1999) and subsequently followed up with optical photometry and spectroscopy. Isochrone fits to the temperatures and luminosities of low-mass PMS stars in USco indicate that its age is approximately 5 Myr with little spread (Preibisch & Zinnecker 1999).

A handful of the USco candidates identified via x-ray emission (such as those presented Kunkel 1999) have yet to be confirmed at other wavelengths. Because they are spread so far apart, spectroscopic confirmation of USco membership and investigation of stellar properties was made more efficient by the development of multi-object spectrographs (e.g., Preibisch et al. 2002). A proliferation of wide-field surveys has now increased the known membership to several hundred (Ardila et al. 2000; Preibisch et al. 2001, 2002).

2.2.4.1 Very low mass members

More recent work has extended the USco census well into the substellar regime and uncovered nearly 100 brown dwarfs, primarily through large-area optical and near-infrared photometric surveys, along with dedicated spectroscopic follow-up. For example, Ardila et al. (2000) uncovered 138 USco candidates, 20 of which have available spectroscopy including features indicative of very low mass, and 10 of these are likely substellar (assuming a spectral type boundary of M6). Further studies by Preibisch et al. (2001), Martín et al. (2004), Slesnick et al. (2006a), and Lodieu et al. (2006) increased the number of known BDs in USco to ~60. Additional very low mass USco members were recently presented byLodieu et al. (2011) and Dawson et al. (2011), but these were not known at the time of our own survey planning. Since these objects are dispersed over many square degrees on the sky, it was only possible for us to photometrically monitor a small fraction of them. This made it especially important to select pulsation candidates with solid membership evidence and accurate photometry and spectral types for placement on the H-R diagram.

2.2.4.2   H-R diagram

As with the other clusters under consideration, we assimilated data on candidate very low mass objects, from which we deduced effective temperatures and bolometric luminosities. Spectral types for BDs and VLMSs in USco were derived to approximately half a subclass by Ardila et al. (2000), Preibisch et al. (2002), Martín et al. (2004), Slesnick et al. (2006a), Lodieu et al. (2006), and Slesnick et al. (2008). Slesnick et al. (2006a; 2008) were the only authors to list effective temperatures in their work, but the adopted conversion from spectral type to effective temperature employed values typical of field M dwarfs. To account for the lower surface gravity of young objects, we instead estimated new T_{eff} values using the intermediate temperature scale derived by Luhman et al. (2003b), as described above in §2.2.1.2. For all other sources, we have also converted the derived spectral types to temperature using this scale. We adopted conservative uncertainties in T_{eff} of 100 K.

In addition to estimating temperatures, we derived bolometric luminosities from J-band photometry since these were not provided in the literature. An exception is Slesnick et al. (2006a; 2008), but they did not list uncertainties. We lifted J-band photometry where available from the original sources, or from the 2MASS point source catalog, depending on which had lower uncertainties. Extinction in USco is very low, so we did not correct for this. Bolometric corrections were determined by fitting the values used by Slesnick et al. (2008) as a function of J-K and interpolating to the colors of our sample. Finally, we adopted the mean distance to USco of 145±2 pc, which is very accurately determined from Hipparcos parallaxes. However, since the the spatial spread of individual members may be up to 15–20 pc (Preibisch et al. 2002), we include this systematic effect in the estimation of uncertainties on bolometric luminosities.

The resulting H-R diagram of 324 very low mass USco members known as of 2007 with spectral types M4 and later is presented in Fig. 2.4. Evidently many of these objects are potential pulsation candidates, and we selected for observation several of those whose positions appear to overlap with the deuterium-burning instability strip.

2.2.5   Taurus

The Taurus-Auriga star-forming region is a collection of dark clouds with a well-known population of young stars dispersed over many square degrees of sky. With the discovery of
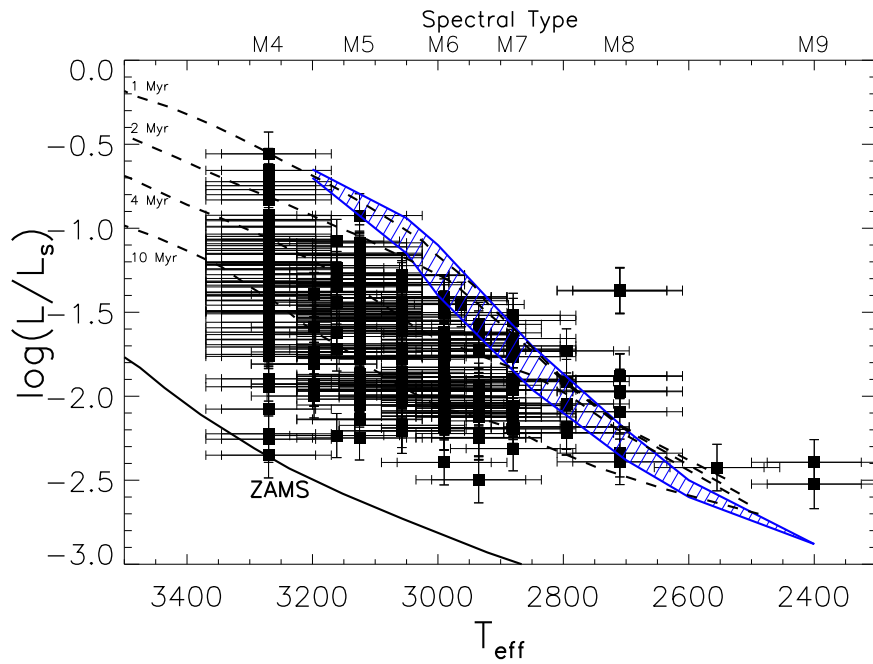
Figure 2.4 Known low-mass Upper Scorpius members with spectral types M4 and later are plotted on the H-R diagram, along with the deuterium-burning instability strip from PB05 (blue dashed region). Effective temperature (T_{eff}) is in Kelvins, and luminosity is in solar units (L_{S}). We have overplotted isochrones from Baraffe et al. (1998). With typical errors of 75 K in temperature and 0.15–0.2 dex in log luminosity, many of the data points are on or near the instability strip, suggesting that they might exhibit pulsation.

the M6 brown dwarf V410 X-ray 3 (Strom & Strom 1994), it was also one of the first areas known to host substellar pre-main-sequence objects. Kenyon & Hartmann (1995) began to characterize the low-mass Taurus population in earnest, discovering a number of objects near the substellar limit, along with many other higher mass stars.

Since then, further searches for members have expanded the census of BDs to over 50 (Briceño et al. 2002; Reid & Hawley 1999; Martín et al. 2001; Briceño et al. 2002; Luhman et al. 2003a; Luhman 2004b; Guieu et al. 2005; Luhman 2006; Slesnick et al. 2006b). We collated the Taurus objects with spectral types M4 and later from these sources in order to assess the prospects for observing D-burning pulsation in this region. Unfortunately observations of Taurus were not ultimately carried out, but we nevertheless present the assembled H-R diagram here, in the case that photometric monitoring of promising pulsation candidates is continued in the future.
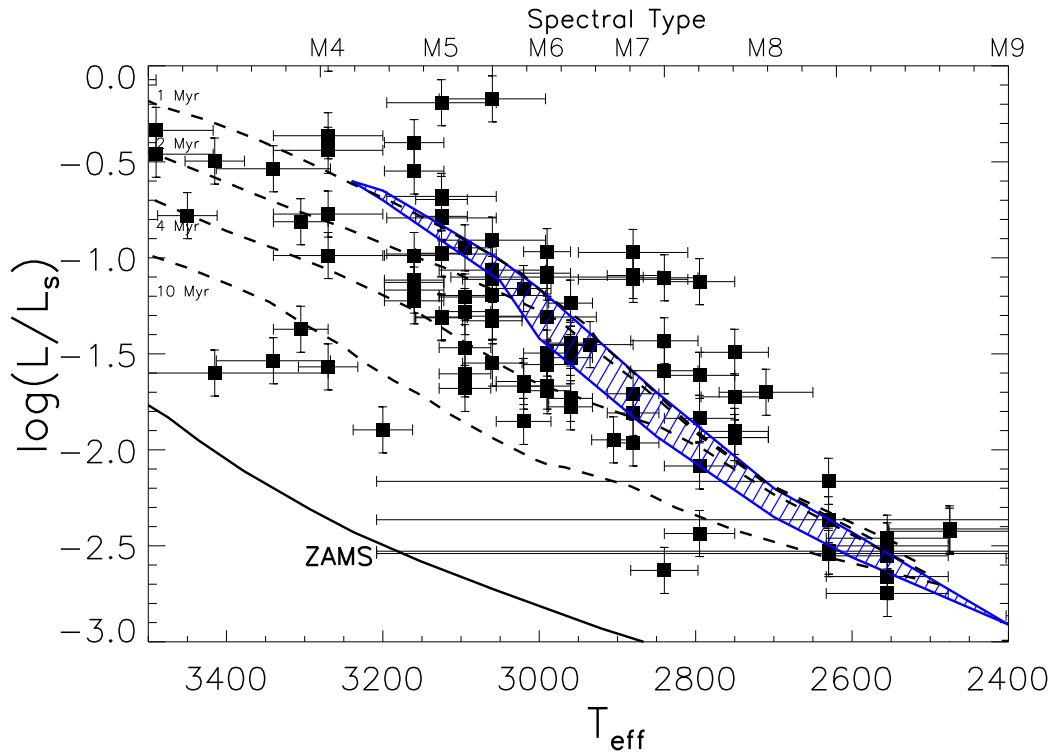
Figure 2.5 Known low-mass Taurus members with spectral types M4 and later are plotted on the H-R diagram, along with the deuterium-burning instability strip from PB05 (blue dashed region). Effective temperature (T_{eff}) is in Kelvins, and luminosity is in solar units (L_{S}). We have overplotted isochrones from Baraffe et al. (1998). With typical errors of 75 K in temperature and 0.15–0.2 dex in log luminosity, many of the data points are on or near the instability strip, suggesting that they might exhibit pulsation.

2.3 Identifying pulsation: detection of periodic signals

Compilation of a list of suitable very low mass objects falling on or near the deuterium-burning instability strip is the first step in initiating a campaign to detect pulsation. However, just as crucial as target selection is the planning of the observations themselves. Since the phenomenon is predicted to involve sinusoidal light curve variations with ∼1–4-hour periods and unknown amplitude, we aimed to optimize the photometric observations for both precision as well as sensitivity to signals on these timescales.

To ensure that the planned photometric setups were suitable for the detection of low-amplitude pulsation, we adopted a period detection algorithm and performed feasibility simulations with it prior to executing any observations. Here we describe the basic strategies employed to detect periodic signals, and the mathematical principles underlying them.

2.3.1 The Fourier transform periodogram for signal detection

While many sophisticated period detection algorithms exist today, perhaps the most basic and well known is the Fourier transform (FT). Essentially a method of decomposing a function into its sinusoidal components, it returns the relative strengths of different frequencies that are present in data. While the FT has been largely superseded by other techniques that are faster and have more predictable noise properties, it remains a cornerstone of signal detection theory. We can use the basic properties of the FT to understand and predict how photometric datasets with particular precisions and time sampling and properties will appear in frequency space.

In the case of an infinite data stream, represented by $f(t)$, the Fourier transform, $F(\nu)$, is given by

$$F(\nu) = \int_{-\infty}^{\infty} f(t)e^{-i\nu t}, \tag{2.1}$$

omitting a normalization factor. This computation is of course invalid for realistic datasets since they are not only finite in length, but also have a discrete data acquisition rate set by the exposure cadence, as well as gaps due to daylight and weather interruptions. However, we can nevertheless compute a truncated version of the FT over the points in time where data is available. The result is not the true Fourier transform, but rather a version exhibiting lower frequency resolution as well as aliasing–leakage of a signal into other frequencies. This

discrete Fourier transform (DFT) is given by

$$F(\nu) = \frac{2}{N} \sum_1^N f(t_k) e^{-i\nu t_k} = \frac{1}{N} \sum_1^N f(t_k)(\cos(-\nu t_k) + i \sin(-\nu t_k)), \qquad (2.2)$$

where N is the total number of data points, and t_k are the time stamps of each point (with corresponding value $f(t_k)$). The normalization factor $2/N$ is such that the peak value of the Fourier transform matches the amplitude of the input time series, $f(t_k)$, if the latter is a pure sinusoid (i.e., no noise). Typically, only the amplitude of the DFT is considered, and its absolute value comprises the classical periodogram, P:

$$P(\nu) = (\frac{2}{N}(\sum_1^N f(t_k) \cos(-\nu t_k))^2 + (\sum_1^N f(t_k) \sin(-\nu t_k))^2)^{1/2}. \qquad (2.3)$$

When $f(t)$ is a sinusoid, the corresponding FT is a Dirac delta function, $\delta(\nu)$–infinite response at a single frequency. The DFT, on the other hand, contains signals at multiple frequencies, by virtue of gaps in the data stream. The particular response of a signal in frequency space is often referred to as the window function. As we will show below, every true signal–originally a simple delta function– becomes convolved with this pattern when the Fourier transform is performed over discrete data points. Thus it is important to know the form of the window function for a given dataset, so that one can distinguish between the case of multiple true signals and a single signal with a number of aliases.

Insight into the effect of dataset length, cadence, and other temporal features in the data acquisition on the window function can be gained by considering the properties of the FT in more detail. We can model the DFT by taking an input sinusoidal time series and multiplying it by a series of hat and comb functions that represent gaps when no data was taken. To illustrate how this works, we define several functions and timescales. The Dirac Comb (otherwise known as the Shah or replication function), $III_\tau(t)$, is an infinite collection of delta functions, evenly spaced at timescale τ:

$$III_\tau(t) = \sum_{n=-\infty}^{\infty} \delta(t - n\tau). \qquad (2.4)$$

The hat function, $\Pi_\tau(t)$, is designed to filter out data on timescales longer than τ :

$$\Pi_\tau(t) = \begin{cases} 1 & \text{for } |t| \leq \tau/2 \\ 0 & \text{otherwise} \end{cases} \tag{2.5}$$

For an observing run of total duration T, nightly hours D, and cadence C, we can describe the time sampling, $w(t)$ as follows:

$$w(t) = \{[\mathrm{III}_C(t) \cdot \Pi_D(t)] \star \mathrm{III}_1(t)\} \cdot \Pi_T(t), \tag{2.6}$$

where $\mathrm{III}_1(t)$ refers to a comb function with peaks spaced at one day intervals, and $\star$ is a convolution. This scenario assumes that data were taken at an even rate every night, without interruption. It is in any case a good toy model for showing how different data taking setups affect the eventual ability to detect periodic signals. Once again representing the true data (for example, a light curve) with the function $f(t)$, the observed data is then $f(t) \times w(t)$. Each function has an FT, which we denote $F(\nu)$ and $W(\nu)$, respectively. In Fourier space, a product of functions becomes a convolution, i.e.,

$$f(t) \cdot g(t) \leftrightarrow F(\nu) \star G(\nu), \tag{2.7}$$

where $\leftrightarrow$ represents the FT for any functions f and g with corresponding Fourier transforms F and G. Thus a Fourier transform of the data is not $F(\nu)$, but instead $F(\nu) \star W(\nu)$. $W(\nu)$ is typically referred to as the window function, and it is this pattern that determines how a collection of sinusoidal signals will appear in frequency space.

What does the window function look like? We can use the mathematical properties of Fourier transforms to illustrate its chief features. We note that the Fourier transforms of the Hat and Dirac comb are simple analytical functions:

$$\mathrm{III}_\tau(t) \leftrightarrow \frac{1}{\tau}\mathrm{III}_{1/\tau}(\nu), \tag{2.8}$$

and

$$\Pi_\tau(t) \leftrightarrow \tau\,\mathrm{sinc}(\pi\nu\tau). \tag{2.9}$$

Therefore, we find that the window function corresponding to $w(t)$ is

$$W(\nu) = \{[\frac{1}{C}\text{III}_{1/C}(\nu) \star D\text{sinc}(\pi\nu D)] \cdot \text{III}_1(\nu)\} \star T\text{sinc}(\pi\nu T). \qquad (2.10)$$

Each of the functions involved in $W(\nu)$ has a particular effect on the window function, which we show pictorially in Fig. 2.6. First, the part within the braces is convolved by $T\text{sinc}(\pi\nu T)$, which is a sinc function of width $\sim T^{-1}$. This represents a lower limit on the frequency resolution. In other words, the longer the time series, the narrower the peaks of any sinusoidal signals found in Fourier space. Next, the term $\text{III}_1(\nu)$ is a Dirac comb with spacing of one cycle per day (cd^{-1}). The rest of the window function (i.e., part in brackets) will be multiplied by this function, resulting in an FT with evenly spaced values; this is the primary reason why aliases from ground-based data appear at 1 cd^{-1} intervals. Next, we have the term $D\text{sinc}(\pi\nu D)$, which has width of approximately $1/D$. Thus, this main part of the window function will be narrower the longer the time spent observing during each night is. Finally, the function $\frac{1}{C}\text{III}_{1/C}(\nu)$ is a comb of spacing $1/C$. Since it is present in a convolution, the window function pattern will repeat and hence contain no new information after an interval of $1/C$. Conversely, if one extracts the periodogram values between $-1/(2C)$ and $1/(2C)$, then to reconstruct the function at sampling rate C. In fact, the FT as we have defined it is symmetric, so one actually only needs the values from 0 to $1/(2C)$. This is the basis of the well-known Nyquist limit, which states that if function does not have any structure at frequencies higher than $1/(2C)$, then sampling at a rate $1/C$ (or cadence C) is sufficient to completely recover its form.

As we can now see, the duration of an observing run, data cadence, and fraction of the night spent observing have implications for the appearance of sinusoidal signals in the DFT. If we assume that an input function, $f(t)$, may be represented by a sum of sinusoids, then its FT, $F(\nu)$, will be a series of delta functions, each indicating the presence of a signal at that frequency. When we take into consideration the convolution with the window function, $W(\nu)$, then each signal takes on a width of $\sim T^{-1}$, and some of its power leaks into additional peaks offset by 1 cd^{-1}. The height of these aliases drops off as the separation from the main signal reaches $\sim D^{-1}$. This model for the appearance of the DFT is accurate for observations that do not contain interruptions either within a night or between nights. For more unevenly sampled data, the window function is increasingly complex and does not
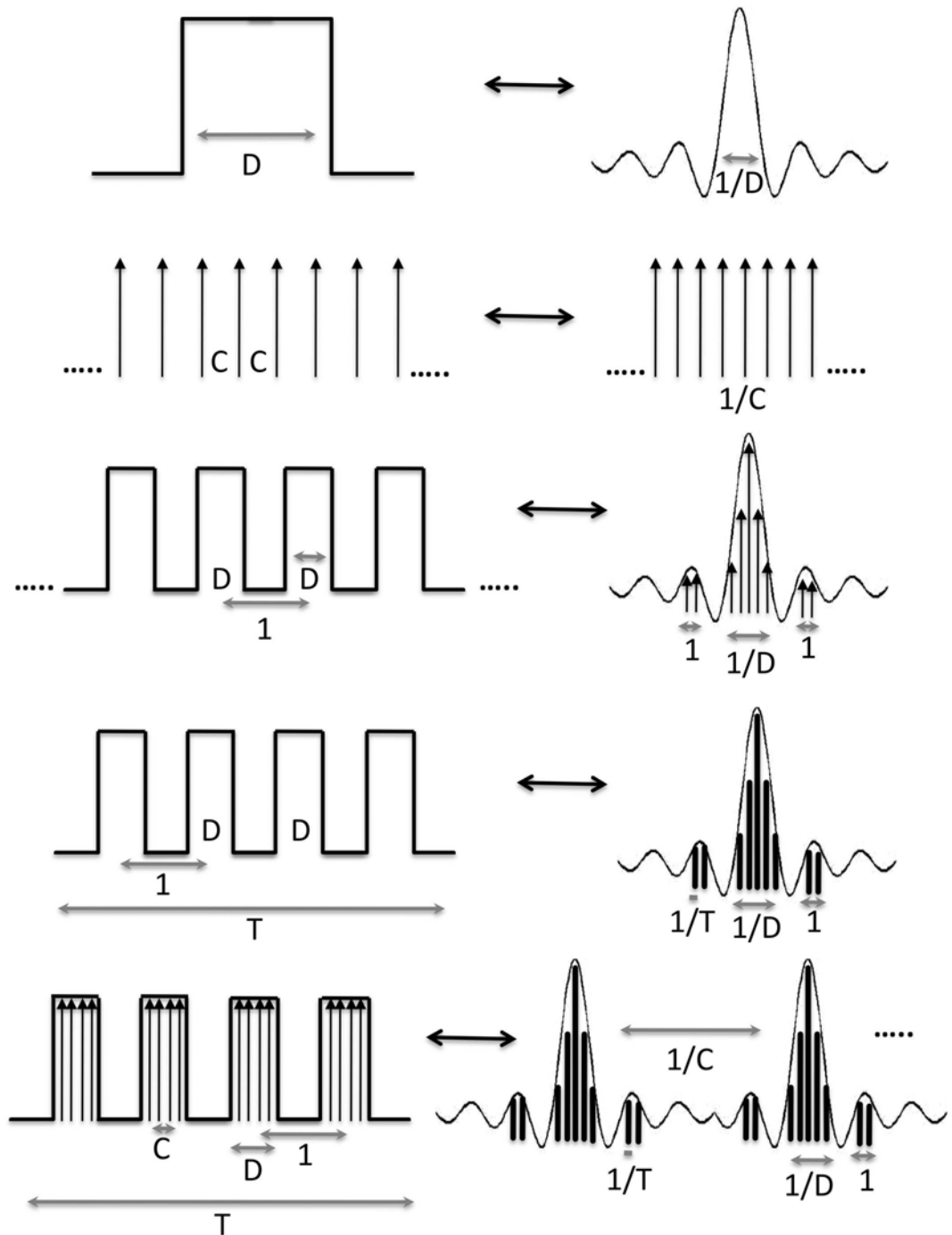
Figure 2.6 We illustrate the relationship between various timescales in the data acquisition sampling pattern (left side) and the corresponding window functions (right side). The timescales D, C, and T are defined in the text, and horizontal arrows represent the Fourier transform. Vertical arrows are Dirac delta functions, and the undulating pattern (as in the top right) is a sinc function. Series of dots imply that the displayed functions continue ad infinitum.

have a well-defined Nyquist limit. Nevertheless, it can be derived by setting all data points equal to one and computing the DFT.

2.3.2 Period-finding prescriptions

To simulate our datastreams and their window functions in advance, as well as analyze the eventual light curves, we tested several signal detection algorithms. Since pulsation is expected to be sinusoidal or nearly so, a Fourier transform (FT) should be sufficient to detect the phenomenon in our light curves. While the FT and its discretized version are fairly straightforward and easy to use, they can be computationally intensive. The Fast Fourier Transform (FFT) was developed to provide a quicker routine when evenly spaced data are available. A number of additional tools have been developed over the years for the identification of periodic behavior in light curves. These include the Lomb-Scargle periodogram (Lomb 1976; Scargle 1982; Horne & Baliunas 1986), SigSpec (Reegen 2007), Phase Dispersion Minimization (Stellingwerf 1978), and phase-binned analysis of variance (ANOVA; Schwarzenberg-Czerny 1989, 1996). Each has its own advantages, depending on the type of statistic desired and whether the behavior under investigation is expected to be sinusoidal or some other form of periodicity. For example, an advantage of the Lomb-Scargle periodogram is that the false alarm probability (FAP) may be calculated analytically if the background noise is white. FAPs for detected peaks may be determined from the prescription of Horne & Baliunas (1986), which is valid even for datasets with non-uniform time spacing. They estimated FAPs based on large simulations of data with added Gaussian noise, and their result depends on the number of independent frequencies, which they denote N_i. The formula for the parameter N_i is a function of the total number of data points and has been shown to significantly overestimate FAPs for small datasets (Reegen 2007). This issue is not of great concern to the current study, given the typical 300–500 points from each observational run. However, the test must still be used with caution, since it assumes all noise sources are white. In reality, datasets tend to be at least partially correlated and frequency-dependent red noise (see §2.3.4) contributes significantly to the light curve RMS on $\sim$1 day and longer timescales. As a result, the FAP may be an underestimate.

Despite shortcomings, the Lomb-Scargle periodogram is useful for rapidly identifying objects with no detectable periodic variability. We used it as an initial procedure to cull each of our datasets of non-variables. With a selection criterion of FAP < 1%, we assembled an initial set of possible periodic variables for additional analysis. We then subjected the

much smaller set of remaining light curves to a higher frequency resolution analysis with the DFT algorithm using the Period04 program (Lenz & Breger 2005). This package not only calculates DFTs of the data, but it also has the capability to take peaks identified in frequency space and perform a Marquardt non-linear least-squares fitting algorithm (Bevington & Robinson 1992) to fine tune the frequencies, phases, and amplitudes. While its results are similar to those from the Lomb-Scargle periodogram, Period04 oversamples frequencies by a factor of 20 and contains an extended analysis package to calculate phases, subtract out signals, and search for periodicities at lower levels.

The statistical significance of any detected signals is an important consideration; since the amplitudes of D-burning pulsation are not predicted by theory, we must therefore be cautious about identifying low-level signals that may in fact be noise. Fortunately Breger et al. (1993) has performed extensive simulations of sinusoidal signals in the presence of noise, and has identified the 99% confidence threshold for detection in the DFT. They find this to be reached at a signal-to-noise ratio of 4.0, where the noise is measured locally around the frequency of the signal. This is a crucial point, as most realistic noise sources do not produce uniform power distributions in frequency space (e.g., §2.3.4). The Breger et al. (1993) result allows us to assess the likelihood of a signal being real, regardless of the frequency at which it appears or what the mean periodogram noise level is.

Once a signal has been detected with confidence, it is useful to determine errors for the derived frequencies and amplitudes. Although these may be computed analytically in terms of the average light curve noise and number of data points Breger et al. (1999), this approach is known to underestimate the true uncertainties. The least-squares fit also provides an error matrix, but neither of these methods fully account for the properties of noise in the frequency domain. We have therefore opted to run a set of 500 Monte Carlo simulations with Period04 for each object displaying periodic variability. The detected signals are subtracted out, and remaining noise data points are randomly rearranged such that the original timestamps are preserved. The identification of periodogram peaks and least-squares fit to the light curve is then carried out as before for each simulated light curve. The distribution of frequencies and amplitudes returned by these simulations then determine our uncertainties. Since the distributions are not strictly Gaussian, we estimate $1-\sigma$ uncertainties based on the values enclosing 68% of the simulated data. For signals that are near the detection limit, the simulations take into account the possibility that noise

causes an alias to be selected instead of the true peak.

After a periodicity has been identified and its parameters refined, one can then search for further significant frequencies in the residual periodogram, which is derived from the original light curve after the fitted sinusoid has been subtracted out. The least-squares analysis is repeated simultaneously for all identified frequencies, resulting in an adjusted set of parameters. We find Period04 to be the best-suited periodogram tool in the search for pulsation, since it is not only efficient in fitting for signals at multiple frequencies, but it also does so in a relatively conservative manner. Comparisons with other period detection programs have shown that although Period04 may detect fewer signals, it is generally more reliable, in the sense that noise peaks are less likely to be included in the final list of identified frequencies Breger et al. (2011). The fact that the algorithm does not hinge on an assumption of white noise further boosts our confidence in the results.

To account for the possibility of periodic variability that departs significantly from a sinusoid (e.g., eclipsing binary), we also considered the phase dispersion minimization method. The popular algorithm by Stellingwerf can identify periods in distinctly shaped light curves, but tests (B. Sesar 2011, private communication) have shown a similar program developed by Kunkel (1999) to do so with higher accuracy. We have experimented with this so-called "super-smoother" algorithm in cases where variability other than brown dwarf pulsation may be operating.

2.3.3   Selecting time baseline and cadence: white noise simulations

We have so far only hinted at the relationship between noise in the time domain and noise in the frequency domain. Since all realistic time series are subject to errors, their associated periodograms will be a sum of whatever signals are present (modulo the window function) with a noise spectrum. To model the composite DFT, we need to have an idea of what this noise looks like. Stellar photometry typically consists of multiple noise components, but only the random, or "white" aspect is easy to predict without prior knowledge of an observational setup and a target object's temporal properties. Therefore in performing feasibility simulations to assess the ability to detect pulsation, we have only incorporated Gaussian errors. We will discuss the complications introduced by systematic, or "red," noise in §2.3.4.

The goal of our white noise simulations was to identify the minimum amplitude for pul-

sation that would be detectable via various combinations of photometric cadence, precision, and total observing duration. All three of these parameters influence the mean noise level in the periodogram, and hence the SNR at which a periodic signal may be identified. Setting a threshold SNR (for example, 4.0, as discussed above) results in a corresponding amplitude limit, which we can estimate by further manipulating the mathematics of the DFT.

In general, the uncertainty in the periodogram may be estimated via Parseval's theorem, which states that the integral of square of the uncorrelated noise in the time domain equals the integral of the power of the noise across all frequency space:

$$\int_{-\infty}^{\infty} (f(t))^2 \mathrm{d}t = \int_{-\infty}^{\infty} |F(\nu)|^2 \mathrm{d}\nu, \tag{2.11}$$

where $F(\nu)$ here has been defined without the $2/N$ normalization factor. An alternate form of the theorem arises when the time series is finite with N data points:

$$\sqrt{< F(\nu)^2 >} = \sqrt{\sum_{1}^{N} f(t)}. \tag{2.12}$$

This identity enables us to calculate the signal-to-noise ratio (SNR) of a signal detection when the amplitude and noise level are known in advance. If we return the normalization factor to the definition of the DFT, as in Eq. 2.2, then the left side becomes

$$\frac{N}{2}\sqrt{< F(\nu)^2 >} \equiv \frac{N}{2} \times \text{Noise}, \tag{2.13}$$

where "Noise" represents the RMS of the DFT periodogram. The right side of Eq. 2.13 is simply the RMS of the time series, which we denote σ_f. Since we have normalized the DFT so that the height of any peaks are equal to the amplitude of the corresponding sinusoids, we can equate a "Signal" with amplitude, denoted A.

Combining these facts, we see that the SNR in the Fourier domain is given by

$$\frac{S}{N} = \left(\frac{A}{2\sigma_f}\right)\sqrt{N}, \tag{2.14}$$

where σ_f represents the RMS error in a typical magnitude measurement. N can also be specified by $T \times f/C$, where T is the number of nights of data, f is the fraction of each day available to observations, and C is the photometric cadence in data points. Obviously the

best signal-to-noise will be achieved with the highest photometric precision. However, it is not so clear as to how one should choose the total observing duration and fraction of the day spent taking data so as to optimize the periodogram SNR at a particular frequency. Eq. 2.14 yields similar S/N for large T and small f (many nights of observing with sparse data collection) as it does for smaller T and larger f (a few nights with excellent coverage). Ideally, an observing run would be as long as possible and encompass as large a fraction of the night as possible. However, this is not always practical, depending on a given observatory's time allocation process. Often a compromise must be struck between the two parameters. The value of T sets the precision at which the frequency of a signal may be determined in the periodogram. The value f, on the other hand, controls the accuracy of the frequency estimate, insofar as it sets the heights of surrounding aliases, and hence how easily a true signal may be confused with periodogram peaks differing by intervals of 1 cd^{-1}. The optimal values of T and f thus depend very much on the available time as well as the particular sampling pattern and photometric noise. They are best selected by simulating each observing run separately.

Before performing any simulations, we outline our minimum requirements for the detection of pulsation. Since the phenomenon is predicted to encompass periods from $\sim$1–4 hours, we must tune the time sampling for sensitivity to frequencies between 6 and 24 cd^{-1}. The Nyquist theorem tells us that we just then sample at an average rate of at least two data points per hour–or 30 minute cadence. We would like to leave room for error and also the possibility of combining data points to increase signal-to-noise, so we enlarge this requirement to a cadence of at least 15 minutes.

As for the maximum desirable timescale, this need not be much longer than 4 hours for the purposes of pulsation detection, unless we suspect large errors in the period predictions of PB05. However, there are other important reasons to lengthen the total observing duration to multiple days. Young stars are known to be variable on these longer timescales, and their rotation periods typically range from 1–10 days. By collecting data over a week or two instead of a single night, we have the chance to detect (and distinguish) not only pulsation but rotation-related flux changes, as well as perform auxiliary studies of young star variability phenomena.

The final element needed for input to white noise simulations is the photometric precision. Realistically, we can expect to reach precisions of a few millimagnitudes with ground-

based differential photometry (as discussed in Chapter 3). Furthermore, previous ground-based observing campaigns (e.g., Hartman et al. 2005; Everett & Howell 2001; Gilliland et al. 1993) have demonstrated that sub-millimagnitude photometric precision is possible on stars as faint as $R = 16.3$. Atmospheric scintillation prevents ground-based photometric from achieving better than fractional millimagnitude precision, while second-order extinction effects raise this limit further in the near-infrared bands. While our brown dwarf targets are generally quite dim ($I = 17$ to 21), we nevertheless planned for precisions of $\sigma \sim 0.01$ magnitudes, achieved by combining sets of two or three closely-spaced exposures.

To see the effect of different combinations of window functions and photometric precision on pulsation detection, we now provide several examples of observing setups considered for the campaign. We have considered two ground-based scenarios, as well as one space-based telescope (HST), for which we proposed and later received time. We require detection of a pulsation mode at greater than 99.9% confidence, or a signal-to-noise ratio of at least 4.0 in the DFT as prescribed by Breger et al. (1993). We have generated artificial light curves with periods of 1–4 hours (as expected for deuterium-burning pulsation), and added Gaussian noise at a level typical of either ground-based CCDs (~ 0.01 magnitudes) or space-based instruments (~ 0.005 magnitudes). Adopting various observing cadences and total times as well as different pulsation amplitudes, we obtain corresponding sets of artificial data and Fourier spectra, from which the known pulsation signal can be extracted and its significance evaluated.

We illustrate example simulations of data expectations from various telescopes in Figs. 2.7 through 2.9. In these cases, the input light curve was a sine curve with 2 hour period. The first of the simulated scenarios was a 14 night observing run with 6 hours of data per night and 7 minute photometric cadence. This yields 84 hours of photometry and a total number of data points $N = 720$. Using $N = 720$ and $\sigma = 0.01$ in Eq. 2.14, and setting the signal-to-noise ratio threshold to be 4.0 for a detection confidence of 99.9%, we find that we can detect periodic signals down to amplitudes of 0.003 magnitudes. While the simulation itself (Fig. 2.7) confirms this, it also shows that the window function includes significant aliasing, which may result in misidentification of the true pulsation peak. Care must be taken to obtain follow-up confirmation of any periodicities identified (potentially via a new time series with different sampling). Furthermore, the simulation underlines the importance of obtaining data over a long time baseline, so that frequency resolution is
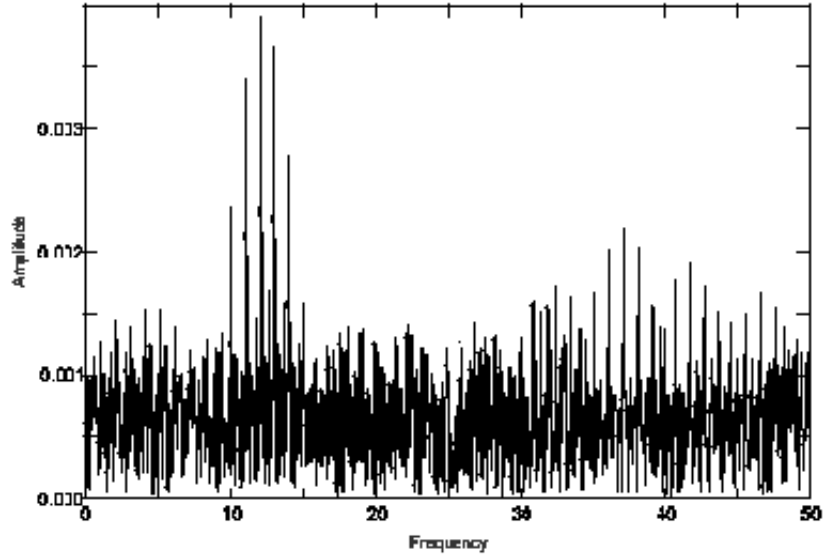
Figure 2.7 This periodogram simulation assumes 14 nights of ground-based data with 6 hours each, taken at a cadence of 7 minutes per exposure and typical estimated photometric precision of 0.01 magnitudes. Amplitudes are in magnitudes, and frequency is in units of cycles per day. The peak at 12 cycles/day is visible at a signal-to-noise ratio of 4.3; the peaks surrounding it are aliases due to daily gaps in the data and can be easily removed, as shown by our simulations.

adequate for accurately measuring frequencies of the detected signals.

In preparation for possible observing time on a space telescope, we have also simulated a time series with the *Hubble Space Telescope* (*HST*). The 97-minute orbit of this facility and scheduling constraints are such that the cadence, time sampling gaps, and total observing baseline are very different from those associated with ground-based telescopes. Based on what we know about the data-taking possibilities, we have simulated 40 orbits at 6 minute cadence and a 0.005 magnitude photometric precision. If we apply Eq. 2.14 we see that pulsation amplitudes of a millimagnitude should be reachable with *HST*. Again, the simulation cautions us that several prominent aliases will appear along with any signal in the periodogram.

Finally, we have simulated the scenario of a ground-based *network* of telescopes, such as what will eventually be available through the Las Cumbres Observatory Global Telescope (LCOGT). The advantage of this setup is that observations may be carried out continuously on the same field, as long as data from different telescopes may be satisfactorily merged. As a result, a shorter total duration of observation is required to reach the same detection
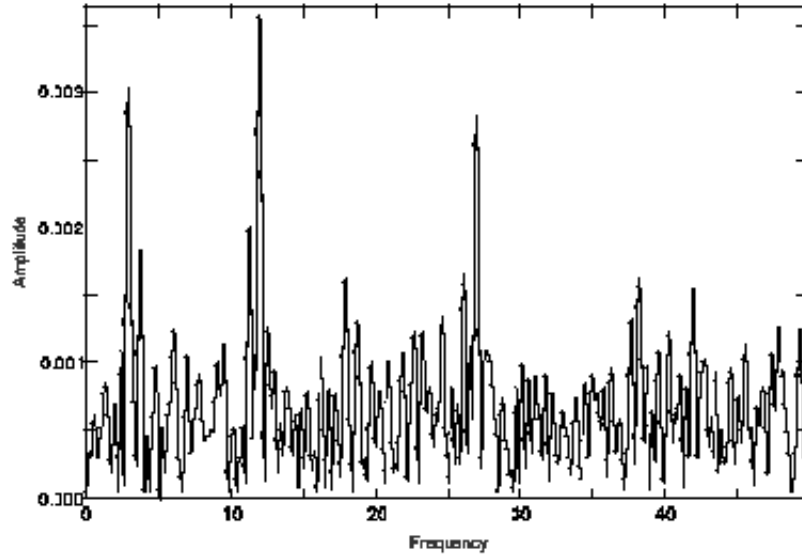
Figure 2.8 *HST* observations are simulated over 40 orbits at 6 minute cadence and 0.005 magnitude photometric precision. The peak at 12 cycles/day is visible at S/N = 4.2 (i.e., barely a significant detection), and the other peaks are aliasing due to gaps in the *HST* data.

limit. We have simulated a 4-day time series, leading to a predicted detection limit of 3 millimagnitudes for pulsation with a 2-hour period. Unlike the other ground and space-based telescope scenarios, the global network enables an alias-free periodogram. Thus, we can trust that signals detected above the selected S/N threshold are true periodicities in the light curve.

The series of white noise simulations have shown that with a fairly "typical" observing setup, we should be able to probe pulsation down to amplitudes in the 1–3 millimagnitude range. This is an order of magnitude lower than any previously reported short-period variability in young BDs and VLMSs. Based on the simulation results and the availability of various telescopes, we chose to anchor our campaign with a series of ∼2-week ground-based observing runs, collecting data for as much of each night as possible at 5–10 minute cadences.

2.3.4   Red noise and other systematics

A concern when using artificial datasets to simulate a time series is that the included Gaussian uncertainties do not represent realistic error sources. More typical noise often
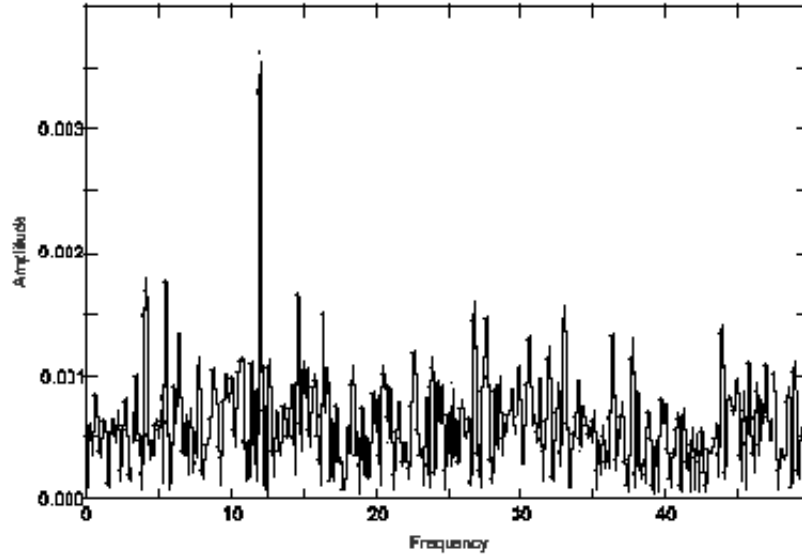
Figure 2.9 We simulate the Fourier periodogram of a light curve with a 2 hour period and added Gaussian noise, resulting from data taken by a ground-based global telescope network with continuous observing at 0.01 magnitude precision for 4 days. The expected peak at 12 cycles/day appears at S/N = 4.6.

has significantly correlated components, often referred to as "red noise". It is frequency-dependent and tends to contribute significantly to the light curve RMS on ∼1 day and longer timescales, whether through slow atmospheric changes or drifting instrumental features. Consequently, SNR values from white noise simulations can be somewhat overestimated at low frequency and underestimated at high frequency.

We cannot predict in advance how strong or frequency-dependent red noise will be in a particular dataset. However, looking ahead to some of the data that we collected as part of the ground-based photometric campaign with the CTIO 1.0 m telescope (§5.1.1), we can use a large collection of periodograms to illustrate systematic effects in the data. Such trends are often seen when color-airmass effects are not taken into account in the light curves, resulting in the appearance of intra-night variability. To examine the typical variability power distribution in frequency-amplitude space, we generated a mean periodogram from ∼1500 objects in each of the 2007 and 2008 fields, as seen in Fig. 2.10. This plot clearly displays a steep increase in the noise floor toward low frequencies, in addition to the mathematical clustering of "significant" peaks around integer frequencies due to the 1 day alias. We identify this effect as red noise and fit it with an exponential of form $P = a_0 + a_1/(f + a_2)$,

where P is power, f is frequency, and a_0, a_1, and a_2 are constant fitting parameters such that power declines to match the white noise baseline at $\sim 15\text{cd}^{-1}$ (e.g., "$1/f$" noise; Press 1978). The model for this $1/f$ component was later incorporated into our computation of detection limits for this particular dataset (§5.1.1.1).

As we can see, it is only after a dataset is acquired that its complete noise properties may be assessed. Nevertheless, the region of the periodogram where pulsation signals are expected (i.e., 6–24 cd^{-1}) is located at high enough frequencies that it should be relatively unaffected by the systematic effects seen in the example above. Thus we contend that the detection limits based on white noise simulations will remain relatively accurate.

2.4 Planning of the observing campaign

To amass a statistically significant sample of observations of BDs and VLMSs in several different young clusters and star-forming regions, our photometric monitoring program drew on a number of small-to-medium-sized telescopes. The white noise simulations suggested that runs of approximately two weeks apiece at 5–10 minute cadences offered the best chance of probing variability to below the 0.01 magnitude level on sub-hour timescales in these objects. Choice of photometric band was more of an open question, as the wavelength dependence of pulsation amplitudes is unknown and cannot be effectively determined without complex three-dimensional stellar simulations. Instead, we narrowed down the selection of filters by aiming to maximize signal-to-noise ratios in brown dwarfs, whose spectral energy distributions peak just longward of 1 μm, or approximately the J band. Complicating this picture are abundant TiO absorption features present in late-type stars, which have been suggested to make variability amplitudes larger at shorter wavelengths such as R or I band (Percy et al. 2001; Maiti 2007). Along with the fact that the longer wavelength near-infrared bands are preferentially affected by atmospheric absorption and variable sky emission, this motivated us to focus mainly on the I band. Practical issues, such as the field of view (FOV) size of detectors, also determined in part the filters available for observation. Many optical imagers (e.g., R, I), tend to have larger FOVs than those operating in the near-infrared (e.g., J, H, K) and are available for longer durations.

In addition to assessing combinations of time sampling and wavelength, we also considered the merits of observing with ground- versus space-based telescopes. Competition
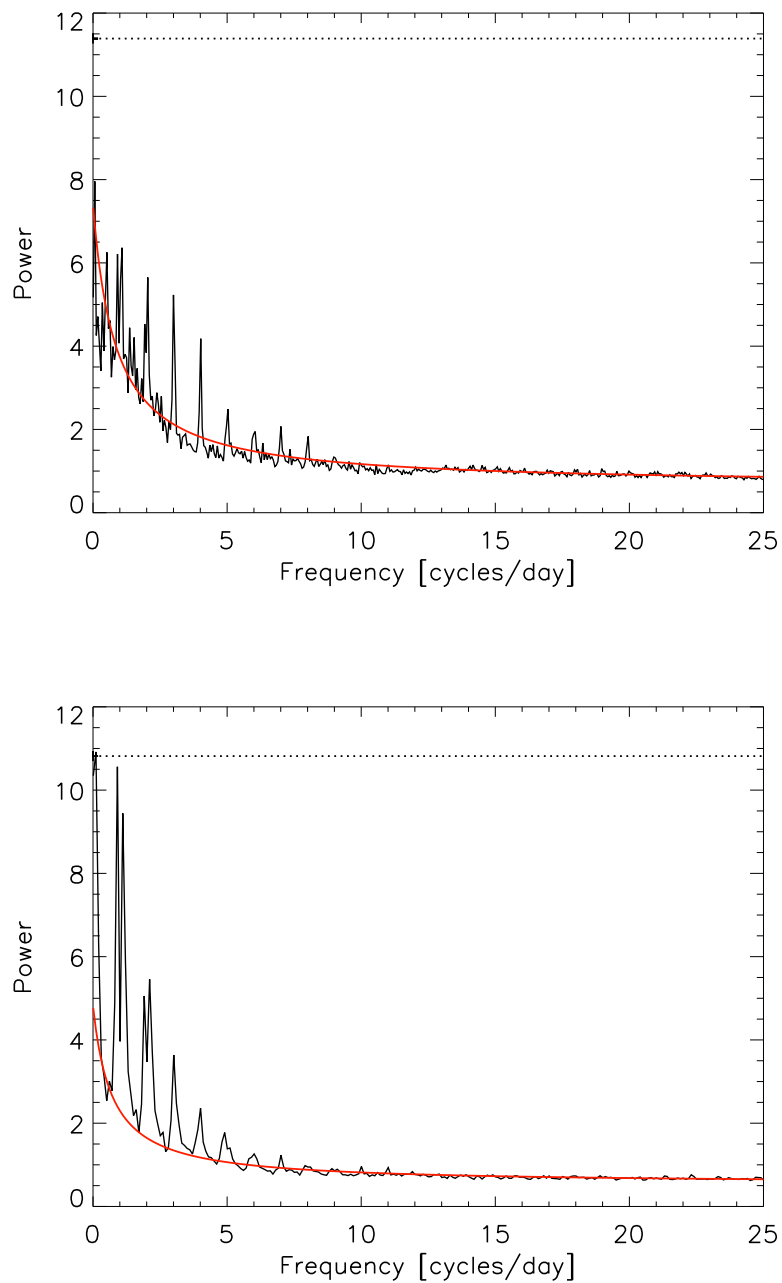
Figure 2.10 We present the average Lomb-Scargle periodograms for the ensemble of 2007 (top) and 2008 (bottom) data. Dashed lines show the analytically determined 99% detection limit, as estimated with the Lomb-Scargle formalism. Red curves indicate our fit to the noise as a function of frequency, disregarding the systematic peaks at integer values. The roughly constant noise floor continues out to the Nyquist limit at ∼65 (2008) and ∼100 c d^{-1} (2007).

for the latter is higher, but the lack of atmosphere is a distinct advantage when obtaining photometry from space. In preparation for both of these possibilities, we review some of the differences in observing strategy below. Additional details on the observing time ultimately awarded, along with the specific fields of view, bands, and exposures are provided in Table 2.3 as well as the discussion of individual clusters in Chapter 4.

2.4.1   Ground-based telescopes

Small (meter-class) ground-based telescopes were the backbone of the campaign, since they offered the largest continuous blocks of observing time. Furthermore, time on the Palomar 60-inch ("P60") telescope was acquired early on to perform tests of the observing strategy and variable-aperture data reduction procedures on several BDs in the Upper Scorpius association; this confirmed that photometric precisions of less than 0.01 magnitudes would be achievable with these modest apertures.

A ground-based observing run in the search for periodic variability functions best with limited interruptions, whether due to weather or other observational programs. We opted to obtain time on the P60, since the robotic setup enables an observer to gather data over many nights without being physically present. Unfortunately, scheduling of any one program is limited to 4–5 hours per night, or less when transient events receive priority. Most of the young clusters selected for our campaign are visible during the winter months (November to February) when cloud cover in the northern hemisphere is prominent. As a result, we also opted to obtain time on the Cerro Tololo Interamerican Observatory 1.0-meter telescopes ("CTIO 1.0 m"), operated by the SMARTS Consortium through the National Optical Astronomy Observatory. Located in the mountains of Chile, the CTIO 1.0 m enjoys mostly clear skies during northern hemisphere winter months and observers have full control of the telescope for the duration of their awarded time.

Efforts to use the Las Cumbres Observatory Faulkes North Telescope and the PAIRITEL robotic observatory to observe targets in Taurus were foiled by bad weather and scheduling problems. Therefore, we did not collect data on brown dwarfs in this region.

2.4.2   Space-based telescopes

Space telescopes offer a chance for deeper variability searches since the lack of atmosphere minimizes systematic errors in photometry, affording signal-to-noise ratios close to the Pois-

son limit. They also fulfill the need for dense and continuous time sampling by staring at a single patch of sky for extended periods of time without the inconveniences of weather, daytime interruption, or synoptic scheduling. Our white noise simulations (§2.3.3) demonstrated that the exquisite sensitivity of the *Hubble Space Telescope* can enable detection of brown dwarf pulsations down to amplitudes of several millimagnitudes over $\sim$35 orbits, even though observations may cover at most 60 minutes of each 97 minute orbit (because of visibility restrictions).

Additional progress may be made by observing in the infrared. While this band is not traditionally favored for photometric time series work, it has several advantages for the detection of low-amplitude variability in BDs. Because of their cool temperatures, BDs are brightest at wavelengths near 1 μm and thus should be amenable to relatively high signal-to-noise photometry in the near to mid-infrared. Optical observations reveal that variability in low-mass cluster members at the 1–10% level can be attributed to primarily rotational modulation of spots and variable accretion. The amplitude of brightness fluctuations produced by these mechanisms is expected to decrease with wavelength (e.g. Frasca et al. 2009), thereby reducing confusion between pulsation and other sources of variability. Thus while the amplitude range and wavelength dependence of pulsation are unknown (the linear stability theory of PB05 predicts only periods, as a function of mass), the lower temperature contrast between any magnetic spots or accretion flows and the photosphere may enhance the detection probability in the infrared.

As a result of the promising prospects for detection BD pulsation from space, we ultimately obtained time on both the *Hubble Space Telescope* with the Wide Field Camera 3 (WFC3) and the *Spitzer Space Telescope* with the Warm mission Infrared Array Camera (IRAC; Fazio et al. 2004; Werner et al. 2004). A primary challenge in planning these observations was the relatively small FOVs of the CCD detectors, which requires careful selection of targets. In the case of WFC3, we chose to further restrict the field size to one of two chips, or $162'' \times 81''$ since this "subarray mode" permits a higher data cadence. The field center (see Table 2.3) was chosen so as to maximize the number of brown dwarf targets for which either previous light curves or position on the H-R diagram suggest pulsational variability.

The *Spitzer*/IRAC fields are slightly larger, at $5.22' \times 5.22'$; during the Warm mission observations may be carried out in a 3.6 μm band, and a 4.5 μm band. We experimented

with the position of the 3.6 μm field as well as its orientation with respect to the 4.5 μm field, whose center is offset by $\sim$6.7′, to optimize the pointings and include as many pulsation candidates as possible.

In Table 2.3 we show the full set of observing runs planned and executed for the photometric monitoring campaign. Data for spectroscopic follow-up was also obtained, and is described later in Chapter 6.

Table 2.3. Photometric observations comprising the pulsation search campaign

Cluster	Telescope	Instrument	Field center (R.A., decl.)	FOV size	Dates	Duty cycle	Exposure times (seconds)	Band
σ Ori	CTIO 1.0m	Y4KCam	5:38:00.6, -02:43:44	20′×20′	Dec. 27, 2007–Jan. 7, 2008	25%	360	I, R
Cha I	CTIO 1.0m	Y4KCam	11:09:51.0, -77:27:44	20′×20′	May 13–25, 2008	25%	600	i, r
USco	CTIO 1.0m	Y4KCam	16:11:08, -22:12:04	20′×20′	May 13–16; 21–22 2008	15%	600	i, r
USco	CTIO 1.0m	Y4KCam	16:17:57.5, -23:45:41	20′×20′	May 23–25, 2008	15%	600	i, r
USco	P60	(CCD)	16:13:17.5, -19:27:00	12.′5×12.′5	June 1–14, 2008	13%	300	ip
IC 348	P60	(CCD)	3:44:21.8, +32:05:43	12.′5×12.′5	Nov. 17–23, Nov. 28–29, 2008	18%	240	ip, Cr
σ Ori	CTIO 1.0m	Y4KCam	5:39:31.1, -02:37:26	20′×20′	Dec. 14–24, 2008	28%	600	I, R
USco	P60	(CCD)	16:17:46.3, -20:54:18	12.′5×12.′5	May 14–30, 2009	13%	300	ip, rp
σ Ori	*Spitzer*	IRAC	05:38:23.3, -02:40:29	5.′2×5.′2	Oct. 22–23, 2009	100%	23.6	3.6 μm
σ Ori	*Spitzer*	IRAC	05:38:26.4, -02:47:13	5.′2×5.′2	Oct. 22–23, 2009	100%	23.6	4.5 μm
IC 348	*HST*	WFC3	03:44:19.5, +32:06:20	162″×81″	Jan. 29–Feb. 4, 2011	47%, 30%[a]	128, 171, 192	F814W

Note. — Lower-case band letters refer to the Sloan (SDSS) system; where R-band (r, R or Cr) observations are listed, there were at most two per night, to assess general colors of objects (but not enough to study variability). Abbreviations are as follows: P60 is the Palomar 60-inch telescope, *HST* is the Hubble Space Telescope, WFC3 is the Wide-Field Imaging Camera 3, IRAC is the Infrared Array Camera. Note: [a] The two duty cycles listed for the *HST* run refer to that of a single orbit (images were acquired for 46 of 97 minutes), and that of a single day (visits took place over ~7 hours, and further observations did not resume until approximately one day later).

Chapter 3

The Art and Science of Precision Photometry

3.1 Approaching the limits of photometric precision

With limited guidance from theory, the prospect of detecting D-burning pulsation in a relatively faint sample of brown dwarfs is a bit daunting. The potentially low amplitudes of this phenomenon require that we measure flux variations in these objects as precisely as possible. Photometric measurements are straightforward in principal, but much of the challenge in reducing uncertainties to better than the 1% level lies in the careful calibration of data as well as the removal of flux contributions from neighboring objects, sky background, and other potentially time-dependent "contaminants". In uncrowded stellar fields, CCD aperture photometry delivers optimal precision of point sources without detailed knowledge of the point-spread-function (PSF) shape of individual objects. Since our target clusters have typical stellar separations of $20''$ and above, we have focused on the former approach, as opposed to PSF fitting.

Typical pre-processing of images removes the CCD bias level and normalizes the detector response via flatfielding such that every digital count represents roughly the same number of incoming photons. The standard approach to performing photometry then involves a summation of all counts within an aperture of chosen size, centered on the object of interest. This is followed by subtraction of a background contribution estimated from the measurement of sky counts in an annulus surrounding the object and scaled to the area within the aperture. If the enclosed area does not encompass most of the object's light, a correction can be made to account for the missed flux. The final result may then be converted to an instrumental magnitude and potentially calibrated for atmospheric extinc-

tion against measurements of other sources. These procedures are typically sufficient for producing differential light curves with uncertainties of order 1% under normal sky transparency (i.e., seeing FHWM $\lesssim 2''$). Nonetheless, aperture photometry involves a number of parameters that can be fine-tuned to further optimize precision. The choice of aperture and annulus size, as well as the offset of the annulus from the central object, depends on the object brightness, seeing, and other factors such as proximity of neighboring stars. But to deliver excellent photometric performance, one should first know what level of precision is *theoretically* possible with the particular detector and observational conditions. In what follows, we will describe the basic expectations for photometry in the bright and faint-object limits, as well as provide a comparison to actual performances achieved with various telescopes in our campaign.

3.1.1   Bright targets

For bright point sources, the stellar photon signal dominates sky background and other sources of noise. For a particular seeing width σ (in arcseconds), peak stellar photon count M (per pixel) at a fixed exposure time, image sampling n arcseconds per pixel, and an aperture radius in pixels expressed as $f\sigma/n$ pixels (where f is typically between 3 and 7), the stellar profile $s(r)$ in counts as a function of pixel radius from the object centroid can generally be modeled as a Gaussian for ground-based observations:

$$s(r) = Me^{-r^2n^2/2\sigma^2}. \tag{3.1}$$

Hence the total stellar photon signal S measured over the aperture area is:

$$S = 2\pi \int_0^{f\sigma/n} Mg * re^{-r^2n^2/2\sigma^2} dr = 2\pi Mg\frac{\sigma^2}{n^2} * (1 - e^{-f^2/2}), \tag{3.2}$$

where g is the detector gain in electrons per ADU (the quantum efficiency of optical CCD detectors is such that roughly one electron is produced for every incoming photon). This estimate assumes that the image is well sampled (i.e., the psf size is at least a few pixels, and the area within that circular aperture is well approximated by the summation of the areas of the individual pixels). When photon noise dominates the photometric uncertainty,

the expected error is given by Poisson statistics:

$$\sigma_S = \sqrt{S} = \sqrt{2\pi M g \frac{\sigma^2}{n^2} * (1 - e^{-f^2/2})}. \tag{3.3}$$

The signal-to-noise ratio (S/N) of the stellar flux measurement is thus

$$\text{S/N} = S/\sqrt{S} = \sqrt{2\pi M g \frac{\sigma^2}{n^2} * (1 - e^{-f^2/2})}. \tag{3.4}$$

The best precision achievable thus depends on the saturation limit of the detector (which restricts M), as well as the gain setting and image sampling. For a nominal pixel size of $0.4''$, gain 2.0 e^- ADU^{-1}, saturation limit 60000 counts, seeing full width at half maximum (FWHM) $1.5''$ ($\sigma \sim 0.6$), and aperture size $f\sigma = 2 \times \text{FWHM} \sim 5\sigma$, an S/N value in excess of 1500 is achievable in theory. In practice, other effects, such as stellar scintillation, flatfielding errors, detector non-linearity, and read noise tend to introduce additional uncertainties that often limit S/N to values well short of this.

As illustrated by Eq. 3.4, the maximum attainable precision is not very amenable to adjustments once detector properties are established. The gain, g, may have multiple settings, but the size of the CCD pixel full well (maximum value for M) is generally fixed, as is the sampling (n). While increasing the photometric aperture f allows up to twice the amount of signal to be collected, it does so with diminishing returns; larger apertures also include more sky noise. Variations in the seeing, σ, can spread photons over a larger number of pixels, enabling more signal to be collected if exposure time can be increased to compensate. However, precision improvements related to seeing cannot be relied upon since astronomers do not control sky conditions! An alternative solution to attaining higher precision is to "manually" spread the signal over more pixels by defocusing the optics. This technique can substantially increase the number of photons collected while averaging out errors over more pixels. The method requires longer exposure times and is limited by the rate at which the psf becomes asymmetric as the focus is changed from its optimal value–a telescope-specific property. For stars brighter than $V = 9$–10, the time to saturation is still too short to achieve high-precision photometry from the ground without specialized techniques (e.g., López-Morales 2006).

3.1.2 Fainter targets

Under many circumstances, the photon signal does *not* dominate aperture counts and other sources of photometric uncertainty, such as sky background and readnoise, make significant contributions to the noise budget. This is the case for our observations of brown dwarfs using meter-class telescopes.

Among the sources of photometric error, readnoise is a detector-specific quantity, and its variance per pixel is usually denoted R^2. Dark current, atmospheric scintillation, as well as fluctuating electron-to-digital count conversion may also contribute to noise, but we will omit them here since these effects are often negligible compared to most other sources of error. The remaining contributions to photometric measurement uncertainty come directly from stellar and sky photons, and are well modeled by Poisson statistics. If we again denote the total number of stellar photon counts in the aperture S (as in Eq. 3.2), the average number of sky photon counts *per pixel*, c, the area within the aperture A_{ap}, and the area within the sky annulus A_{an} (both measured in pixels), then we can mathematically represent the calculation of stellar flux performed by aperture photometry:

$$F = S + A_{\mathrm{ap}} * c - \frac{A_{\mathrm{ap}}}{A_{\mathrm{an}}} A_{\mathrm{an}} * c = S + A_{\mathrm{ap}} * c - A_{\mathrm{ap}} * c. \tag{3.5}$$

Here F is the measured photon flux, free from sky background, the second term on the right-hand side is sky background within the aperture, and the third term represents the sky subtraction, as determined from the measurement in the surrounding annulus. Although the latter two terms should cancel on average to leave only the stellar component of the flux, their *errors* do not. Using this equation, we can estimate the expected photometric uncertainty in the presence of significant sky background. Based on Poisson statistics, we assume that the uncertainty in S is $\sqrt{S}$ and the uncertainty in the second term is $\sqrt{A_{\mathrm{ap}} * c}$, since both are a measure of total counts in the aperture. The uncertainty in the third term differs, however, because c itself is computed here as an average (or median in most practical cases, but the statistics should be similar assuming there are no major contaminating features within the sky annulus). What is measured is $A_{\mathrm{an}} * c$, the sky counts within the annulus. Since c is then determined as an average over the A_{an} pixels, its uncertainty is then reduced by a factor of $\sqrt{A_{\mathrm{an}}}$ compared to the spread of values within

the annulus:

$$\sigma_c = \frac{\sqrt{c}}{\sqrt{A_{\text{an}}}}. \tag{3.6}$$

Using propagation or errors, the total variance in the flux measurement is:

$$\sigma_F^2 = S + A_{\text{ap}} * c + A_{\text{ap}}^2 * \frac{c}{A_{\text{an}}} + A_{\text{ap}}R^2 = \sigma_F^2 = S + A_{\text{ap}} * c + \frac{A_{\text{ap}}}{A_{\text{an}}}A_{\text{ap}} * c + A_{\text{ap}}R^2. \tag{3.7}$$

Thus the signal-to-noise ratio (neglecting dark current, A/D converter error, and scintillation noise) is:

$$\frac{\text{S}}{\text{N}} = \frac{S}{\sigma_F} = \frac{S}{\sqrt{S + A_{\text{ap}}(1 + \frac{A_{\text{ap}}}{A_{\text{an}}})(c + R^2)}}, \tag{3.8}$$

which is the standard CCD equation. We note that S and σ_{F} here must be measured in photons (or equivalently, electrons). Hence ordinarily S and c should be converted from digital counts via multiplication by the gain, g.

We can now see that for a given star and fixed sky background, the signal-to-noise ratio depends primarily on the aperture size. It is somewhat intuitive that good photometry of bright stars can be obtained with a relatively large aperture, since the radius at which the sky background begins to dominate stellar photon counts can be up to a factor of a few times the FHWM, whereas the opposite is true for faint stars. But typical aperture photometry routines do not take advantage of this fact since differential measurements involving multiple stars in the same field of view often require the same aperture size for all targets. A common approach is to choose an intermediate aperture, such that the S/N is not particularly compromised for either faint or bright objects.

3.1.3 Adopted seeing-limited aperture photometry method

In the quest for high-precision photometry, we considered alternatives to the usual fixed-aperture routines. Deeg & Doyle (2001) highlighted a promising option by showing that different apertures can be used for different targets, as long as their sizes are scaled from image to image in accordance with seeing variations. This method works well for purely differential photometry, since expressing the aperture size in terms of a fixed multiple of the seeing FWHM ensures that the same fraction of the stellar flux is being measured in each image. How should one go about choosing apertures if they are allowed to vary among different stars, and the goal is to maximize S/N on all targets? From Eq. 3.8, it is

possible to solve for an optimal aperture size corresponding to a particular star and fixed sky background. Writing the aperture radius again as a multiple, f, of the seeing width σ, we have the aperture area in pixels:

$$A_{\mathrm{ap}} = \pi f^2 \frac{\sigma^2}{n^2}, \tag{3.9}$$

where n is the pixel sampling as in Eq. 3.1. Regarding n, σ, the sky background c, the readnoise R^2, and the annulus area as constants (A_{an} is generally set by the seeing and not the properties of the star itself), S/N in Eq. 3.8 can be maximized as a function of f:

$$\frac{\mathrm{d(S/N)}}{\mathrm{d}f} = 0 = \frac{\mathrm{d}}{\mathrm{d}f} \left(\frac{S(f)}{\sqrt{S(f) + \pi f^2 \frac{\sigma^2}{n^2}(1 + \pi f^2 \frac{\sigma^2}{n^2 A_{\mathrm{an}}})(c + R^2)}}, \right) \tag{3.10}$$

where $S(f)$ is given in Eq. 3.2. This equation does not have an analytical solution, but by plugging in typical numerical values, we can see that for a Gaussian psf, S/N *does* reach a maximum for a particular value of the aperture radius $f\sigma$. Shown in Figs. 3.1 and 3.2 are psf profiles and corresponding runs of S/N as a function of aperture radius for several stars of different brightness; these trends confirm that the optimal aperture size is smaller for fainter objects.
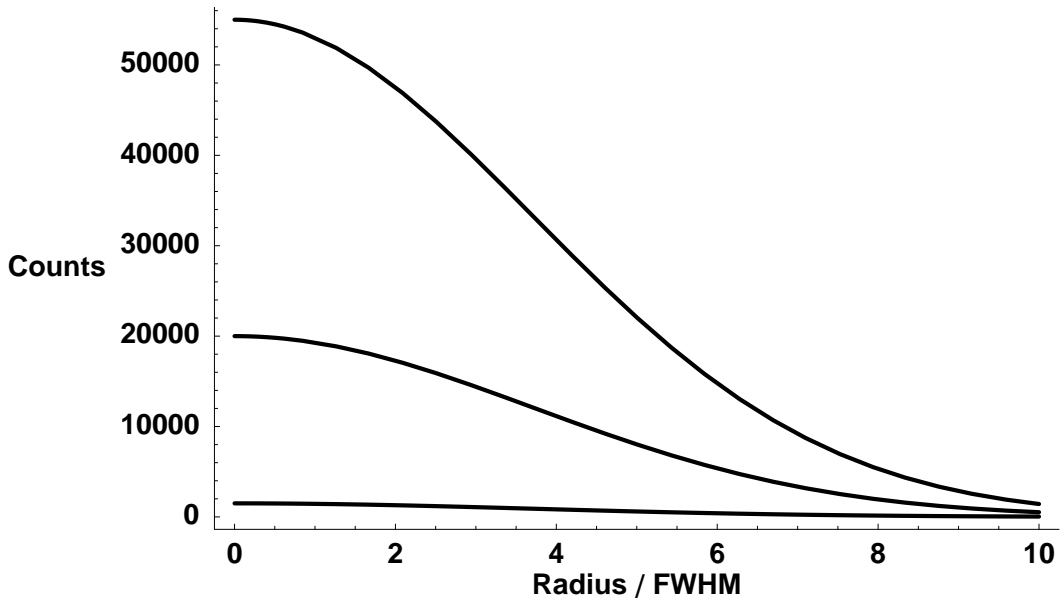
Figure 3.1 Gaussian flux profiles for three stars with different brightness but the same psf
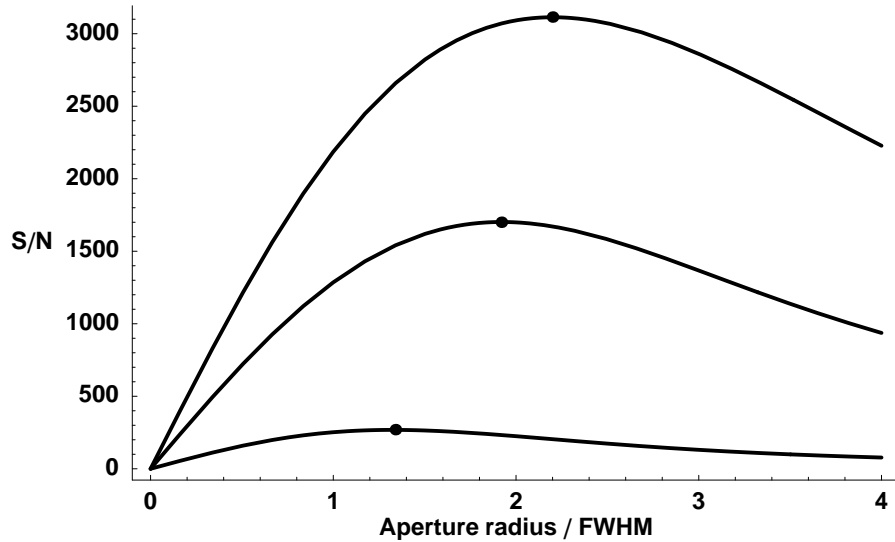
Figure 3.2 S/N as a function of aperture radius (in units of seeing FWHM) for three stars of different brightness, as in Fig. 3.1. Dots mark the radius at which S/N reaches its maximum.

Deeg & Doyle (2001) have also pointed out that the optimal aperture varies quite slowly with σ. We illustrate this behavior in Fig. 3.3, where the S/N of a single star under different seeing conditions is plotted as a function of aperture radius. If a single aperture is chosen and its ratio to σ is maintained to conserve measured flux throughout these varying conditions (e.g., constant f), it will only be perfectly optimized to one value of the seeing. However, as seen in Fig. 3.4, the predicted S/N for these un-optimized apertures is generally within a few percent of the maximum S/N, for a "typical" range of FWHM (= 2.355σ) such as 1–2.5″. Consequently, the strategy of tailoring apertures to the brightnesses of individual stars and scaling them up or down proportionally with seeing changes should maintain *nearly* optimal S/N from frame to frame. This variable aperture approach was incorporated by Deeg & Doyle (2001) into VAPHOT, a publicly available aperture photometry script linked to standard *IRAF* routines.

Since our own observational program aims to maximize S/N for targets occupying a range of brightnesses, we have elected to use VAPHOT for our ground-based photometry. The program enables high-precision differential photometry without the need for multiple trials of different aperture sizes or aperture corrections. It dynamically determines the best apertures for all desired photometric targets on a single input frame with seeing representative of the average for the entire run. The ratio of the calculated aperture sizes to the
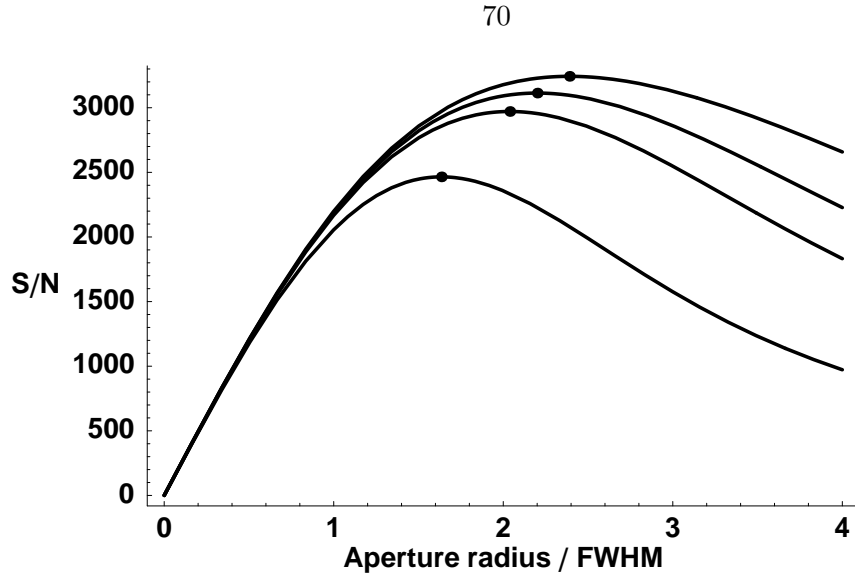
Figure 3.3 S/N as a function of aperture radius (in units of seeing FWHM) for a single star in different seeing. The selected FWHM values are 3.1, 3.7, 4.3, and 6.3 pixels running from the top curve to the bottom. For each curve, the maximum count value is adjusted such that the total number of photons received is the same regardless of the psf width. Dots mark the radius at which S/N reaches its maximum; larger seeing values lead to lower S/N.

FWHM of the psf is then fixed, and aperture sizes in all other frames are scaled relative to those determined for the chosen "typical" frame. All measurements on an object should thereby recover the same fraction of its total flux from frame to frame and night to night, in the limit that the psf is circularly symmetric. In reality, the psf is not perfectly symmetric, and this assumption introduces the need for a small correction to the measured fluxes. We have not applied such a correction here but discuss a method that we have used to reduce the error using image subtraction photometry in §3.2.

For all ground-based data, we have carried out aperture photometry with the scaled aperture sizes using the IRAF *phot* task, including redetermination of the object centroids before aperture placement. Typical aperture radii on CTIO 1.0 m Y4KCam images were 10.5 pixels ($\sim 3''$) for bright stars and 7 pixels ($\sim 2''$) for faint targets such as BDs. For the P60 CCD, they were 5–8 pixels (~ 2–$3''$). We did not perform aperture corrections since this introduces additional errors and our instrumental magnitudes differ from their flux-corrected counterparts by the same constant value–a situation entirely suitable for differential photometry. We have measured the sky background around each object within an annulus extending between 4.5 to 6 times the FWHM.

We carried out differential photometry with a suite of reference stars for which peak
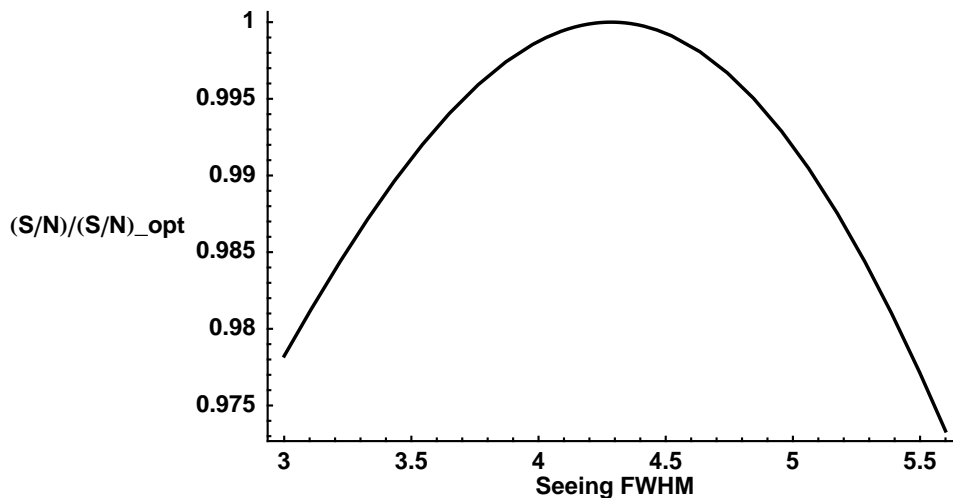
Figure 3.4 Ratio of S/N achieved when aperture radius is fixed with respect to seeing FWHM, to the S/N possible if apertures could be re-optimized for different seeing conditions (as in the dots in Fig. 3.3). In general, the aperture radius must be a constant multiple of the seeing FWHM, so that the same portion of the stellar flux is measured in each frame. This constant multiple is optimized to a particular median value of seeing, but when conditions change, S/N is no longer maximized. The plotted trend shows that the predicted S/N over a typical range of seeing variation (3–6 pixels) nevertheless varies only by a few percent from optimal.

flux remained below the detector saturation and linearity limits on all nights. In each of the fields, we selected an initial set of 10–20 bright ($I \sim 13$) reference stars and summed their fluxes in each image. Tests of several weighting schemes, such as the one suggested by Sokoloski et al. (2001) did not produce substantially different results. Differential magnitudes relative to this ensemble magnitude were computed for each of the reference stars in turn, with that particular star removed from the ensemble. We computed the light curve RMS values, and objects with variability visible by eye or RMS more than one standard deviation above the average RMS for that magnitude were removed from the ensemble. The process was repeated with the new subset of reference stars until no outliers remained. The final ensembles consisted of 4–10 reference stars. Based on this comparison reference, differential light curves were generated for all objects with signal below the saturation limit but at least five times the background.

The primary difficulty we have encountered in producing high-precision photometry with VAPHOT is the implicit assumption of a psf fixed in both size across the image and in

shape from night to night. The psf size across the Y4KCam detector is in fact known to vary by up to 25% from the center to corner[1]. Stellar profiles from the P60 detector also vary in shape since tracking and focus change subtly throughout the exposures. As provided, VAPHOT determines the seeing FWHM in each image by fitting a Gaussian profile to a single bright star specified by the user. This value is then used to scale the apertures for *all* other objects in the field. We altered the script to instead output an average psf of several bright stars across the field. In addition, we found that the calculated optimal apertures for all but the faintest targets were too small, in that the aperture scaling based on psf size estimates introduced significant noise on night-to-night timescales. Doubling the aperture sizes for targets with $I < 18$ reduced RMS spreads over the entire observing duration by more than 50% in most cases. Therefore, we adopted the larger aperture sizes for all objects in the brighter half of our CTIO 1.0 m samples and for all P60 targets. These improvements confirm that neglecting spatial variations and non-Gaussian shapes in the point spread function introduces substantial artificial variability in photometry with relatively small apertures.

3.1.4 Diffraction-limited aperture photometry for space-based data

Unlike the seeing-limited case, fixed-aperture photometry is sufficient for precision space-based photometry. Thanks to the lack of atmosphere, no reference ensemble is needed to calibrate out airmass and sky background variations, and object fluxes may simply be compared in sequence. For observations with both *Spitzer*/IRAC and *HST*/WFC3, we computed optimal aperture sizes for individual targets and kept these constant across all images. In addition to the calculated sizes, we tested several larger apertures as well as a variety of sky annulus widths and radii for background subtraction. Since the psfs of detectors are somewhat undersampled, the flux from targets is concentrated within several pixels, or in the case of IRAC, the central pixel. Inaccurate aperture centering can thus lead to erroneous brightness fluctuations in the resulting light curve. We determined moment centroid positions by calculating position-weighted flux averages within a 3×3 (IRAC) or 4×4 (WFC3) pixel box. Points for which the centroid algorithm failed due to a cosmic ray or other bad pixel effect were omitted from the data. Apertures were placed at the centroid locations and the enclosed sky-subtracted flux was determined with the IRAF *phot* task.

---

[1] See http://www.lowell.edu/users/massey/obins/y4kcamred.html for details.

For *Spitzer*/IRAC images, apertures with radii from two to four pixels were tested, along with sky annuli from 2 to 9 pixels. We adopted the aperture resulting in the lowest RMS light curve spread, which was 2 pixels for most targets. Conversion to the magnitude scale was accomplished by incorporating the published IRAC zero point values, aperture corrections, and location-dependent array response provided by the handbook. For *HST*/WFC3, light curve RMS values were relatively insensitive to the selected aperture size, most likely because the targets exhibited substantial systematic variability. We found that 6 pixel apertures and 6 to 11 pixel sky annuli provided the lowest flux variations.

3.1.5   Actual data performance

The theoretical expectations outlined in the previous sections provide guidance in assessing data performance. Although random noise associated with photometric flux determination can be minimized by carefully choosing aperture sizes and exposure times, there may remain significant systematic effects. Direct comparison of a large collection of light curve RMS values with the theoretical limits indicates whether further adjustments might be made to optimize the photometric precision.

By convention, we have first calibrated all data to the magnitude scale:

$$m = -2.5 \log F + C, \tag{3.11}$$

where C is a zero point dependent on the photometric waveband, exposure time, and atmospheric extinction. When systematic errors associated with C can be neglected or eliminated, the uncertainty in the magnitude, σ_m, is related simply to the flux uncertainty, σ_F, via error propagation:

$$\sigma_m^2 = \sigma_F^2 \left(\frac{\partial m}{\partial F} \right)^2 = \sigma_F^2 (2.5 \log e)^2 \left(\frac{1}{F} \right)^2. \tag{3.12}$$

Since S/N is defined as $\frac{F}{\sigma_F}$, we can write the magnitude uncertainty in terms of the signal-to-noise ratio:

$$\sigma_m = (2.5 \log e) \left(\frac{\sigma_F}{F} \right) = (2.5 \log e) \left(\frac{S}{N} \right)^{-1} = 1.0857 \left(\frac{S}{N} \right)^{-1}. \tag{3.13}$$

To assess the quality of our ground-based light curves from the CTIO 1.0 m telescope, we

extracted photometry on ~3200 unsaturated point sources identified in the σ Orionis fields and another ~1500 objects in the Cha I field. On timescales of one night, we find that the floor of the distribution is well accounted for by photon and sky noise, plus an additional allowance of ~0.0015–0.0025 magnitudes in systematic error. We illustrate the comparison of actual data with the theoretical limits in Figs. 3.5 and 3.6.

The uncertainties for our unbinned CTIO 1.0 m data range from 0.002 magnitudes for the bright reference stars, to just over 0.01 for the brown dwarfs near $I = 17$, and 0.1 at the faint end where targets reach $I = 21$. We display the RMS spreads from a single night in Figs. 3.5 and 3.6. On the longer timescales corresponding to the observing duration, RMS light curve fluctuations are increased by up to 50% over these values because of night-to-night systematic effects.

Photometric performance with other telescopes was more difficult to assess since we only extracted photometry for young clusters members, many of which are intrinsically variable. In addition, data from the P60 suffers from strong systematic effects due to the lack of guiding and bad pixel columns on the detector. light curve RMS values reached as low as 0.002 magnitudes on single night timescales, consistent with the expectations of photon and sky noise. However, the RMS spreads in other cases were substantially larger, as seen in Fig. 3.7. The same was true for our space-based *HST*, which we suspect is dominated by aperiodic variability. Photometry from *Spitzer* was also dominated by systematic effects, but in this case we were able to remove most of them (see §3.3.1.3). Resulting light curve spreads were ~25% larger than the Poisson limit, which is typical for the IRAC instrument (Deming et al. 2011).
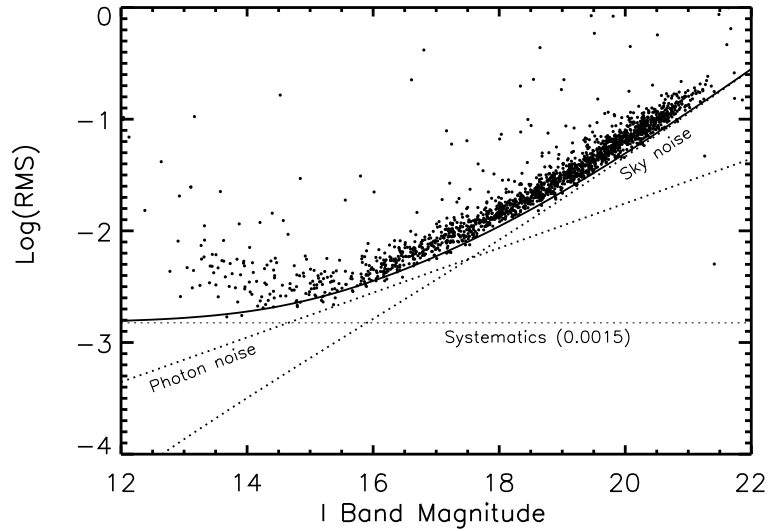
Figure 3.5 Data from a single night of the 2007 CTIO 1.0 m observations of the σ Orionis cluster, as compared with the Poisson and sky noise limits. RMS values are in magnitudes. We find that the photometric performance over this timescale is well in line with the predictions, modulo a small systematic component.
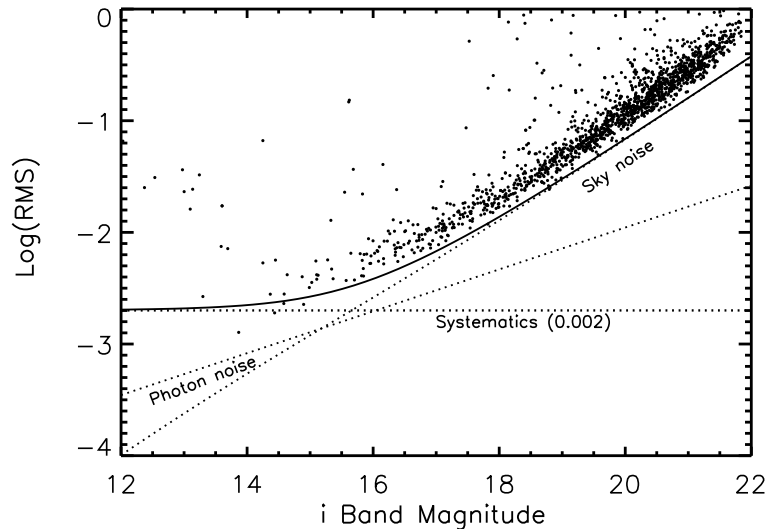
Figure 3.6 Data from a single night of the 2008 CTIO 1.0 m observations of the Cha I cluster, as compared with the Poisson and sky noise limits. RMS values are in magnitudes. We once again note that the photometric performance is in line with the theoretical expectations plus a small systematic allowance. Sky conditions during this run were highly variable, resulting in increased spread in the fainter light curves compared to the σ Ori observations.
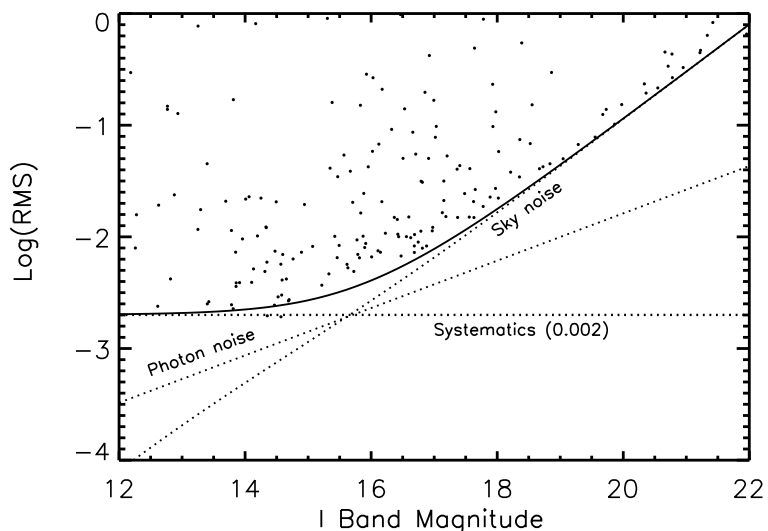
Figure 3.7 Data from a single night of the 2008 P60 run on IC 348 is in good agreement with the Poisson and sky noise limits. RMS values are in magnitudes; the large scatter is primarily due to intrinsic variability, since the majority of targets are young cluster members.

3.1.6 Absolute photometry

The search for pulsation-induced variability in young BD and VLMS light curves relied mainly on differential photometry, with comparison to constant reference stars for the ground-based data. This approach works well over relatively small fields of view since atmospheric properties are coherent and sky-related variability may be effectively removed. Absolute photometry, on the other hand, entails more careful calibration and rarely exceeds the 1–2% precision level. In addition, the requirements of our observations were such that it was not efficient to observe standard fields frequently or collect multi-color data. Telescope motion compromises object pixel placement, thereby introducing flatfielding error effects. Filter changes are also associated with focus shifts and small position increments which often degrade data quality. Thus most of the observations were carried out strictly in the I or an equivalent band.

Standard magnitudes and color information are nevertheless useful in distinguishing between the intrinsic properties of different variable sources, and we obtained such data for the subset of σ Orionis observations performed at the CTIO 1.0¿m telescope. We obtained one or two R-band exposures of each field on every night of the 2007 and 2008 runs. To derive

the Cousins R and I magnitudes, we also observed a spatially dense Stetson photometric standard field in NGC 2818 at several different airmasses and performed aperture-corrected photometry on over 500 stars with available Stetson R and I magnitudes (Stetson 2000). The conversions from the CTIO filter ("r" and "i") magnitudes were determined by fitting the following linear trends across a wide range of magnitudes and colors, as well as several airmass values (X):

$$I = i + (\epsilon_I + k_I' X)(R - I) + k_I X + Z_I \tag{3.14}$$

$$R = r + (\epsilon_R + k_R' X)(R - I) + k_R X + Z_R \tag{3.15}$$

$$R - I = \epsilon_{RI}(r - i) + Z_{RI}, \tag{3.16}$$

where ϵ is an extinction coefficient and k denotes an airmass coefficient. Aperture-corrected photometry of these sources resulted in an R-band zero point $Z_R = 22.908$, I-band zero point of $Z_I = 22.140$, and small airmass coefficients ($k_I \sim -0.06$; $k_I' \sim 0.002$) consistent with typical values for CTIO. Based on these conversions, we derived average Cousins R and I magnitudes for all targets in the field within the linearity limit corresponding to $I \sim 12.5$.

For objects covered in prior photometric surveys of σ Ori, our I and R values are in good agreement with those reported previously. For example, photometric data for the 59 objects in our fields observed by Sherry et al. (2004) show an average offset of 0.025±0.10 magnitudes in the I band and 0.035±0.20 magnitudes in the R band when compared to our values. The scatter is consistent with that expected from both the listed uncertainties and intrinsic variability.

3.2   Modified image subtraction photometry technique

Assessment of our ground-based data showed that the achieved photometric precisions were largely in line with the predicted random noise level on individual nights. However, several concerns over light curve variations on longer timescales prompted us to perform an independent test of our results with a different set of photometric reduction procedures. For a few of the target brown dwarfs, flux from faint sources near our object apertures may have interfered with proper sky subtraction during aperture photometry. In addition, night-to-night variations in the mean magnitude of many sources suggests that spatial and temporal psf variations as well as slightly non-circular psf shape may be significant enough

to alter the photometric zero point. Comparison tests of psf fitting photometry and image subtraction (e.g., Mochejska et al. 2002) have shown that the latter method can result in significantly smaller light curve scatter. Therefore, we opted to employ the method of differential image analysis (Alard & Lupton 1998; Mochejska et al. 2002) to produce separate photometric datasets with reduced sensitivity to crowding and other psf effects. The Hotpants package (Becker et al. 2004) compares the fluxes of objects in every exposure to their counterparts in a selected reference image, thereby enabling a differential brightness measurement. Images are first accurately aligned to a common grid. A high-quality stacked reference image is then convolved with a time-dependent kernel which is mathematically optimized to reproduce the psf (size and shape) in all individual images. The science images are then subtracted from the convolved reference to reveal residuals possibly indicative of variability.

We applied image subtraction to the ground-based data from the CTIO 1.0 m Y4KCam; images from the P60 CCD proved too difficult to model with a reference frame because of the large position shifts and the frequently asymmetric shapes of the psfs. Neither did we attempt this method on the *Spitzer* or *HST* datasets since the psfs are too undersampled to accurately determine a kernel. Furthermore, direct subtraction of *HST*/WFC3 images resulted in photometry that was equivalent to that obtained from unsubtracted images.

In general, we found that subtraction from the Y4KCam reference template produced relatively clean images, with background consistent with the levels expected from noise properties of the input images. By specifying spatial variations of the background and psf kernel, we are able to obtain subtracted images devoid of systematic effects. Systematic residual flux is detectable above the background only in the brightest stars, where it appears in saturation-related peaks or a circular pattern with alternating positive and negative flux on either side. As pointed out by Alard & Lupton (1998), the latter pattern is likely the effect of small-scale atmospheric turbulence, which causes offsets of the psf centers even in well-aligned frames. We measured the residual flux in each subtracted image by performing nearly the same aperture photometry routines as described in §3.1.3. Inputs for aperture placement and size were determined from the convolved, unsubtracted images. To convert the measurements to differential magnitudes, we also measured fluxes of each star in the reference template, again using the same optimal aperture sizes determined by VAPHOT for the more standard photometry discussed in §3.1.3. Magnitudes were then computed relative

to the reference frame. For a selection of variables in which the signal dominated noise, we confirmed that the image subtraction routine produced the same light curves as the photometry performed on un-subtracted images, to within the photometric uncertainties. This technique is a hybrid version of the variable-aperture and image subtraction methods, the second of which typically involves an aperture correction even to compute the differential magnitude. Our approach thus eliminates important systematic noise contributions and should perform significantly better than either method alone.

We expected the photon and sky noise components of the image subtraction light curves to be similar to those derived from standard optimal aperture photometry. But since image subtraction photometry involves measurements on *residuals* (with at least an order of magnitude less flux, even for variable objects) resulting from the image subtraction optimization process, the light curves should be much less sensitive to errors in psf and aperture size. To test this assumption, we plot in Figs. 3.8 and 3.9 the RMS light curve spread as a function of magnitude over the duration of each observing CTIO 1.0 m run for the different photometry methods. We find that while doubling the aperture sizes (as explained in §3.1.3) offers improvement in photometric precision in the standard optimal aperture method, image subtraction photometry indeed significantly outperforms both of these approaches. To assess each method in comparison with the expected uncertainties, we have estimated the Poisson and sky noise components, based on the variable aperture size as a function of magnitude as well as the mean sky background value over all nights of each run. Apart from the brightest 3% of objects which are affected by our neglect of CCD non-linearity ($I \lesssim 14$), the combination of image subtraction and optimal aperture selection produces light curves consistent with the analytically determined photon and sky noise floors plus a 0.002–0.0025 magnitude systematic uncertainty over the entirety of each run. These curves are shown in Fig. 3.8; they pass slightly below, as opposed to *through* the data distribution because of differing sky background from night to night. Based on this assessment, we have adopted as our final CTIO datasets the image subtraction results for targets with $I > 14$, and light curves from standard aperture photometry with double-sized apertures for $I < 14$.

3.3 Beating down the systematic noise

Depending on the telescope and detector setup (e.g., location, wavelength, pixel size) as well as the details of the observations (e.g, target characteristics, exposure times), optimal aperture photometry with image subtraction does not always produce the highest achievable precision. As we have alluded to previously, a series of additional systematic effects can contribute significant noise. Not all of these effects appear in every observing setup. It is important to know which of them may be present, and how to avoid or properly remove them from the data. We divide these effects into two categories, depending on the magnitude of the noise they contributed to our particular observations. Kjeldsen & Frandsen (1992) provide a more comprehensive overview of the multifarious noise sources that crop up in high-precision differential photometry. Here we focus primarily on those that affected our particular datasets, and the specific methods developed to mitigate them.

3.3.1 The "1–10% effects": guiding, fringing, pixel-phase variation, and asymmetric psfs

3.3.1.1 The interplay of guiding and flatfielding

Precise and accurate flatfielding are an important component of high-precision time series photometry, particularly in the scenario that object positions are not fixed on the detector for the duration of observations. This might occur if target fields or filters are interchanged, or if guiding and/or tracking is not functioning well. Errors and non-linearities associated with flatfielding lead to artificial flux variations in a target as it wanders over areas of differing sensitivity on the detector. the correlated nature of these brightness fluctuations tends to produce red noise (see §2.3.4) in the periodogram, complicating the search for periodic signals such as those expected from pulsation. Every effort was therefore made to ensure that the applied calibrations included as much information as possible about the intrinsic spatial response of the detector.

The first step in minimizing flux variations related to flatfielding errors is to reduce random spatial noise by median combining as many flatfield images as possible. The contribution to the overall photometric noise budget can be estimated per pixel with Poisson statistics:

$$\sigma_F = \sqrt{C \times N \times g}, \tag{3.17}$$
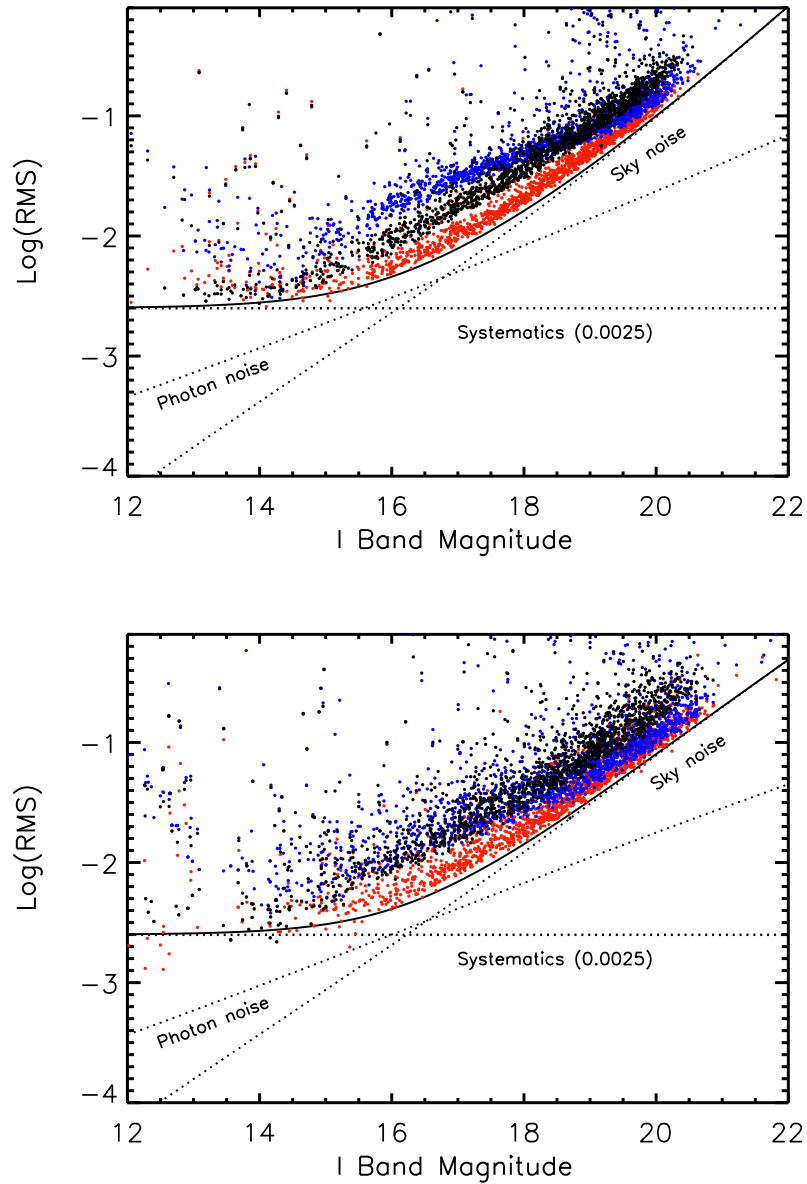
Figure 3.8 Spread of photometry over the duration of each σ Ori observing run with the CTIO 1.0 m telsecope, as a function of magnitude for three methods of variable-aperture photometry. The 2007 field is represented on the top, while the 2008 field is on the bottom. Blue dots represent photometry with the calculated optimal apertures, black dots are the same photometry with double-sized apertures, and red dots are the result of image subtraction followed by photometry with optimal-sized apertures. RMS values are in magnitudes. While the first two methods exhibit systematic errors, particularly in the middle magnitude range, the trends for image subtraction photometry in both fields are well described by a combination of photon noise, sky background, and a small systematic contribution. Larger deviations at the bright end are due in part to CCD non-linearity. Points lying significantly above the trend signify variable objects or erroneous photometry (e.g., bad pixel or saturation effects) that were later removed.
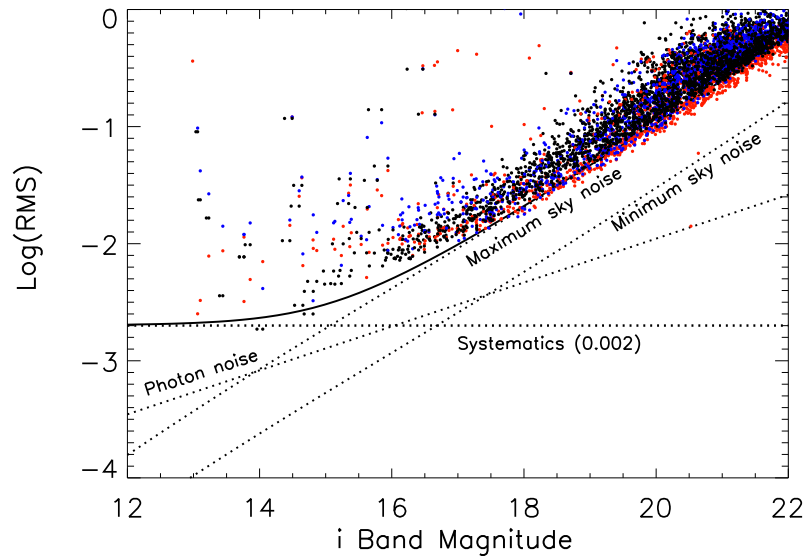
Figure 3.9 Spread of photometry over the duration of the Cha I observing run, as a function of magnitude for three methods of variable-aperture photometry. Symbols are as in Fig. 3.8; RMS values are in magnitudes. Since the sky background level varied greatly from night to night, we have marked its minimum and maximum values. Once again, image subtraction photometry offers the best performance, apart from the brightest objects with $i < 15$.

where σ_F is the uncertainty in flux units, C is the typical flatfield count level in ADU, N is the number of flatfields combined to make the composite, and g is the gain in electrons per ADU. The uncertainty in magnitudes is given by Eq. 3.13:

$$\sigma_M = 1.0857/\sqrt{C \times N \times g}. \tag{3.18}$$

Pixel non-linearity and saturation limits restricts the number of counts that may be accumulated in a flatfield image. Exposing the flat lamp for just long enough to reach half well capacity is a safe way to avoid these effects. For a typical half-well level of 50,000 electrons, about 20 flatfields are needed to reach a precision of 1 millimagnitude per pixel. Since photometric apertures usually encompass more than one pixel, the corresponding random photometric uncertainty is well below this level.

With the CTIO 1.0 m telescope, we typically collected at least 11 flatfield exposures per night per filter, each with a minimum of 25,000 ADU (36,000 e^-). The expected noise contribution of 0.0015 magnitudes per pixel was well below the Poisson limit of most sources. For the P60 robotic telescope, the observing pipeline takes 9 flatfields per band, each with a level of $\sim$16,000 ADU ($40,000e^-$). Again, the estimated noise contribution is very small, at 0.0017 magnitudes per pixel.

Other types of noise inherent to flatfielding are more systematic in nature. A common source of error comes from the type of background used to illuminate the flatfield exposure. Since this is often a telescope dome or blank screen, systematic differences arise between the assumed flatfield response and that of the sky. Repeat exposures of the sky at dawn or dusk avoid this problem, but such "sky flats" may only be taken when weather conditions permit–as opposed to "dome flats", which may be acquired at virtually any time. For two of our runs with the CTIO 1.0 m telescope (Dec. 2007 and Dec. 2008), we were able to acquire the desired 11 sky flatfields per night. However, for a third run (May 2008), cloudy skies at the beginning and end of many nights prevented this. Moreover, using sky flats from one night to calibrate the images of another night was infeasible since several new out-of-focus dust particle shadows appeared on the detector each day. For the P60 robotic system, sky flats were never acquired as part of routine observations, due to the manual intervention required. As a result, we resorted to domeflat calibration on much of the data.

To account for the difference between the two types of flatfield images, an illumination

correction can be applied. In the case of the CTIO Y4KCam, this was derived by previous observers from a large set of dome and sky flatfield images[2]. As shown in Fig. 3.10, the correction is substantial–up to 10% from the center toward the corners of the images. If left uncorrected, photometry of targets that drift across the detector will be systematically affected. Although the guiding CTIO 1.0 m guiding system restricted such movement to a few pixels over the course of a night, we nevertheless applied the illumination correction to reduce systematic noise as much as possible. The correction was also necessary for subsequent derivation of absolute magnitudes for our targets based on standard star observations. On the second night of the December 2007 CTIO observing run, we adjusted the field center by 100 pixels. Subsequent photometry showed systematic changes of up to ~1%, indicating some flatfielding errors unaccounted for with the illumination correction.
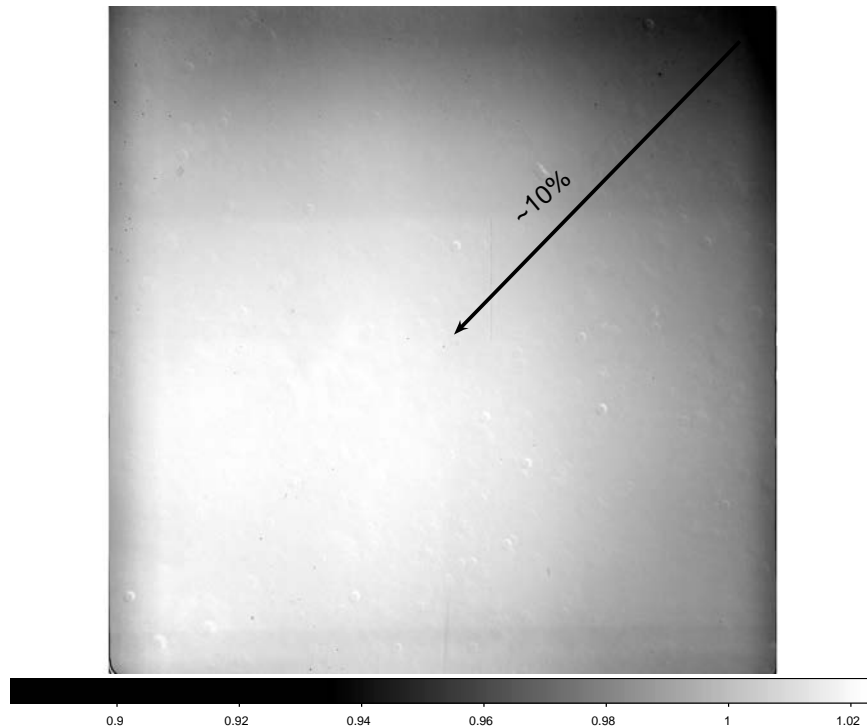
Figure 3.10 Illumination correction for the CTIO 1.0 m telescope Y4KCam, provided by P. Massey

For the P60 telescope, guiding was not available at the time of observations, and tracking errors led to a typical drift of 10–20″ per hour with occasional jumps of up to 10″ over

[2]http://www2.lowell.edu/users/massey/obins/y4kcamflats.html

the course of a 5 minute exposure. Consequently, the positions of targets on the detector executed large spatial ($\sim 1'$) excursions over the course of a typical 4–5 hour observing block. The resulting time series displayed RMS photometric spreads larger than the values expected from Poisson and sky background noise sources. Although some of the flux variation may be due to intrinsic variability of the young stars in our monitoring campaign, we suspected that they were explained by a combination of flatfielding errors and crossing object positions over the numerous bad pixel columns.

The P60 calibration pipeline works only with dome flatfields, so that the lack of illumination correction could contribute to unaccounted inter-pixel sensitivity differences. During a dusk-time manual control session on the telescope, we acquired a set of 29 sky flatfield exposures, which we median combined and compared with the standard dome flat. Surprisingly, assessment of the two types of flatfields showed that dome flats on the P60 are quite comparable (to 0.1%) to sky flats, apart from a long, narrow shadow on the left side. The corresponding illumination correction image is shown in Fig. 3.11. Therefore, we did not find it necessary to apply any illumination corrections to the P60 data and instead attribute the systematic effects seen in our photometry to an unknown source of flatfielding error.

3.3.1.2 Long-wavelength fringing

Fringing is an inconvenient effect that often appears at near-infrared wavelengths and contributes to systematic noise in photometry. Since the typical CCD thickness is 20 μm or less, long-wavelength emission from nearly monochromatic light sources reflects multiple times within the CCD to create a complicated interference pattern superimposed on the images. The effect usually appears in the presence of strong OH night sky lines, or in the case of space-based observations, when images are acquired through narrow-band filters. Fringing is additive and fixed with respect to detector position, but its strength varies throughout the night, depending on sky conditions. The pattern is completely dependent on the detector construction and in theory can be analytically modeled. In practice, however, the best models of fringing are generated by directly combining background-subtracted, object-masked on-sky images. Fig. 3.13 displays an example of a CTIO 1.0 m Y4KCam image of the a σ Orionis cluster field severely affected by fringing. The same field with fringes removed is shown for comparison. The P60 CCD displays a different fringe pattern, a $7.2'$ portion of which is shown in Fig. 3.12.
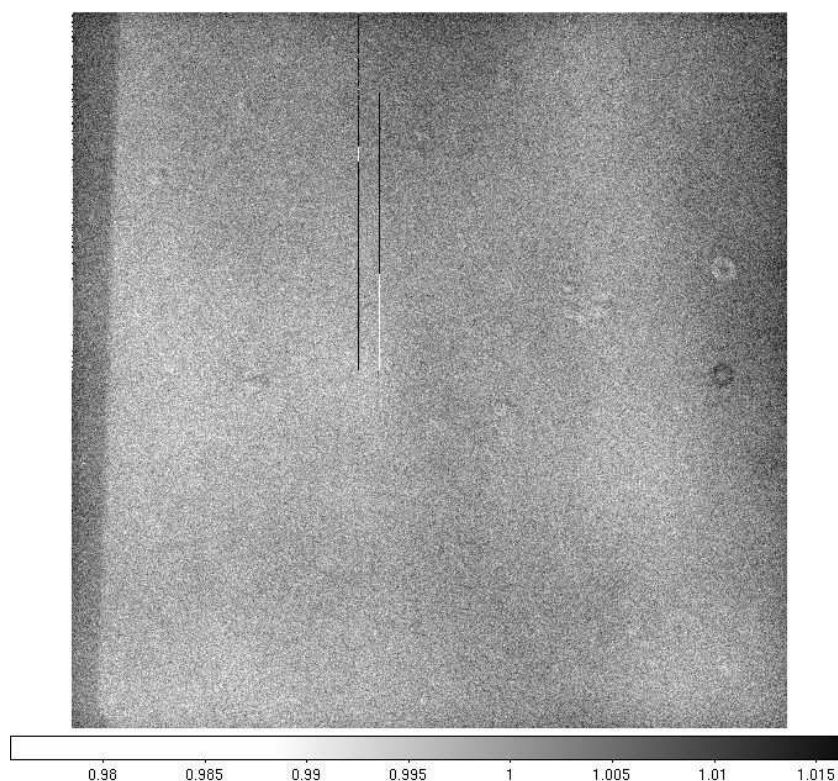
Figure 3.11 Illumination correction for the P60 CCD, generated by dividing a set of sky flatfields by dome flatfields

In our experience fringe amplitudes can reach between a few and ten percent with respect to the background. Since the fringe pattern is spatially stable, it does not necessarily need to be removed for fixed staring differential photometry. In principle, sky annulus measurements should retrieve the correct background value–modulo the mean fringe pattern value–as long as the same inner and outer radius is used for each image. Therefore, one might expect fringing to shift a differential light curve by a constant value for all data points. However, as is the case with imperfect flatfield correction, any movement of targets across the detector causes background variations to become embedded in the resulting photometry. It is thus the combination of imperfect tracking or guiding and strong background gradients due to fringing that introduce additional systematic noise into a time series.

While some filters have now been designed with the suppression of fringe-related sky emission in mind, these were not available for much of our observations. Both detectors that we used for ground-based photometric time series suffered from fringing: The CTIO 1.0 m
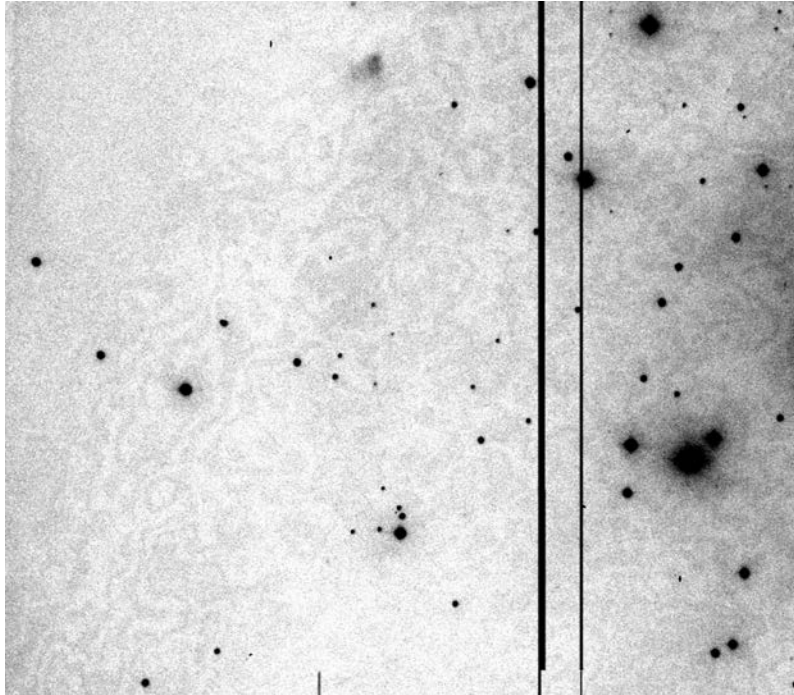
Figure 3.12 An image from the Palomar 60" CCD camera displays fringing in the Kron *I* band. Variable background is due to nebulosity in the region, while vertical dark stripes are bad pixels. Fringing can be seen as the wavy pattern in the background.

Y4kCam and the Palomar 60" camera. In the case of the Y4KCam, we find that in the Cousins *I* band fringing typically fluctuates on scales of 30–50″, with amplitudes reaching 2% with respect to the background. While guiding generally kept stars on the same pixel, steep gradients in the fringe pattern and an unexplained 4–5 pixel drift in x position throughout the night affected background subtraction for aperture photometry, introducing artificial variability on the same levels as potential rapid rotation or pulsation signatures. For the P60 CCD, on the other hand, fringes reach up to 7% amplitude compared to the background, whereas the spatial variation is on much smaller scales of ∼30″. The lack of guiding resulted in a folding of the fringe trends into the photometry. Fortunately a change to the i_p filter at the beginning of our first run suppressed fringing to negligible levels in subsequent images.

The overall goal of obtaining high precision photometry demanded that fringe effects be calibrated out of the time series data. Since poor guiding and tracking cannot be remedied after the fact, we developed a procedure to effectively model and subtract the fringing from all affected images. Our adopted method worked well with the Y4KCam CCD and may
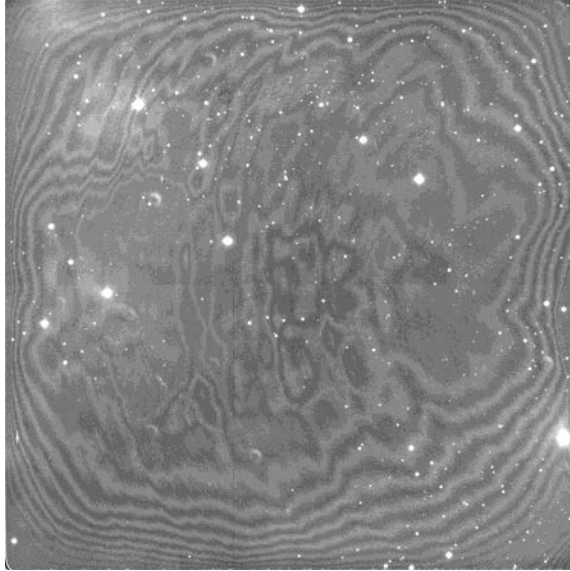
Figure 3.13 Images from the CTIO Y4kCam with I-band fringing (top) and fringes removed (bottom)

be extended to data from other imaging instruments. It involves first capturing the fringe pattern itself by taking exposures of sparsely populated areas of sky, which we refer to as fringe fields. Collection of fringe field images was done at times when the science target were not visible, so as to not interrupt or cut short the time series. Exposure times for fringe fields were similar to those used for the science observations. With the CTIO 1.0 m telescope, we amassed a total of 68 fringe flats in the Cousins I band and 49 in the Sloan i band, all at a 360 second exposure time.

Once fringe flatfields have been acquired, isolation of the fringe pattern requires extraction of the two-dimensional continuum sky background as well as stellar point sources. We generated object masks for each field, eliminating images with highly saturated stars. We modeled the background to second order and subtracted it from each image, leaving a fringe pattern with mean value zero. In the case of the Y4KCam, bias levels vary in different quadrants, so we allowed the fit to vary in each of the four regions. A high signal-to-noise master fringe frame devoid of stars and background was created by median combining the individual fringe images, incorporating the object masks.

To defringe an image, it is necessary to subtract the master fringe frame scaled by the value determined to best reproduce the time-dependent fringe amplitude. The scaling constant, c, may be calculated by minimizing the variance in the subtracted image, S, assuming that its mean is zero (this is valid since the background has been subtracted from all frames):

$$0 = \frac{\mathrm{d}}{\mathrm{d}c}\sigma_S^2 = \frac{\mathrm{d}}{\mathrm{d}c}\sigma_{(I-cF)}^2 = \frac{\mathrm{d}}{\mathrm{d}c}(\sum(I - cF)^2) = -2\sum IF + 2s\Sigma F^2, \qquad (3.19)$$

where I refers to the pixels in the science image, and F refers to those in the fringe image. This gives

$$c = \sum IF / \sum F^2, \qquad (3.20)$$

where the summations are over all pixel values in each image.

This computation for the scaling constant c only holds if the spatial noise in the fringe image (F) is dominated by the fringes themselves, and not random background noise. Otherwise, the value of c will be underestimated, and fringes will not be removed at their full amplitude. This issue was particularly apparent in the May 2008 dataset from the CTIO 1.0 m telescope, for which we did not acquire enough fringe fields to create a high

signal-to-noise composite fringe image. To overcome this problem, we eliminated most background noise by spatially smoothing the median-combined master fringe image on scales smaller than the fringe pattern, as seen in Fig. 3.14.

Fringe scaling values were computed to minimize the difference between the master fringe image and each background-subtracted, object-masked image. After a first round of fringe subtraction from the fringe field images themselves, we repeated the above steps but instead used the processed images from the previous iteration to determine the sky background. This resulted in a slightly more accurate master fringe frame.

To defringe the science fields, we followed the same procedures, subtracting the scaled master fringe frame from the science images in two iterations. The second round again included the more accurate sky background, as determined from the first round fringe-subtracted images. Fringe subtraction was successful in removing background variations down to the 0.1% level (as in the bottom panel of Fig. 3.13), suitable for our photometric purposes.

3.3.1.3 Pixel-phase effects

The systematic uncertainties introduced by imperfect guiding, flatfielding, and fringe patterns are largely reflective of interpixel sensitivity variations. However, when the psf of a detector is undersampled (i.e., the psf size is comparable to the pixel scale), *intrapixel* sensitivity effects can also come into play. This was the case with our photometry from *Spitzer*/IRAC–the most undersampled detector employed for photometric time series observations.

Our first pass at the photometry revealed that most objects suffer from the well known IRAC pixel-phase effect: although target positions were restricted to a single pixel, movement of the centroid within the pixel introduces position-correlated flux changes of up to 10% due to response variations within individual pixels (Morales-Calderón et al. 2006; Deming et al. 2011). The x and y centroid positions executed not only several small jumps, but also an oscillatory motion with period $\sim$60 minutes due to the subtle effect of a thermal cycling battery heater on *Spitzer* pointing. As a result, most of the light curves from channel 1 exhibited periodic fluctuations of up to $\sim$4% amplitude, along with additional systematics of up to 10%, or 0.1 magnitudes. We display a typical example of x and y trends as a function of time in Fig. 3.15. The effect is about half as large in channel 2 but still
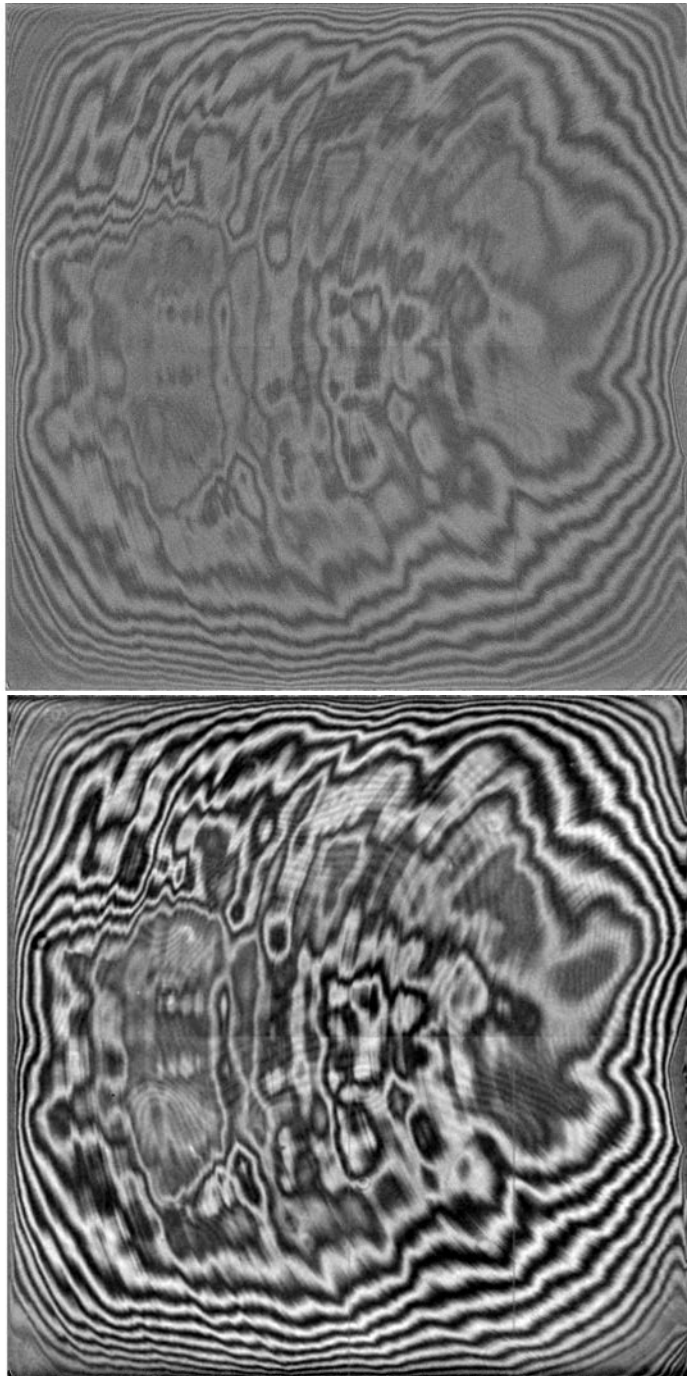
Figure 3.14 Composite fringe frame before (top) and after (bottom) smoothing

significant enough to require removal in many of the light curves.

The Warm *Spitzer* mission guide presents a method to correct these effects by providing a model of the sensitivity variations within a pixel. However, the model was derived from

observations of a single bright star and does not account well for differences in the response patterns of different pixels. We found that the proposed correction algorithm was not adequate for removing the pixel-phase related noise from our light curves. Typical signal-to-noise ratios were 55–60% of that estimated based on the Poisson limit, whereas previous work with warm *Spitzer* data suggests that we should be able to achieve upwards of 75–80% (Deming et al. 2011). On the other hand, subtraction of a median-fit trend from each light curve confirmed that the white noise level did indeed reach a level consistent with these predictions.

To recover the additional $\sim$20% in S/N, we explored several methods for removing noise due to the pixel-phase effect. The failure of the model based on a single bright star implied that the spatial response differs significantly from pixel to pixel. Therefore, we attempted to fit each object's flux with polynomials as a function of x and y position. Unfortunately this approach proved problematic for several reasons. First, the pointing during our Astronomical Observation Request (AOR) traced out a region in x-y space that was neither homogeneous nor large compared to the pixel size (e.g., Fig. 3.15). Rather, small pointing jumps led to centroid positions occupying three somewhat discrete areas of the pixel. In addition, we were concerned that intrinsic variability of our young cluster sources could complicate the fitting process.

Plots of flux versus x, y, and phase (distance from a fixed point near the center of the pixel) did not exhibit tight trends, suggesting that accurate removal of systematic effects would not be feasible. As a result, we opted to fit a Gaussian functional form to each object's spatial flux distribution (e.g., Fig. 3.16). The Warm *Spitzer* guide[3] suggests that a double Gaussian function (i.e., sum of Gaussians in the x and y directions) is the best-fitting pixel sensitivity model based on bright star data. However, because of the incomplete spatial coverage within each pixel, we suspected that a single Gaussian with adjustable center would work as well. Our adopted pixel sensitivity model thus consisted of four free parameters:

$$\Delta F e^{-((x-x_0)^2 + (y-y_0)^2)/2\sigma^2} + F_0, \tag{3.21}$$

where ΔF is the height of the Gaussian function, x and y are the positions with respect to the center of the pixel, x_0 and y_0 are the offsets of the peak flux response from the center

---

[3]http://ssc.spitzer.edu/irac/warmfeatures
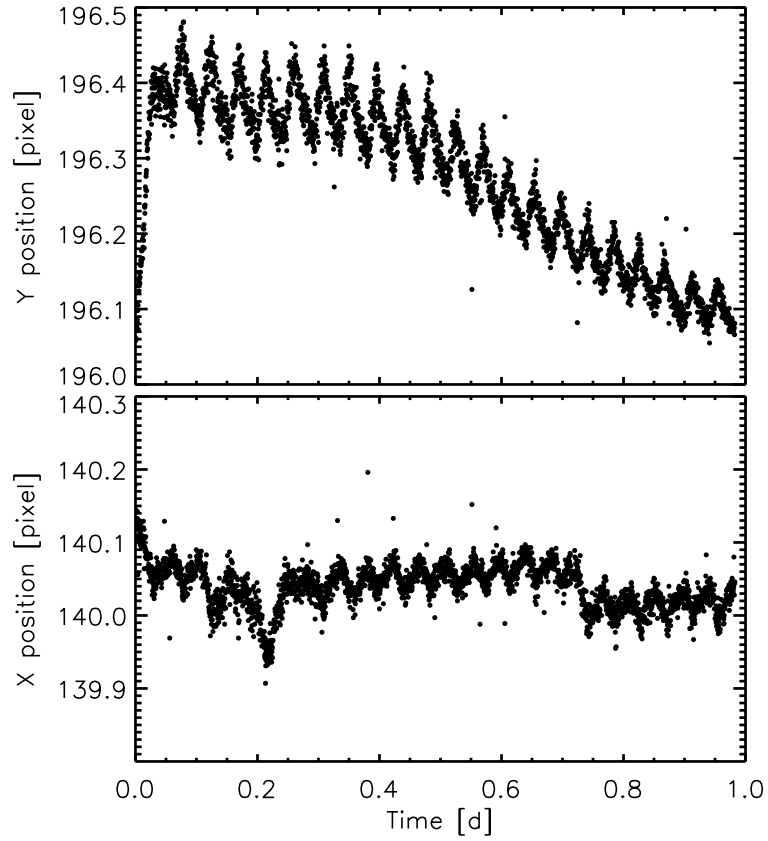
Figure 3.15 X and Y pixel centroid positions of one of our targets (S Ori J053817.8-024050) as a function of time. Since telescope pointing affects all targets in a similar fashion, both the short-timescale ($\sim$0.04 d) oscillations and the more systematic trends are typical of the centroid behavior of other observed objects as well. Outlier points indicate where the centroiding algorithm has failed (e.g., because of a cosmic ray hit or other artifact).

of the pixel, and σ is the width of the Gaussian. F_0 is a constant determined so that the function averages to 1.0 over the entire pixel.
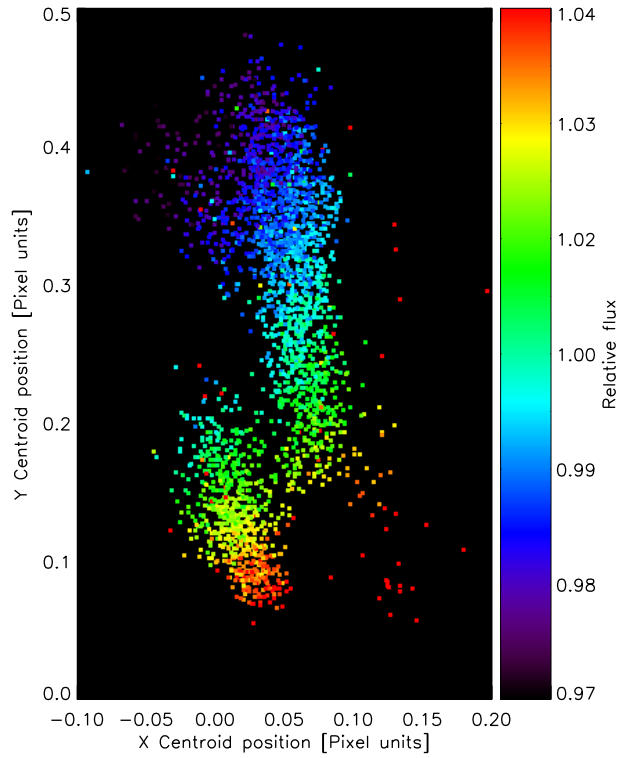
Figure 3.16 Variations in the flux of object SOri J0538217.8-024050 measured within a single pixel. The pixel is centered at [0,0] and extends to ±0.5 in the x and y directions. Only a portion of the pixel is depicted here.

To identify the best-fitting pixel-phase function we created a script to iterate through a reasonable range in the four parameters, perform the pixel-phase correction based on each set, and assess the presence of pixel-phase noise in the resulting light curve. This assessment was performed by generating a periodogram in the range of frequency space where the pixel-phase oscillation dominates: 21.5–25 cycles/day (corresponding to periods of ~1–1.1 hours, and unfortunately very close to the pulsation signature that we seek). It is here that a large peak is seen in the periodograms of raw light curves (Figs. 4.3). We present as the "corrected" light curve the one for which the integrated periodogram in this region is minimized. In some cases the initial periodogram did not display a peak associated

with the pixel-phase effect, and so we did not apply any correction. Since the correction process only targets a small region of frequency space in the periodogram, it should preserve variability that is intrinsic to the objects, if present.

We emphasize that we have chosen the symmetric Gaussian pixel-phase model out of convenience and lack of knowledge of the underlying distribution; the true pixel sensitivity function is likely to be much more complicated (e.g., Ballard et al. 2010). The presented light curves may thus have systematic inaccuracies. In addition, since the correction process removes only variation on the known ~1 hour period of the thermal oscillation, it is not obvious as to whether variation on longer timescales is intrinsic to the sources or undercorrection of the pixel-phase effect. We caution that any Warm *Spitzer* studies attempting to assess variability whose precise nature (i.e., light curve shape) is not known in advance will face this issue.

3.3.2 The "0.1% effects": scintillation noise, color-airmass effects, and aperture placement

A number of the light curves displayed zero-point changes on timescales of one or more days. These variations appeared even among some of the brightest targets but did not seem to occur systematically across all objects. We suspect that slow changes in the pointing, and thus object mapping, in x-y pixel coordinates and other parameters such as seeing and airmass affect the photometry in a position-dependent way. To investigate associated trends in the light curves, we fit object magnitudes linearly as a function of psf FWHM and ellipticity, sky counts, object x and y position, relative centroid position, as well as airmass. The fit to most light curves was only weakly dependent on these parameters. Out of concern for unnecessary addition of noise to the data, we did not remove these low-level trends. In various regimes (e.g., short exposure time, long wavelength, etc.), additional uncertainties will be incurred. Since for the brightest targets our aim was to obtain differential photometry at the sub-1% precision level, we considered additional sources of noise due to atmospheric refraction and transmission effects: stellar scintillation and second-order (color-dependent) extinction. Further low-level errors may be introduced in the data reduction stage, in the form of inaccurate centroiding. We discuss these three effects and their contributions to our time-series data below.

3.3.2.1   Scintillation

Stellar scintillation comes about as a result of atmospheric turbulence, which introduces small but rapid variations in the measured stellar flux. Appearing as additional white noise in light curves, its amplitude depends on a number of factors, including telescope altitude and size. Estimates for the stellar scintillation are typically made via the parameterization by Young (1967), although the effect is further reduced if differential photometry is performed on stars within a typical coherence length of $\sim 12'$ (Ryan & Sandler 1998):

$$\frac{\sigma}{F} \sim 0.09 D^{-2/3} X^{1.75} e^{h/8000m} (2t_{\mathrm{exp}})^{-1/2} \qquad (3.22)$$

where σ is the standard deviation in flux introduced by scintillation, F is the total stellar flux, D is the telescope diameter in centimeters, X is airmass, h is the telescope altitude in meters, and t_{exp} is the exposure time in seconds. We see from the above equation that scintillation noise can be suppressed by employing a larger telescope aperture and/or longer exposures. In cases where this would result in severe saturation of stars, a neutral density filter or aperture stop technique have also been successfully used to achieve high photometric precision while avoiding the scintillation noise inherent in observations with smaller telescopes (López-Morales 2006). And of course, scintillation is completely avoided by employing telescopes in space (e.g., our data from *Spitzer* and *HST*).

Fortunately for our ground-based observations, scintillation was a minor contribution to the overall photometric noise budget. With the CTIO 1.0 m telescope, the expected brightness fluctuations were less than 6×10^{-4} magnitudes, based on exposure times of 6–10 minutes, an altitude of 2215 m, and airmasses less than 2.0. For our P60 observations with five-minute exposure times, we estimated scintillation noise to be even smaller: less than 5×10^{-4} magnitudes. Thus, compared with other noise sources in our data, scintillation effects could be safely neglected.

3.3.2.2   Color-airmass effects

Atmospheric transparency variations are another potential source of low-level correlated noise in differential light curves, particularly when there are differences in color between the late-type objects in our sample and the brighter stars in the reference ensemble. To first order, extinction effects due to changing airmass cancel out in differential photome-

try. However, second-order color terms can introduce significant trends in the light curves if target objects are substantially redder than the reference ensemble (e.g., Young et al. 1991). Atmospheric extinction is weaker at longer wavelengths, and this can emerge as a gradual brightening of differential light curves for fainter, redder objects as airmass decreases. While this behavior was visible in some of the very blue field stars for which we serendipitously obtained photometry, it was not visible in the light curves of faint cluster members in our sample. The absence of significant airmass-flux correlations down to the several-millimagnitude noise level confirmed this finding. We suspect that the lack of obvious trends is due to the relatively weak dependence of extinction on wavelength beyond $\sim$7000 Å. Variable extinction due to changing atmospheric conditions could also produce artificial offsets in the object brightness, whereby the differential magnitudes would correlate with reference ensemble magnitude rather than airmass. Again, we fit the light curves of low-mass stars and brown dwarfs for this effect, but did not detect significant trends and hence did not apply any corrections to the data. This conclusion is echoed by Kraus et al. (2011), who also did not find significant trends in I-band P60 data.

In the case of the CTIO observations of σ Orionis cluster members, further confirmation of negligible color-airmass correlations comes from a derivation of extinction coefficients based on standard star photometric data (we did not obtain extensive color information from other fields or setups). Since the airmass during our observations was restricted to be less than 2.0 while the $R - I$ values of our targets covered a range of $\sim$2.0, the small value of the color-dependent extinction coefficient (k_I', as defined in §3.1.6) suggests that we are justified in neglecting the flux-airmass trends. These secondary color effects should contribute at most 0.004 magnitudes of variation to the light curves–generally far less than other sources of noise and variability, and therefore difficult to remove without compromising the data.

3.3.2.3 Centroiding and aperture placement

For well-sampled data, determination of object centroid positions for flux measurements is straightforward. However, inaccuracies begin to appear when the aperture size is comparable to the pixel scale. An estimate for flux changes as a function of aperture centering error was derived by Irwin et al. (2007). Typically, we chose aperture sizes from 1.5 to 2.5 times the psf FWHM for our ground-based data analysis. In observations with 1.5″ seeing (corre-

sponding to aperture sizes of $\sim 3.0''$), an error of 0.1 pixel (or ~ 0.03–$0.04''$ for the P60 and CTIO 1.0 m CCDs, respectively) would result in a flux change of $\sim 1.5 \times 10^{-6}$–tiny enough to be neglected. However, had we used smaller apertures, of order $1.5''$, the photometry change associated with the same centroiding error would have increased by more than three orders of magnitude, at the level of the Poisson noise for our brightest targets. An additional effect hindering accurate centroid determination is asymmetric psf shape. We have attempted to address this by applying image subtraction and defer the reader to §3.2 for further discussion of this problem. These factors may explain why photometry with twice the calculated optimal aperture size often exhibited higher precision than that derived with the optimal apertures (see §3.1.3).

Centroiding error was also an issue for our Warm *Spitzer* observations, specifically because of the need to remove pixel-phase effects (§3.3.1.3). Tests of random object placement within a pixel have confirmed that the moment centroid is more accurate than the typically used intensity weighted means of the marginal profiles in x and y (S. Carey 2010, private communication). We have therefore computed the moment centroid for all IRAC and WFC3 data.

Chapter 4

Pulsation Search Results

4.1 σ Orionis cluster

Of particular interest to our pulsation search is σ Orionis, one of few young clusters with very low mass members claimed to exhibit periodic variability on timescales of 2–5 hours, as reported by Bailer-Jones & Mundt (2001); Zapatero Osorio et al. (2003), and Scholz & Eislöffel (2004). However, apart from the latter study which presented 23 periodic objects in the northern reaches of the cluster, no comprehensive variability studies have been carried out in the main portion of the cluster. A campaign by Caballero et al. (2004) resulted in the measurement of three rotation periods from a sample of 28 candidate brown dwarfs, while the studies by Bailer-Jones & Mundt (2001) and Zapatero Osorio et al. (2003) contributed another two. Other work by Hernández et al. (2007) and Lodieu et al. (2009) present evidence for generic variability based on sparsely sampled photometry over year timescales. We have taken advantage of the numerous prior single-pointing surveys to select a sample of $\sim$150 likely young BDs and VLMSs distributed throughout σ Orionis, in which we not only searched for pulsation but also investigated overall variability properties (Chapter 5). Observations took place with both the CTIO 1.0 m telescope and the *Spitzer* Space Telescope, as described below.

4.1.1 Target fields

Our ground-based observations targeted two fields (Fig. 4.1) selected to avoid bright stars such as σ Ori AB itself, while maximizing both the density of confirmed or suspected low-mass cluster members and number of objects with previously observed variability. We

cross-correlated the positions of objects in our fields with the sources mentioned in §2.2.1 to assemble a final list of confirmed and likely members appearing in our imaging data.

We list the results of this cross correlation in Table 4.1, where we provide alternate identifications based on previous membership surveys of the cluster (we omit studies that are primarily follow-up). In particular, "S Ori," objects are from Béjar et al. (1999, 2001), "r" and "4771-" ids are from Wolk (1996)'s x-ray-selected source list, "SO" objects are from Hernández et al.'s 2007 list of candidate cluster members, and Mayrit numbers are from the Mayrit catalog compiled by Caballero (2008). All other ids in Table 4.1 correspond to the author(s)'s initial followed by their own numbering system: SWW numbers refer to the survey of Sherry et al. (2004); KJN is the survey of Kenyon et al. (2005), SE is Scholz & Eislöffel (2004), M refers to Maxted et al. (2008), B is for Burningham et al. (2005), and F is Franciosini et al. (2006). Source HH446 is from from Andrews et al. (2004). The six objects without ids were found in this work (see §7.1.1). We also note that several of the objects identified in Sherry et al. (2004) are duplicated in their list and thus only included once here (SWW103 is SWW207; SWW126 is SWW162). Based on the finder chart provided by Béjar et al. (1999), we also conclude that S Ori 26 is incorrectly identified by Lodieu et al. (2009); the actual object is their UGCS J05:39:15.76-02:38:26.3, a proper-motion selected σ Ori member.

In addition, Table 4.1 contains a membership evidence column referring to photometric and spectroscopic measurements that confirm the object's youth and/or cluster membership, e.g., Hα or Na emission lines indicative of low gravity, forbidden emission lines (OI, NII, SII; "FL"), presence of Li absorption, radial velocity ("v_r") consistent with the σ Ori mean ($27 < v_r < 37$ km s^{-1}; Jeffries et al. 2006), infrared excess from $Spitzer$ indicative of a disk ("D"), and proper motion ("(PM)") consistent with $sigma$ Ori membership (we have applied parentheses since this latter criterion is not enough to definitively select members but is useful for eliminating some non-members). Disks noted as "EV" or "TD" refer to evolved and transitional disks, respectively, as classified by Hernández et al. (2007). We note that while Luhman et al. (2008b) did not explicitly list which stars have infrared excesses indicative of disks, we have used their photometry (derived from Spitzer images acquired by Hernández et al. (2007) and Scholz & Jayawardhana (2008)) to identify disk-bearing candidates (§7.4). Unsurprisingly, we recover all but one of the disks already identified by Caballero et al. (2007) and Hernández et al. (2007) from the same images. We therefore

do not include Luhman et al. (2008b) in our disk references, except in the case of the one newly-identified disk-bearing object, 2MASS J05375398-0249545. We do not list objects that are saturated in our photometry or were presented in the above references but later determined to be non-members. Objects with evidence both for and against membership are listed with an "NM" along with the the specific criterion suggesting non-membership.
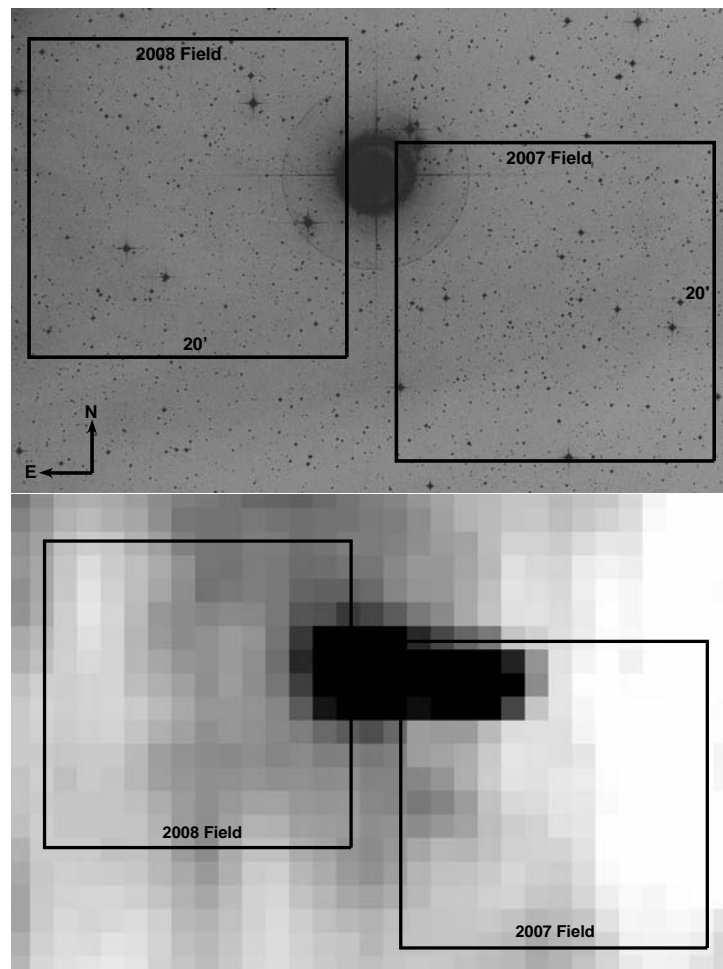
Figure 4.1 Observed σ Orionis fields are superimposed on a Palomar Observatory Sky Survey 2 (POSS2) red image (top) obtained from the Digitized Sky Survey (DSS) and an Infrared Astronomical Satellite (IRAS) 100 μm image (bottom). The 2007 field is centered at R.A. = $05^h38^m00.6^s$ and decl. = $-02°43'46.3''$, while the coordinates of the 2008 field are R.A. = $05^h39^m31.2^s$, decl. = $-02°37'25.9''$. σ Ori itself is the bright object near center, and greater extinction is seen in the 2008 field than in that from 2007.

Table 4.1. Confirmed and candidate σ Orionis members in our photometric sample

Object	Other IDs	SpT	Variable?	Membership evidence	Refs
2MASS J05372806-0236065	SO59				13
2MASS J05373648-0241567	S Ori 40, KJN75, SO116	M7		v_r, Hα, Li, Na	1,4,5
2MASS J05373784-0245442	SWW184, SO123		Y[13]	(PM)	12
2MASS J05373790-0236085					
2MASS J05374413-0235198					
2MASS J05375161-0235257	SWW125, F1, Mayrit 797272, SO214	M1-3		Hα, Li	7
2MASS J05375206-0236046	KJN62, M182, Mayrit 790270			(v_r NM?[9]), Li, Na, (PM)	4,9,12
2MASS J05375398-0249545	SWW221, Mayrit 1129222		Y[12]	D, (PM)	12,14
2MASS J05375404-0244407	SWW68, SO240			(PM)	12
2MASS J05375486-0241092	SWW174, B237, SO247, Mayrit 809248			v_r, (Na NM?[10]), D, (PM)	10,12,13
2MASS J05375745-0238444	S Ori 12, KJN39, M162, SO271, Mayrit 728257	M6		v_r, Li, Na, D, (PM)	1,4,5,9,12,13
2MASS J05375840-0241262	SWW53, KJN18, M118, SO283, Mayrit 767245			v_r, Li, Na, (PM)	4,9,12
2MASS J05375970-0251033	SO293				
2MASS J05380055-0245097	SWW140, M178, F4,SO297, Mayrit 861230			v_r, Na, (PM)	9,12
2MASS J05380107-0245379	SWW180, M85, SO300, Mayrit 873229		Y[13]	Na, D, (PM)	9,12,13
2MASS J05380552-0235571	S Ori J053805.5-023557, M186, SO327, Mayrit 588270			v_r, Na, D, (PM)	9,12,13
2MASS J05380826-0235562	SWW41, F9, SO362, Mayrit 547270		Y[13]	Hα, Li, D, (PM)	2,12,13
2MASS J05380994-0251377	SWW52, M133, SO374, Mayrit 1073209		Y[13]	v_r, Na, D, (PM)	9,12,13
2MASS J05381175-0245012	SO385				
2MASS J05381265-0236378					
2MASS J05381315-0245509	SWW98, SO396, Mayrit 757219		Y[13]	D, (PM)	12,13
2MASS J05381330-0251329	KJN48, M137, SO401, Mayrit 1045207			v_r, Li, Na, (PM)	4,9,12
2MASS J05381589-0234412	SO424				
2MASS J05381610-0238049	S Ori J053816.0-023805, SWW12, KJN11, M167, Mayrit 447254			v_r, Li, Na, (PM)	4,9,12

Table 4.1—Continued

Object	Other IDs	SpT	Variable?	Membership evidence	Refs
2MASS J05381741-0240242	S Ori 27, KJN60, M146, Mayrit 488237	M7 (M6.5[3])	Y[15]	v_r, Li, Na, (PM)	1,3,4,9,12
2MASS J05381778-0240500	S Ori J053817.8-024050, SWW5, F17, SO435, Mayrit 498234		Y[13]	D, (PM)	12,13
2MASS J05381824-0248143	SWW40, M174, SO444, Mayrit 835208			v_r, Na, D(EV), (PM)	9,12,13
2MASS J05381834-0235385	S Ori J053818.2-023539, KJN76, M203, F19, SO446, Mayrit 396273			v_r, (Na NM?[4]), (PM)	4,9,12
2MASS J05381886-0251388	SWW39, M136, SO451, Mayrit 1016202			v_r, Na, D, (PM)	9,12,13
2MASS J05381914-0235279	SO454			(PM)	12
2MASS J05382021-0238016	S Ori J053820.1-023802, SWW131, M168, F20, SO460, Mayrit 387252	M4		v_r, Hα, Li, Na, (PM)	1,2,3,9,12
2MASS J05382050-0234089	r053820-0234, SWW124, M106, SO462, Mayrit 380287	M4	Y[12,13]	v_r, Hα, Li, Na, D, (PM)	1,3,9,12,13
2MASS J05382088-0246132	S Ori 31, SO465, Mayrit 710210	M7	Y[15,16]	(PM)	1,12
2MASS J05382089-0251280	M138, SO466, Mayrit 994201			v_r, Na, (PM)	9,12
2MASS J05382307-0236493	SWW103, B51, SO482, Mayrit 329261		Y[13]	v_r, (Na NM?[10]), D, (PM)	10,12,13
2MASS J05382332-0244142	S Ori J053823.3-024414, SWW139, KJN15, M52, F25, Mayrit 589213			v_r, Li, (PM)	4,9,12
2MASS J05382354-0241317	S Ori J053823.6-024132, SWW3, B229, M121, F26, SO489, Mayrit 459224			v_r, Na, (PM)	9,10,12
S Ori J053825.1-024802	S Ori 53				
2MASS J05382543-0242412	S Ori J053825.4-024241, SO500, Mayrit 495216	M6	Y[6,12]	v_r, Hα, FL, D, (PM)	6,8,12,13
2MASS J05382557-0248370	S Ori 45	M8.5	Y[15,16,17]	v_r, Hα, Li, FL	1,3,5
2MASS J05382623-0240413	S Ori J053826.1-024041, KJN58, M141, SO509, Mayrit 395225	M8 (M5,M6[6])	Y[15]	v_r, Li, Na, (PM)	1,4,6,9,12
2MASS J05382684-0238460	S Ori J053826.8-023846, B368, M163, SO514, Mayrit 316238			v_r, Hα, Li, Na, D, (PM)	2,9,10,12,13
2MASS J05382725-0245096	4771-41, F32, KJN7, SO518, Mayrit 609206			v_r, Hα, Li, FL, D	1,3,13
2MASS J05382750-0235041	S Ori J053827.5-023504, SWW67, M96, F33, SO520, Mayrit 265282	M3.5		v_r, Hα, Li, Na, D, (PM)	2,9,12,13
2MASS J05382774-0243009	SWW87, F34, SO525			v_r, Hα, Li, (PM)	2,12
2MASS J05382848-0246170	SWW188				
2MASS J05382896-0248473	S Ori J053829.0-024847, M170, SO537, Mayrit 803197	M6		v_r, Na, D	1,8,9,13
2MASS J05383141-0236338	SWW50, SO562, Mayrit 203260			v_r, Hα, Li, D, (PM)	2,12,13

Table 4.1—Continued

Object	Other IDs	SpT	Variable?	Membership evidence	Refs
2MASS J05383157-0235148	r053831-0235, SWW49, F44, SO536, Mayrit 203283	M0		v_r, Hα, Li, D, (PM)	1,2,3,12,13
2MASS J05383160-0251268	SWW178, SO564, Mayrit 947192			(PM)	12
2MASS J05383284-0235392	r053832-0235b, SO572, F54			v_r, Hα, Li	2
2MASS J05383302-0239279	F50, SO576			(PM NM?[12])	
2MASS J05383335-0236176	SWW130, F52, SO582			(PM)	12
2MASS J05383388-0245078	S Ori J053833.9-024508, KJN36, M202, Mayrit 571197			(v_r NM?[9]), Li, Na, D, (PM)	4,8,9,12
2MASS J05383405-0236375	r053833-0236, SWW66, F54, SO587, Mayrit 165257	M3.5		v_r, Hα, Li, FL, D	1,2,3,13
2MASS J05383460-0241087	S Ori J053834.5-024109, SWW80, SO598, Mayrit 344206		Y[13]	D, (PM)	12,13
2MASS J05383669-0244136	S Ori J053836.7-024414, SWW16, M63, SO621, Mayrit 508194			v_r, Hα, Li, (PM)	2,9,12
2MASS J05383745-0250236	SWW11, M155, SO628, Mayrit 870187			v_r, Na, (PM)	9,12
2MASS J05383858-0241558	S Ori J053838.6, KJN44, B215, M114, SO641, Mayrit 368195	M5.5		v_r, Li, Na, (PM)	4,6,9,10,12
2MASS J05383902-0245321	SWW31, M156, SO646, Mayrit 578189		Y[13]	v_r, Hα, Li, D, (PM)	2,9,12,13
2MASS J05383922-0253084	SO648			(PM NM?[12])	
2MASS J05385317-0243528	SWW47, F106, SO785, Mayrit 489165		Y[13]	v_r, Hα, Li, (PM)	2,12
2MASS J05385382-0244588	S Ori J053853.8-024459			(PM)	12
2MASS J05385492-0228583	SWW10, SE77, KJN21, SO797, Mayrit 449020		Y[11]	v_r, Li, Na, (PM)	4,12
2MASS J05385492-0240337	S Ori J053854.9-024034			D	8
2MASS J05385542-0241208	S Ori J053855.4-024121, Mayrit 358154	M5	Y[12]	Hα, FL, D, (PM)	7,8,12
2MASS J05385623-0231153	K1.02-91				
2MASS J05385922-0233514	SO827, SWW227, F118, Mayrit 252059		Y[13]	v_r, Hα, Li, D, (PM)	2,12,13
2MASS J05385946-0242198					
2MASS J05390052-0239390	4771-1056, F122				
2MASS J05390115-0236388	KJN9, M213, F124, SO841, Mayrit 249099			v_r, Li, Na,(PM)	4,9,12
2MASS J05390193-0235029	SO848, S Ori J053902.1-023501, Mayrit 264077	M3	Y[13]	Hα, FL, D, (PM)	7,8,12,13

Table 4.1—Continued

Object	Other IDs	SpT	Variable?	Membership evidence	Refs
2MASS J05390276-0229558	SWW28, F126, SO855, Mayrit 453037			v_r, Hα, Li, (PM)	2,12
S Ori J053903.2-023020	S Ori 51				
2MASS J05390357-0246269	SWW122, SO865, Mayrit 687156		Y[13]	D, (PM)	12,13
2MASS J05390449-0238353	S Ori 17, SO870, Mayrit 334118	M6		Li	1,5
2MASS J05390458-0241493	SO871, Mayrit 458140		Y[12]	D, (PM)	12,13
2MASS J05390524-0233005	SWW175, KJN4, F131, SO877, Mayrit 355060			v_r, Li, Na, (PM)	4,12
2MASS J05390540-0232303	4771-1075, KJN7, F132, SO879, Mayrit 374056		Y[13]	v_r, Hα, Li	1,2,3
CTIO J05390664-0238050					
2MASS J05390759-0228234	r053907-0228, SWW121, SE82, F137, SO896, Mayrit 571037	M3		v_r, Hα, Li, (PM)	1,2,3,12
2MASS J05390760-0232391	4771-1092, F138, SO897, Mayrit 397060			v_r, Hα, Li, D(TD)	2,13
2MASS J05390808-0228447	S Ori 8, SE83, SO901, Mayrit 558039			D(EV), (PM)	12,13
2MASS J05390821-0232284	S Ori 7, SWW108, SO902, Mayrit 410059			(PM)	12
2MASS J05390878-0231115	SWW129, SO908, Mayrit 461051			D, (PM)	12,13
2MASS J05390894-0239579	S Ori 25, F140, SO911, Mayrit 433123	M7.5 (M6.5[5])	Y[15]	v_r, Hα, Li, (PM)	1,5,12
2MASS J05391001-0228116	S Ori J053909.9-022814, KJN33, SO917	M5		NM?[12,4], D(EV)	1,4,12,13
2MASS J05391003-0242425	SO918, Mayrit 552137			(PM)	12
S Ori J053910.8-023715	S Ori 50				
2MASS J05391139-0233327	SOri J053911.4-023333, KJN42, SO925, Mayrit 425070	M5		v_r, Li, Na, (PM)	1,4,12
2MASS J05391151-0231065	SWW195, F144, SO927, Mayrit 497054			v_r, Hα, Li, D, (PM)	2,12,13
2MASS J05391163-0236028	4771-1038, KJN8, SWW153, F145, SO929, Mayrit 403090			v_r, Hα, Li	1,2,3
2MASS J05391232-0230064	SWW203, F147, SO933, Mayrit 544049			(PM)	12
2MASS J05391308-0237509	SOri 30, SO936, Mayrit 438105	M6		D, (PM)	1,8,12,13
2MASS J05391346-0237391	F148, SO940, Mayrit 441103			(PM)	12
2MASS J05391447-0228333	SOri J053914.5-022834, SWW95, SE88, F149, SO946, Mayrit 631045	M3.5		v_r, Li, (PM)	1,3,12

Table 4.1—Continued

Object	Other IDs	SpT	Variable?	Membership evidence	Refs
2MASS J05391510-0240475	SOri 16, SO957, Mayrit 538122			(PM)	12
2MASS J05391576-0238262	SOri 26	M4.5		(PM)	1,12
2MASS J05391582-0236507	SO967, K1.02-4, F151, Mayrit 468096			D, (PM)	12,13
2MASS J05391699-0241171	F153, SO976, M578123		Y[13]	(PM)	12
2MASS J05391883-0230531	4771-0910, SO984, F157, Mayrit 596059			v_r, Hα, Li, D	2,13
2MASS J05392023-0238258	S Ori 5, SWW60, SO999, Mayrit 551105			(PM)	12
2MASS J05392097-0230334	S Ori 3, KJN20, F160, SO1005, Mayrit 633059			v_r, Li, Na, (PM)	4,12
2MASS J05392174-0244038	SO1009, Mayrit 735131			D(EV)	13
2MASS J05392224-0245524	S Ori J053922.2-024552, SO1013				
2MASS J05392286-0233330	r053923-0233, SWW185, F161, SO1017, Mayrit 590076	M2	Y[13]	v_r, Hα, Li, (PM)	1,2,3,12
2MASS J05392307-0228112					
2MASS J05392319-0246557	S Ori 28, KJN64, Mayrit 872139		Y[15]	(v_r NM?[9]), Li, Na, (PM)	4,9,12
2MASS J05392341-0240575	S Ori 42	M7.5	Y[15]	Hα, D	1,8
2MASS J05392435-0234013	SWW127, M191, F164, SO1027			v_r, Hα, Na, (PM NM?[12])	2,9
2MASS J05392519-0238220	SWW135, F165, SO1036, Mayrit 622103		Y[13]	v_r, Hα, Li, D	2,13
2MASS J05392524-0227479	B157, SO1037			v_r, Na, (PM NM?[12])	10
2MASS J05392560-0238436	HH446, Mayrit 633105			(PM)	12
2MASS J05392561-0234042	SWW7, SO1043, Mayrit 623079				
2MASS J05392633-0228376	SOri 2, SWW164, SE93, SO1050, Mayrit 764055		Y[11]	D, (PM)	12,13
2MASS J05392677-0242583	SWW45, SO1057, Mayrit 756124		Y[13]	D(EV), (PM)	12,13
2MASS J05392685-0236561	S Ori 36, KJN74, M177, SO1059			v_r, Li, Na (bin?), D	4,8,9,13
2MASS J05393056-0238270	SO1081, SWW222, B260, F169			Hα (NM?[2,10])	2,10
2MASS J05393234-0227571	SO1092, Mayrit 861056				
2MASS J05393432-0238468	S Ori 21, KJN61, M126, SO1108, Mayrit 761103			v_r, Li, Na, (PM)	4,9,12

Table 4.1—Continued

Object	Other IDs	SpT	Variable?	Membership evidence	Refs
2MASS J05393673-0231588	B237			v_r, (Na NM?[10])	10
2MASS J05393759-0244304	S Ori 14, KJN49, M169, SO1135, Mayrit 942123			v_r, Li, Na, (PM)	4,9,12
2MASS J05393931-0232252	S Ori 4, SWW107, M117, SO1151, Mayrit 839077			(PM)	12
2MASS J05393982-0231217	SO1153, Mayrit 871071		Y[13]	D	13
2MASS J05393982-0233159	F174, SO1154, Mayrit 841079		Y[13]	D, (PM)	12,13
2MASS J05393998-0243097	F175, SO1155			D	13
2MASS J05394057-0239123	SO1162, B233			v_r, Na, (PM NM?[12])	10
2MASS J05394318-0232433	S Ori J053943.2-023243, SWW75, SO1182, Mayrit 897077		Y[13]	D, (PM)	12,13
2MASS J05394411-0231092	SO1189, Mayrit 936072				
2MASS J05394433-0233027	S Ori 11, M110, SO1191, Mayrit 910079	M6		v_r, Na, (PM)	1,9,12
2MASS J05394725-0241359	SWW192				
2MASS J05394770-0236230	B179, , SO1216			v_r, Na, (PM)	9,10,12
2MASS J05394784-0232248	SO1217, Mayrit 969077				
2MASS J05394799-0240320	SWW32, SO1219, Mayrit 986106			(PM)	12
2MASS J05394806-0245571	S Ori J053948.1-024557, SWW92, SO1220			(PM)	12
2MASS J05394826-0229144	S Ori J053948.1-022914, SE108	M7	Y[11]	NM?[8,12]	1
2MASS J05394891-0229110	SWW126, B319			(v_r NM?[10]), Na	10
2MASS J05395038-0243307	SO1235, Mayrit 1082115		Y[13]		
2MASS J05395056-0234137	S Ori J053950.6-023414, KJN19, M115, SO1238, Mayrit 992084			v_r, Li, Na, (PM)	4,9,12
2MASS J05395236-0236147	S Ori J053952.3-023615, M104			Na, (v_r NM?[9]), (PM)	9,12
2MASS J05395248-0232023	SO1250				
2MASS J05395313-0243083	SO1256, Mayrit 1110113				
2MASS J05395313-0230294	M209			v_r, Na	9
2MASS J05395362-0233426	SO1260, Mayrit 1041082		Y[13]	D, (PM)	12,13

Table 4.1—Continued

Object	Other IDs	SpT	Variable?	Membership evidence	Refs
2MASS J05395433-0237189	S Ori J053954.3-023720, M98, SO1268, Mayrit 1045094	M6		v_r, Na, D(TD), (PM)	6,8,9,12,13
2MASS J05395645-0238034	SOriJ053956.4-023804, B143, M93, SO1285, Mayrit 1081097			v_r, Na, D, (PM)	10,12,13
2MASS J05395753-0232120	S Ori J053957.5-023212, M131, SO1295, Mayrit 1114078			v_r, Na, (PM)	9,12
2MASS J05400338-0229014	SO1337, Mayrit 1250070				
2MASS J05400453-0236421	S Ori J054004.5-023642, KJN73, M102, SO1338, Mayrit 1196092		Y[15]	v_r, Na, D, (PM)	4,8,9,12,13
2MASS J05400525-0230522	S Ori J054005.1-023052, M143, SO1344, Mayrit 1245076	M5		v_r, Hα, Li, Na, D	1,3,9,13
2MASS J05400708-0232446	S Ori J054007.1-023245, M125, SO1353, Mayrit 1249081			v_r, Na, (PM)	9,12
2MASS J05400867-0232432	SO1359, Mayrit 1273081				
2MASS J05400889-0233336	SO1361, Mayrit 1269083		Y[13]	D	13

Note. — References are as follows: [1]Barrado y Navascués et al. (2003), [2]Sacco et al. (2008), [3]Zapatero Osorio et al. (2002), [4]Kenyon et al. (2005), [5]Muzerolle et al. (2003), [6]Caballero et al. (2006), [7]Caballero et al. (2008), [8]Caballero et al. (2007), [9]Maxted et al. (2008), [10]Burningham et al. (2005), [11]Scholz & Eislöffel (2004), [12]Lodieu et al. (2009), [13]Hernández et al. (2007), [14]Luhman et al. (2008b), [15]Caballero et al. (2004),[16]Bailer-Jones & Mundt (2001), [17]Zapatero Osorio et al. (2003).

4.1.2 Ground-based data acquisition & reduction

A field centered on R.A. = $05^{\rm h}38^{\rm m}00.6^{\rm s}$ and decl. = $-02°43'46.3''$ (J2000) in the σ Ori-onis cluster was observed for 12 consecutive nights from 2007 December 27 to 2008 January 7 with the CTIO 1.0 m telescope and Y4KCam detector. A second field at R.A. = $05^{\rm h}39^{\rm m}31.2^{\rm s}$, decl. = $-02°37'25.9''$ was observed from 14 to 24 Dec 2008. During this second run, two repeat observations per night were also obtained of the first field, such that long-term photometric trends might be investigated. Skies were clear and photometric for the majority of observations, with little moon and seeing from $0.9''$–$1.8''$. The CCD consists of a 4064×4064 chip with 15 μm pixels, corresponding to a scale of $0.289''$ pixel^{-1} and an approximately $20' \times 20'$ field of view. Because readout occurs in quadrants, bias levels vary in the four regions. This effect unfortunately cannot be completely calibrated out, because both the mean bias level across the amplifiers as well as the two-dimensional spatial dependence are highly time variable, as seen in the behavior of the overscan region and bias images. Our photometry is largely unaffected by this issue since sky subtraction takes into account local bias levels around our targets. However, we have masked out data in the central 20 columns and rows of the CCD where rapid spatial variation in the bias between different quadrants prevents proper background extraction. The amplifiers have gains from 1.33 to 1.42 electron ADU^{-1} and readout noise $\sim$7 electron pixel^{-1}.

The observations targeted 153 candidate very-low-mass σ Ori members, including some 15 spectroscopically confirmed young brown dwarfs (see Table 4.1). Our goal of acquiring high-precision time series photometry on these objects required accumulation of as much signal as possible while maintaining an observing cadence well under the $\sim$1 hour timescales of interest for short-period signals. Theoretically, the shortest detectable sinusoidal period is twice the cadence; we elaborate on this relationship in §5. In practice, exposure times are limited by contamination from large numbers of cosmic ray hits and diffraction spikes from saturation of numerous nearby bright stars when count levels reach 50,000 ADU. As a compromise between these competing effects, we initially chose an exposure time of 360 seconds in the Cousins I band, where the optical spectral energy distribution of brown dwarfs nears its maximum. During the 2008 observations, we increased integrations to 600 seconds for slightly improved signal-to-noise. Due to the consistent night-to-night observing conditions, these setups did not need to be adjusted throughout the runs. With a detector

read-out time of 90 seconds in the unbinned mode, the resulting cadences were 7.5 and 11.5 minutes per photometric data point in the 2007 and 2008 run, respectively. The corresponding total observation times were 72 and 60 hours, resulting in 523 and 338 data points.

Careful calibration procedures were followed to ensure that the ultimate photometry was restricted mainly by source and sky background noise inherent to the measurements. Sets of bias images and dome flats were acquired daily. Since dome flatfield images taken with the CTIO 1.0 m telescope are known to deviate from the true pixel sensitivity distribution by up to 10% toward the corners of the detector, we only used sky flatfields. Twilight sky flats were obtained at the beginning and end of each night in the I band. Uniform bright sky illumination and detector response can be achieved with exposures of at least 10 seconds (to mitigate shutter shading effects) and less than a few minutes (to avoid the appearance of many stars in the flatfield). Conditions allowed for four consecutive sky flats with flux levels averaging 30,000 counts, providing a good representation of pixel sensitivity variations within the linearity limit of the CCD. We checked that the combination of all eight twilight flats per night should contribute an uncertainty of less than 0.002 magnitudes per pixel to the photometry, sufficient for our precision requirements. For two nights when thin cirrus prevented uniform twilight exposures, we incorporated observations from adjoining nights into the composite flatfield after confirming that the detector sensitivity did not change significantly over 24 hour timescales. In a few cases, new dust did appear on the CCD window midway through the night and its corresponding "donut" could not be adequately removed from the images. Affected areas were noted and confirmed not to lie in close proximity to any of our photometric targets or potential reference stars. We ensured that the pointing remained stable by choosing the same guide star from night to night and centering it in the same pixel of the guide camera.

We cleaned the images of cosmic rays with the IRAF *cosmicrays* utility. This detects and replaces sharp, non-stellar sources appearing more than five standard deviations above the background. Rare cosmic ray hits coincident with the stars and brown dwarfs are not removed in this way and must be identified separately in the later light curves. Standard reductions, including subtraction of biases and flatfielding, were carried out with the IRAF *imred* package. Images were split into quadrants, and each corrected with a high-order fit to its individual overscan, to account for highly variable bias structure at the edge between

the bottom and top amplifiers. Quadrants were subsequently trimmed and pasted back together to form a seamless image. Residual two-dimensional bias structure was removed by subtracting a master frame of 20 median-combined zero images.

Because the I band[1] extends well beyond 8000 Åand the typical CCD thickness is 20 μm or less, our images suffer from fringing, as explained in §3.3.1.1. We removed the fringing using the procedures detailed therein. Since no fringe field exposures were taken during the 2008 run, we used the same 2007 master frame for this data, resulting in slightly higher residuals. We found that these steps effectively removed fringes in some 95% of images if liberal object masking was applied, especially in the northeast corner of the field where stray light from a bright nearby star reflected into the detector field of view. The remaining 5% of images were corrected by manual defringing. Fringe subtraction was successful in removing background variations down to the 0.1% level, suitable for our photometric purposes. Images were then aligned to the same x-y coordinates with a small flux-preserving shift using the IRAF script IMAL2 provided by Deeg & Doyle (2001). This script takes as input a number of bright reference stars across an image, determines their centers using the IRAF *imcentroid* task, and outputs the mean shift in x and y. It then uses the IRAF *imshift* task to perform the shift calculated for each image.

We performed variable aperture photometry with and without image subtraction on the final images, as explained in §3.2. In addition, we calibrated R and I-band magnitudes to the Cousins system following the procedures in §3.1.6. The majority of objects in our cluster sample were also detected in the 2MASS survey, which provides J, H, and K_s-band data. We cross-referenced the positions of likely cluster members to identify all 2MASS sources in our sample. Since young VLMSs and BDs have very red colors, all but the faintest (e.g., $I > 20$) have $J/H/K_s$ detections. Table 4.2 contains a compilation of our own absolute photometry of confirmed and candidate σ Orionis members, along with the corresponding 2MASS magnitudes.

---

[1]Filter profiles are available here: http://www.astronomy.ohio-state.edu/Y4KCam/Filters/y4kcam_Ic.txt

Table 4.2.   Photometry of confirmed and candidate cluster members in the σ Ori sample

Object	R	I	J	H	K
2MASS J05372806-0236065	16.37±0.03	15.10±0.03	13.74±0.03	13.08±0.03	12.80±0.03
2MASS J05373648-0241567	19.88±0.07	17.90±0.05	15.47±0.05	14.94±0.05	14.56±0.10
2MASS J05373784-0245442	15.22±0.03	14.00±0.03	12.69±0.03	11.95±0.02	11.72±0.03
2MASS J05375161-0235257	14.49±0.03	13.27±0.03	11.89±0.03	11.17±0.02	10.98±0.02
2MASS J05375206-0236046	19.23±0.05	17.26±0.04	15.14±0.04	14.55±0.04	14.20±0.06
2MASS J05375398-0249545	18.17±0.04	16.77±0.03	14.52±0.03	13.25±0.02	12.46±0.03
2MASS J05375404-0244407	15.85±0.03	14.49±0.03	13.02±0.03	12.34±0.03	12.10±0.02
2MASS J05375486-0241092	17.08±0.04	15.36±0.04	13.50±0.03	12.90±0.03	12.64±0.03
2MASS J05375745-0238444	18.12±0.05	16.25±0.04	14.23±0.03	13.63±0.03	13.29±0.03
2MASS J05375840-0241262	17.19±0.04	15.32±0.04	13.29±0.03	12.70±0.02	12.42±0.03
2MASS J05375970-0251033	12.80±0.10	12.05±0.03	10.69±0.03	9.87±0.02	9.71±0.02
2MASS J05380055-0245097	16.23±0.04	14.52±0.04	12.73±0.03	12.08±0.02	11.82±0.02
2MASS J05380107-0245379	16.16±0.04	14.47±0.04	12.41±0.03	11.62±0.02	11.12±0.02
2MASS J05380552-0235571	19.61±0.06	17.69±0.04	15.28±0.04	14.77±0.06	14.24±0.07
2MASS J05380826-0235562	15.18±0.03	13.86±0.03	12.14±0.03	11.38±0.02	11.05±0.02
2MASS J05380994-0251377	15.24±0.03	13.88±0.03	12.34±0.02	11.57±0.02	11.24±0.02
2MASS J05381175-0245012	13.16±0.12	12.22±0.03	10.47±0.03	9.72±0.02	9.43±0.02
2MASS J05381315-0245509	14.66±0.03	13.51±0.03	12.07±0.03	11.26±0.02	10.77±0.02
2MASS J05381330-0251329	18.54±0.05	16.62±0.04	14.57±0.03	14.00±0.03	13.63±0.04
2MASS J05381589-0234412	14.06±0.02	13.37±0.02	12.37±0.03	11.75±0.02	11.59±0.02
2MASS J05381610-0238049	16.85±0.04	15.22±0.04	13.58±0.03	12.88±0.02	12.61±0.03
2MASS J05381741-0240242	19.24±0.05	17.22±0.05	14.83±0.03	14.31±0.04	14.09±0.05
2MASS J05381778-0240500	16.77±0.04	15.00±0.04	13.20±0.03	12.58±0.02	12.24±0.02
2MASS J05381824-0248143	15.23±0.03	14.18±0.03	12.76±0.03	12.02±0.02	11.80±0.02
2MASS J05381834-0235385	20.39±0.08	18.24±0.05	15.45±0.04	14.83±0.05	14.49±0.08
2MASS J05381886-0251388	15.71±0.03	14.25±0.03	12.81±0.02	12.04±0.02	11.73±0.02
2MASS J05381914-0235279	14.26±0.02	13.46±0.02	12.31±0.03	11.57±0.02	11.39±0.02
2MASS J05382021-0238016	16.06±0.04	14.33±0.04	12.58±0.03	11.86±0.02	11.61±0.02
2MASS J05382050-0234089	17.00±0.06	14.55±0.05	12.65±0.03	11.92±0.02	11.65±0.02
2MASS J05382088-0246132	19.43±0.06	17.46±0.04	15.19±0.04	14.57±0.05	14.16±0.08
2MASS J05382089-0251280	19.13±0.05	17.09±0.05	14.78±0.03	14.21±0.03	13.87±0.05
2MASS J05382307-0236493	17.14±0.04	15.65±0.03	13.80±0.03	13.17±0.03	12.78±0.02
2MASS J05382332-0244142	16.86±0.04	15.17±0.04	13.46±0.03	12.85±0.02	12.56±0.02
2MASS J05382354-0241317	16.89±0.04	15.13±0.04	13.29±0.03	12.74±0.03	12.40±0.02
S Ori J053825.1-024802	21.64±0.29	20.31±0.09	-	-	-
2MASS J05382543-0242412	18.77±0.05	16.96±0.04	14.88±0.03	14.16±0.04	13.57±0.03
2MASS J05382557-0248370	22.38±0.38	20.03±0.09	16.67±0.11	16.02±0.13	15.59±0.21
2MASS J05382623-0240413	19.03±0.05	17.05±0.04	14.91±0.04	14.28±0.04	13.92±0.06

Table 4.2—Continued

Object	R	I	J	H	K
2MASS J05382684-0238460	18.12±0.05	16.17±0.04	14.11±0.04	13.48±0.03	13.21±0.04
2MASS J05382725-0245096	13.85±0.03	12.95±0.02	11.96±0.03	10.79±0.03	9.94±0.03
2MASS J05382750-0235041	15.99±0.04	14.45±0.04	12.83±0.03	12.11±0.02	11.86±0.03
2MASS J05382774-0243009	15.04±0.03	13.67±0.03	12.19±0.03	11.45±0.02	11.29±0.02
2MASS J05382848-0246170	16.33±0.03	15.06±0.03	13.82±0.03	13.20±0.03	12.94±0.03
2MASS J05382896-0248473	19.05±0.05	17.06±0.05	14.82±0.04	14.28±0.04	13.88±0.06
2MASS J05383141-0236338	15.31±0.04	13.89±0.03	12.17±0.03	11.47±0.02	10.99±0.03
2MASS J05383157-0235148	14.98±0.03	13.83±0.03	11.52±0.03	10.71±0.02	10.35±0.02
2MASS J05383160-0251268	14.54±0.03	13.53±0.02	12.11±0.03	11.18±0.02	10.98±0.02
2MASS J05383284-0235392	13.60±0.04	12.71±0.02	11.54±0.03	10.90±0.02	10.73±0.03
2MASS J05383302-0239279	17.84±0.04	16.23±0.04	14.59±0.03	14.02±0.03	13.70±0.04
2MASS J05383335-0236176	14.77±0.03	13.45±0.03	12.05±0.03	11.29±0.02	11.11±0.03
2MASS J05383388-0245078	18.01±0.04	16.15±0.04	14.25±0.03	13.68±0.03	13.35±0.04
2MASS J05383405-0236375	15.37±0.04	13.77±0.04	11.98±0.03	11.33±0.02	11.08±0.03
2MASS J05383460-0241087	16.38±0.04	14.86±0.04	13.10±0.03	12.45±0.02	12.12±0.03
2MASS J05383669-0244136	16.13±0.04	14.35±0.04	12.54±0.03	11.89±0.03	11.62±0.03
2MASS J05383745-0250236	16.43±0.04	14.63±0.04	12.81±0.03	12.18±0.02	11.92±0.02
2MASS J05383858-0241558	18.33±0.05	16.48±0.04	14.56±0.03	13.96±0.03	13.65±0.04
2MASS J05383902-0245321	15.77±0.04	14.39±0.03	12.91±0.03	12.20±0.02	11.89±0.03
2MASS J05383922-0253084	14.72±0.03	13.83±0.02	12.70±0.03	12.04±0.03	11.87±0.02
2MASS J05385317-0243528	14.93±0.03	13.78±0.02	12.23±0.03	11.51±0.03	11.30±0.03
2MASS J05385382-0244588	20.09±0.06	17.93±0.04	15.45±0.04	14.94±0.05	14.59±0.09
2MASS J05385492-0228583	17.18±0.04	15.51±0.03	13.80±0.03	13.20±0.03	12.87±0.03
2MASS J05385492-0240337	20.90±0.09	18.75±0.04	15.92±0.07	15.17±0.06	14.71±0.11
2MASS J05385542-0241208	19.94±0.06	18.09±0.04	15.62±0.10	14.84±0.05	13.97±0.06
2MASS J05385623-0231153	15.36±0.02	14.58±0.02	13.42±0.03	12.77±0.02	12.52±0.03
2MASS J05385922-0233514	16.31±0.03	14.95±0.03	12.89±0.03	11.98±0.02	11.40±0.03
2MASS J05390052-0239390	12.79±0.02	12.46±0.01	11.66±0.03	11.22±0.02	11.11±0.02
2MASS J05390115-0236388	16.73±0.03	15.17±0.03	13.52±0.03	12.89±0.03	12.61±0.03
2MASS J05390193-0235029	17.51±0.03	16.13±0.03	14.45±0.04	13.38±0.03	12.61±0.03
2MASS J05390276-0229558	15.80±0.03	14.27±0.03	12.61±0.03	12.00±0.02	11.69±0.02
S Ori J053903.2-023020	22.49±0.35	20.68±0.06	-	-	-
2MASS J05390357-0246269	15.86±0.03	14.34±0.03	12.84±0.03	12.12±0.02	11.86±0.03
2MASS J05390449-0238353	18.95±0.04	16.99±0.04	14.77±0.04	14.19±0.03	13.80±0.04
2MASS J05390458-0241493	15.93±0.02	14.87±0.02	13.96±0.04	12.91±0.04	12.22±0.04
2MASS J05390524-0233005	16.56±0.03	15.01±0.03	13.39±0.03	12.72±0.02	12.46±0.03
2MASS J05390540-0232303	13.15±0.02	12.55±0.01	11.55±0.03	10.86±0.02	10.67±0.02
2MASS J05390759-0228234	15.83±0.03	14.42±0.03	12.88±0.03	12.14±0.02	11.96±0.03

Table 4.2—Continued

Object	R	I	J	H	K
2MASS J05390760-0232391	13.54±0.09	12.82±0.03	11.30±0.03	10.57±0.02	10.26±0.02
2MASS J05390808-0228447	17.59±0.04	15.89±0.03	14.14±0.03	13.52±0.03	13.25±0.04
2MASS J05390821-0232284	17.59±0.04	15.80±0.04	13.80±0.03	13.25±0.03	12.92±0.03
2MASS J05390878-0231115	16.62±0.03	15.04±0.03	13.04±0.03	12.16±0.02	11.70±0.02
2MASS J05390894-0239579	19.53±0.05	17.39±0.04	14.65±0.03	14.13±0.04	13.74±0.05
2MASS J05391001-0228116	17.68±0.03	16.13±0.03	14.60±0.03	14.00±0.04	13.78±0.05
2MASS J05391003-0242425	15.18±0.02	14.30±0.02	12.97±0.03	12.21±0.03	11.97±0.02
S Ori J053910.8-023715	22.60±0.37	20.82±0.06	-	-	-
2MASS J05391139-0233327	18.31±0.04	16.48±0.04	14.45±0.03	13.93±0.03	13.57±0.04
2MASS J05391151-0231065	14.04±0.02	13.11±0.02	11.99±0.03	11.19±0.02	10.73±0.02
2MASS J05391163-0236028	13.71±0.09	12.93±0.03	11.62±0.03	10.97±0.03	10.75±0.02
2MASS J05391232-0230064	16.50±0.04	14.66±0.04	12.61±0.03	12.05±0.03	11.73±0.02
2MASS J05391308-0237509	19.44±0.05	17.52±0.04	15.24±0.04	14.75±0.04	14.31±0.07
2MASS J05391346-0237391	16.89±0.04	15.22±0.03	13.41±0.03	12.77±0.02	12.50±0.03
2MASS J05391447-0228333	16.37±0.03	14.89±0.03	13.34±0.03	12.65±0.03	12.34±0.03
2MASS J05391510-0240475	18.85±0.04	16.88±0.04	14.67±0.03	14.04±0.03	13.66±0.04
2MASS J05391576-0238262	19.09±0.08	17.21±0.01	14.95±0.06	14.38±0.06	14.09±0.06
2MASS J05391582-0236507	16.45±0.03	14.93±0.03	13.25±0.03	12.54±0.03	12.22±0.03
2MASS J05391699-0241171	17.56±0.03	15.99±0.03	14.29±0.03	13.63±0.02	13.37±0.04
2MASS J05391883-0230531	13.23±0.02	12.55±0.02	11.40±0.03	10.64±0.03	10.34±0.02
2MASS J05392023-0238258	17.44±0.04	15.61±0.04	13.61±0.03	13.04±0.03	12.78±0.02
2MASS J05392097-0230334	17.52±0.04	15.59±0.04	13.29±0.03	12.75±0.03	12.44±0.03
2MASS J05392174-0244038	13.25±0.09	12.58±0.03	11.10±0.03	10.40±0.02	10.22±0.02
2MASS J05392224-0245524	19.03±0.04	17.22±0.04	15.32±0.04	14.84±0.05	14.41±0.08
2MASS J05392286-0233330	15.36±0.03	14.16±0.03	12.83±0.03	12.13±0.02	11.87±0.03
2MASS J05392319-0246557	19.31±0.05	17.35±0.04	15.33±0.04	14.78±0.04	14.34±0.07
2MASS J05392341-0240575	21.92±0.20	19.47±0.05	16.73±0.13	15.92±0.12	15.55±0.21
2MASS J05392435-0234013	15.52±0.03	14.27±0.03	12.98±0.03	12.27±0.03	12.06±0.02
2MASS J05392519-0238220	13.84±0.07	13.08±0.02	11.31±0.03	10.45±0.02	10.00±0.02
2MASS J05392524-0227479	18.42±0.03	16.94±0.03	15.55±0.04	14.79±0.05	14.56±0.08
2MASS J05392560-0238436	18.23±0.03	17.29±0.02	15.25±0.04	14.28±0.03	13.65±0.04
2MASS J05392561-0234042	16.71±0.04	15.00±0.04	13.20±0.03	12.54±0.02	12.25±0.05
2MASS J05392633-0228376	16.94±0.04	15.28±0.03	13.50±0.03	12.84±0.02	12.56±0.02
2MASS J05392677-0242583	17.03±0.03	15.46±0.03	13.18±0.03	12.40±0.03	12.12±0.02
2MASS J05392685-0236561	20.00±0.06	17.97±0.04	15.46±0.04	14.84±0.05	14.49±0.07
2MASS J05393056-0238270	16.66±0.03	15.29±0.03	13.81±0.03	13.18±0.03	12.95±0.03
2MASS J05393234-0227571	13.25±0.04	12.50±0.02	11.18±0.02	10.50±0.02	10.33±0.02
2MASS J05393432-0238468	19.20±0.05	17.19±0.04	14.76±0.03	14.19±0.04	13.79±0.05

115

Table 4.2—Continued

Object	R	I	J	H	K
2MASS J05393673-0231588	18.73±0.03	17.26±0.03	15.71±0.05	15.04±0.06	14.76±0.09
2MASS J05393759-0244304	18.63±0.05	16.63±0.04	14.38±0.03	13.82±0.03	13.38±0.03
2MASS J05393931-0232252	17.37±0.04	15.52±0.04	13.44±0.03	12.90±0.02	12.53±0.03
2MASS J05393982-0231217	13.79±0.07	13.06±0.02	11.84±0.03	10.90±0.02	10.22±0.02
2MASS J05393982-0233159	15.90±0.03	14.84±0.02	12.22±0.03	10.96±0.02	10.07±0.02
2MASS J05393998-0243097	12.52±0.02	12.29±0.01	10.65±0.03	9.92±0.02	9.53±0.02
2MASS J05394057-0239123	18.87±0.04	17.27±0.03	15.40±0.05	14.67±0.05	14.41±0.08
2MASS J05394318-0232433	16.31±0.03	14.74±0.03	13.03±0.03	12.30±0.02	11.91±0.02
2MASS J05394411-0231092	13.18±0.11	12.61±0.03	11.21±0.03	10.51±0.02	10.33±0.02
2MASS J05394433-0233027	18.33±0.04	16.47±0.04	14.29±0.03	13.72±0.03	13.37±0.04
2MASS J05394725-0241359	17.27±0.02	16.37±0.02	15.09±0.04	14.24±0.03	14.00±0.06
2MASS J05394770-0236230	16.67±0.03	15.12±0.03	13.47±0.03	12.77±0.02	12.53±0.03
2MASS J05394784-0232248	13.16±0.12	12.62±0.03	10.97±0.03	10.29±0.02	10.08±0.02
2MASS J05394799-0240320	15.21±0.03	13.85±0.03	12.43±0.03	11.65±0.02	11.43±0.02
2MASS J05394806-0245571	15.45±0.03	14.15±0.03	12.92±0.03	12.28±0.02	12.03±0.02
2MASS J05394826-0229144	20.81±0.10	18.79±0.04	16.42±0.09	15.59±0.10	15.19±0.14
2MASS J05394891-0229110	16.04±0.04	14.61±0.03	13.28±0.03	12.59±0.03	12.30±0.03
2MASS J05395038-0243307	14.03±0.06	12.99±0.03	11.77±0.03	10.98±0.02	10.77±0.02
2MASS J05395056-0234137	17.18±0.04	15.48±0.03	13.68±0.03	13.00±0.03	12.73±0.03
2MASS J05395236-0236147	15.70±0.03	14.34±0.03	12.89±0.03	12.19±0.02	11.94±0.03
2MASS J05395248-0232023	13.32±0.02	12.65±0.01	11.51±0.03	10.88±0.02	10.66±0.03
2MASS J05395313-0243083	13.14±0.05	12.24±0.02	11.13±0.03	10.47±0.02	10.27±0.03
2MASS J05395313-0230294	20.33±0.07	18.41±0.04	16.20±0.08	15.82±0.12	15.56±0.23
2MASS J05395362-0233426	15.59±0.03	14.39±0.03	12.82±0.03	12.06±0.03	11.59±0.03
2MASS J05395433-0237189	19.13±0.05	17.14±0.04	14.75±0.03	14.21±0.04	13.80±0.05
2MASS J05395645-0238034	17.01±0.04	15.28±0.04	13.35±0.03	12.79±0.02	12.43±0.03
2MASS J05395753-0232120	16.82±0.04	15.10±0.04	13.31±0.03	12.69±0.02	12.36±0.02
2MASS J05400338-0229014	13.94±0.05	12.94±0.02	11.72±0.03	11.03±0.02	10.81±0.02
2MASS J05400453-0236421	19.95±0.05	17.92±0.04	15.30±0.05	14.81±0.05	14.27±0.07
2MASS J05400525-0230522	17.70±0.04	15.92±0.04	13.95±0.03	13.37±0.03	13.07±0.03
2MASS J05400708-0232446	16.84±0.04	15.17±0.03	13.42±0.03	12.81±0.02	12.54±0.03
2MASS J05400867-0232432	15.66±0.04	13.78±0.04	11.77±0.03	11.15±0.02	10.85±0.02
2MASS J05400889-0233336	14.49±0.28	13.39±0.11	11.50±0.03	10.55±0.02	9.91±0.02

Note. — We list R- and I-band photometry derived from our data and calibrated to the Cousins band, along with J, H, and K magnitudes taken from the 2MASS survey. Several brown dwarfs were too faint to be detected in 2MASS and hence we do not list values for these longer wavelength bands.

4.1.3 Spitzer data acquisition

For our infrared observations with *Spitzer*, we selected a field of view to both maximize the number of BDs observed and also provide some overlap with the ground-based sample (see §2.4.2). The final list of targets–shown in red in Fig. 4.6–included five confirmed and two candidate BDs in σ Orionis, with three in the 3.6 μm field and four in the 4.5μm field. In addition, we observed serendipitously seven other known σ Ori cluster members in the f ields which likely are too massive (e.g., >0.1 $M_\odot$) to exhibit pulsation but are nonetheless valuable targets for investigation of other types of young star variability. This brought the total sample to 14 objects–six in the 3.6 μm field, and eight in the 4.5 μm field. Fewer objects were placed in the 3.6 μm field because of scheduling constraints on the required orientation. Details on each target are provided in Table 4.3, including coordinates as well as 2MASS identifications. All except S Ori 31 and S Ori 53 are spectroscopically confirmed members of the σ Ori cluster; both have colors and spectral type consistent with low-mass σ Ori membership, while the former also has a proper motion consistent with membership (Lodieu et al. 2009). In addition, we consider object SWW 188 a new spectroscopically confirmed member since it exhibits weak Na I absorption indicative of low surface gravity in the low-resolution spectra that we obtained.

4.1.4 Spitzer data reduction

Prior predictions and limits on the amplitudes ($\lesssim$0.01 magnitudes) and timescales ($\sim$1–4 hours) of pulsation guided our observational setup. The ability to detect light curve periodicities at a particular amplitude (A) depends on both the photometric noise level (σ) as well as the total number of data points (N), as explained in §2.3.3. When identifying a periodic signal in a periodogram, the signal-to-noise ratio in frequency space is roughly equal to $A\sqrt{N}/(2\sigma)$ and must be larger than $\sim$4.0 for 99.9% certainty. We set a target of several millimagnitudes for the minimum detectable periodic amplitude in all objects apart from the faintest two BDs. In addition, data had to be taken frequently enough to probe periodicities on timescales close to an hour. Accordingly, observations were carried out over a 24 hour period from 22 to 23 October 2009 (Astronomical Observation Request key 35146240 and program identification 60169). Exposure times were 23.6 seconds each, resulting in a cadence of $\sim$30 seconds, and a total of 2730 data points.
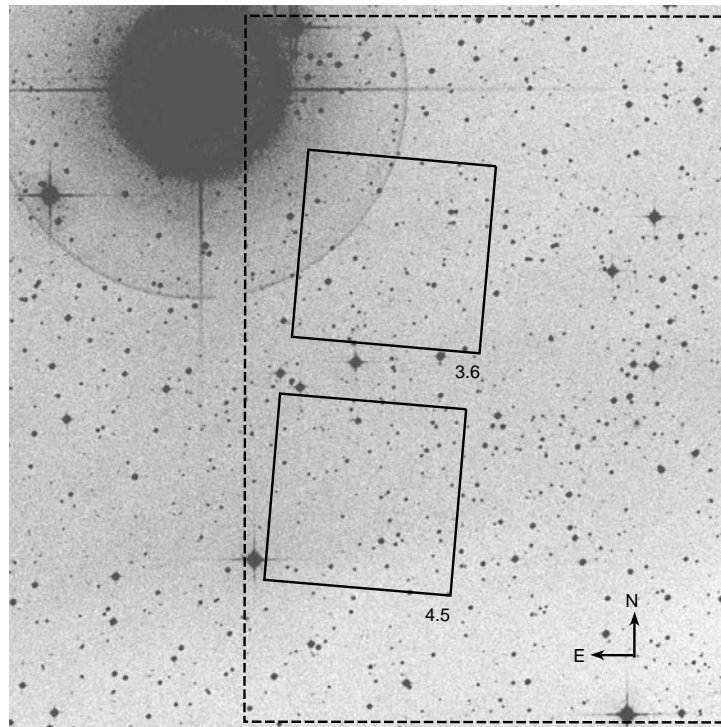
Figure 4.2 The *Spitzer* IRAC 3.6 and 4.5 μm fields in σ Ori are overlaid on a Palomar Observatory Sky Survey 2 (POSS2) red image obtained from the Digitized Sky Survey (DSS). A portion of our $20\times20'$ *I*-band ground-based campaign with the CTIO 1.0 meter telescope is also shown for reference (dashed region).

Table 4.3.   Confirmed and candidate σ Orionis cluster members observed with *Spitzer*

Object	I	3.6	4.5	SpT	Ref	Optical variability
4771-41	12.95±0.02	-	8.84±0.02	K5	1	Aperiodic: RMS=0.23 mags
SWW40	14.18±0.03	-	11.61±0.01	M3	1	Periodic: 4.47d, 0.013 mags
S Ori J053817.8-024050	15.00±0.04	11.68±0.01	-	M4	1	Periodic: 2.41d, 0.008 mags
SWW188	15.06±0.03	-	12.61±0.01	M2	1	-
S Ori J053823.6-024132	15.13±0.04	12.17±0.05	-	M4	1	Periodic: 1.71d, 0.017 mags
S Ori J053833.9-024508	16.15±0.04	-	12.52±0.03	M4	1	Aperiodic: RMS=0.06 mags
S Ori J053826.8-022846	16.17±0.04	12.71±0.03	-	M5	1	-
S Ori J053825.4-024241	16.96±0.04	12.96±0.03	-	M6	2	Aperiodic: RMS=0.16 mags
S Ori J053826.1-024041	17.05±0.04	13.65±0.01	-	M6	2	-
S Ori J053829.0-024847	17.06±0.05	-	12.91±0.03	M6	3	-
S Ori 27	17.22±0.05	13.13±0.01	-	M7	4	-
S Ori 31	17.46±0.04	-	13.67±0.02	M7	4	-
S Ori 45	20.03±0.09	-	15.05±0.05	M8.5	4	Periodic: 0.3d, 0.034 mags
S Ori 53	20.31±0.09	-	17.5±0.4	M9	5	-

Note. — I-band magnitudes are taken from Cody & Hillenbrand (2010). 3.6- and 4.5-μm-band photometry is the median value determined over our light curves, with conservative uncertainties including systematic errors due to poor knowledge of intrapixel sensitivity distributions as well as intrinsic variability. Values listed in the optical variability column are either the RMS spread of aperiodic light curves over a ~2 week period, or the period and amplitude of periodic light curves. References: (1) this work; (2) Caballero et al. (2006); (3) Caballero et al. (2007); (4) Barrado y Navascués et al. (2003); (5) Barrado y Navascués et al. (2001)

Observations at both wavelengths take place simultaneously, with one of the fields in each of the 3.6 μm and 4.5 μm cameras. Therefore, we collected data only in a single band for each of our targets. The orientation of the two fields is shown in Fig. 4.2, and the centers were R.A. = $05^h38^m23.3^s$, decl. = $-02°40'29''$ (3.6 μm) and R.A. = $05^h38^m26.4^s$, decl. = $-02°47'13''$ (4.5 μm). The position angle was -94.7° east of north for both fields. Since our aim was to produce photometric time series with as high a precision as possible, we elected not to dither. Keeping the positions of all sources fixed within a single pixel reduces the effect of flux variations introduced by pixel-to-pixel sensitivity differences not fully corrected by flatfielding, although intrapixel sensitivity variation (the "pixel-phase effect") remains an issue and is addressed in §3.3.1.3.

For data acquired from the *Spitzer*/IRAC camera, all basic calibrations are performed via pipeline, as explained in the handbook[2]. As of version 18.12.0, the IRAC pipeline provided images at several different stages of processing, from raw unreduced frames to final photometry-ready data. However, at the time of writing there were still a number of problems resulting from the transition to the Warm *Spitzer* mission. Standard bias and dark subtraction, flatfielding, linearity, and flux calibrations have been applied to create the basic calibrated data (BCD) files. Further corrections, including automated removal of cosmic rays and the column pull-down effect, have been performed to create a set of corrected BCDs (CBCDs). Since these procedures were fine-tuned to cryogenic mission data, they left numerous column pull-down artifacts as well as a residual bias pattern in our data. Therefore, we elected to carry out the final set of reductions manually, starting with the BCDs.

Because there are no laboratory-generated bias frames corresponding to warm mission conditions, we retained the bias subtraction applied by the pipeline and modeled the remaining uncorrected pattern. Fortunately the residuals largely consist of vertical bands in which brightness remained relatively constant throughout our observations. A procedure to median stack all images for each channel, mask out the objects, and reset each column to its mean value was performed by S. Carey (2010, private communication). Subtraction of the resulting vertical striped bias correction image from all BCDs effectively removed the residual patterns.

The column pull-down effect, in which counts are reduced throughout columns with

---

[2]http://irsa.ipac.caltech.edu/data/SPITZER/docs/irac/iracinstrumenthandbook/

bright (>35,000 DN) sources, was also not fully corrected for in the pipeline. Unlike in cryogenic mission data, flux values associated with pull-down now differ above and below the source, in addition to following an approximately exponential trend as a function of y position on the array. We were provided an updated pulldown correction code (D. Paladini 2010, private communication), which satisfactorily modeled and removed this effect.

With data at the 3.6 and 4.5 μm wavelengths, the pixel-phase effect (i.e., oscillations in the measured flux introduced by uncorrected intrapixel sensitivity variations) is more pronounced now than in the cryogenic mission. We developed a technique (§3.3.1.3) to remove the resulting fluctuations from light curves (see Fig. 4.3) and were successful in reducing the noise level to within ∼80% of the expected Poisson limit.

Even with careful placement of apertures and correction for intrapixel sensitivity variations, many of the light curves contained deviations beyond the expected white noise level that were not characteristic of the underlying stellar variability. Points with particularly large flux suggested cosmic ray hits within the stellar PSF. These occurrences appear random and uncorrelated, and thus are unlikely to represent real short-term astrophysical behavior. Since we did not dither, it was not possible to remove these without binning images or data points. We elected instead to filter erroneous flux values directly out of the light curves with a 3-σ clipping algorithm. The raw and corrected light curves are displayed in Fig. 4.3, along with the periodograms used to assess the pixel-phase effect and search for intrinsic periodicities.

4.1.5   Periodic variability detection

The main focus of our photometric campaign is the detection of variability on short timescales (i.e., 1–10 hours). It is in this regime that observations of surprisingly fast-rotating VLMSs and BDs have been reported and deuterium-burning pulsation has been proposed. Rotating magnetic spots on young low-mass stars typically manifest themselves at a level of a few percent in light curves, whereas amplitudes of the pulsation effect are thus far unconstrained by existing theory (Palla & Baraffe 2005). Therefore it is crucial to probe the data for potentially weak signals, with careful attention to the noise limit, which is generally frequency-dependent. We produced Frequencyourier transform periodograms for all σ Ori cluster members in the fields, including both the raw and pixel-phase-corrected IRAC light curves.
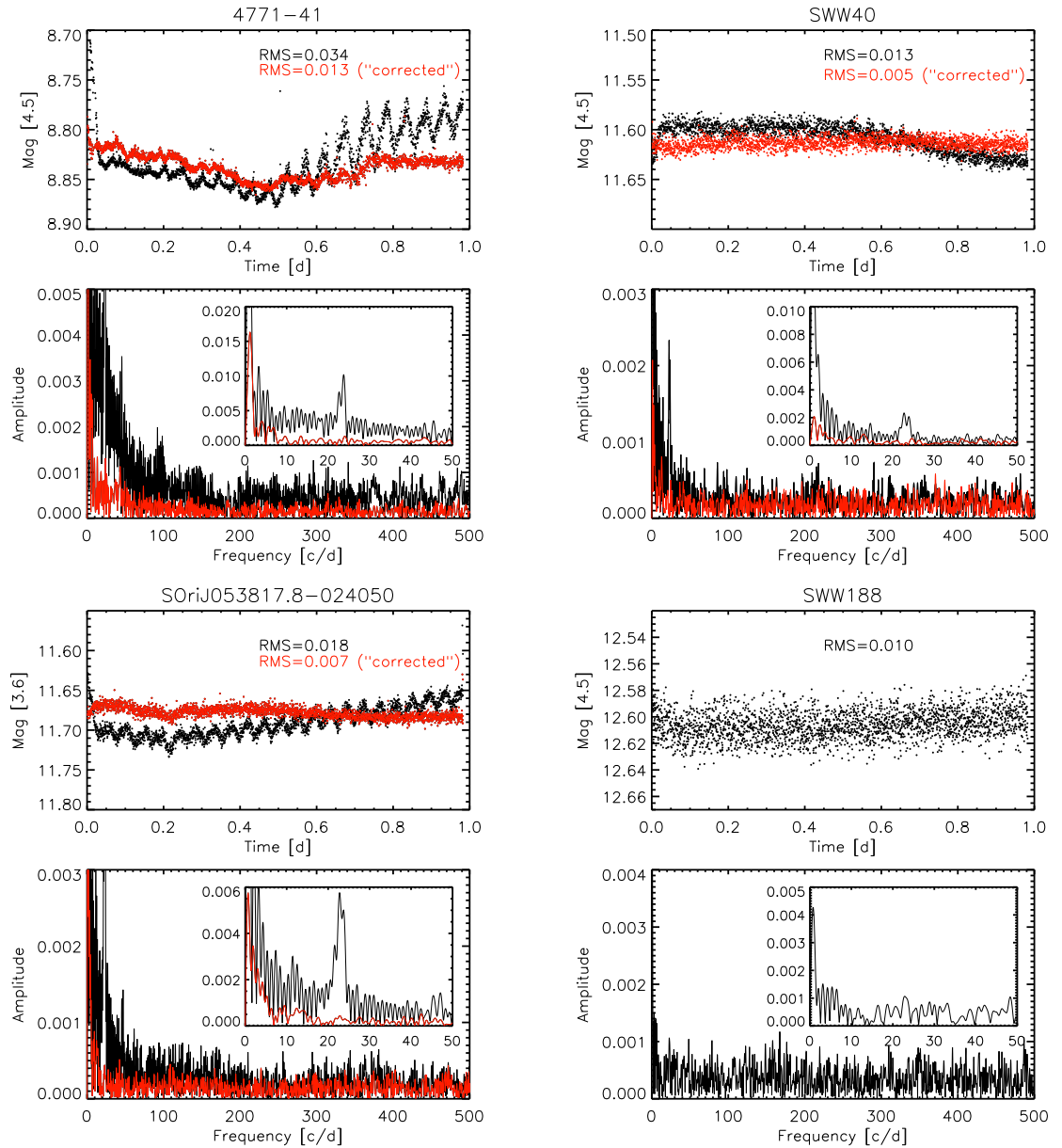
Figure 4.3 Light curves and periodograms for all Warm *Spitzer*/IRAC targets, in order of decreasing optical brightness. Object identifications are listed above each light curve, and the band (3.6 or 4.5 μm) is noted in the y-axis label. Black indicates the raw light curve and periodogram, whereas red shows them after correction for intrapixel sensitivity effects. Objects with no red points did not require correction. Periodogram frequencies are given in cycles per day. Insets show the same periodograms zoomed in to the low-frequency range where the signature of the pixel-phase oscillation is visible ($\sim$22–24 cd^{-1}).
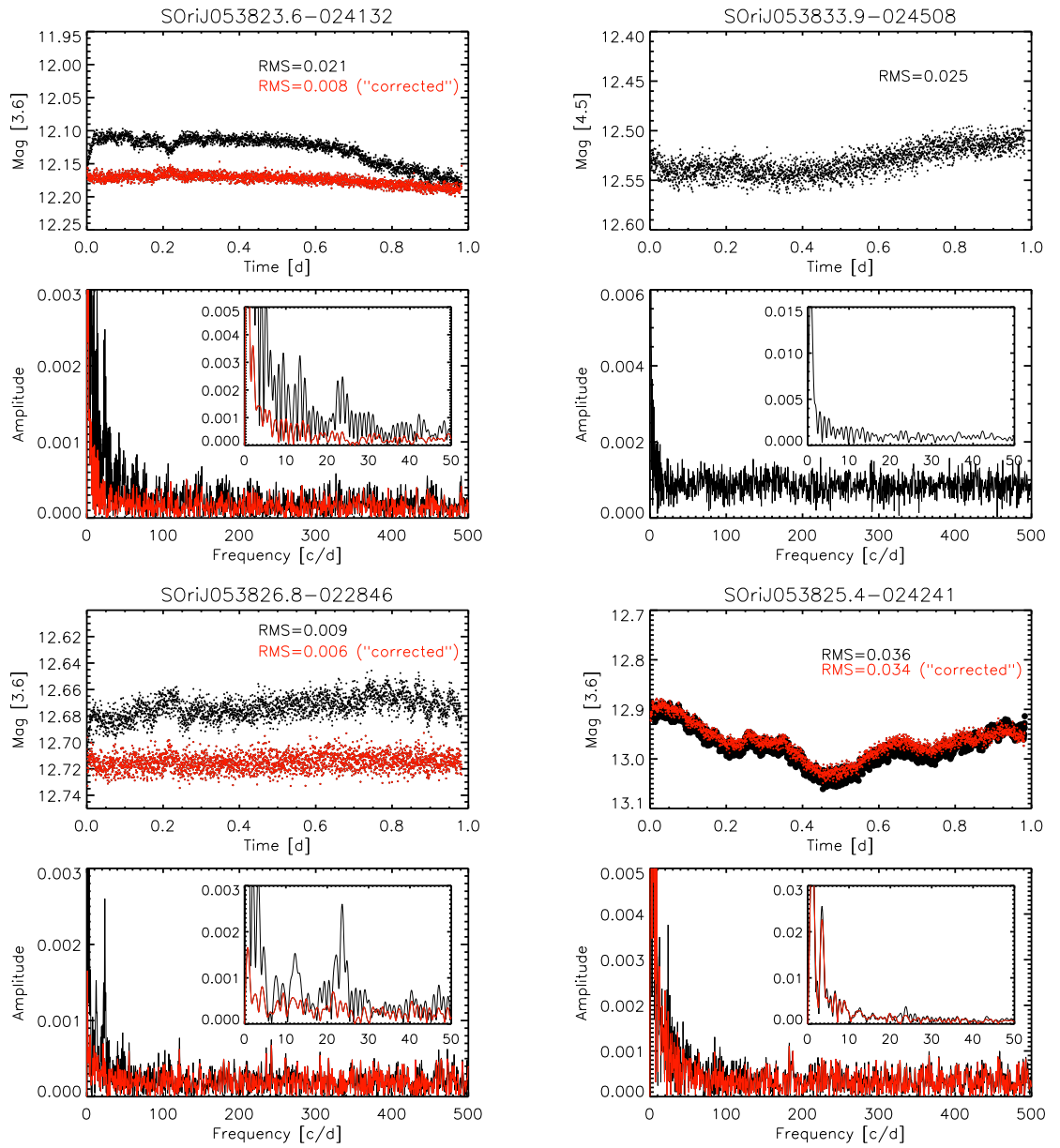
Figure 4.3 –Continued
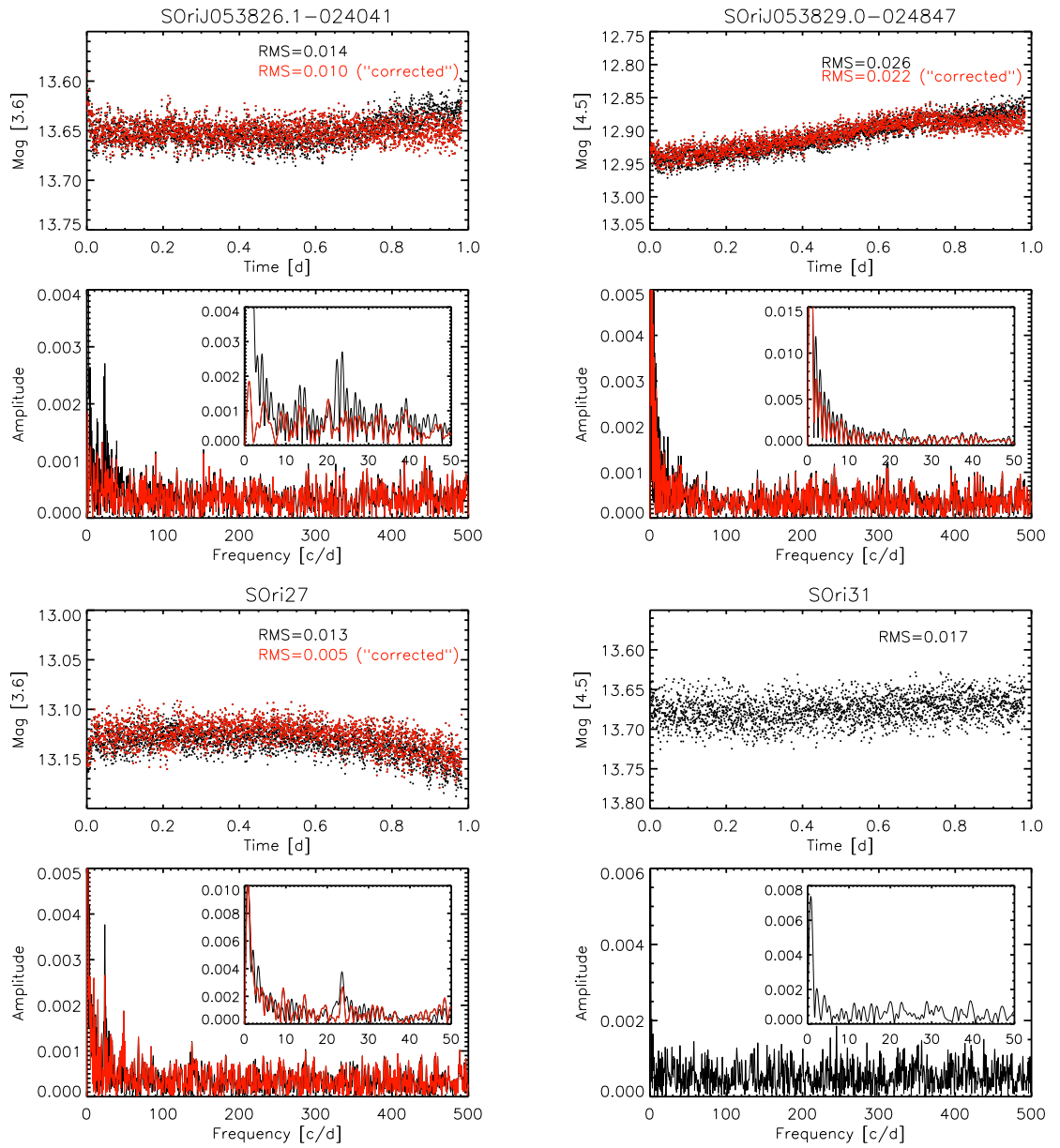
Figure 4.3 –Continued
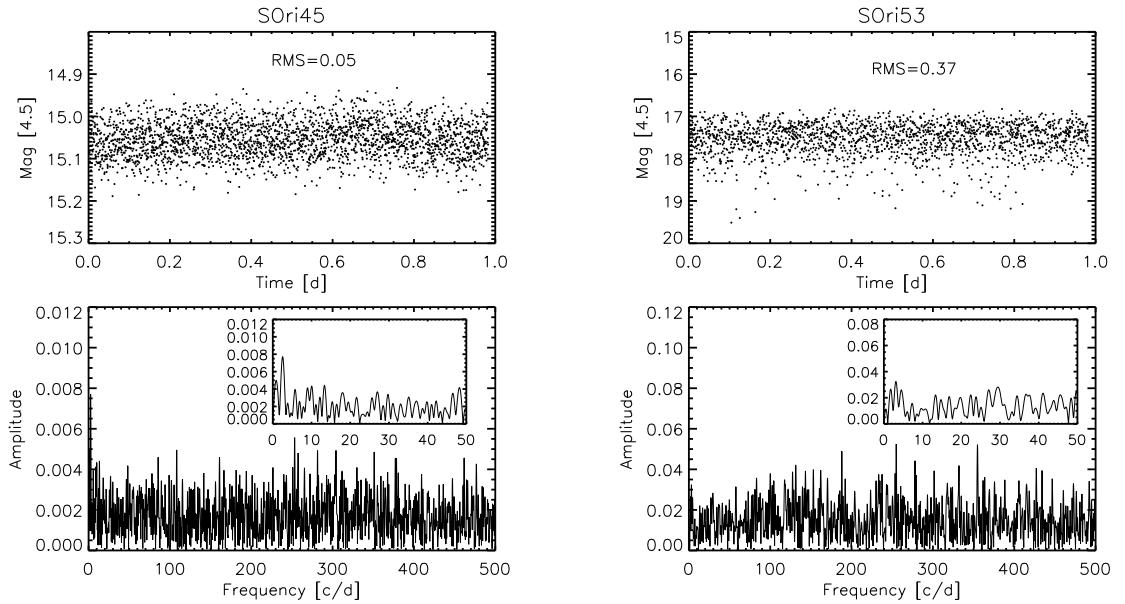
Figure 4.3 –Continued

Since our data are very evenly spaced, modulo daytime gaps (we were fortunate in that nighttime weather was pristine), the Nyquist limit stipulates that signals may be detected up to half the sampling frequency–corresponding to 15 minute timescales in the 2007 CTIO 1.0 m observations, 23-minute time scales in the 2008 CTIO 1.0 m observations, and one minutes for those from *Spitzer*/IRAC. Because of the long time baseline for each set of ground-based observations, we are also sensitive to periodicities up to the total durations of those runs (12 and 11 days for the respective CTIO runs). However, since most types of photometric errors produce red noise on night-to-night timescales, the minimum detectable variability level at low frequencies is generally a factor of a few higher than amplitudes observable at higher frequencies (shorter timescales; see Fig. 2.10).

In the case of the *Spitzer* data, the periodogram does not suffer from aliasing, so true signals are relatively easy to identify if they rise high enough above the noise baseline. In most cases, the periodograms display a relatively uniform mean from frequencies at a few cycles per day (cd^{-1}) out to the Nyquist limit at 1440 cd^{-1}. This white noise level depends on the magnitude of the source and ranged from 0.001 to 0.004 magnitudes in the periodogram. Examination of the periodograms revealed that the pixel-phase correction process substantially lowered the noise level, enabling better sensitivity to periodicities outside the 1–1.1 hour range of the pixel-phase oscillation. The two exceptions were SOri 27

and 4771-41. The former was centered near the edge of two pixels, making a fit to the spatial distributions difficult without resorting to a more complex non-Gaussian function. Object 4771-41 is exceedingly bright, and residual variability seen in the final light curve may be a figment of the correction process.

The majority of periodograms are relatively featureless at frequencies of 5 cd^{-1} and above, reflecting minimal variability in the input light curves. In the low-frequency region from one to several cd^{-1}, many of the periodograms steadily rise in a "$1/f$" fashion indicative of systematic or "red" noise trends on timescales of one or more days. We have used the 4-σ criterion, equivalent to 99.9% certainty, to vet possible signals. A selection of typical periodograms from the ground-based data is presented in Fig. 4.4.

4.1.6   Prospects for pulsation

Periodic variability is virtually ubiquitous in the ground-based dataset, as is expected for young cluster members with spotted surfaces. Period of order one day or longer can be attributed to rotational modulation of these dark features and hence associated with the rotation rate. In the range of $\sim$1-7 hours, we not only do not detect signs of pulsation, but we also see no evidence of spot-modulated variability. Within the uncertainties of cluster membership verification, there are approximately 40 young objects in our sample with masses less than $\sim$0.1 $M_\odot$. We thus conclude that our ground-based I-band data do not bear out PB05's predictions for pulsational instabilities. If any of our BDs or VLMSs is pulsating, then they must be doing so at amplitudes below $\sim$0.01–0.02 magnitudes. Our observations are inconsistent with reports of short-period variability in young σ Ori brown dwarfs observed by Bailer-Jones & Mundt (2001) and Zapatero Osorio et al. (2003); details on the failure to redetect periodicities in these objects are provided in Appendix A. The H-R diagram of *observed* σ Ori objects with available spectral types, including those derived in Chapter 6, is presented in Fig. 4.5.

We reach a similar conclusion based on the *Spitzer*/IRAC mid-infrared dataset. The lack of periodic signals in the 1–4 hour range suggests that none of the σ Ori cluster members in our sample exhibits deuterium-powered pulsation at a level above several millimagnitudes. However, the strength of this conclusion depends on the likelihood that one or more targets fall on the PB05's predicted pulsation instability strip. We plot their positions in Fig. 4.6. If we assume a distance of 350 pc for the σ Ori cluster, then all seven BDs in the IRAC
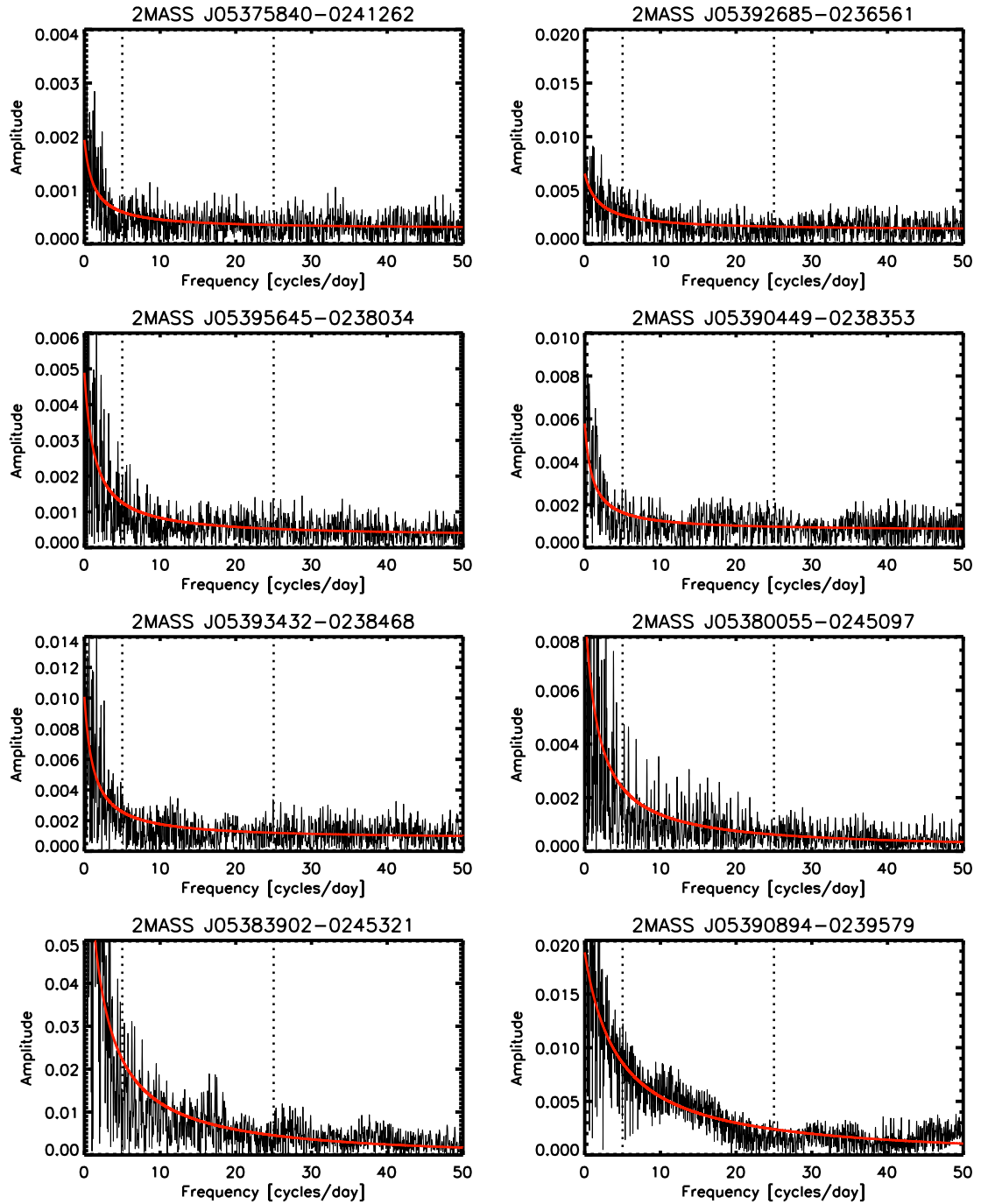
Figure 4.4 Periodograms of selected σ Ori targets observed with the CTIO 1.0 m telescope. Vertical dashed lines indicated the region of frequency space ($\sim$5–25 cd^{-1}) where pulsation is predicted. Red curves mark $1/f$ profile fits to the noise level.
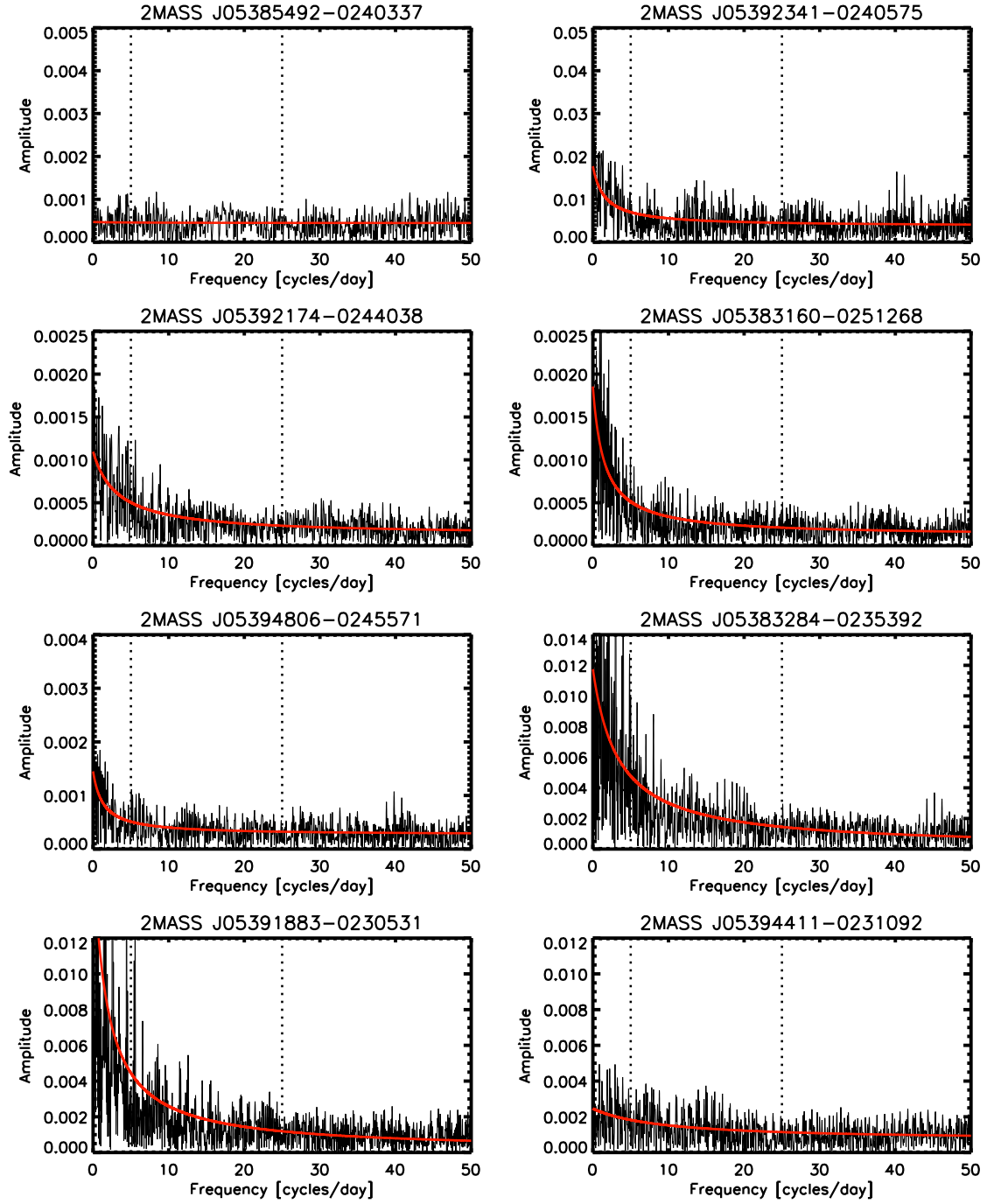
Figure 4.4 –Continued
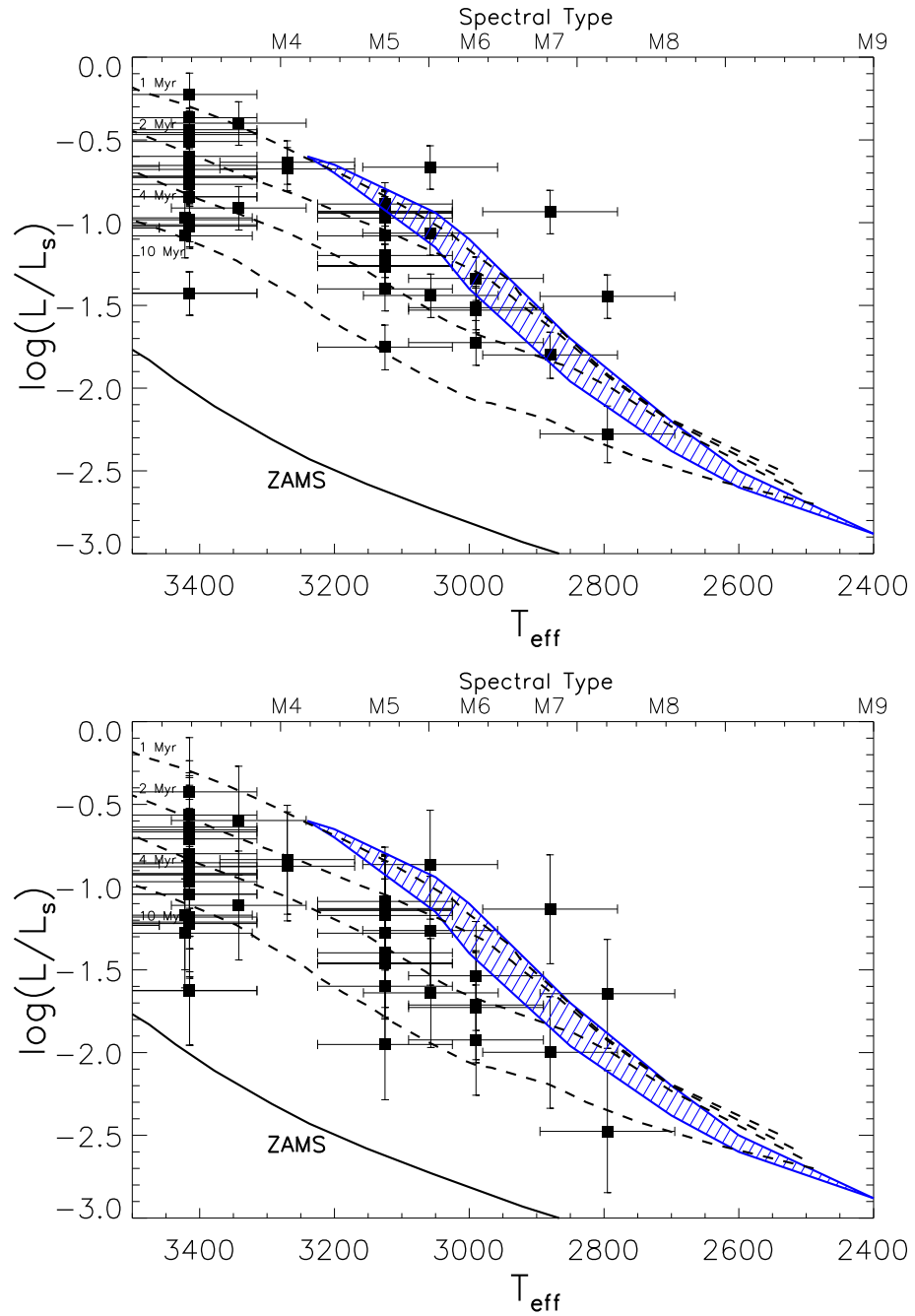
Figure 4.5 The instability strip for pulsating brown dwarfs and very low mass stars included in our observational sample is shown in blue, along with isochrones from Baraffe et al. (2003) and the sample of spectroscopically confirmed low-mass members of the σ Ori cluster observed with the CTIO 1.0 m telescope. Effective temperature (T_{eff}) is in Kelvins, and luminosity is in solar units (L_{S}). In the top panel we assumed a distance of 440 pc, while in the bottom we changed this to the alternate value of 350 pc.

sample (S Ori J053825.4-024241, S Ori J053826.1-024041, S Ori 31, S Ori J053829.0-024847, S Ori 53, S Ori 27) may be on the instability strip, to within the uncertainties. If we instead adopt a distance of 440 pc, then the VLMS S Ori J053826.8-022846 becomes an additional candidate, whereas the position of S Ori 45 falls slightly off the strip. Thus one would naively assume that a handful of our targets have temperatures and luminosities consistent with those required for pulsational instability. The same expectation applies to the larger ground-based dataset. Nevertheless, the significant size of the measurement uncertainties compared with the width of the strip must be taken into account. We carry out an analysis to this effect in §7.1.
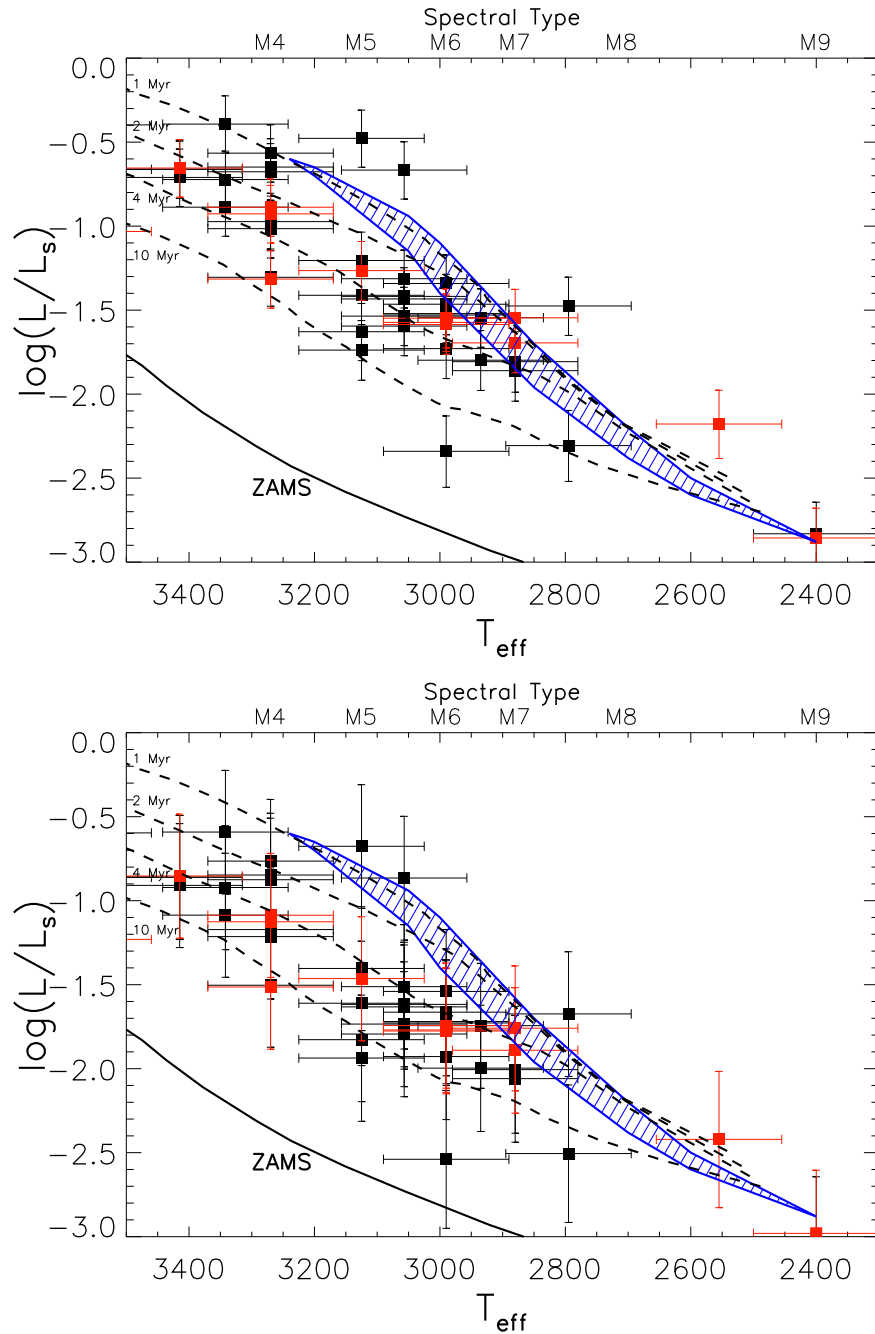
Figure 4.6 The instability strip for pulsating brown dwarfs and very low mass stars is shown in blue, along with isochrones from Baraffe et al. (2003) and a sample of spectroscopically confirmed low-mass members of the σ Ori cluster drawn from Barrado y Navascués et al. (2003). Effective temperature (T_{eff}) is in Kelvins, and luminosity is in solar units (L_{S}). In the top panel we assumed a distance of 440 pc, while in the bottom we changed this to the alternate value of 350 pc. Targets observed with Spitzer IRAC appear in red. A number of these objects are on or near the predicted instability strip, suggesting that they might exhibit pulsation.
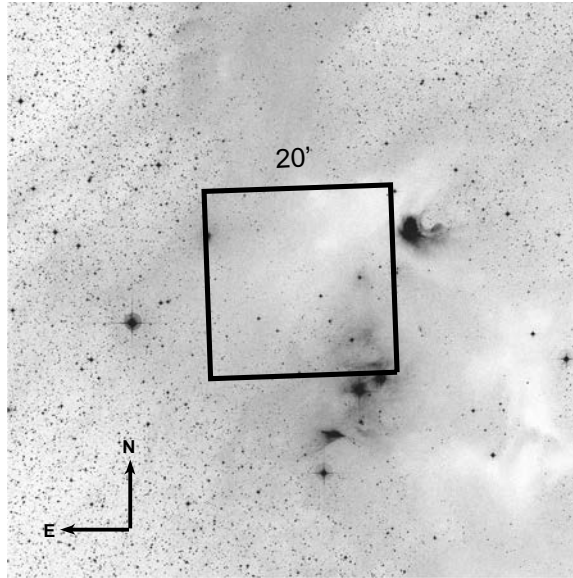
Figure 4.7 The Cha I field observed with the CTIO 1.0 m telescope is shown superimposed on a Digital Sky Survey image. Extinction in this region is highly variable, and we have avoided the most nebulous dark cloud region toward the west.

4.2 Chamaeleon I cluster

4.2.1 Target objects

The search for D-burning pulsation in the Chamaeleon I cluster involved observation of a single field with the CTIO 1.0 m telescope during our May 2008 observing run. This FOV was selected to maximize the number of BDs monitored and also avoid some of the dense nebulosity in this region; it is displayed in Fig. 4.7.

Since the initial target compilation was based on Luhman's (2007) work, we added several additional references to the list of sources for Cha I members. Luhman & Muench (2008) and Luhman et al. (2008a) presented a total 15 new Cha I members based on *Spitzer* IRAC data showing infrared excesses indicative of disks. Muzić et al. (2011) also announced two new candidate brown dwarfs in the cluster, for which follow-up spectroscopy awaits. As it turns out, only one of these newly identified candidates (2MASS J11091297-7729115; Luhman & Muench 2008) is in our observed field and bright enough for optical photometry. Including the census of Luhman (2007), we observed a total of 32 Cha I members, of which 6 have spectral types consistent with substellar status (spectral type M6 and later) and

22 more are likely very low mass stars with (M4 or later). While there are ten additional members in our field, two with spectral type M9 were too faint, three were closely blended with companions, and five were too saturated for precise photometry.

We have compiled the existing photometric and spectroscopic data on all 32 cluster members, including optical through near-infrared photometry and spectral types in Table 4.4. Correlation of these properties with variability features is discussed in Chapter 5; here we focus on the search for pulsation in Cha I BDs and VLMSs.

4.2.2   Preliminary data reduction

Since data for Cha I was acquired with the instrument used for the ground-based σ Orionis dataset– the CTIO 1.0m Y4KCam– we followed the same data calibration procedures, as detailed in §4.1.2. The main difference for this observing run was that sky conditions were not photometric, and just over two nights were lost to clouds. In addition, telescope building maintenance caused a new accumulation of dust specks on the detector each night, which had to be cleaned off on several occasions. As a result of these conditions, sky flatfield calibrations could not be consistently performed. We acquired dome flatfields at the beginning and end of each night to calibrate out dust "donuts", but these are known to misrepresent the true pixel sensitivity distribution by up to 10% (see §3.3.1.1). Therefore, we carried out flatfielding with sky flats on nights where at least seven were available, and when clouds precluded the acquisition of sky flats, we instead relied on the dome flats but performed an illumination correction using the high signal-to-noise composite provided by P. Massey[3]. Residual dust donuts remained on some images, as debris occasionally fell onto the CCD window during the middle of the night. Since these defects could not be removed, we were careful to note which positions were affected and flag stars whose photometry might be compromised.

We were also somewhat concerned that there may be scaling offsets between images calibrated by sky and dome flats, but tests for nights on which both were available suggested that this was at most a few tenths of a percent per pixel. Given this nearly negligible difference, we used sky flats on nights 1, 7–9, and 11. Night 4 was ended early by clouds and nights 5, 6, and 14 were completely lost to bad weather, resulting in a run of 11 total nights between 13 May 2008 and 26 May 2008. All exposures were acquired over 600 seconds

---

[3]http://www.lowell.edu/users/massey/obins/y4kcamred.html

133

Table 4.4. Cha I objects observed

Object	Other ID	SpT	i	J	H	K_s
2MASS J11105076-7718031	ESO Halpha 568	M4.25	14.38	12.044±0.023	11.101±0.023	10.748±0.024
2MASS J11105359-7725004	ISO 256	M4.5	17.51	14.271±0.030	12.507±0.027	11.339±0.021
2MASS J11065906-7718535	T23	M4.25	12.97	11.204±0.026	10.423±0.021	10.003±0.024
2MASS J11070925-7718471	ISO 91	M3	-	14.902±0.042	12.581±0.021	11.476±0.023
2MASS J11071668-7735532	Cha Halpha 1	M7.75	16.38	13.342±0.024	12.668±0.026	12.174±0.024
2MASS J11071860-7732516	Cha Halpha 9	M5.5	-	13.733±0.026	12.492±0.023	11.803±0.024
2MASS J11072040-7729403	ISO 99	M4.5	13.00	11.134±0.024	10.547±0.023	10.259±0.021
2MASS J11073519-7734493	CHXR 76	M4.25	14.39	12.127±0.023	11.279±0.023	10.954±0.021
2MASS J11073686-7733335	CHXR 26	M3.5	15.18	11.593±0.030	10.045±0.035	9.348±0.027
2MASS J11073775-7735308	Cha Halpha 7	M7.75	17.03	13.613±0.030	12.900±0.026	12.421±0.030
2MASS J11074245-7733593	Cha Halpha 2	M5.25	15.26	12.210±0.024	11.243±0.026	10.675±0.021
2MASS J11075225-7736569	Cha Halpha 3	M5.5	15.07	12.292±0.024	11.520±0.023	11.097±0.019
2MASS J11081850-7730408	ISO 138	M6.5	16.77	14.057±0.030	13.466±0.035	13.040±0.032
Cha J11081938-7731522	-	M4.75	-	-	-	-
2MASS J11082238-7730277	ISO 143	M5	15.51	12.570±0.024	11.651±0.027	11.095±0.023
2MASS J11083952-7734166	Cha Halpha 6	M5.75	15.06	12.263±0.027	11.479±0.024	11.038±0.027
2MASS J11085421-7732115	CHXR 78C	M5.25	15.01	12.310±0.026	11.555±0.023	11.224±0.024
2MASS J11085596-7727132	ISO 167	M5.25	17.08	13.514±0.031	12.293±0.026	11.619±0.025
2MASS J11093543-7731390	-	M8.25	-	15.936±0.092	15.022±0.087	14.412±0.101
2MASS J11094260-7725578	C7-1	M5	15.91	12.329±0.027	11.175±0.026	10.552±0.028
2MASS J11094742-7726290	B43	M3.25	16.62	12.767±0.027	11.228±0.023	10.236±0.022
2MASS J11094918-7731197	KG 102	M5.5	15.64	13.057±0.036	12.229±0.039	11.802±0.034
2MASS J11095336-7728365	ISO 220	M5.75	-	14.300±0.039	13.020±0.026	12.233±0.025
2MASS J11100192-7725451	LM04_419	M5.25	17.46	13.833±0.032	12.605±0.026	12.021±0.03
2MASS J11100785-7727480	ISO 235	M5.5	17.79	13.545±0.030	12.097±0.026	11.342±0.023
2MASS J11101153-7733521	-	M4.5	14.24	12.183±0.031	11.192±0.023	10.783±0.019
2MASS J11103481-7722053	LM04_405	M4	-	12.038±0.023	10.718±0.024	10.034±0.019
2MASS J11103644-7722131	ISO 250	M4.75	16.52	12.724±0.027	11.369±0.026	10.667±0.021
2MASS J11103801-7732399	CHXR 47	K3	11.90	9.741±0.027	8.687±0.047	8.277±0.029
2MASS J11104141-7720480	ISO 252	M6	17.29	13.860±0.030	12.891±0.027	12.266±0.023
2MASS J11120288-7722483	-	M6	-	13.588±0.030	12.941±0.044	12.510±0.030
2MASS J11120351-7726009	ISO 282	M4.75	-	13.626±0.024	12.587±0.025	11.842±0.023

Note. — Spectral types and i-band magnitudes are from Luhman (2004a) and Luhman (2007); J, H, and K magnitudes are from 2MASS. Objects with the alternate identification LM04 are from the catalog of Martí et al. (2004). The disk column indicates whether mid-infrared *Spitzer* data exhibits an excess.

in the SDSS i band.

In addition to the care paid to flatfielding, we also devoted attention to removal of the fringing pattern, which was slightly different in i band than that found for the I band used during σ Orionis cluster observations with the same detector. We obtained 49 new fringe flatfield exposures over the course of the run, with which we assembled a master fringe frame. Further procedures adopted for fringe removal are discussed in §3.3.1.2, and we were once again successful in removing this effect down to a level that was indistinguishable from the sky background.

4.2.3 Aperture photometry

The observed field in Cha I is not overly crowded, but it does display significant background gradients due to extinction variations within the cluster. As with the σ Orionis data, we suspected that image subtraction photometry might purge the light curves of systematics and offer better precision for the fainter targets. Therefore we performed and compared several different variable-aperture photometry procedures: optimal apertures (as a function of magnitude), apertures twice the computed optimal size, and image subtraction with optimal apertures. We once again found that the double-sized apertures provided the lowest RMS light curve spreads over the entire observing run, for the brighter objects (i.e., $i \lesssim 17$). For substellar targets ($i \gtrsim 17$), variable-aperture image subtraction photometry offered the best performance. In producing the final light curves, we used the $i = 17$ boundary to determine which of these two photometry approaches to adopt for each object. On individual nights, on the other hand, the three methods were more comparable to each other.

In the interest of fully mining the dataset and potentially identifying new Cha I members, we performed photometry on all 1548 objects in the field that were bright enough for detection in individual images ($i \lesssim 22$). Differential magnitudes were derived with respect to the total flux of the four brightest but unsaturated, non-variable reference stars. Coincidentally, most of these were located in the bottom two CCD quadrants, where an electronic problem resulted in unusable data on the first night of the observing run; few suitable reference stars were found in the top section. Since the same references must be used on all nights, this prevented us from deriving light curves for *any* objects on the first night, except in the case of image subtraction photometry, which only compares objects to

themselves. As a result, most light curves had 278 data points for the entire run, out of a possible 304. For those stars in the top two Y4KCam quadrants, light curves with 304 points were produced from image subtraction.

The RMS spread of the final light curves ranged from several millimagnitudes for the brightest targets to just over 0.1 magnitude for the faintest brown dwarfs and background stars. Based on the the signal-to-noise estimate in Eq. 2.14, we then expect to probe periodic signals with minimum amplitudes between 0.0015 and 0.04 magnitudes.

4.2.4 Prospects for pulsation

The excellent precision of the light curves put us in a position to search for pulsation as well as longer timescale periodicities. Previous variability studies by Carpenter et al. (2002) and Joergens et al. (2003) found evidence for periodicities among a small sample of Cha I objects, but their time sampling was too sparse to definitively confirm these. With our higher cadence data, we have set out to probe light curves for periodic variability due to either pulsation or rotation-modulated spot features. The latter will be explored in more depth as part of our extended variability analysis in §5.3.

4.2.4.1 Periodic variability search

The Nyquist limit stipulates that signals may be detected up to half the sampling frequency– corresponding to 23 minute timescales. Because of the long total time baseline, we are also sensitive to periodicities up to the total observing run duration (13 days, since the last night was lost to bad weather). As with the σ Orionis dataset, the minimum detectable variability level at low frequencies is somewhat larger than amplitudes observable at higher frequencies (i.e., shorter timescales), the overall trend is well fit with a $1/f$ curve.

For each of the Cha I members in the sample, we carefully analyzed the periodograms for signs of periodicities on the few-hour timescales predicted for D-burning pulsation. Only four objects have estimated masses above ~ 0.4 $M_\odot$, and so most are candidates for the instability. Among the objects with clear periodicities on timescales of 1 day and above (see Table 5.3), we removed the best-fit trend (based on multi-sine fits with Period04) to produce a pre-whitened light curve. The search for few-hour periodicities was then carried out on this residual.

We display the collection of periodograms in Fig. 4.8. The majority of light curves con-

tain low-frequency variations, most of which are due to intrinsic erratic variability. Despite sensitivity to few-millimagnitude levels, we do not find any evidence for variability with periods less than 16 hours, apart from one field object that is presumably a pulsator. A few periodograms display low-level signals in the range where pulsation is expected, but none of these meet the 99% significance level criteria, and we find most to be aperiodic variables (§5.1.2). Furthermore, the light curves do not show clean trends when phased to these periods. We conclude that none of the objects in the Cha I sample are periodic on 1–5 hour timescales, at least above the amplitude levels probed by the data.

4.2.4.2   Comparison with theoretical expectations

Four Cha I objects in our sample fall squarely on the instability strip when we convert spectral types to temperatures using the scale of Luhman et al. (2003b). A further 24 have spectral types later than M4 and therefore may be burning deuterium and subject to pulsation. We plot the full sample of Cha I members in our field on the H-R diagram in Fig. 4.9. Given the computed temperature and luminosity values, along with their uncertainties, it is very unlikely that the adopted observational parameters are incorrect to the extent that no objects in the sample overlap the D-burning instability strip. We quantify this probability statistically in §7.1. It therefore appears that the theoretical expectation of pulsation at observable amplitudes in BDs and VLMSs is not borne out by this data.

4.3   IC 348 cluster

IC 348 is an appealing target in the search for pulsation, since it is relatively compact ($< 1^{\circ 2}$), and its membership is very well characterized (Luhman et al. 2003b; Muench et al. 2007). Several previous photometric studies have identified numerous periodic variables, which are presumably the result of rotating spotted surfaces (Cohen et al. 2004; Littlefair et al. 2005; Cieza & Baliber 2006, and references therein). The typical periods found fall near 2–3 days, but several objects have reported periods as short as 5 hours. Since their locations are well off of the cluster center, they may mistakenly be field stars. We were motivated to revisit IC 348 since not all of the cadences in the above-mentioned monitoring programs were sufficiently fast to detect pulsation in the ∼1–4 hour period range. In addition, IC 348 harbors many BDs and VLMSs whose properties overlap the theoretical
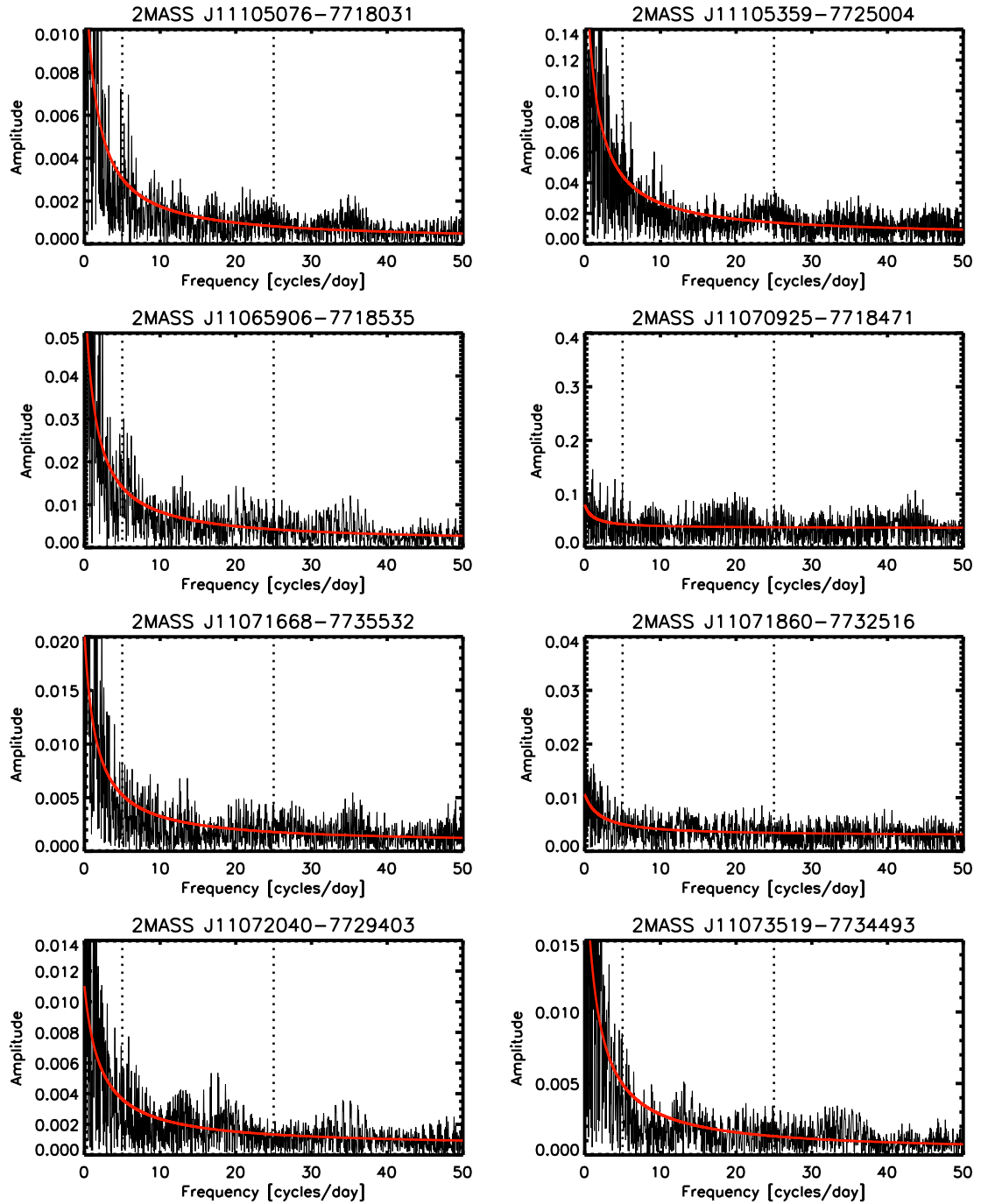
Figure 4.8 Periodograms of selected Cha I targets. Vertical dashed lines indicated the region of frequency space ($\sim$5–25 cd^{-1}) where pulsation is predicted. Red curves mark $1/f$ profile fits to the noise level.
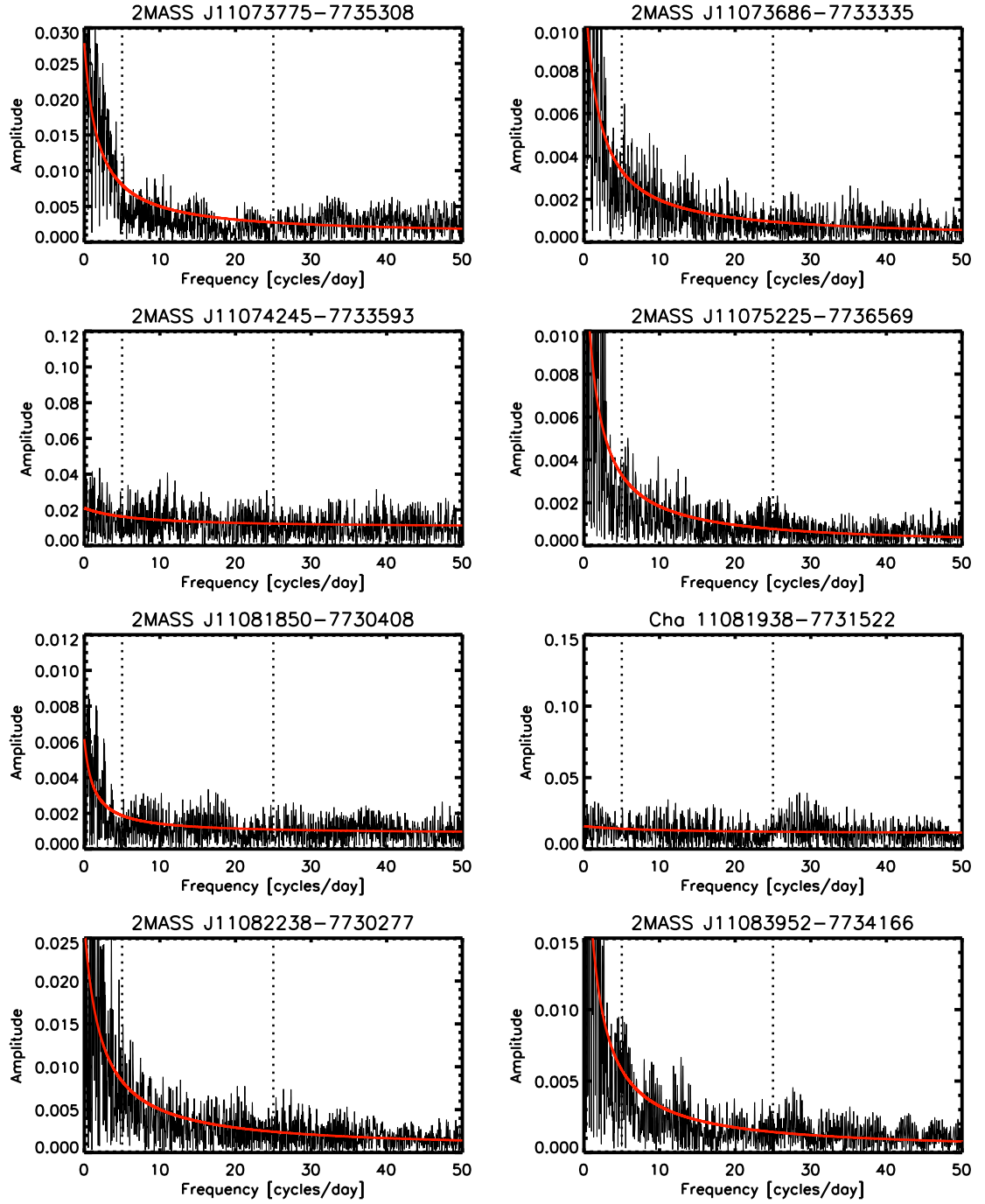
Figure 4.8 –Continued
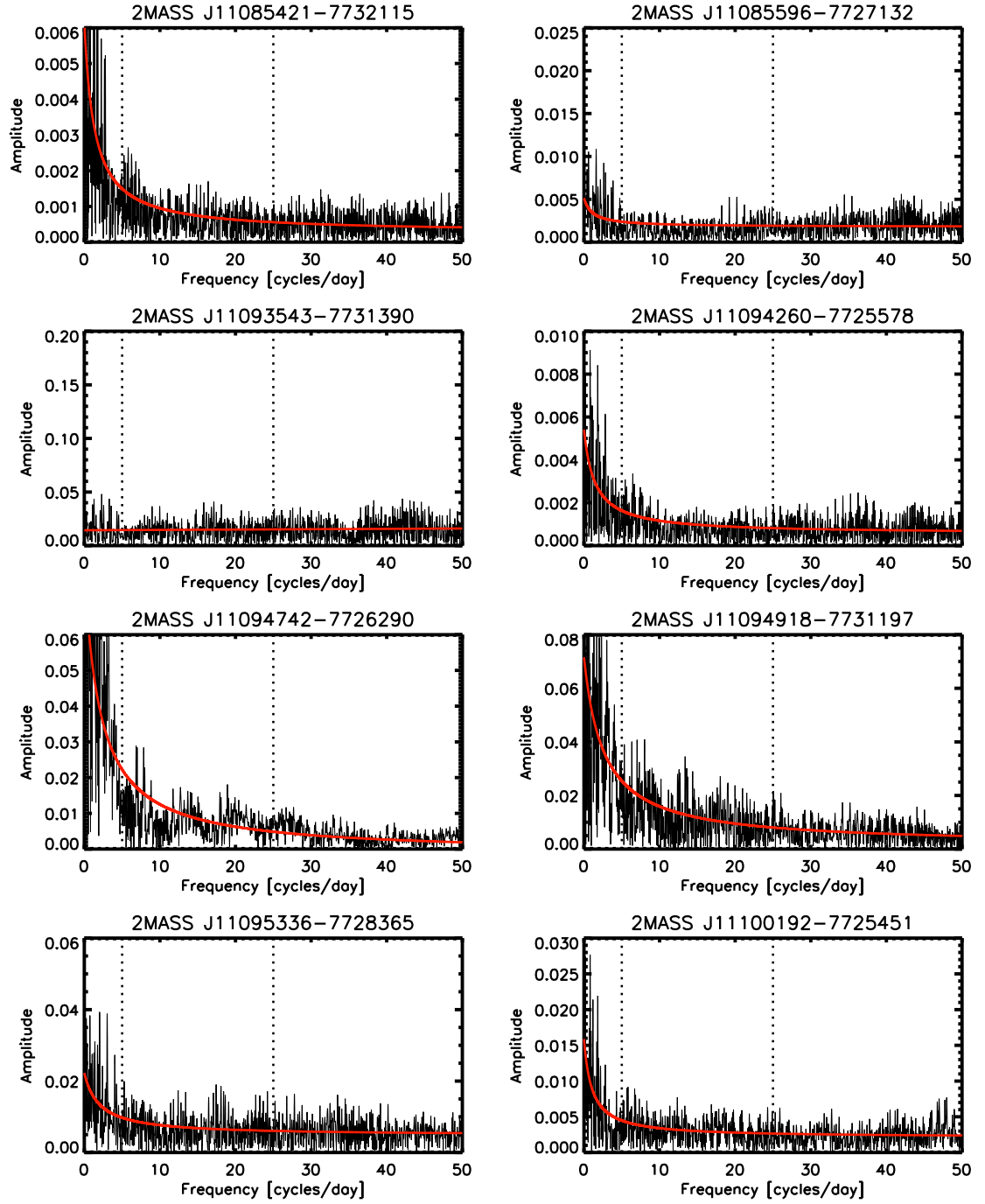
Figure 4.8 –Continued
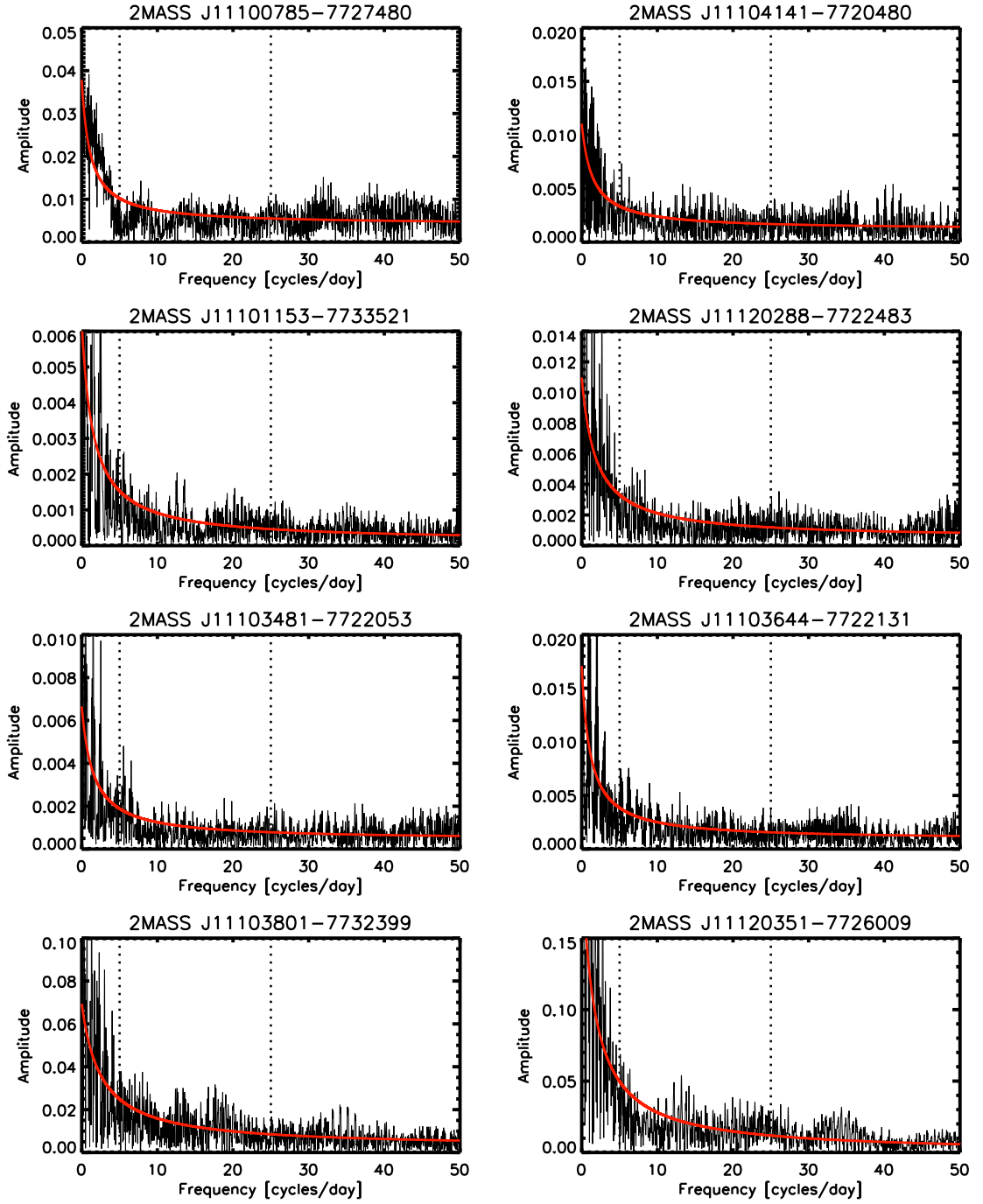
Figure 4.8 –Continued
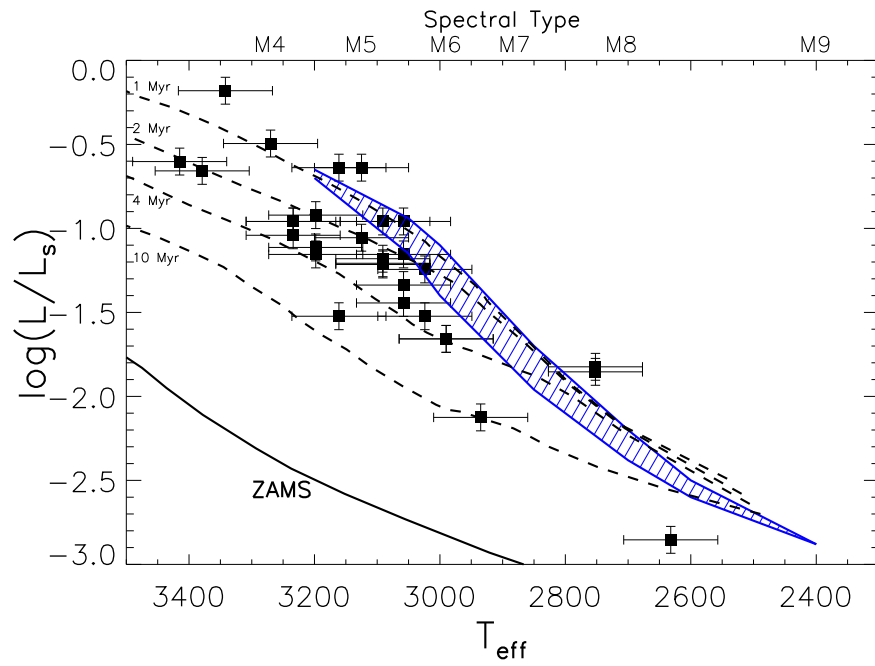
Figure 4.9 We plot the Cha I members in our CTIO 1.0 m field on the H-R diagram, along with the deuterium-burning instability strip from PB05 (blue dashed region). Effective temperature ($T_{\rm eff}$) is in Kelvins, and luminosity is in solar units ($L_{\rm S}$). Isochrones are as in Fig. 4.5. Several of the observed objects appear to lie directly on the strip.

D-burning instability strip, as shown in Fig. 2.3. Thus we set out to obtain time series photometry of this cluster, using both the Palomar 60-inch telescope and the *Hubble Space Telescope.*

4.3.1   Target fields

The $\sim 12'.5 \times 12'.5$ ground-based field of view encompassed a significant spatial extent within IC 348, including the nebulous region in the cluster center. The *HST* Wide Field Camera 3 (WFC3) field is much smaller, with a full field of view of $162'' \times 162''$. To maximize the data cadence we opted to observe in the subarray mode, for which only one of two $81'' \times 162''$ chips was used. Since the ground-based photometry preceded the *HST* observations by more than three years, we were able to select several faint BD pulsation candidates that required photometry at the higher sensitivity levels afforded by *HST*. Therefore the WFC3 field did not cover an additional region, but rather fell within the previous ground-based FOV, including four BDs and and two VLMSs. Two of these (L761 and L1434) do not have ground-based light curves since they suffered from low signal-to-noise. Simultaneous observations with *HST*'s other imaging CCD, the Advanced Camera for Surveys (ACS) were acquired, but since the FOV could not be selected in advance it fell well outside IC 348 and unfortunately did not contain any known members. Both the ground- and space-based fields are illustrated in Fig. 4.10.

Selection of low-mass IC 348 cluster objects was carried out by considering the sources presented by Luhman et al. (2003b) and (Luhman et al. 2005b). In addition to these references, Muench et al. (2007) provide a list of new low-mass IC 348 members selected by disk excess as well as a cross-match of *Chandra* x-ray sources with near-IR photometry, but none of their objects appears in our field. A total of 144 members fell within the ground-based FOV, including 24 BDs (i.e., objects with spectral types M6 or later) and 65 VLMSs (M4–M6). We did not extract photometry for some BDs that were too faint for adequate signal-to-noise. There are also a number of brighter stars within the field for which we did not obtain data since their psfs were saturated and often distorted by nebulosity and scattered light within the central region of the cluster where several bright B stars lie. We present the compilation of very-low-mass IC 348 members monitored for the pulsation campaign in Tables 4.5 and 4.6.
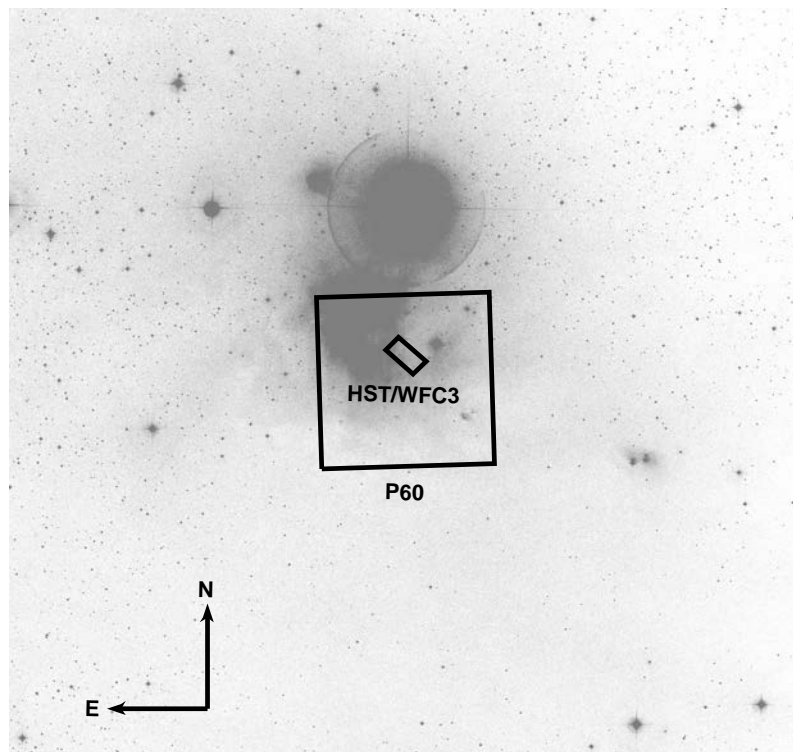
Figure 4.10 The IC 348 fields observed with the Palomar 60-inch telescope ($12'.5 \times 12'.5$) and HST ($81'' \times 162''$) are shown superimposed on a Digital Sky Survey image. The bright B star binary o Per lies just to the north.

Table 4.5.   IC 348 cluster members observed with the P60

Object	2MASS ID	I	J	K	SpT
L13	2MASS J03435964+3201539	19.46	13.45	10.78	M0.5
L23	2MASS J03443871+3208420	13.97	11.19	9.97	K3
L26	2MASS J03435602+3202132	15.62	12.29	10.56	K7
L31	2MASS J03441816+3204570	15.37	12.09	10.54	G1
L32	2MASS J03443788+3208041	14.18	11.69	10.48	K7
L35	2MASS J03443924+3207355	13.21	10.83	9.95	K3
L37	2MASS J03443798+3203296	13.18	11.45	10.44	K6
L40	2MASS J03442972+3210398	14.10	11.93	10.76	K8
L41	2MASS J03442161+3210376	14.99	12.49	11.28	K7
L46	2MASS J03441162+3203131	16.24	12.78	11.22	G8
L48	2MASS J03443487+3206337	13.45	11.50	10.60	K5.5
L49	2MASS J03435759+3201373	19.63	14.56	11.89	M0.5
L51	2MASS J03441297+3201354	19.56	15.09	12.43	-
L52	2MASS J03444351+3207427	14.98	12.12	10.89	M1
L55	2MASS J03443137+3200140	18.06	13.63	11.65	M0.5
L56	2MASS J03440499+3209537	13.02	11.55	10.71	K3.5
L58	2MASS J03443854+3208006	14.24	11.94	10.90	M1.25
L61	2MASS J03442228+3205427	15.23	12.54	11.27	K8
L65	2MASS J03443398+3208541	13.69	11.85	10.98	M0
L66	2MASS J03442847+3207224	13.53	11.67	10.85	K6.5
L68	2MASS J03442851+3159539	14.16	12.00	11.13	M3.5
L69	2MASS J03442702+3204436	13.69	11.95	11.14	M1
L71	2MASS J03443257+3208558	14.32	12.11	11.13	M3
L72	2MASS J03442257+3201536	14.31	12.12	11.15	M2.5
L74	2MASS J03443426+3210497	14.36	12.14	11.13	M2
L75	2MASS J03444376+3210304	14.26	12.75	11.60	M1.25
L82	2MASS J03443740+3206118	13.89	12.09	11.15	K7
L83	2MASS J03443741+3209009	14.93	12.49	11.44	M1
L91	2MASS J03443919+3209448	14.76	12.59	11.52	M2
L92	2MASS J03442366+3206465	14.20	12.24	11.37	M2.5
L97	2MASS J03442554+3206171	15.98	12.82	11.59	M2.25
L98	2MASS J03443860+3205064	14.88	12.47	11.52	M4
L99	-	14.78	12.89	11.90	M3.75
L103	2MASS J03444458+3208125	15.73	12.89	11.87	M2
L105	2MASS J03441125+3206121	14.32	12.39	11.47	M0
L108	2MASS J03443869+3208567	14.46	12.49	11.57	M3.25
L115	2MASS J03442999+3209210	17.18	13.58	12.02	M2.5
L116	2MASS J03442155+3210174	14.57	12.66	11.70	M1.5

Table 4.5—Continued

Object	2MASS ID	I	J	K	SpT
L119	2MASS J03442125+3205024	15.19	12.80	11.84	M2.5
L123	2MASS J03442457+3203571	15.36	12.85	11.81	M1
L124	2MASS J03435463+3200298	14.90	12.57	11.73	M4.25
L125	2MASS J03442166+3206248	14.56	12.52	11.59	M2.75
L128	2MASS J03442017+3208565	14.84	12.73	11.83	M2
L140	2MASS J03443568+3203035	15.78	13.47	12.31	M3.25
L142	2MASS J03435619+3208362	14.65	12.63	11.73	M0
L145	2MASS J03444129+3210252	14.69	12.65	11.80	M4.75
L146	2MASS J03444261+3206194	13.99	12.55	11.74	M1
L149	2MASS J03443698+3208342	15.66	13.07	12.10	M4.75
L153	2MASS J03444276+3208337	15.95	13.21	12.22	M4.75
L156	2MASS J03440678+3207540	15.31	13.00	12.12	M4.25
L158	2MASS J03444016+3209129	16.50	13.36	12.25	M5
L159	2MASS J03444760+3210555	16.60	13.57	12.29	M4.25
L160	2MASS J03440257+3201348	14.87	12.74	12.03	M4.75
L163	2MASS J03441122+3208161	15.12	12.78	12.07	M5.25
L165	2MASS J03443545+3208563	16.15	13.28	12.33	M5.25
L166	2MASS J03444256+3210025	16.85	13.65	12.43	M4.25
L167	2MASS J03444116+3210100	16.71	14.04	12.62	M3
L168	2MASS J03443134+3210469	15.84	13.52	12.40	M4.25
L169	2MASS J03441776+3204476	15.78	13.15	12.28	M5.25
L174	2MASS J03440410+3207170	15.01	13.02	12.13	M1.5
L182	2MASS J03441820+3209593	15.74	13.21	12.30	M4.25
L187	2MASS J03440613+3207070	16.36	13.31	12.42	M4.25
L190	2MASS J03442922+3201157	17.93	14.33	12.86	M3.75
L192	2MASS J03442364+3201526	18.54	14.47	12.97	M4.5
L194	2MASS J03442724+3210373	15.88	13.74	12.66	M4.75
L198	2MASS J03443444+3206250	16.07	13.38	12.54	M5.5
L199	2MASS J03435721+3201337	-	-	-	M6.5
L203	2MASS J03441810+3210534	18.24	16.04	13.90	M0.75
L205	2MASS J03442980+3200545	16.46	13.58	12.82	M6
L207	2MASS J03443030+3207426	17.16	14.01	12.70	M3.5
L210	2MASS J03442001+3206455	15.81	13.52	12.59	M3.5
L215	2MASS J03442894+3201378	-	-	-	M3.25
L217	2MASS J03444303+3210151	16.07	13.54	12.64	M5
L221	2MASS J03444024+3209331	16.57	14.11	13.03	M4.5
L228	-	18.28	15.07	13.43	M0.5
L230	2MASS J03443551+3208046	16.30	13.66	12.78	M5.25

Table 4.5—Continued

Object	2MASS ID	I	J	K	SpT
L234	2MASS J03444520+3201197	-	-	-	M5.75
L237	2MASS J03442356+3209338	15.74	13.56	12.76	M5
L243	2MASS J03440770+3205050	16.71	14.01	12.98	M4.5
L252	2MASS J03442912+3207573	15.79	13.70	12.88	M4.5
L253	2MASS J03443165+3206534	16.10	13.58	12.82	M5.5
L254	2MASS J03435379+3207303	16.07	13.71	12.87	M4.25
L255	2MASS J03443569+3204527	16.10	13.70	13.01	M5.75
L256	2MASS J03435526+3207533	16.08	13.61	12.99	M5.75
L259	2MASS J03440362+3202341	16.44	13.54	12.88	M5
L266	-	16.04	13.73	12.93	M4.75
L276	2MASS J03440920+3202376	19.06	14.97	13.55	M0
L277	2MASS J03443943+3210081	16.06	13.91	13.10	M5
L278	2MASS J03443103+3205460	16.75	14.03	13.18	M5.5
L287	2MASS J03444111+3208073	17.97	14.59	13.45	M5.25
L298	2MASS J03443886+3206364	16.60	13.98	13.26	M6
L300	2MASS J03443896+3203196	16.40	14.11	13.35	M5
L301	2MASS J03442270+3201423	18.70	15.15	13.80	M4.75
L302	2MASS J03442027+3205437	17.04	14.24	13.32	M4.75
L303	2MASS J03440442+3204539	16.60	14.06	13.38	M5.75
L308	2MASS J03442122+3201144	21.03	16.18	14.24	M4
L312	2MASS J03435508+3207145	16.80	14.12	13.44	M6
L314	2MASS J03442256+3201277	18.80	15.13	13.80	M5
L322	2MASS J03441959+3202247	17.53	14.74	13.70	M4.25
L324	2MASS J03444522+3210557	17.14	14.56	13.65	M5.75
L325	2MASS J03443005+3208489	17.55	14.63	13.75	M6
L329	2MASS J03441558+3209218	17.64	14.57	13.85	M7.5
L334	2MASS J03442666+3202363	16.88	14.42	13.69	M5.75
L335	2MASS J03444423+3208473	17.34	14.56	13.76	M5.75
L336	2MASS J03443237+3203274	17.63	14.86	14.02	M5.5
L342	2MASS J03444130+3204534	17.02	14.49	13.66	M5
L350	2MASS J03441918+3205599	16.91	14.32	13.60	M5.75
L351	2MASS J03442575+3209059	17.62	14.69	13.76	M5.5
L353	2MASS J03443814+3210215	16.87	14.46	13.70	M6
L355	2MASS J03443920+3208136	18.17	14.88	14.03	M8
L358	2MASS J03441276+3210552	16.79	14.61	13.92	M5.5
L360	2MASS J03444371+3210479	16.40	14.54	13.84	M4.75
L363	2MASS J03441726+3200152	17.97	14.92	14.16	M8
L365	2MASS J03441022+3207344	17.26	14.64	13.92	M5.75

Table 4.5—Continued

Object	2MASS ID	I	J	K	SpT
L366	2MASS J03443501+3208573	17.33	14.84	14.05	M4.75
L367	2MASS J03435915+3205567	17.36	14.68	13.95	M5.75
L373	2MASS J03442798+3205196	17.18	14.84	14.14	M5.5
L382	2MASS J03443095+3202441	18.95	15.48	14.47	M5.5
L391	2MASS J03444658+3209017	18.63	15.38	14.41	M5.75
L396	2MASS J03440233+3210154	17.57	14.98	14.18	M5.25
L405	-	18.34	15.20	14.48	M8
L414	2MASS J03444428+3210368	17.68	15.41	14.68	M5.25
L415	2MASS J03442997+3209394	18.43	15.20	14.36	M6.5
L432	2MASS J03444593+3203567	18.18	15.14	14.27	M5.75
L437	2MASS J03435638+3209591	18.61	15.41	14.62	M7.25
L454	2MASS J03444157+3210394	17.81	15.38	14.61	M5.75
L462	2MASS J03442445+3201437	19.18	15.67	14.58	M3
L468	2MASS J03441106+3201436	20.55	16.53	15.42	M8.25
L555	2MASS J03444121+3206271	16.86	14.28	13.54	M5.75
L603	2MASS J03443341+3210314	19.95	16.33	15.61	M8.5
L611	2MASS J03443035+3209446	19.61	16.35	15.49	M8
L613	2MASS J03442685+3209257	19.80	16.86	16.01	M8.25
L622	-	20.13	17.54	16.91	M6
L690	2MASS J03443638+3203054	20.02	16.62	15.78	M8.75
L703	2MASS J03443661+3203442	20.10	16.65	15.70	M8
L705	-	20.93	17.11	16.27	M9
L725	-	20.91	18.16	17.37	M6
L738	-	20.92	17.47	16.90	M8.75
L1683	2MASS J03441583+3159367	-	-	-	M5.25
L1684	2MASS J03442330+3201544	17.29	14.78	14.05	M5.75
L1889	2MASS J03442135+3159327	-	-	-	-
L1925	2MASS J03440576+3200010	-	-	-	M5.5
L4011	-	-	-	-	-
L4044	-	21.47	17.52	16.59	M9
L30003	2MASS J03435925+3202502	-	-	-	M6

Note. — Identifications beginning with "L" are from the compilation of Luhman et al. (2003b) and references therein, as is the photometry.

Table 4.6.   IC 348 cluster members observed with the *Hubble Space Telescope.*

Object	I	J	K	SpT
L302	17.04	14.24	13.32	M4.75
L350	16.91	14.32	13.60	M5.75
L405	18.34	15.20	14.48	M8
L761	20.03	15.66	15.33	M7
L1434	21.11	18.39	17.44	M6
L4044	21.47	17.52	16.59	M9

Note. — Identifications are from the compilation of Luhman et al. (2003b) and references therein.

4.3.2   Ground-based data acquisition and reduction

Ground-based observations with the P60 took place on a total of 9 nights between 2008 November 17 and November 29. The chosen field center was R.A. = $03^{\mathrm{h}}44^{\mathrm{m}}19.7^{\mathrm{s}}$, decl. = $+32°04'29''$s (J2000), but since the P60 system is subject to tracking inaccuracies (see §3.3.1.1), this position shifted up to $45''$ throughout the run. An exposure time of 300 seconds was chosen to provide sensitivity on the faint brown dwarfs without elongating the psfs too much due to the lack of guiding.

Since this was our first run on the P60, we were not aware that observations in the chosen I-band filter would lead to substantial fringe patterns on the images (§3.3.1.2). Off-cluster fringe images were not available, so we were not able to produce a model for subtraction of the fringe pattern. Fortunately this phenomenon is not significant with the alternate i_p filter, as the associated response function is lower in wavelength regions populated by sky emission lines. Therefore we substituted the i_p filter after the first night and discarded the I-band data since it has a different zero point and could not be incorporated into the differential photometry.

Observations with the robotic P60 telescope are by design automatic and not easily adjustable, apart from selection of exposure times, filters, and pointing center (although this changes slightly over the course of a night). The established data reduction pipeline performs basic calibrations, including bias subtraction, flatfielding, and fitting of the world

coordinate system (Cenko et al. 2006). Although we obtained a series of sky flatfields, we determined that the domeflat images used by the pipeline were sufficient to correct interpixel sensitivity variations (see §3.3.1.1). We subsequently cleaned the images of cosmic rays with the IRAF *cosmicrays* utility, as described for the σ Orionis data. Image alignment was also carried out with ease, since an accurate coordinate system was already superimposed on the calibrated images; we used the *IRAF* program *wregister* to complete this task.

4.3.3 *HST* data acquisition and reduction

We used the *HST* WFC3 ultraviolet/visible (UVIS) CCD to re-observe 4 BDs and 2 low-mass stars in IC 348, as listed in Table 4.6. The UVIS channel is comprised of two chips, each 4096×2051 pixels; since we observed in subarray mode, we only used one of these (UVIS1). Each pixel is $\sim 0.04''$ across, for a total subarray field of view of $\sim 81'' \times 162''$. With a psf size of $0.07''$, the data are somewhat undersampled. Full well of the WFC3/UVIS detector pixels occurs at $\sim 70,000~e^-$, whereas gain is 1.5 e^-/s and readnoise is $\sim 2.95 e^-$. Although the region on the detector is rectangular, the optics of WFC3 are such that the projection onto sky coordinates is distorted into a skewed rhombus, with side angles of $86.1°$.

Observations took place from 2011 January 29 to February 4, for just over 7 hours of each day. Although *HST* is a space observatory, the sun position and other observing constraints resulted in each block of observations ("visit") beginning at roughly the same time everyday. Unfortunately much of visit 5 was compromised since the gyroscopic system failed and the field was lost for a number of hours. The viewing limits of *HST* are such that IC 348 objects may only be observed for 46 minutes of each 97 minute orbit. Therefore we designed exposure times to acquire as many images as possible per orbit, without exceeding the telescope's maximum data downlink rate. These varied among 128, 171, and 192 seconds. All observations were carried out through the F814W filter, which is centered near 8030 Åand similar to I band.

HST/WFC3 data are processed by pipeline, which includes standard bias and flatfield calibration, as well as cosmic ray rejection. The MultiDrizzle program corrects for geometric distortion and optimally combines sets of three of four consecutive images, even for undithered data such as ours. Output image units are provided in electrons per second, thereby allowing fluxes in different images to be compared directly, without regard to

exposure time.

4.3.4 Aperture photometry

Different approaches were chosen to produce ground and space-based photometry, as explained in §3.1.3. For the P60 data, we employed the variable-aperture method to optimize flux measurements in a variety of seeing conditions. Typical apertures were 1–2 times the psf size, depending on object brightness, and sky annulus radii from 4.5–6 pixels were used to subtract background. Few field stars were available in the FOV to serve as constant references; although a number of the known cluster members are stable to within 0.002 magnitudes on 6 hour timescales, they exhibit flux variations in excess of the Poisson expectation over the 12 day duration of the run. It is thus difficult to assess the photometric performance since the majority of objects in the field may be variable (Fig. 3.7). With this caveat, minimum RMS values for the brown dwarfs over the course of a night were in line with sky noise expectations, at ∼1%.

For the *HST*/WFC3 images, apertures were fixed for each target and several different sizes were tested, from 2 to 8 pixels, as were sky annulus radii from 8–12 pixels and 11–16 pixels. Although results did not differ much, the best RMS light curve values were attained with the 6 pixel aperture and the sky annulus extending from 11–16 pixels. Although the Poisson errors are close to 0.001 magnitudes for several targets, the measured RMS light curve spreads are an order of magnitude larger, regardless of the type of photometry employed. Evidently, the flux of these objects is dominated by systematic effects, most of which is probably intrinsic variability. Several higher mass stars fell within the FOV, but photometry on these objects was not carried out due to their high level of saturation.

The final light curves produced for the P60 and *HST* fields were exclusively differential, since we are only interested in short-term flux variations, and photometric zero points are irrelevant. Since objects on the P60 detector tend to cross several bad pixel columns, we made sure that all of the selected reference stars stayed within clean areas of the chip. By eye, the resulting time series from both the P60 and *HST* display copious periodic and erratic variability. Since we did not observe many non-cluster members for comparison, it is difficult to select aperiodic variables as we have done for the σ Ori and Cha I fields. As a result, we focused almost exclusively on periodic variability in IC 348.

4.3.5 Periodic variability detection

We performed a period search analysis as described in §2.3.2 on all IC 348 cluster members observed with the P60 and the *HST*. For the former, we are sensitive to periodicities on timescales from approximately 8 minutes to 12 days. Since we did not obtain data on every night, our sensitivity to periods of more than a few days is not uniform. We therefore focus on the short periods predicted for D-burning pulsation. We generated periodograms from the light curves of all 144 unsaturated objects in the ground-based field. A large fraction of these display variability by eye, much of which is erratic and introduces low-frequency power to the periodogram. In cases where an obvious periodicity appeared on timescales of one day or more (i.e., likely associated with rotation), we fit the overall trend and removed it from the light curve before searching for pulsation signals. Many of the periodograms nevertheless display excess power around 5–10 cd^{-1} that does not reach the 99% significance level and does not correspond to a real periodicity when the light curve is phased to the peak. These are because of the effect that the time sampling pattern for this particular run has on the the frequency response. We present the associated window function in Fig. 4.11 where the power excess is centered around 8 cd^{-1}.

A representative sample of periodograms for P60 targets is shown in Fig. 4.12. The noise levels are relatively flat beyond 10 cd^{-1}, with a floor ranging from a couple millimagnitudes to a few tenths of a percent, depending on the object's magnitude. Since no significant signals appear in the frequency range expected for pulsation, we fit $1/f$ curves to the data for placement of limits on the amplitude of this phenomenon.

For the *HST* program, the Nyquist frequency is ∼101.5 cd^{-1} (a period of 14.2 minutes) and the telescope's orbital frequency is 14.85 cd^{-1} (corresponding to 97 minutes). The latter timescale unfortunately appears as a strong alias in *HST* periodograms, as seen in the window function (Fig. 4.13) and many of the periodograms.

We present the periodograms of *HST* targets in Fig. 4.14. Of the six observed targets, all but object L1434 display flux variations significantly larger the estimated photometric uncertainties. The light curves of objects L405, L350, and L302 change on day-to-day timescales in a manner that is not strictly periodic. L4044 as well exhibits a strong brightening trend (0.15 magnitudes over 7 days). L761, on the other hand, is a periodic variable with a timescale of ∼1.3 days. The apparently intrinsic variability in these objects causes

152
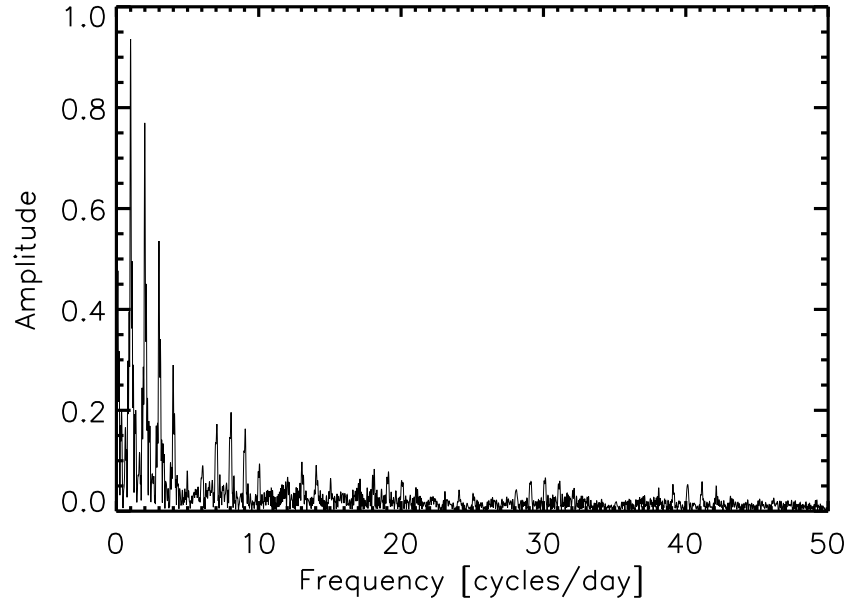
Figure 4.11 The window function for the IC 348 observations with the Palomar 60-inch telescope. A series of aliases is seen centered around a frequency of ∼8 cd^{-1}.

low-frequency signal to leak into the alias at 14.85 cd^{-1}, as seen in the periodograms.

4.3.6 Pulsation Search Results

We have searched for periodicities in our P60 and *HST* data on 1–5 hour timescales, in hopes of detecting pulsation. In fact, there are several candidate IC 348 objects with previously reported periods under 5 hours (Cieza & Baliber 2006), but they are not in our field. Apart from the orbit-related alias, the periodogram noise levels lie in the 1–5 millimagnitude range at the frequencies of interest. Hence we conclude that none of the VLMSs and BDs not oscillate at observable amplitudes. To confirm that a number of our IC 348 targets should be susceptible to the D-burning instability, we have plotted their positions on the H-R diagrams in Fig. 4.15. Since there are two possible distances to the cluster (2.2.3), have produced two different versions. In either case, many objects overlap the predicted D-burning pulsation strip.
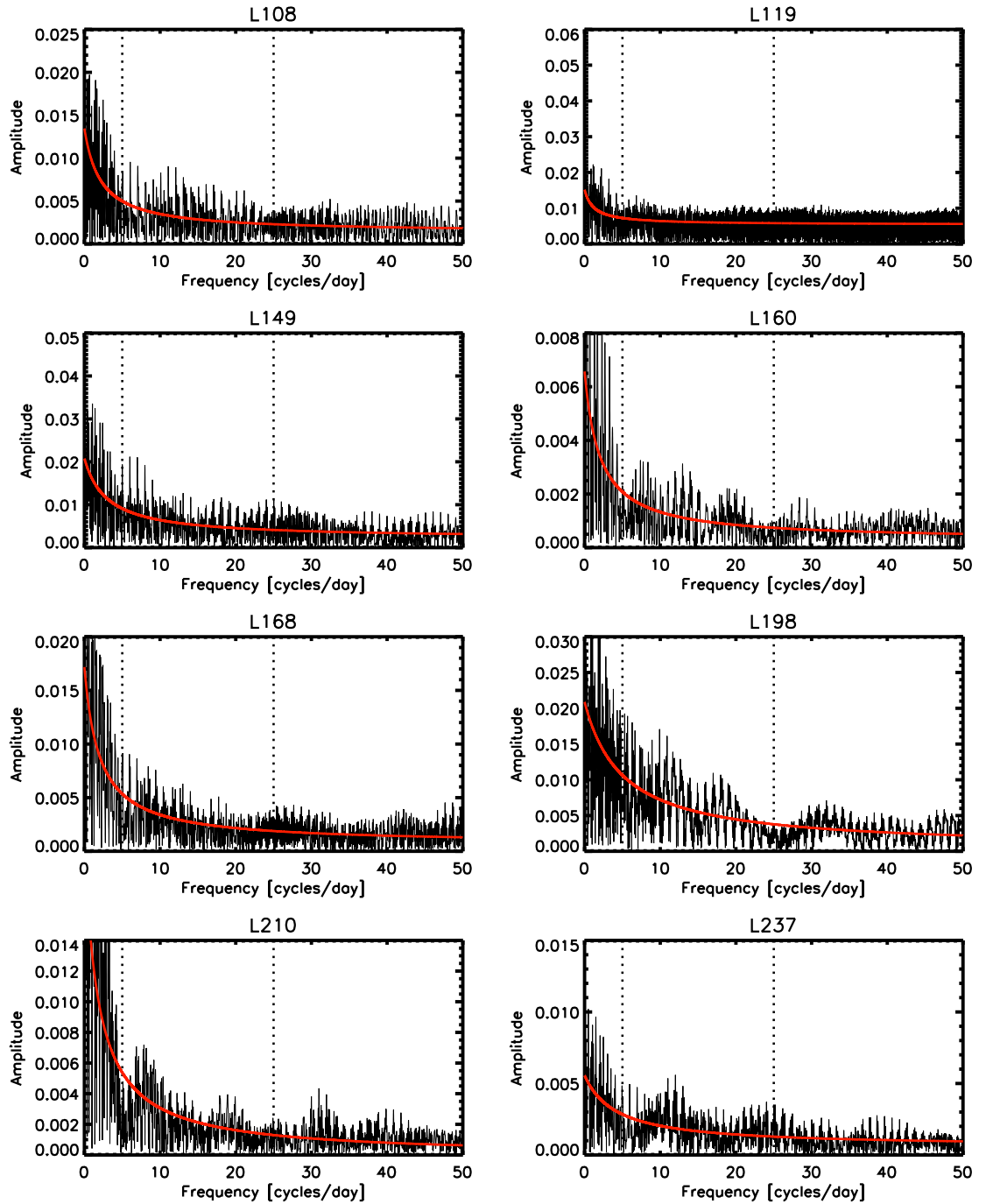
Figure 4.12 Periodograms of selected IC 348 targets observed with the P60. Vertical dashed lines indicate the region of frequency space ($\sim$5–25 cd^{-1}) where pulsation is predicted. Red curves mark $1/f$ profile fits to the noise level.
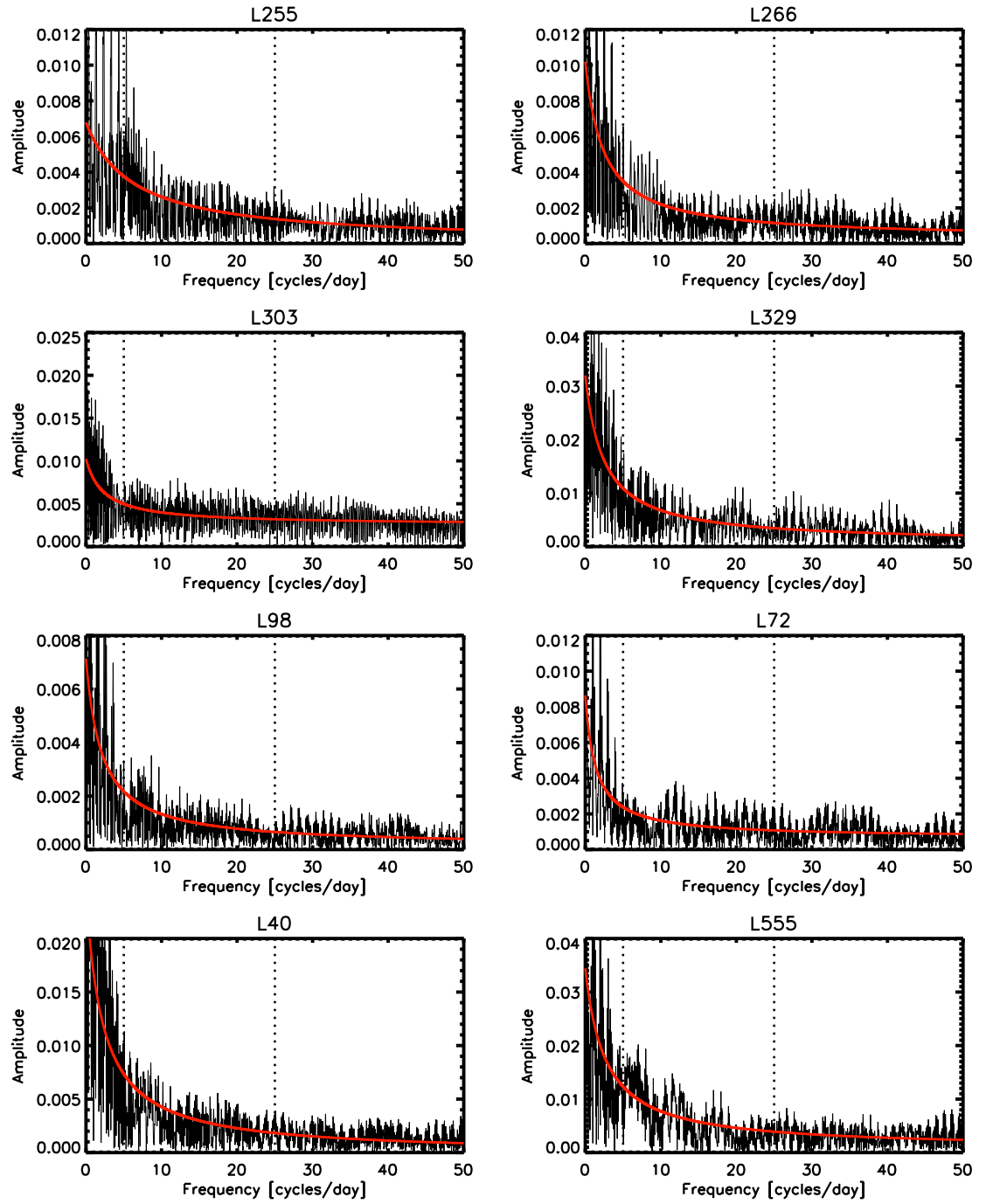
Figure 4.12 –Continued

155
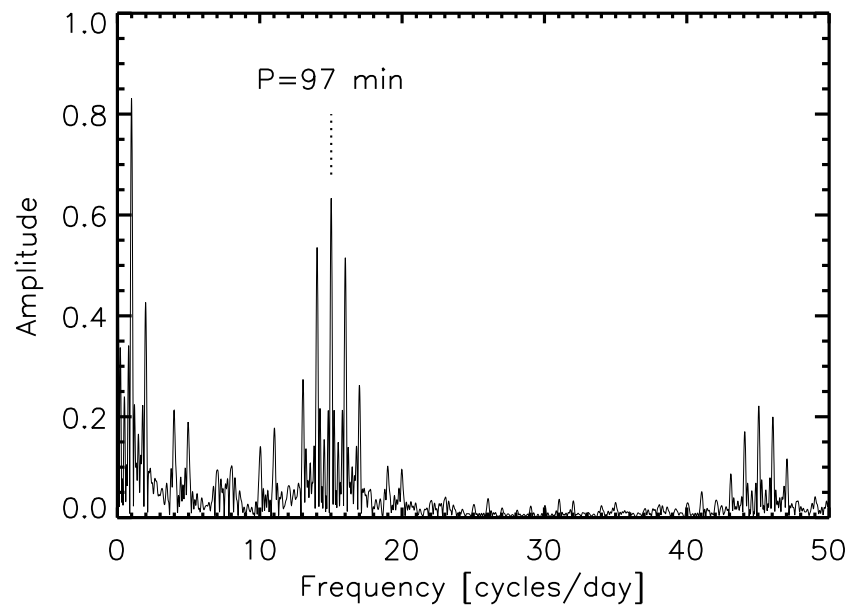
Figure 4.13 The window function for *HST*/WFC3 observations. There is a strong alias at the orbital frequency of 14.85 cd^{-1} (97 minute period).
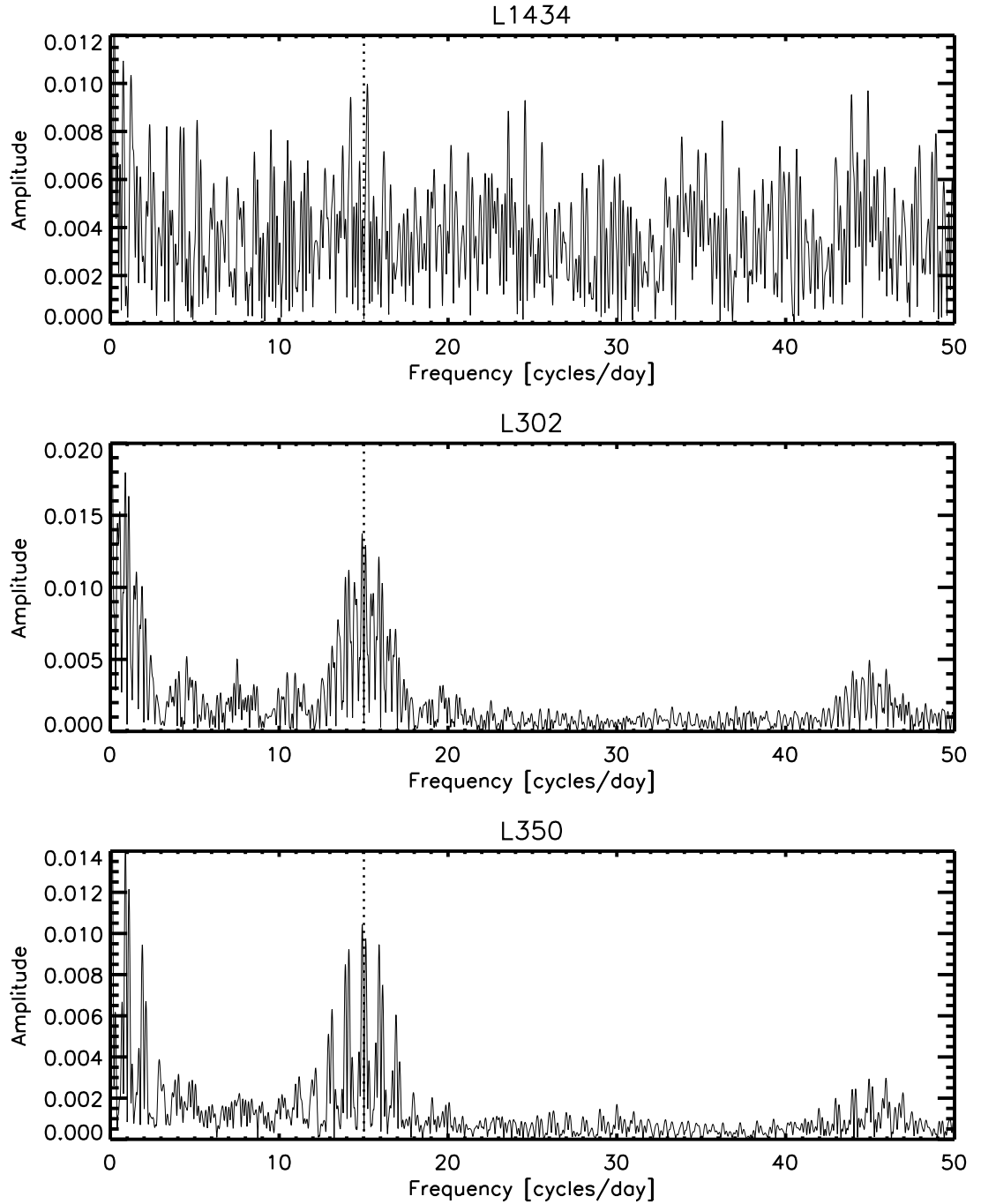
Figure 4.14 Periodograms of IC 348 targets observed with *HST*. The vertical dashed line marks the telescope's orbital frequency, where a strong alias tends to appear.
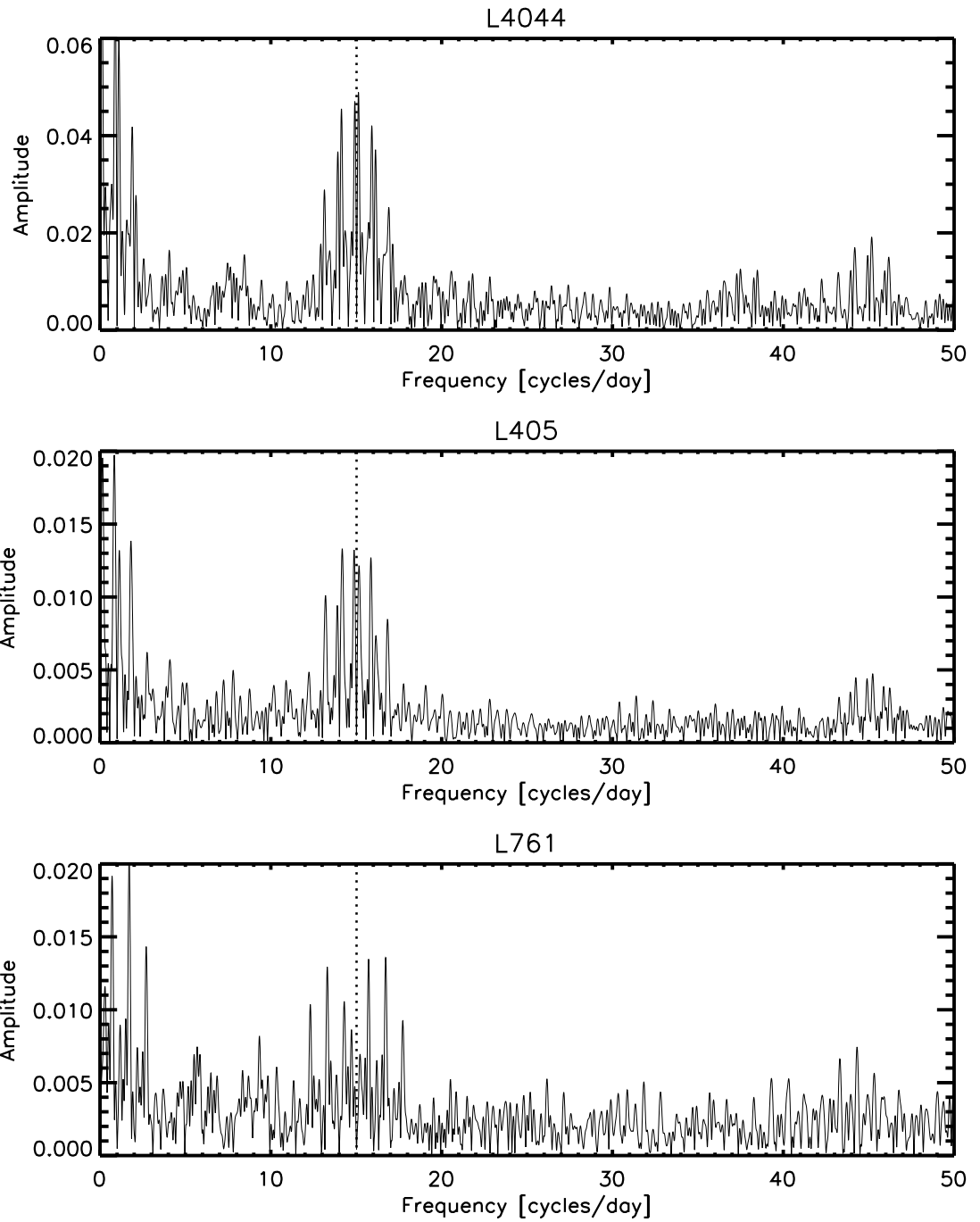
Figure 4.14 –Continued
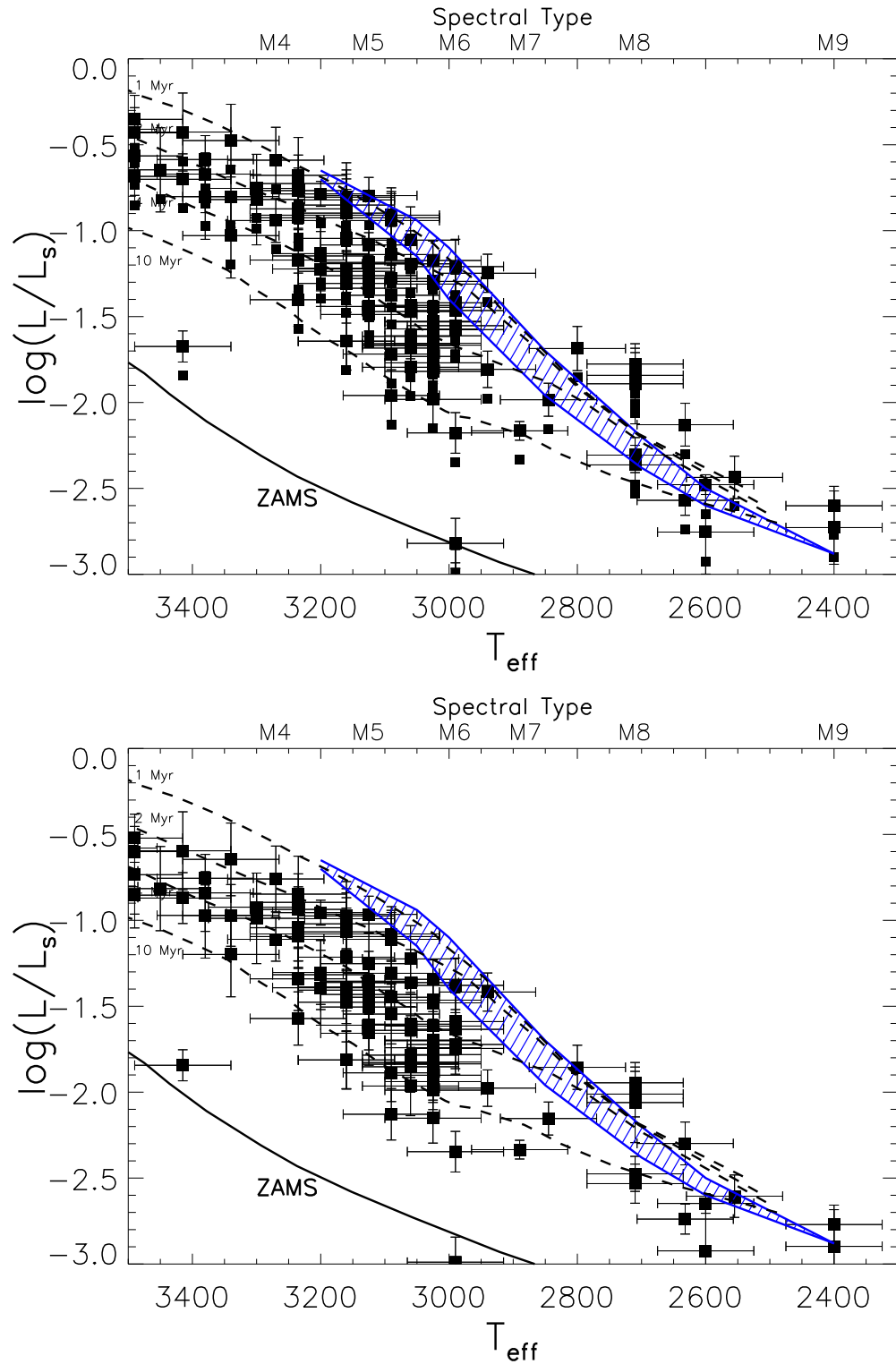
Figure 4.15 We plot the IC 348 members observed with the P60 and *HST* on the H-R diagram along with the deuterium-burning instability strip from PB05 (blue dashed region). Effective temperature (T_{eff}) is in Kelvins, and luminosity is in solar units (L_{S}). Isochrones are as in Fig. 4.5. We show the effect of changing the favored distance (316 pc; top) to the alternate value of 260 pc from Hipparcos parallaxes (bottom). Many targets appear to lie on the strip, particularly for the choice of the 316 pc distance.

4.4 Upper Scorpius

4.4.1 Target fields

The Upper Scorpius (USco) region is one of the most spatially extended young associations, with stars and BDs spread over many tens of degrees on the sky. As a result, few variability studies have been performed here. Although the H-R diagram of catalogued low-mass members (§2.2.4) displays many objects with temperatures and luminosities overlapping the D-burning instability strip, it is difficult to obtain data on more than one at a time. We therefore observed this area on multiple occasions, in fields carefully selected to maximize the number of pulsation candidates.

We observed five different fields in Upper Scorpius, including 5 BDs and 11 VLMSs, which are listed in Table 4.7. Observations on three of the fields were abbreviated to three nights or less because of weather (the CTIO 1.0 m run), and tracking problems (USco members in the first field chosen for observation with the P60 fell too close to the edge of the detector and tended to wander out of the FOV). Since our observations in 2008 and 2009, further low-mass Upper Scorpius members have been discovered by Lodieu et al. (2011) and Dawson et al. (2011). We identified three of these objects from Lodieu et al. (2011) in our first FOV from CTIO 1.0 m Y4KCam monitoring in May 2008. Correlation of the new source lists revealed no additional targets in any of the other observations.

4.4.2 Data reduction and aperture photometry

Standard calibrations were applied in the same manner as described for the P60 data on IC 348 cluster members (§4.3.2) and the CTIO 1.0 m data on Cha I (§4.2). These included removal of fringes (§3.3.1.2) using the master fringe frame created during the May 2008 CTIO 1.0 m observing run. The P60 detector has a number of bad columns that corrupt the photometry of different stars, depending on where the pointing center is located in a given image. We were careful not to select for photometric reference any objects affected by these regions. Similar caution was taken for objects in the CTIO 1.0 m field that were affected by dust donut patterns that could not be removed with flatfielding.

We carried out variable aperture photometry (§3.1.3) on objects in the P60 fields, and image subtraction aperture photometry (§3.2) on the CTIO 1.0 m dataset. For the former, we used aperture sizes that were twice the computed optimal value, while for the latter we

Table 4.7.   Objects in Upper Scorpius observed as part of the pulsation campaign.

Object	Telescope	i	J	SpT	Reference
DENIS-P-J161050.0-221251.6	CTIO 1.0 m	-	12.80	M5.5	1
UScoJ16111705-2213088	CTIO 1.0 m	-	11.64	M5	2
SCH J16111711-22171749	CTIO 1.0 m	17.97	14.34	M7.5	3
UScoJ16113470-2219443	CTIO 1.0 m	-	13.24	M5.75	2
UScoJ16113784-2210275	CTIO 1.0 m	-	11.07	M4	2
SCH J16115737-22150691	CTIO 1.0 m	16.70	13.73	M5	3
SCH J16130306-19293234	P60	16.75	13.45	M5.5	3
SCH J16132809-19245288	P60	16.16	12.92	M6	3
SCH J16172504-23503799	CTIO 1.0 m	17.20	13.74	M5	3
SCH J16173105-20504715	P60	16.49	13.03	M7	3
SCH J16174540-23533618	CTIO 1.0 m	17.44	14.05	M6	3
SCH J16181567-23470847	CTIO 1.0 m	16.18	12.42	M5.5	3
SCH J16182501-23381068	CTIO 1.0 m	17.19	13.72	M5	3
SCH J16183144-24195229	P60	17.76	14.15	M6.5	3
SCH J16183620-24253332	P60	14.75	12.03	M4	3
SCH J16185038-24243205	P60	16.79	13.63	M5	3

Note. — References: (1) Martín et al. (2004); (2) Lodieu et al. (2011); (3) Slesnick et al. (2008)

used the optimal value. Corresponding sizes ranged from 1–2 times the psf, or $\sim$5–15″.

Since we only extracted fluxes for the USco members, as well as a small set of reference stars for the P60 images, it is difficult to assess the overall photometric performance. Some targets may be intrinsically variable, while others have light curve RMS values consistent with that expected from the sky background level. In the P60 dataset, the brown dwarf SCH J16132809-19245288 was unfortunately affected by bad pixel columns, and we had to discard much of the light curve.

4.4.3 Periodic variability detection

We produced discrete Fourier transforms to search for periodicities on a variety of timescales, as described in §2.3.2. We are sensitive to periodicities as short as 10 minutes in all datasets. The longest period detectable varies with the length of each observing run and ranges from less than two days to 16 days. Since some of the runs only had six or fewer total nights, the associated periodograms have lower frequency resolution than the datasets on other clusters, and the search for periodicities is more susceptible to systematic effects. Therefore, while some of the objects display variability on night-to-night timescales, we cannot accurately quantify the possible periodicities. The search for pulsation at 1–4 hour periods, however, is still feasible given the number of data points (30–550, depending on the run) and the fairly low photometric uncertainties of the brown dwarfs (1–3%).

None of the objects showed strong periodic variability, although the light curves of a few displayed night-to-night variations that may be indicative of accretion. We present the associated periodograms in Fig. 4.16. We have fit each with a $1/f$ curve to model the noise floor as a function of frequency. These fits are later used (§7.1) to quantify our limits on pulsation amplitudes.

4.4.4 Pulsation search results

We present the H-R diagram of observed USco objects in Fig. 4.17. Of the 17 very low mass USco members observed, one lies squarely on the instability strip: SCH J16173105-20504715. However, its periodogram does not exhibit any significant signals in the region expected for pulsation. A number of other targets could lie on the strip if their 1–σ temperature and luminosity errors are considered. In §7.1 we will use these uncertainties to assess the statistic likelihood of failing to observe pulsation.
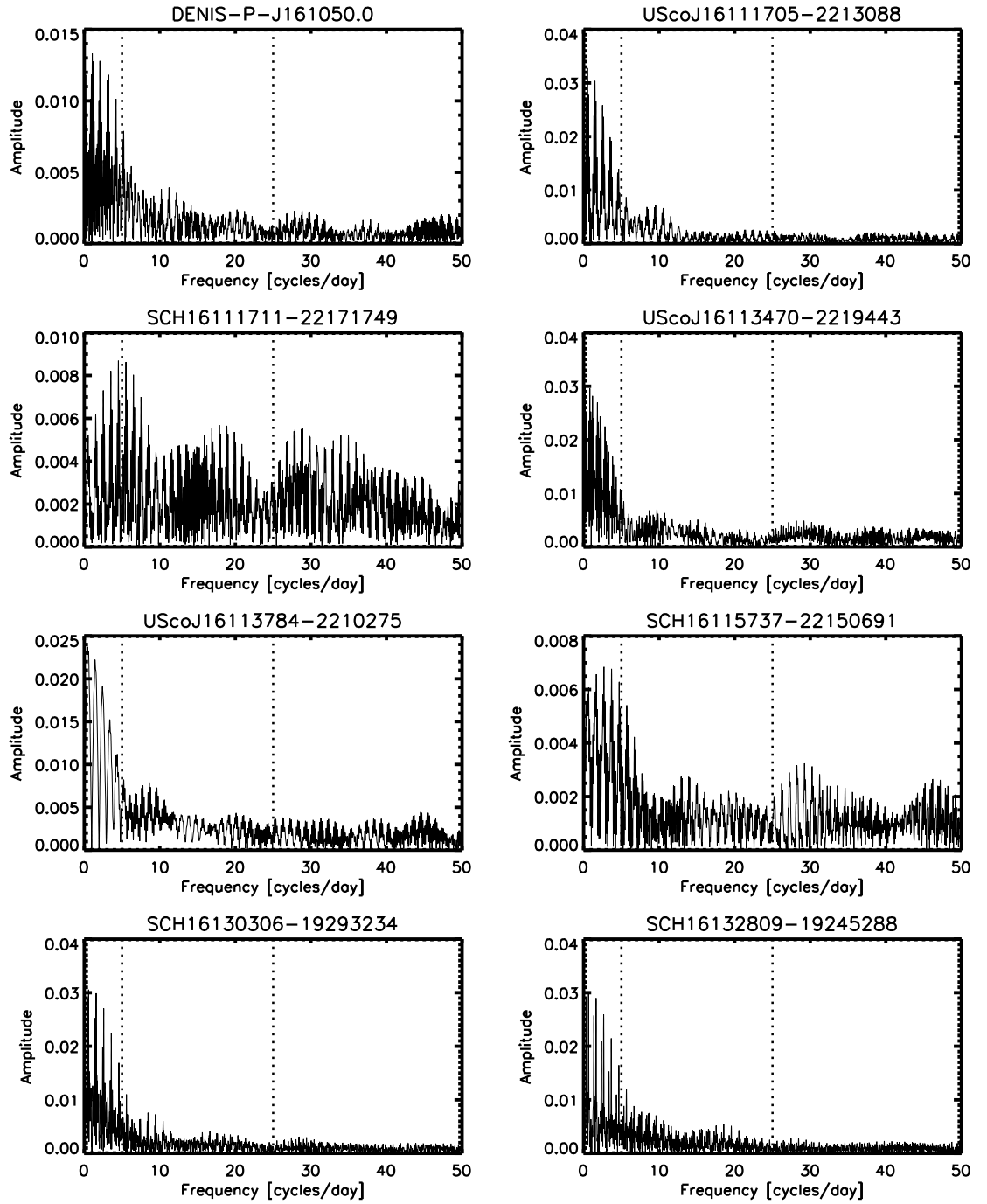
Figure 4.16 Periodograms of USco objects. Vertical dashed lines indicated the region of frequency space ($\sim$5–25 cd^{-1}) where pulsation is predicted. Periodograms with strong undulating patterns correspond to datasets with only three nights of observation and strong systematic effects.
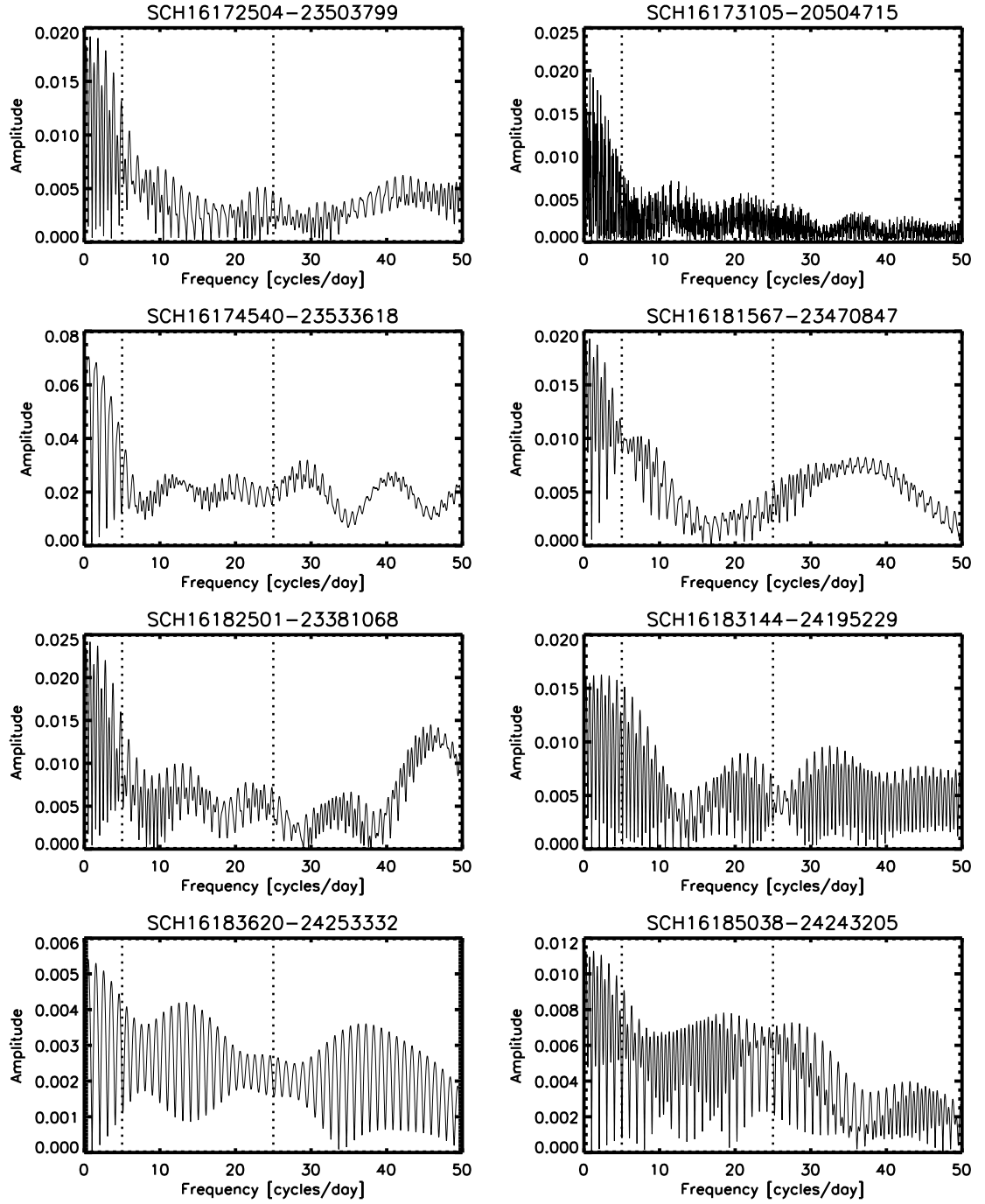
Figure 4.16 –Continued
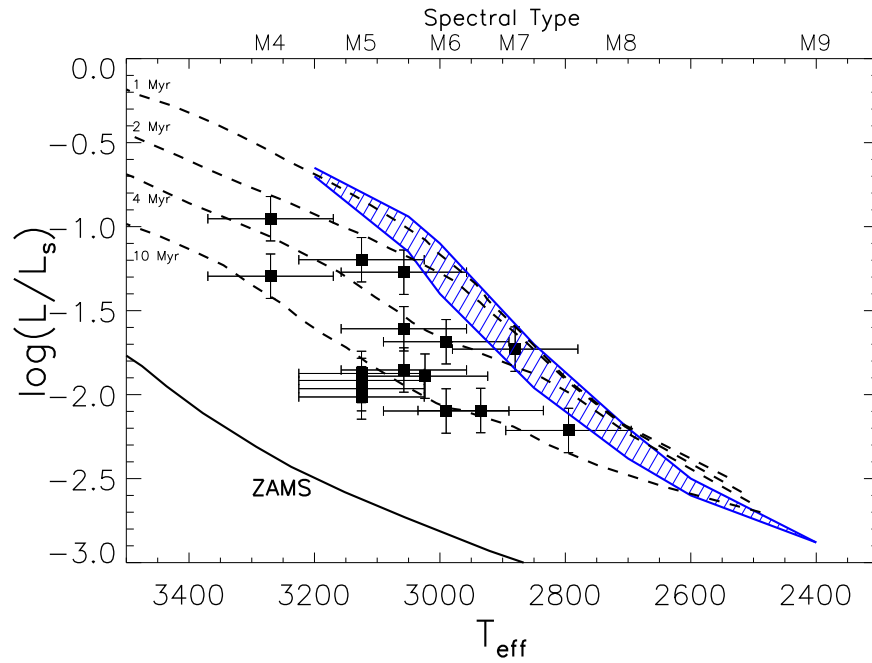
Figure 4.17 The observed sample of USco members is plotted on the H-R diagram, along with PB05's D-burning instability strip. Effective temperature (T_{eff}) is in Kelvins, and luminosity is in solar units (L_{S}). Curves are as in Fig. 4.5.

Chapter 5

The Zoo of Variability in Young Low-Mass Stars and Brown Dwarfs

Although the primary purpose of our photometric monitoring survey was to search for pulsation in young BDs and VLMSs, the high cadence and precision of the data also enabled a detailed exploration of variability properties in slightly higher mass objects as well. Prior surveys of the four clusters studied have generated a fairly large sample of low-mass cluster objects in which to search for variability. Nevertheless, the existing census may not be 100% complete in these regions. To include young VLMSs and BDs that may have escaped previous identification via color-magnitude diagrams, we have produced light curves for all $\sim$3200 unsaturated point sources in the two σ Ori fields and $\sim$1500 sources in the Cha I field. We omitted the other two regions from this analysis because of difficulties in distinguishing variable and non-variable targets (IC 348; §4.3.4) and the expected small sample size of young objects in the FOV (USco).

To avoid biases in variability classification, all subsequent analysis was performed without regard to the objects' membership status. In this way, we can identify new young VLMSs and BD candidates, as well as potentially interesting field stars that happen to lie in the field of view. We have searched for periodicities before performing a more generic variability search (§5.1.2) to limit the number of variables contaminating our analysis of photometric uncertainty as a function of magnitude.

5.1 Variability selection criteria

5.1.1 Periodic variability detection

As an initial test for periodic variability in the data, we produced Lomb-Scargle periodograms for all light curves and removed from the sample targets with no significant signals at the 99% level (see §1.3.2). The collection of periodograms for all targets–variable or not–is also a useful tool for identifying systematic effects in the data that may cause certain frequencies to consistently appear at artificially high probability. This effect is often seen when color-airmass effects are not taken into account in the light curves, resulting in trends that mimic intra-night variability. Because of the very uniform sampling of our datasets, we expect most of these spurious frequencies to occur at or near multiples of 1 cycle per day (cd^{-1}). To quantitatively map out these values, we constructed a histogram from all frequencies corresponding to peaks significant at the 99% level in the Lomb-Scargle periodogram. This diagnostic plot confirms that there are indeed pile-ups near integer frequencies, and we discarded potential variability detections corresponding to periodogram peaks occurring only at these values. As an additional way to identify suspicious frequencies and examine the typical variability power distribution in frequency-amplitude space, we also generated a mean periodogram from all ∼1500 objects in each σ Ori field, as seen in Fig. 2.10.

After removing from consideration targets with either no detectable variability or periodogram peaks only near integer frequency values, we performed additional analysis on the remaining light curves. All exhibited one or more peaks at the 99% significance level in the periodogram. To further probe these signals, we employed Period04 (see §1.3.2) to compute the DFT of the selected light curves. Our input light curves were shifted to zero mean and cleaned of outliers at more than 4 standard deviations. Period04 includes an option to assign weights to each data point, such that deviant points do not overly influence the determination of the periodogram. However, based on our assessment of light curve RMS as a function of magnitude we conclude that uncertainties are difficult to determine on a point-to-point basis. We believe the approach of neglecting weights but removing clear outliers is therefore sufficient to accurately identify the frequencies of variability in the sample.

For each light curve, we used Period04 to identify the largest peak in the periodogram

and extract a preliminary amplitude and phase for each epoch of observation. We then used the program to perform a non-linear least-squares fit for frequency, amplitude, and phase. A corresponding sinusoid was then subtracted from the light curve (this procedure is known as "prewhitening") and a new periodogram was produced. We examined the residuals to determine whether they contained further significant frequencies or were consistent noise. If another suspected peak appeared, the data were once again prewhitened and the original light curve subjected to a multiperiodic least-squares fit (Sperl 1998; Lenz & Breger 2005). We repeated the process until all significant Fourier components were extracted from the data. While significant harmonics appeared in cases where periodic variability was not completely sinusoidal, in no case did we identify multiple unassociated periods in a single object.

The statistical significance of identified peaks is difficult to determine directly but can be estimated from the noise properties of the periodogram. One criterion for detection of a signal to better than 99.9% certainty proposed by (Breger et al. 1993) requires S/N > 4 in the amplitude spectrum (see also Kuschnig et al. 1997). For individual periodograms, noise levels were computed from the prewhitened periodogram as a running mean over boxes of 10 cd^{-1} in frequency. We confirmed that no peaks remained at more than four times the noise baseline. As an additional check that all significant periodic components were removed from the data, we examined the light curve residuals and compared them to the typical RMS of non-variable objects with similar magnitudes (as shown in Fig. 3.8). The values were generally consistent with the noise in the non-variable targets. Errors for the derived frequencies and amplitudes were determined by running sets of 500 Monte Carlo simulations with Period04 (as described in §1.3.2) for each object displaying periodic variability. For signals that are near the detection limit, the simulations take into account the possibility that noise causes an alias to be selected instead of the true peak. This effect is included in our uncertainties listed in Table 5.1, which represent the 3-σ confidence level.

5.1.1.1 Detection limits

Knowledge of our sensitivity to light curve periodicities as a function of both amplitude and frequency is crucial to determining whether lack of variability in some objects is related to detection techniques or real physical properties. Since the signal-to-noise ratio for detection of a periodic signal in a periodogram scales as $A\sqrt{N}/(2\sigma)$ (where A is the amplitude, N is

the total number of data points, and σ is the photometric uncertainty), for long time series it is possible to detect signals with amplitudes well below the level of the uncertainties in light curves. For example, data from our 12 night CTIO observations in 2007 reach a noise level of 0.001 magnitudes in the periodogram for objects near $I = 17$, making detections as low as ~ 0.004 magnitudes (e.g., S/N = 4) possible. Red noise diminishes our ability to distinguish signals below about 5-010 cd^{-1}, or periods longer than a few hours. But across most of the frequency spectrum, sensitivity to periodicities is nearly uniform since the time sampling for both runs was uninterrupted, apart from the consistent daily gaps. We find the mean periodogram to be entirely adequate in eliminating the anomalous peaks, and because of our relatively uniform sampling do not find any deviations other than multiples of one cycle per day.

Nevertheless, to understand our ability to detect variability on longer timescales than that predicted for pulsation, we must determine the frequency dependence of our sensitivity to periodic signals, *in the presence of red noise.* We therefore measure the mean noise level at four characteristic frequencies (0.1, 1.2, 7.4, and 15.2 cd^{-1}; corresponding to periods of 10 days, 0.8 days, 3.2 hours, and 1.6 hours) at intervals of 0.5 magnitudes. The mean noise levels are determined by generating periodograms for all objects not displaying variability (as measured by an RMS within 1–σ of the median for that magnitude). We then measure the power in the periodograms at each of the four frequencies, and average together the values in 0.5 magnitude bins. Since we expect to be able to detect periodic amplitudes at four times the noise level, we have plotted these results for the σ Ori dataset, multiplied by a factor of 4.0, in Fig. 5.1. These values represent the minimum amplitude detectable in a periodic variable, as a function of period and magnitude.

In some cases, objects displayed signs of variability that were too weak to confirm. Those with unexpectedly high residual RMS but no obvious periodogram peaks were set aside for further analysis as part of the aperiodic variability group (§5.1.2). For targets with a possible peak in the periodogram just below the S/N > 4 criterion, we analyzed the light curves produced by both image subtraction and standard aperture photometry; because of the slightly different processing, occasionally a low-level signal appeared with one method but not the others. For the particularly faint BDs with photometry subject to large sky background noise, we required the peak to pass several tests for detection. First, when the putative signal is subtracted from the light curve, any other high-amplitude structure in its

immediate vicinity (e.g, within ~ 5 cd^{-1}) must also disappear. Peaks that prove difficult to remove cleanly are typical of noise. Furthermore, we look for signals with one distinct peak, as opposed to two or more of roughly equal height separated by ~ 1 cd^{-1}. Multiple peaks this close are not probable given the types of variability expected in VLMSs and BDs (e.g., one peak corresponding to the rotation period, and one or more additional peaks due to rotation of a binary companion or pulsation, for which overtones should be separated by at least 5 cd^{-1}).

The final sample of periodic variables contains 84 objects in σ Orionis and 12 objects in Cha I with clear variability by all criteria. Phased light curves for these targets are presented in Figs. 5.2 and 5.3, and their measured properties are listed in Tables 5.1 and 5.3. The majority are VLMSs with roughly sinusoidal variability. However, the shapes of 19 in σ Ori and 3 in Cha I are more characteristic of traditional pulsators or eclipsing binaries, and their blue colors are indicative of locations in the background field. For completeness, these are included in Tables 5.1 and 5.3 as well. We have also identified a small number of objects with possible but questionable periodic variability. In these cases, the RMS of the residual light curves remains significantly larger than the expected noise level after subtraction of the detected signal. Objects in this small sample may consist of either undulating noise levels or other sources of non-periodic variability and are noted as unknown variable type in Table 5.1 .
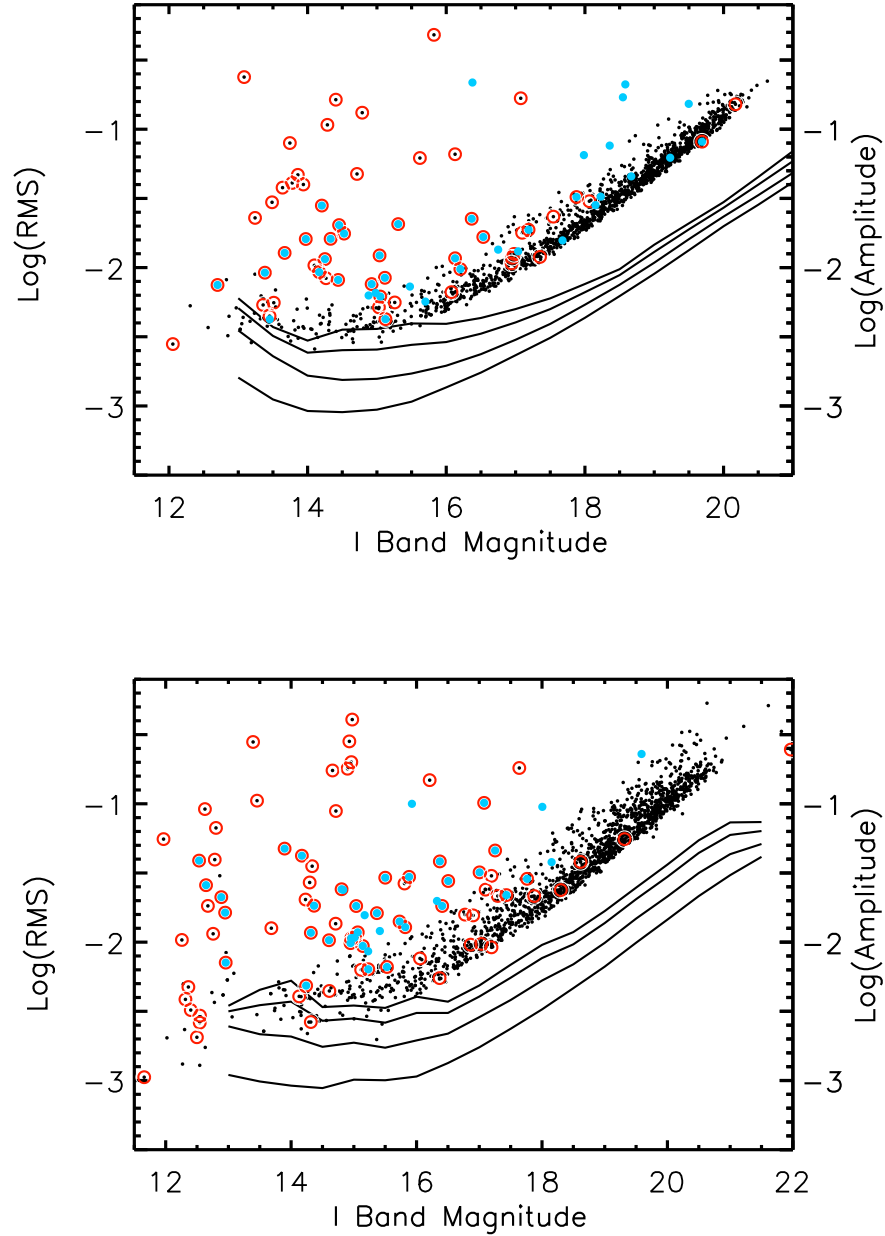
Figure 5.1 Relative to the left axis, spread in σ Ori photometry as a function of magnitude (top: 2007 data; bottom: 2008 data). Detected periodic variables are marked as blue dots, while confirmed and likely cluster members appear as red circles. Relative to the right axis, we plot the 99% sensitivity *amplitude* limit to periodic variability on four different timescales. From the top curve to bottom, these correspond to periods of 10 days, 0.8 days, 3.2 hours, and 1.6 hours. The 2007 field contains 1493 data points, while that from 2008 has 1683. Fewer objects appear at the bright end in the 2007 field because of variations in the underlying distribution of stellar magnitudes and also slightly different saturation limit.

Table 5.1. σ Ori objects with detected periodic variability

Object	Period [d]	err	Amplitude [mag]	err	Variable Type	Member?
2MASS J05372806-0236065	10.47	1.12	0.007	0.001	S	M
2MASS J05373648-0241567	0.79	0.01	0.035	0.004	S	Y
2MASS J05373784-0245442	11.52	0.20	0.021	0.001	S	M
2MASS J05373790-0236085	10.00	0.53	0.004	0.001	S	M[1]
CTIO J05373835-0243516	0.13	0.01	0.275	0.007	EB?	N
CTIO J05373954-0238446	0.61	0.01	0.036	0.006	S	N
2MASS J05374413-0235198	0.63	0.01	0.028	0.005	U	M[2]
CTIO J05374598-0238011	0.12	0.01	0.101	0.005	O	N
2MASS J05375206-0236046	2.03	0.05	0.022	0.002	U	M
2MASS J05375285-0251096	10.78	0.64	0.007	0.001	S	N
2MASS J05375404-0244407	1.90	0.02	0.010	0.001	S	M
2MASS J05375486-0241092	2.98	0.01	0.028	0.001	S	M
2MASS J05375745-0238444	0.61	0.01	0.036	0.014	U	Y
2MASS J05380055-0245097	1.28	0.01	0.025	0.001	S	Y
2MASS J05380655-0250280	0.05	0.01	0.006	0.003	S	N
2MASS J05380678-0245400	8.17	0.33	0.008	0.001	S	N
2MASS J05381265-0236378	2.31	0.06	0.023	0.005	S	M[3]
2MASS J05381330-0251329	2.58	0.03	0.017	0.001	S	Y
CTIO J05381348-0236118	2.10	0.01	0.310	0.001	EB	N
2MASS J05381367-0235385	3.64	0.01	0.450	0.001	EB	N
2MASS J05381522-0236491	9.70	0.63	0.007	0.001	S	N
2MASS J05381610-0238049	0.76	0.01	0.003	0.001	U	Y
2MASS J05381680-0246567	2.38	0.03	0.014	0.002	S	N
2MASS J05381778-0240500	2.41	0.03	0.008	0.001	U	Y
2MASS J05381824-0248143	4.47	0.05	0.013	0.001	S	Y
CTIO J05381870-0246582	0.25	0.01	0.760	0.001	EB	N
2MASS J05381886-0251388	6.62	0.09	0.038	0.002	S/U	Y
2MASS J05381949-0241224	0.11	0.01	0.275	0.026	S	N
2MASS J05382021-0238016	0.96	0.01	0.014	0.004	U	Y
CTIO J05382129-0240318	4.64	0.36	0.350	0.036	EB	N
2MASS J05382188-0241039	1.00	0.01	0.650	0.001	O	N
2MASS J05382332-0244142	0.83	0.01	0.010	0.001	S	Y
2MASS J05382354-0241317	1.71	0.01	0.017	0.001	S	Y
2MASS J05382557-0248370	0.30	0.01	0.034	0.014	S	Y
2MASS J05382750-0235041	2.70	0.02	0.021	0.001	S	Y
2MASS J05382773-0250050	10.94	1.03	0.005	0.001	S	N
2MASS J05383284-0235392	6.34	0.36	0.005	0.001	U	Y

Table 5.1—Continued

Object	Period [d]	err	Amplitude [mag]	err	Variable Type	Member?
2MASS J05383302-0239279	1.11	0.01	0.014	0.001	S	M
2MASS J05383335-0236176	4.41	0.07	0.011	0.001	U	M
2MASS J05383405-0236375	1.13	0.01	0.014	0.001	U	Y
2MASS J05383745-0250236	1.72	0.01	0.021	0.001	S	Y
2MASS J05383858-0241558	1.75	0.01	0.028	0.002	S	Y
CTIO J05390031-0237059	1.34	0.01	0.253	0.039	S	N
2MASS J05390052-0239390	3.11	0.01	0.078	0.002	S	M
2MASS J05390524-0233005	1.92	0.03	0.017	0.002	U	Y
CTIO J05390664-0238050	0.88	0.01	0.020	0.003	S	M[4]
2MASS J05390759-0228234	4.92	0.05	0.025	0.001	S	Y
2MASS J05390808-0228447	1.68	0.02	0.016	0.002	S	Y
2MASS J05390821-0232284	1.79	0.01	0.019	0.001	S	M
2MASS J05390894-0239579	2.64	0.05	0.024	0.003	U	Y
2MASS J05390988-0238164	9.62	0.59	0.123	0.010	S	N
2MASS J05391139-0233327	1.79	0.01	0.025	0.002	S	Y
2MASS J05391163-0236028	11.29	0.26	0.066	0.002	S	Y
2MASS J05391232-0230064	2.08	0.02	0.012	0.001	S	M
2MASS J05391308-0237509	1.96	0.04	0.024	0.004	U	Y
2MASS J05391346-0237391	1.42	0.01	0.009	0.001	S	M
2MASS J05391447-0228333	3.01	0.02	0.032	0.001	S	Y
2MASS J05391576-0238262	0.64	0.01	0.042	0.001	S	M
2MASS J05391582-0236507	2.55	0.02	0.034	0.002	S	Y
2MASS J05391699-0241171	2.97	0.06	0.021	0.002	U	M
2MASS J05391883-0230531	1.82	0.01	0.051	0.001	S/U	Y
2MASS J05392023-0238258	0.95	0.01	0.007	0.002	U	M
2MASS J05392097-0230334	2.92	0.04	0.036	0.003	S	Y
2MASS J05392286-0233330	7.21	0.05	0.059	0.001	S	Y
2MASS J05392435-0234013	4.73	0.15	0.005	0.001	U	M
2MASS J05392560-0238436	8.18	0.42	0.124	0.014	U	M
2MASS J05392561-0234042	3.56	0.10	0.011	0.002	U	M
2MASS J05392633-0228376	2.27	0.01	0.019	0.002	U	Y
2MASS J05393056-0238270	6.28	0.19	0.008	0.001	S	M
2MASS J05393670-0228162	0.10	0.01	2.055	0.001	EB	N
2MASS J05393759-0244304	2.24	0.01	0.035	0.002	S	Y
2MASS J05393833-0235196	1.72	0.04	0.037	0.009	U	N
2MASS J05393931-0232252	2.18	0.02	0.015	0.001	S	M
2MASS J05394433-0233027	0.90	0.01	0.050	0.002	S	Y

Table 5.1—Continued

Object	Period [d]	err	Amplitude [mag]	err	Variable Type	Member?
2MASS J05394770-0236230	0.93	0.01	0.029	0.001	S	Y
2MASS J05394799-0240320	2.76	0.01	0.065	0.001	S/U	M
2MASS J05395038-0243307	7.79	0.15	0.023	0.001	S	M
2MASS J05395056-0234137	3.17	0.02	0.023	0.001	S	Y
2MASS J05395236-0236147	0.93	0.01	0.015	0.001	S	M
2MASS J05395645-0238034	1.67	0.01	0.010	0.001	S	Y
2MASS J05395753-0232120	0.93	0.01	0.010	0.002	U	Y
2MASS J05400338-0229014	8.15	0.16	0.009	0.001	S	M
2MASS J05400453-0236421	0.76	0.01	0.027	0.010	S	Y
2MASS J05400708-0232446	1.55	0.01	0.014	0.001	S	Y

Note. — Periodic variables and their 3–σ uncertainties. We categorize variability type into several types based on light curve appearance (refer to Fig. 5.2): likely eclipsing binaries (EB), fairly sinusoidal (S), periodic but specific shape unknown due to noise or other features (U), or other distinct shape, such as that of a pulsator (O). A few stars marked "S/U" are mostly sinusoidal but have interesting blip-like features over short timescale. We consider objects to be confirmed cluster members ("yes"–Y) if they have either broad Hα in emission, Li in absorption, weak alkali absorption lines (e.g., Na), forbidden emission lines (e.g., OI, NII, SII), or infrared excess indicative of a disk, as listed in Table 4.1. Objects with only proper motions, only variability, no spectroscopic data, or conflicting membership indicators are listed as possible members ("maybe"–M). Non-member classification (N) is reserved for targets whose colors are too blue to be sufficiently young for σ Ori and whose variability type is indicative of a field eclipsing binary or pulsator. The following table entries represent new candidate cluster members based on our photometry, with our astrometrically determined coordinates listed in the object name: [1]With $I = 13.43 \pm 0.01$ and $R = 13.96 \pm 0.02$, and a simple periodic light curve, this object is a candidate σ Ori member; but since its colors fall at the blue edge of the cluster sequence, we emphasize that this is a *tentative* identification. [2]This object is a new candidate brown dwarf, with $I = 18.37 \pm 0.04$ and $R = 20.19 \pm 0.08$. [3]This object is also a new candidate brown dwarf, with $I = 18.27 \pm 0.05$ and $R = 20.25 \pm 0.08$. [4]We identify this object as a new candidate σ Ori member, with $I = 17.04 \pm 0.03$ and $R = 18.72 \pm 0.04$.

174
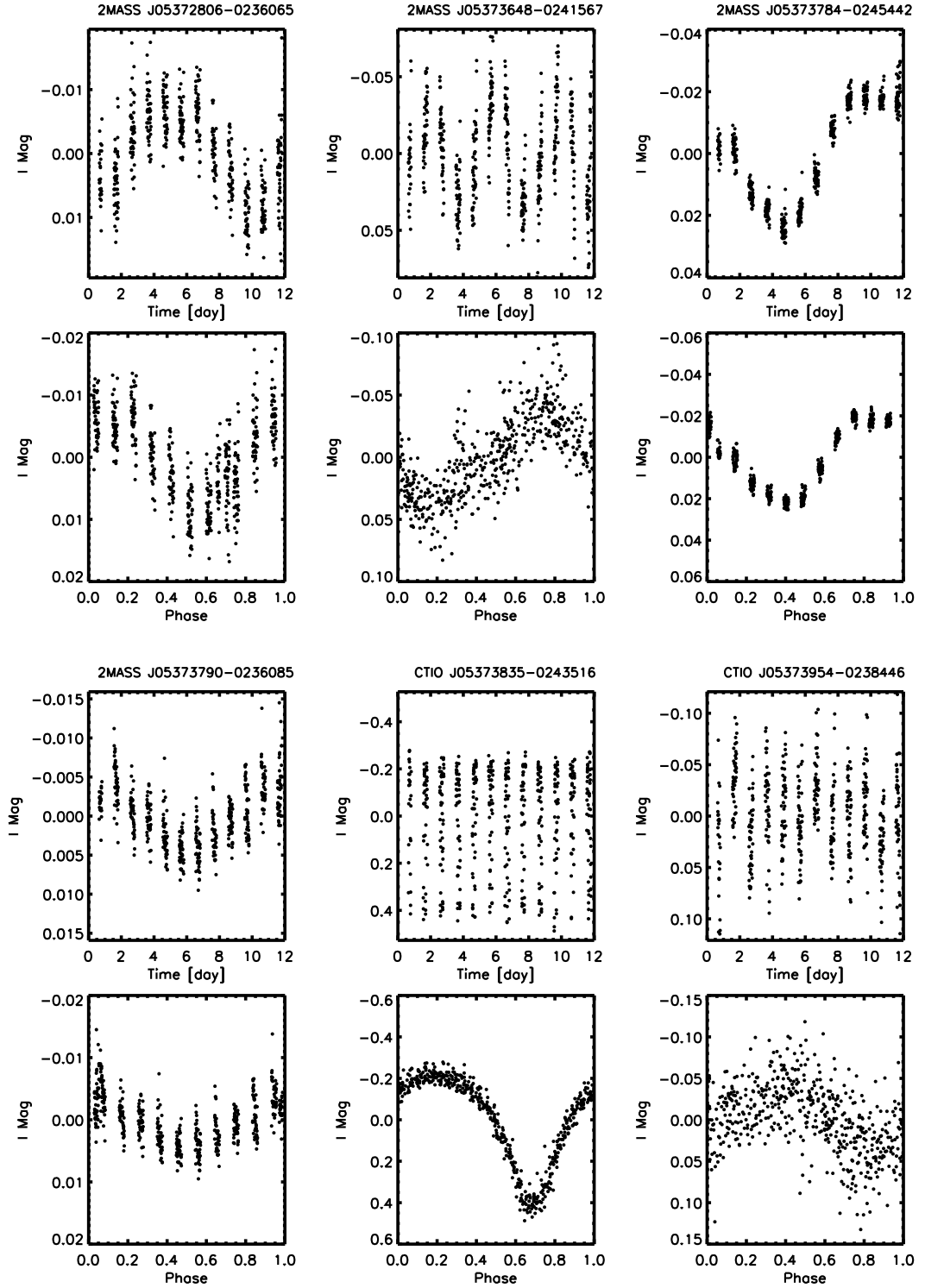
Figure 5.2 Differential σ Ori object light curves with detected periodic variability, in order of right ascension. First and third rows show the original light curve, while those in the second and fourth rows are phased to the detected period. There are also a few that are not likely cluster members; membership status is listed in Table 4.1.
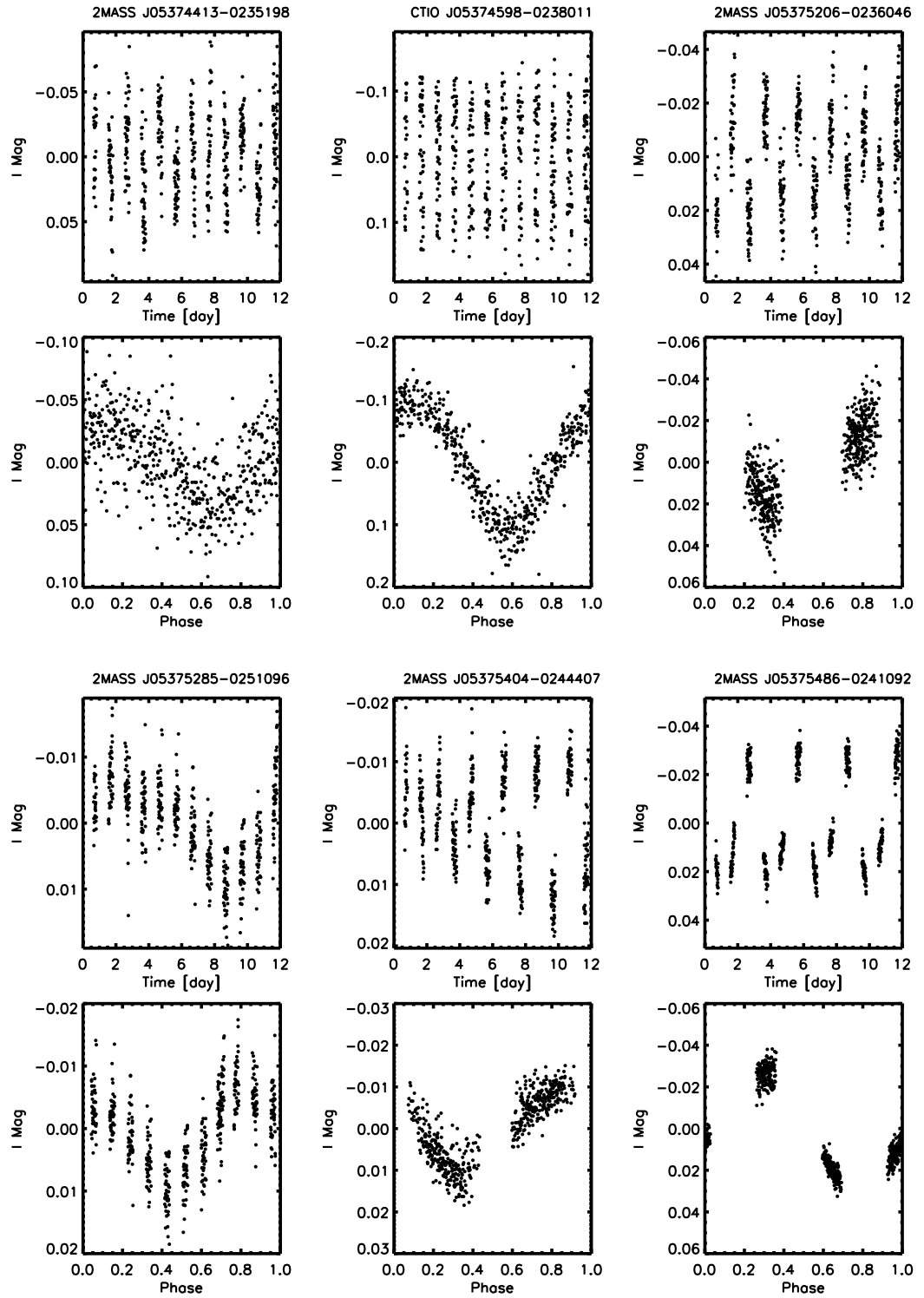
Figure 5.2 –Continued
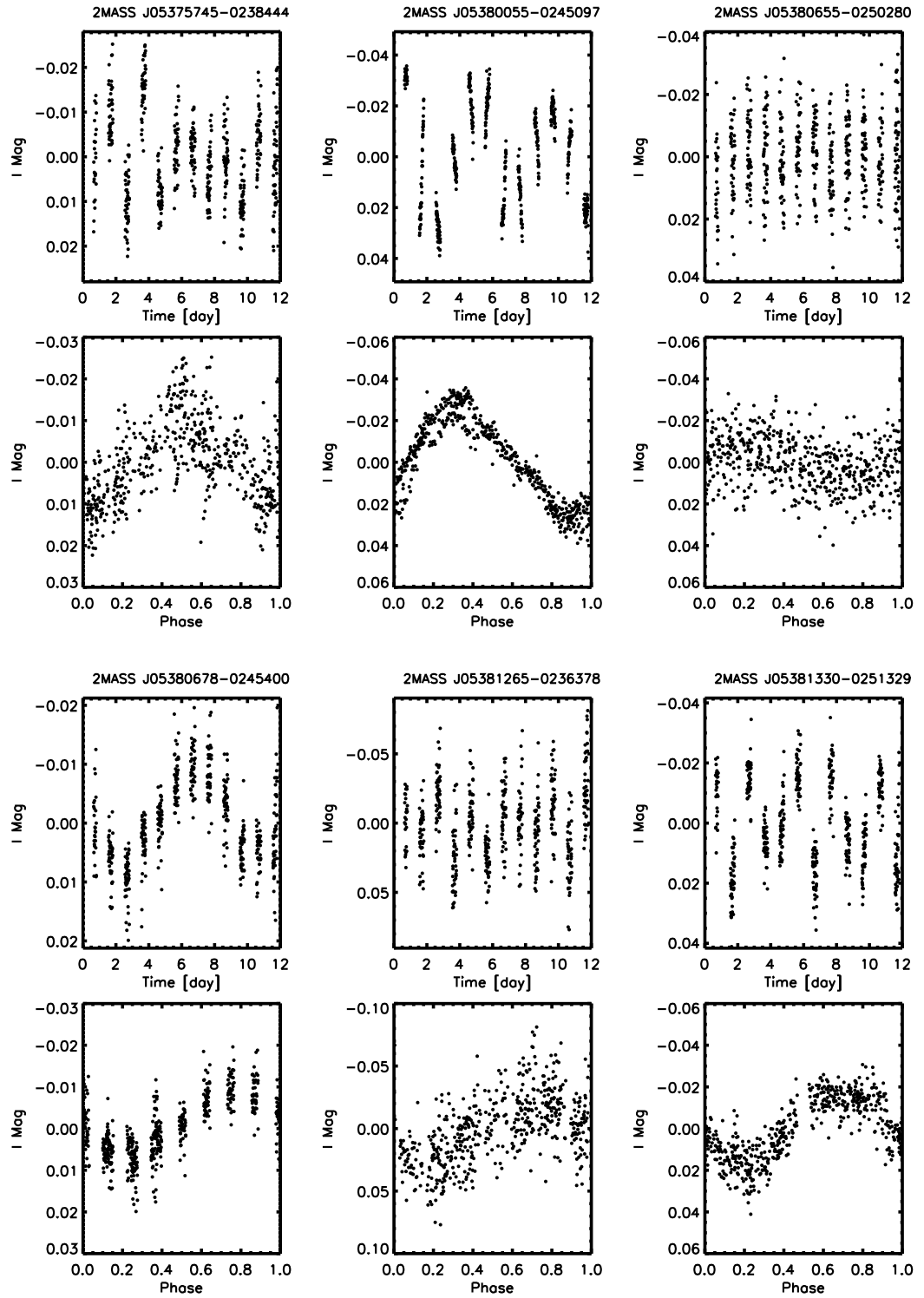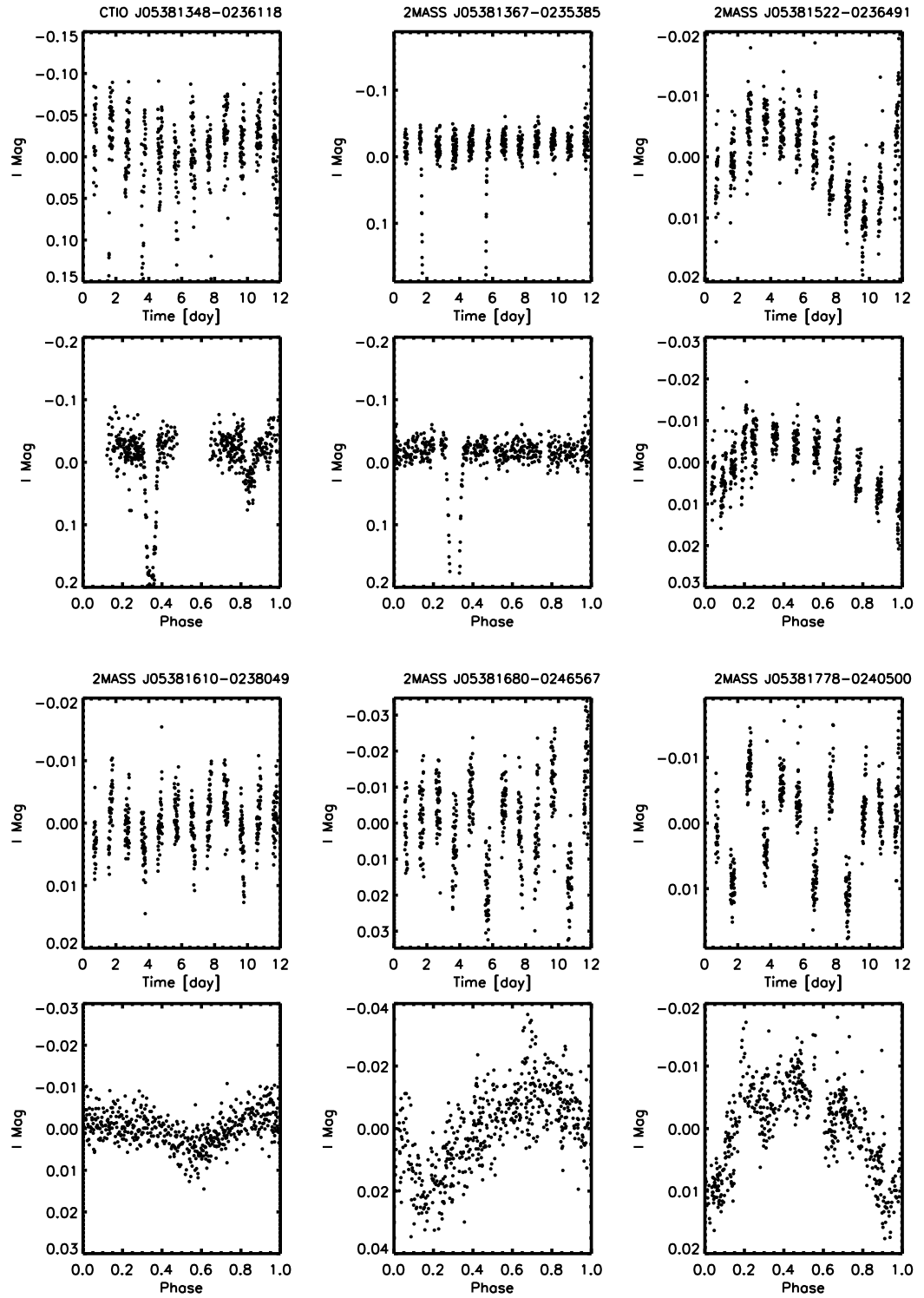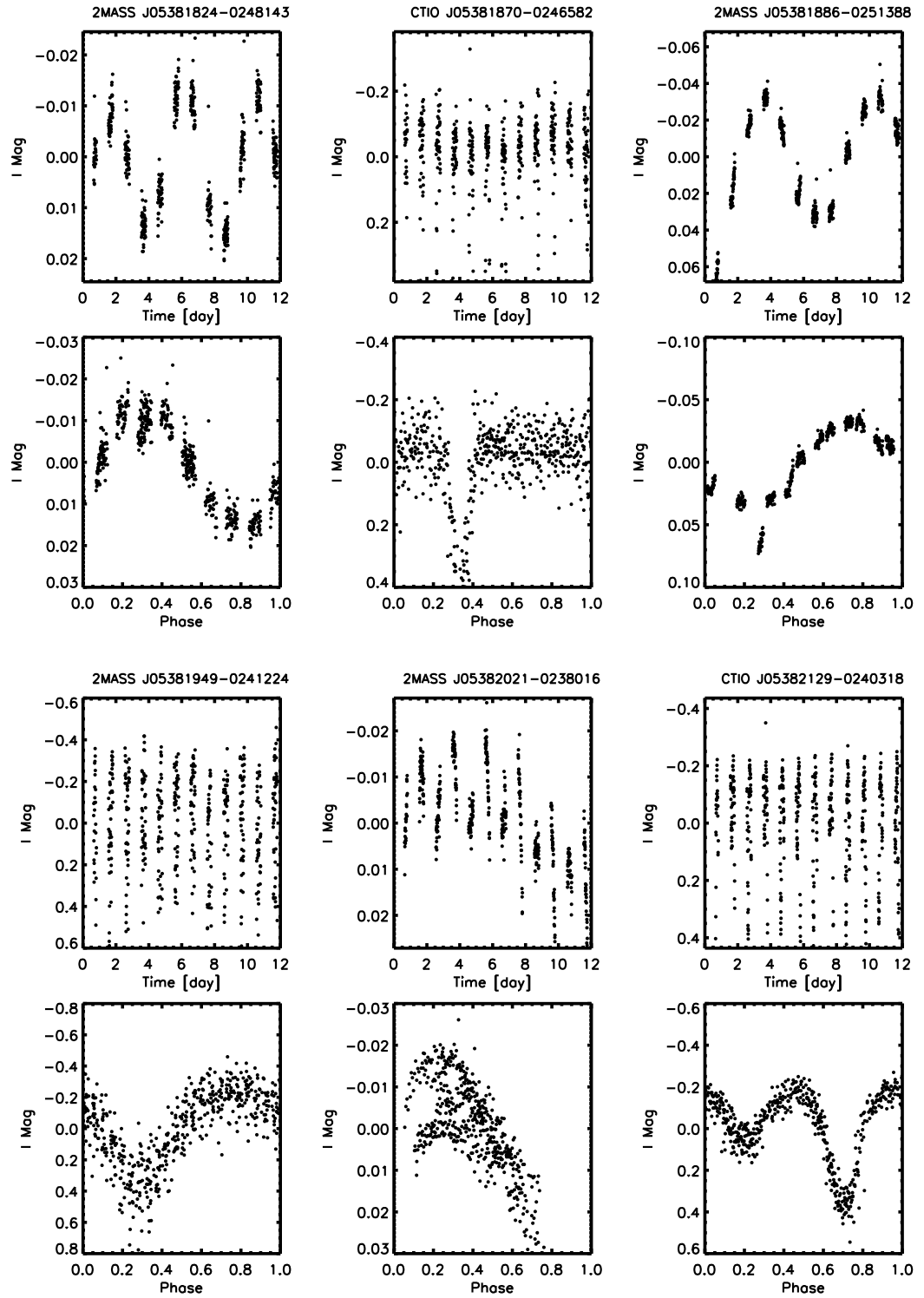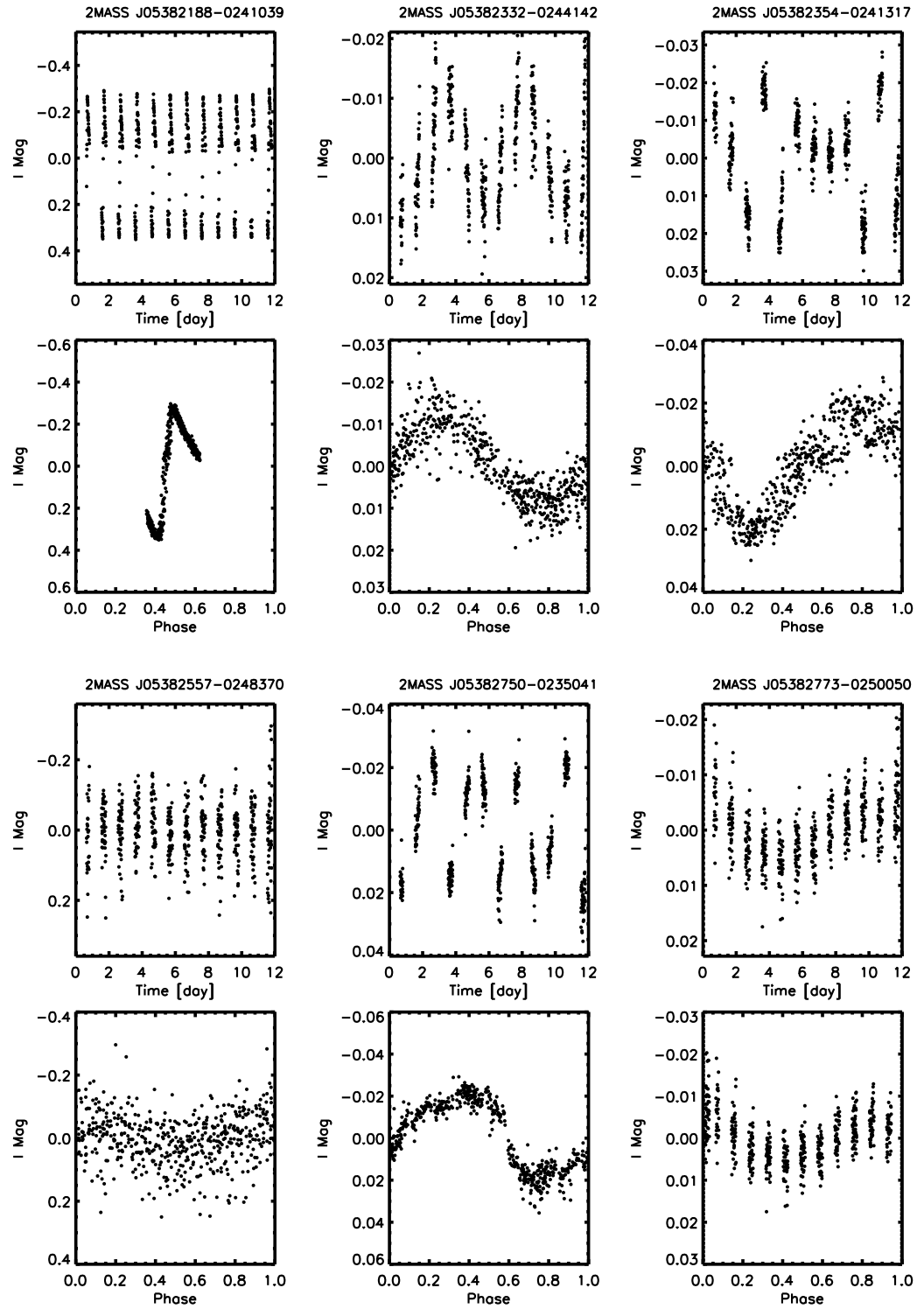
Figure 5.2 –Continued

Figure 5.2 –Continued

Figure 5.2 –Continued

Figure 5.2 –Continued

Figure 5.2 –Continued

CTIO J05390031−0237059

2MASS J05390052−0239390

2MASS J05390524−0233005

CTIO J05390664−0238050

2MASS J05390759−0228234

2MASS J05390808−0228447

Figure 5.2 –Continued

Figure 5.2 –Continued

2MASS J05391308−0237509

2MASS J05391346−0237391

2MASS J05391447−0228333

2MASS J05391576−0238262

2MASS J05391582−0236507

2MASS J05391699−0241171

Figure 5.2 –Continued

Figure 5.2 –Continued

185

Figure 5.2 –Continued

2MASS J05393931−0232252

2MASS J05394433−0233027

2MASS J05394770−0236230

2MASS J05394799−0240320

2MASS J05395038−0243307

2MASS J05395056−0234137

Figure 5.2 –Continued

187
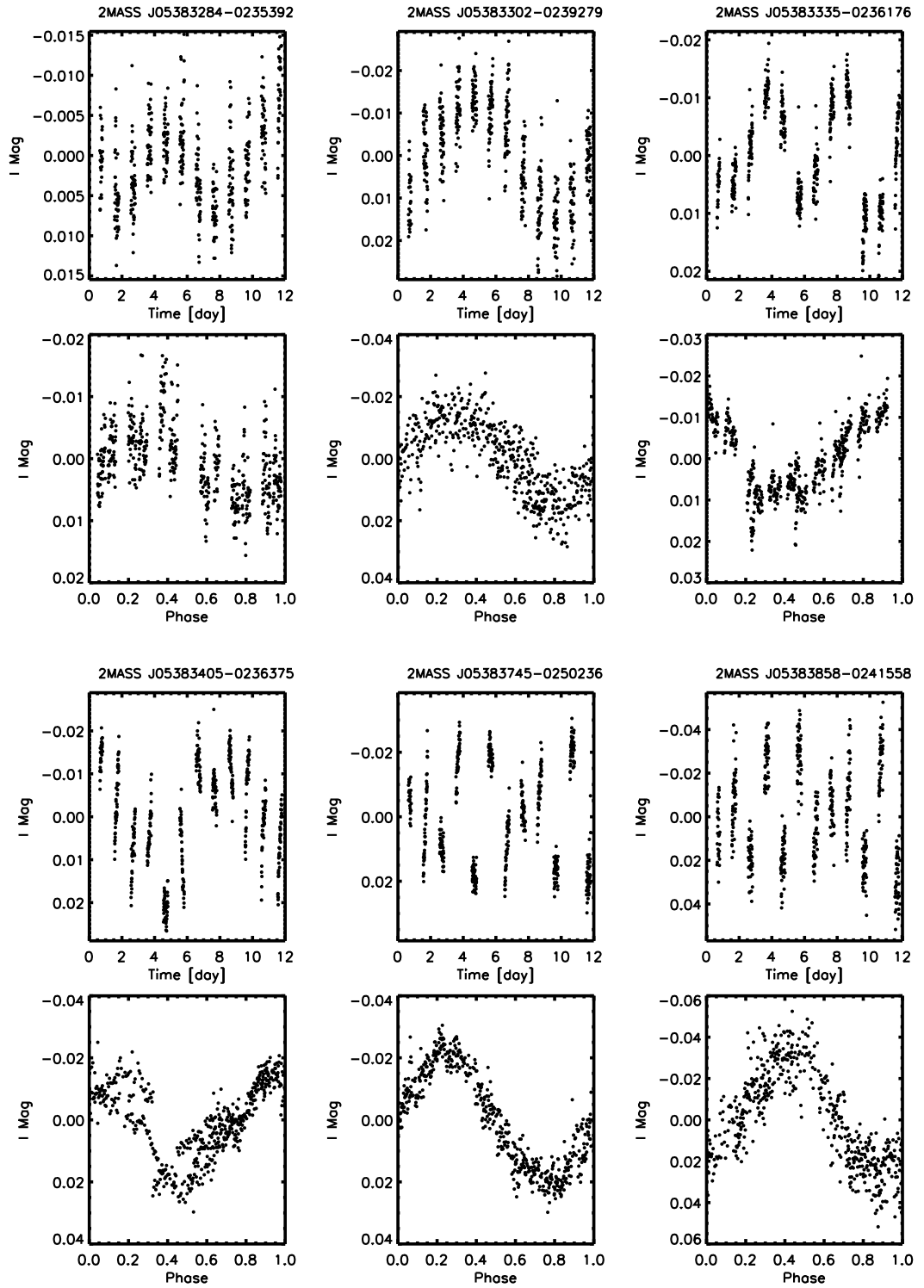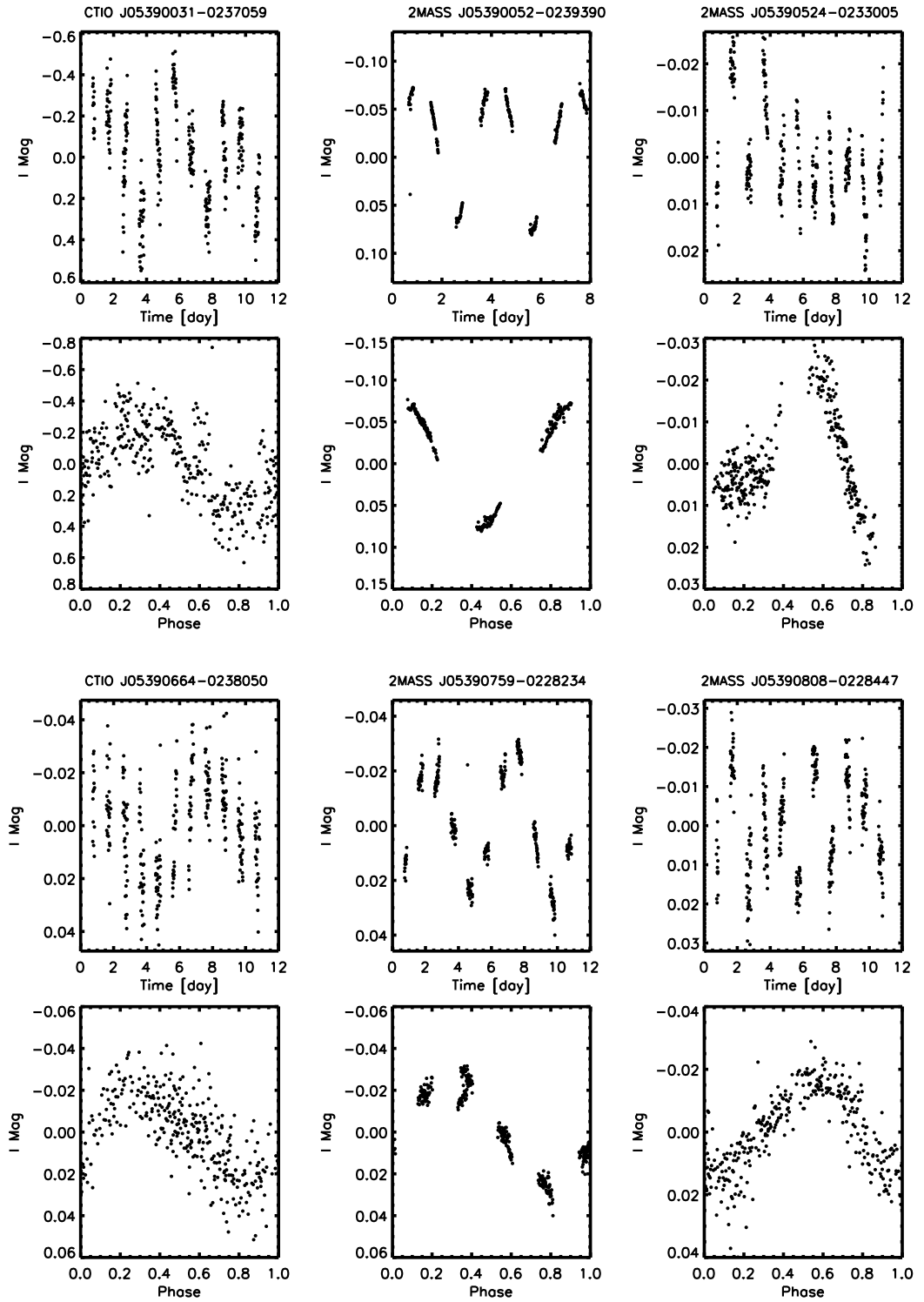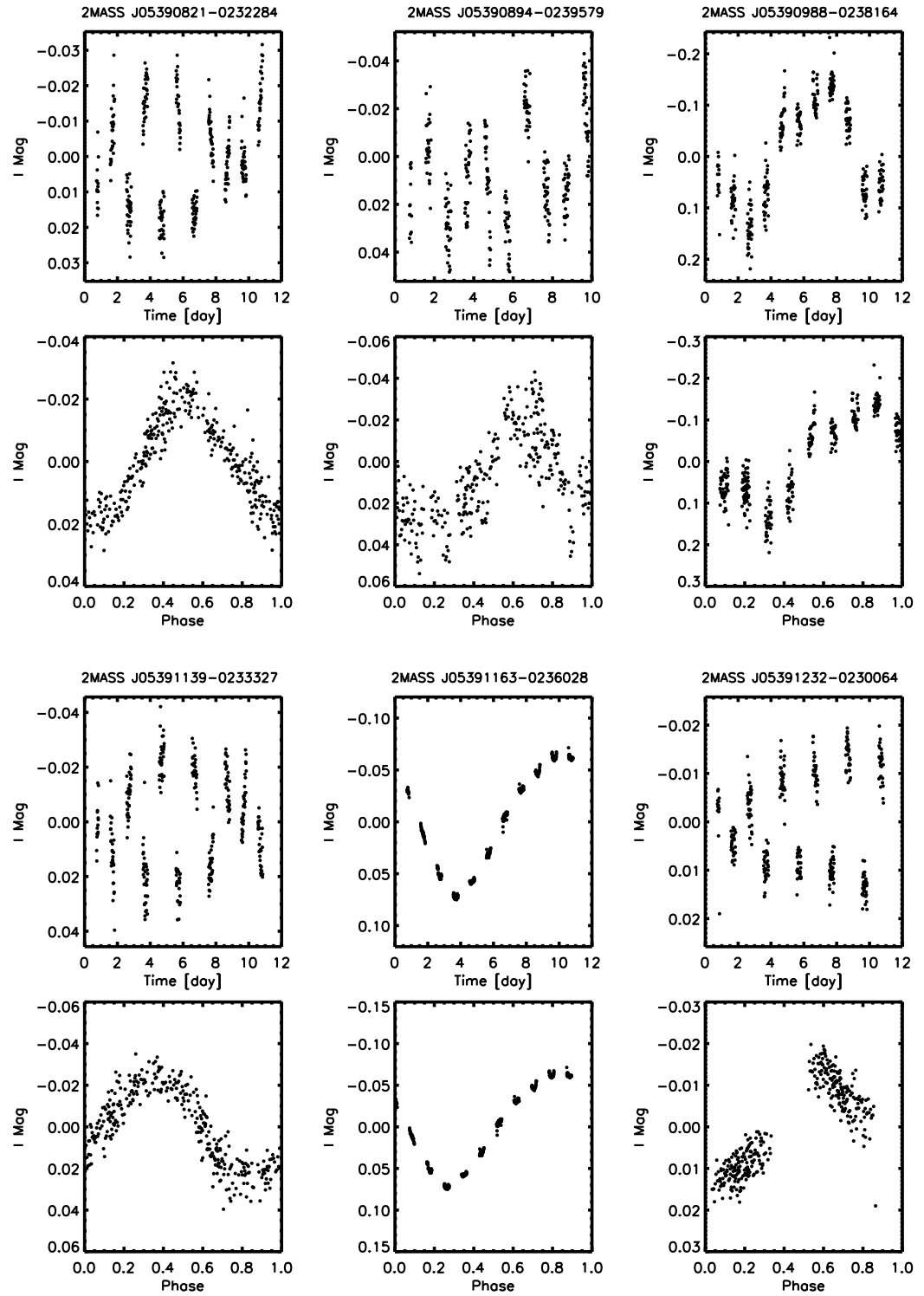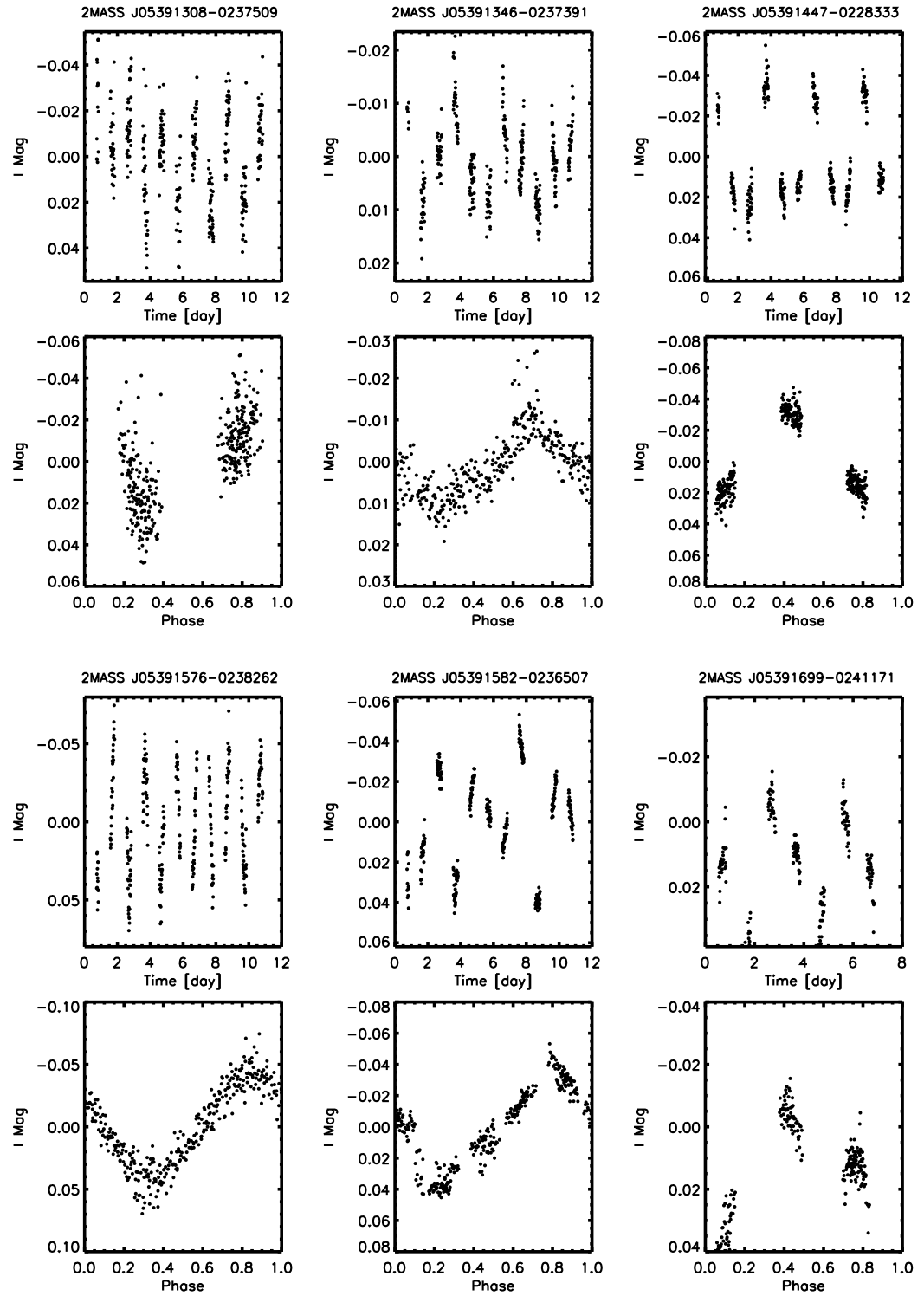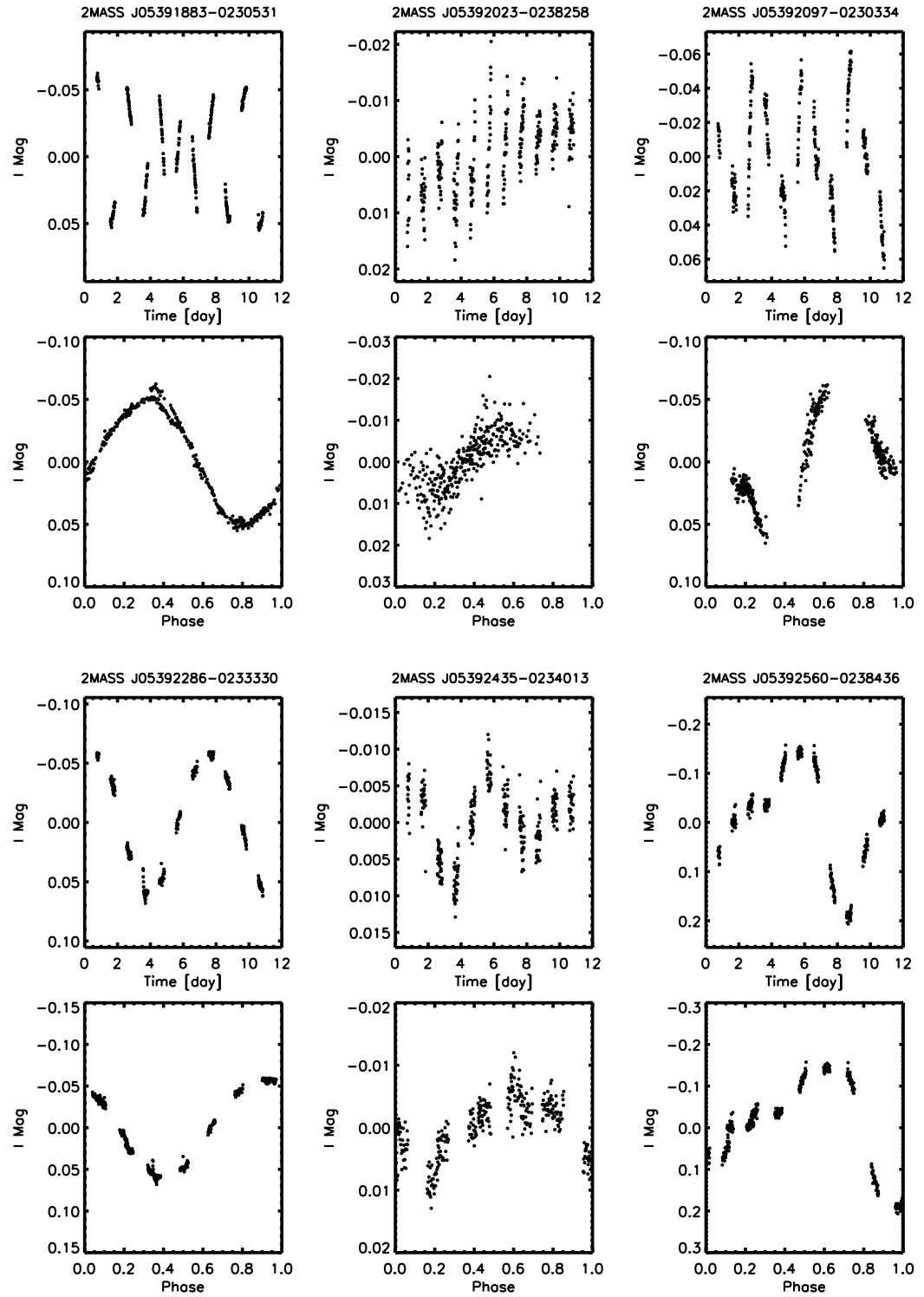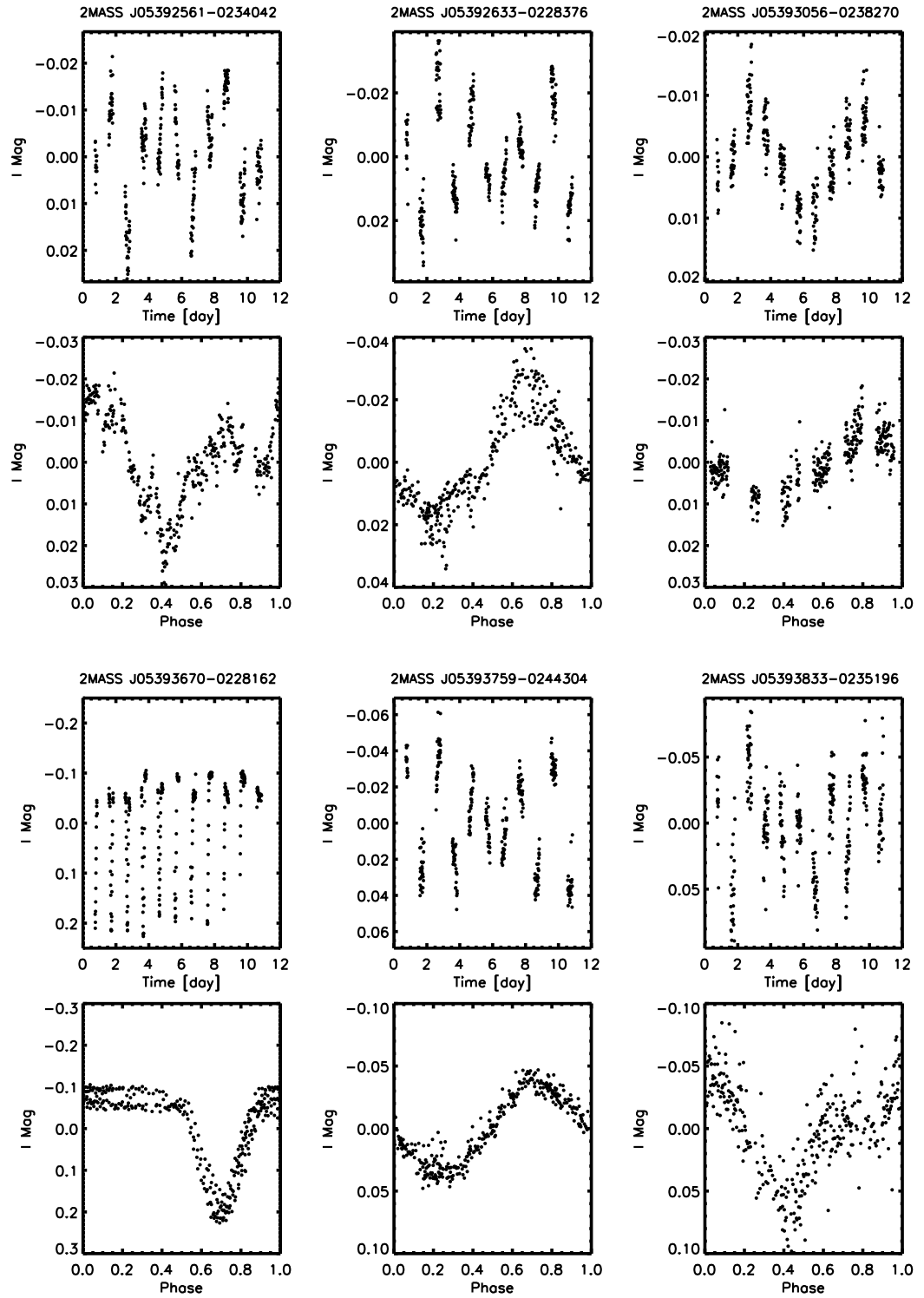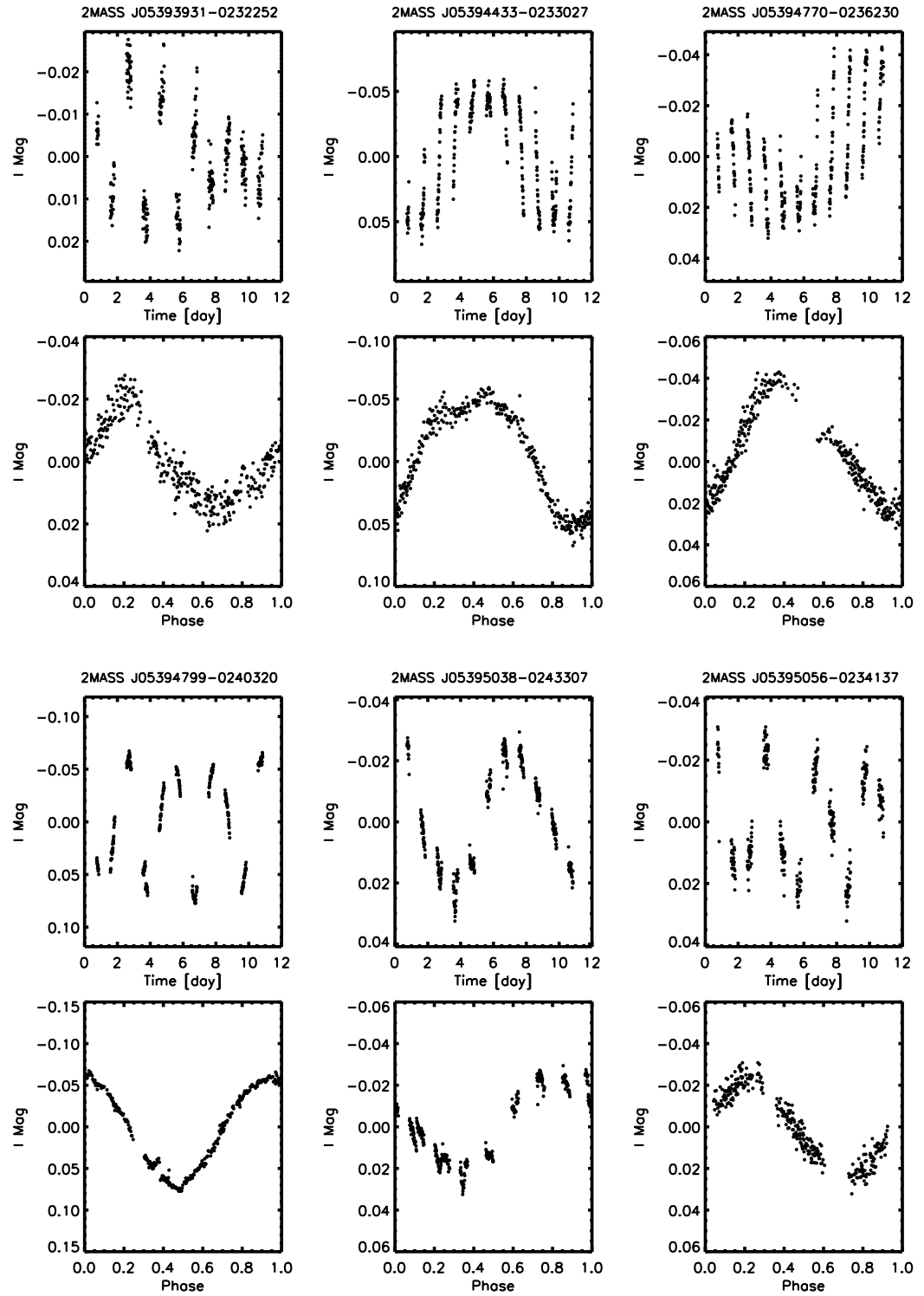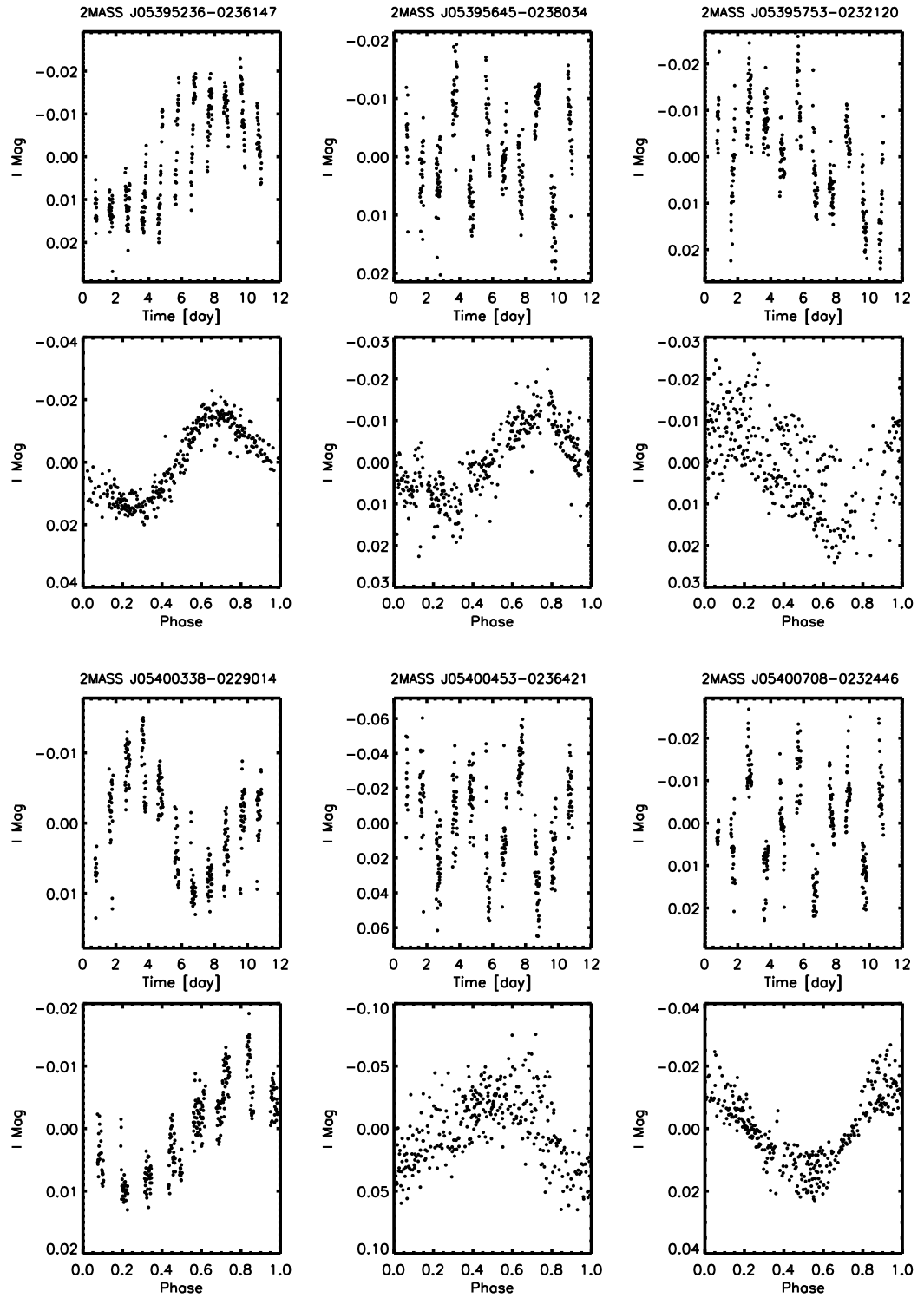
Figure 5.2 –Continued
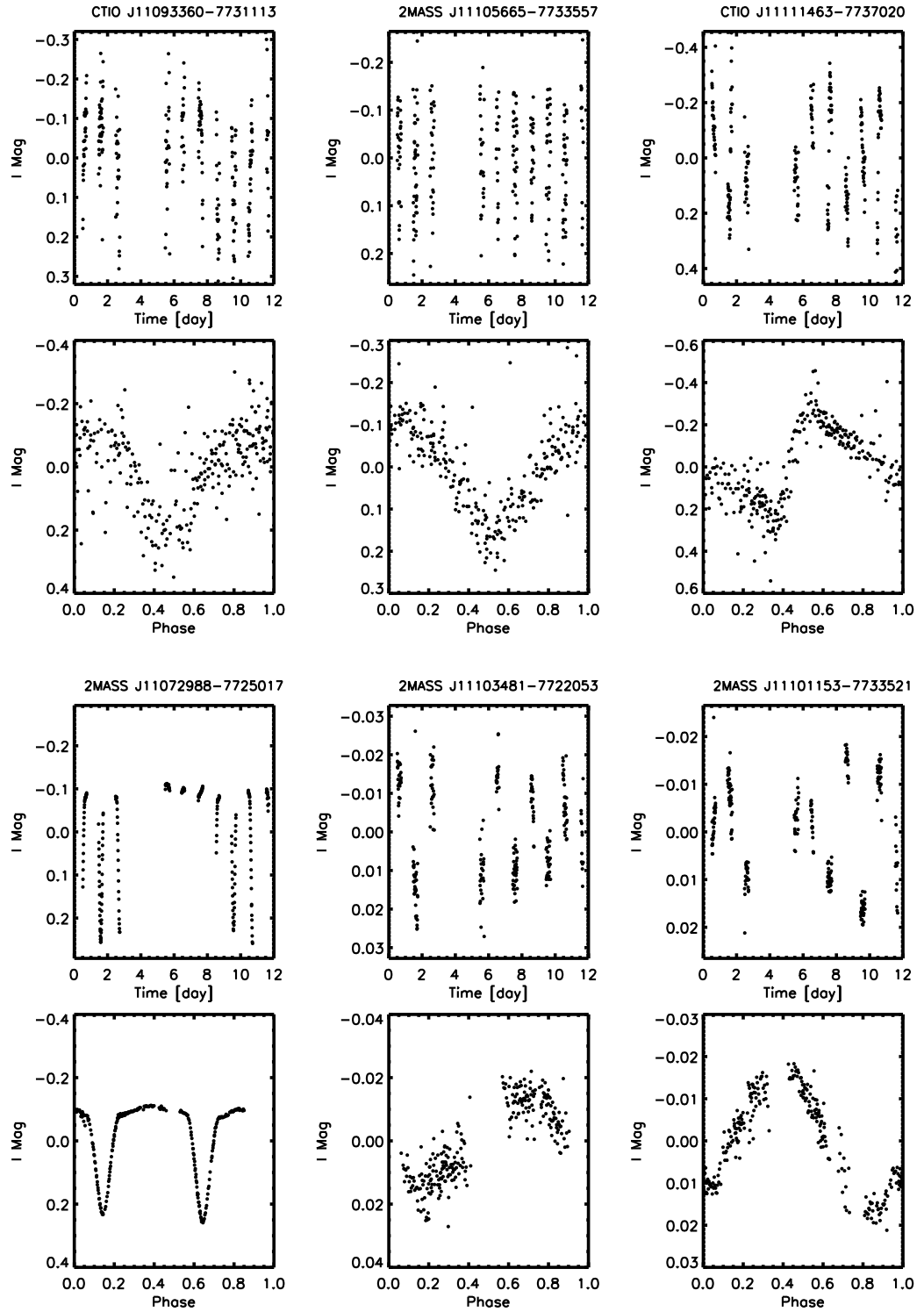
Figure 5.3 Differential Cha I object light curves with detected periodic variability, in order of right ascension. First and third rows show the original light curve, while those in the second and fourth rows are phased to the detected period. Objects without 2MASS identifications are unlikely to be cluster members; membership status is listed in Table 5.3.
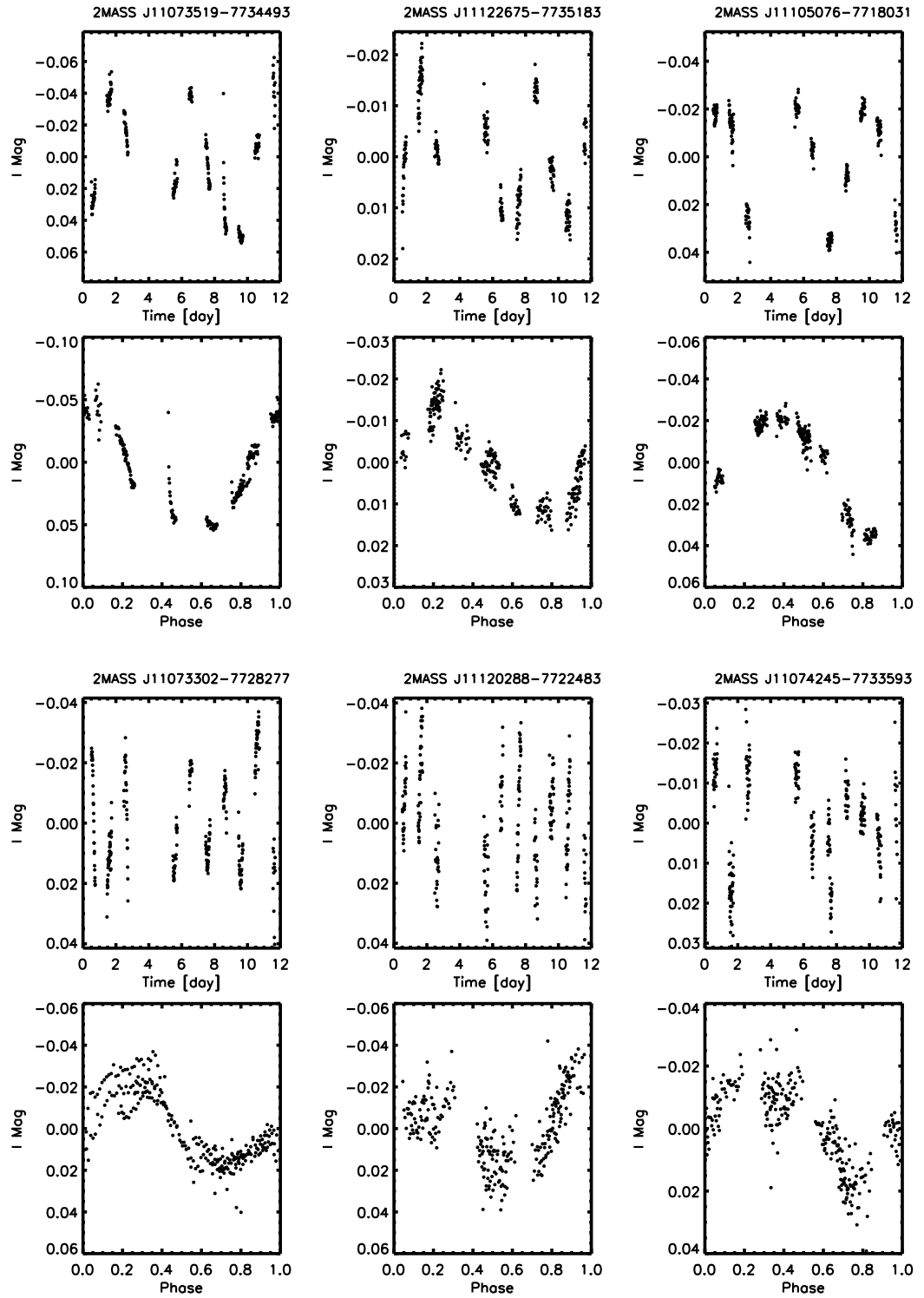
Figure 5.3 –Continued

5.1.2 Aperiodic variability detection

Past monitoring campaigns have revealed not only well-behaved periodic variability among low-mass young cluster members, but also sporadic, aperiodic brightness fluctuations likely indicative of accretion or time-variable disk extinction. While the light curves are a challenge to analyze quantitatively, their features offer clues into the mechanisms behind star-disk interaction. To fully mine our data for variables of all types, we have subjected the light curves in the σ Ori and Cha I fields to a battery of statistical tests in addition to the periodogram analysis. We examine the RMS magnitude spread for light curves of all objects in each of the three observed fields. Plots of RMS versus magnitude are standard tools for not only assessing the photometric performance, but also identifying outliers whose light curve RMS greatly exceeds the expected precision and hence suggests underlying variability. While the overall spread in light curves is well modeled by a combination of Poisson errors, sky background, and a small systematic uncertainty ($\sim$0.002 magnitudes), many outliers that were not identified through the periodogram analysis are obvious in Fig. 5.1–indicating variability of a more erratic sort.

5.1.2.1 Chi-squared analysis

To distinguish between true variables and photometric errors, we disregarded targets with photometry clearly affected by bad pixels, saturation, or close proximity to neighboring stars, as the large RMS values are due to measurement issues rather than intrinsic variability. We subjected the remaining group of objects with inexplicably large RMS to a reduced Chi-squared criterion: if the photometric uncertainty of an individual data point x_i is σ_i, then for a light curve with mean 0 and N total points, we have:

$$\chi^2 = \Sigma \frac{x_i^2}{\sigma_i^2(N-1)}.$$

In addition, the measured standard deviation of the light curve, σ, is given by:

$$\sigma^2 = \Sigma \frac{x_i^2}{(N-1)}.$$

If the individual photometric uncertainties are well represented by some typical value dependent on the object magnitude m, e.g., $\sigma_i \sim \sigma_{\text{typ}}(m)$, then we see that the reduced χ^2

criterion translates to a requirement on the standard deviation:

$$\chi^2 = \frac{\sigma^2}{\sigma_{\text{typ}}(m)^2}.$$

To detect aperiodic variables with an estimated 99% certainty, we select only light curves with $\chi^2 > 6.6$, or, equivalently, a spread of more than 2.58 times the photometric uncertainty. These values are approximate, since the noise is not strictly Gaussian, as assumed by the statistics. We estimated typical photometric uncertainties by performing a median fit as follows to the RMS as a function of magnitude using the combined Poisson, sky, and systematic noise model: The values of all three noise sources were fixed (as a function of magnitude) according to the noise model components derived in §4.2. A constant was then added to the model and adjusted such that half of the RMS light curve values lay above the model, and half lay below. The detected periodic variables as well as all 3-σ outliers were rejected, and the fitting process was iterated until the median-fit function did not change. The variability detection cut-off was then taken to be the median fit, raised by a factor of 2.58. These curves are superimposed on the data in Fig. 5.4.

Like the periodic variability search, the excess RMS analysis was conducted on all objects in the σ Ori and Cha I FOVs with available photometry, irrespective of cluster membership status. After selection of probable variables via the χ^2 criterion, we overplotted in Fig. 5.4 those confirmed or likely to be members. It is evident that the vast majority of high-amplitude variables in our fields are known σ Ori members, and the remainder are therefore good candidates. Objects exhibiting large RMS light curve spreads but not shown as variables (green dots) in Fig. 5.4 were already found to be periodic (e.g., §5) and displayed instead in Fig. 5.1. Quite a few of the identified *periodic* variables lie below the χ^2 detection threshold, indicating the power of the periodogram for identification of variability isolated to specific frequencies. In addition to the χ^2 test, we probed all light curves for variability by calculating the single-band Stetson index (e.g., Stetson 1996), which is a measure of the degree of correlation between successive data points. The distribution of Stetson index as a function of magnitude was fairly tight, such that the number of variables selected was relatively insensitive to the threshold chosen for variability detection. While this test confirmed all cases of aperiodic variability uncovered with the χ^2 criterion, and a number of the previously identified periodic variables, it did not reveal any additional
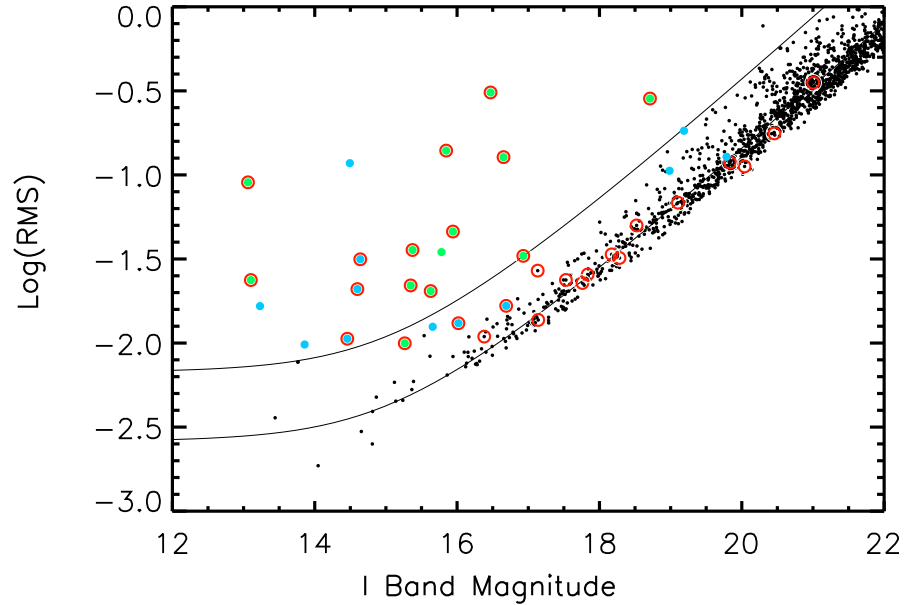
Figure 5.4 RMS spread of light curves for periodic (blue) and aperiodic (green) variables in Cha I. Confirmed cluster members appear as red circles. We plot the estimated total contributions from Poisson, mean sky level, and systematic noise, shifted upward by 0.24 dex so as to match the median of the data (solid line). The curve corresponding to 99% probability of variability detection via the χ^2 test appears above this.

variable objects. This result may reflect a large typical intrinsic light curve scatter for the aperiodic variables in our sample.

In total, we identified 42 aperiodic variables in σ Ori and 13 in Cha I, as listed in Tables 5.2 and 5.3, and shown in Figs. 5.4 and 5.5. In order to explore the relationship between erratic variability and the presence of disks and accretion, we have noted the objects in Table 4.1 with observed infrared or near-infrared excess, and also provide the Hα equivalent width where available in Table 5.2; in §5.5.4 we discuss the correspondence between these quantities.
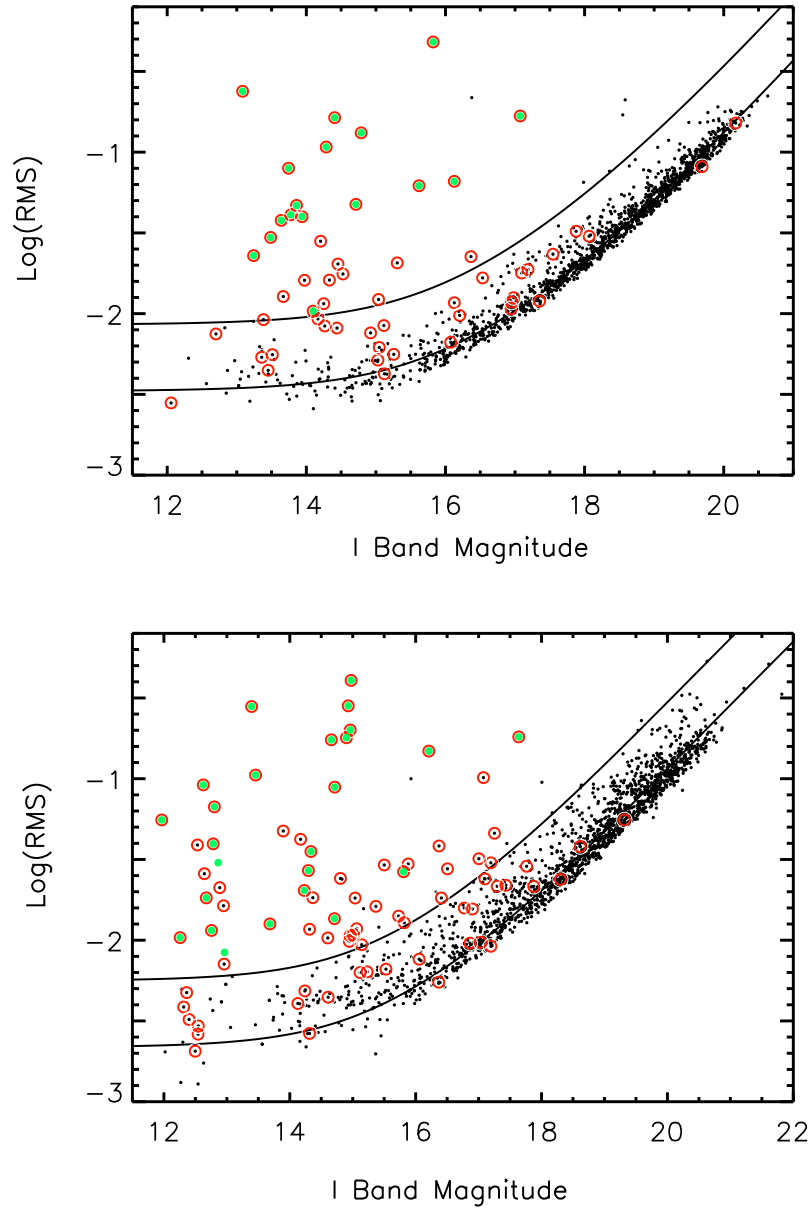
Figure 5.5 Same as Figure 5.1, except now showing σ Ori aperiodic variables in green. We plot the estimated total contributions from Poisson, sky, and systematic noise, shifted upward by 0.12 dex so as to match the median of the data (solid line). The curve corresponding to 99% probability of variability detection via the χ^2 test appears above this.
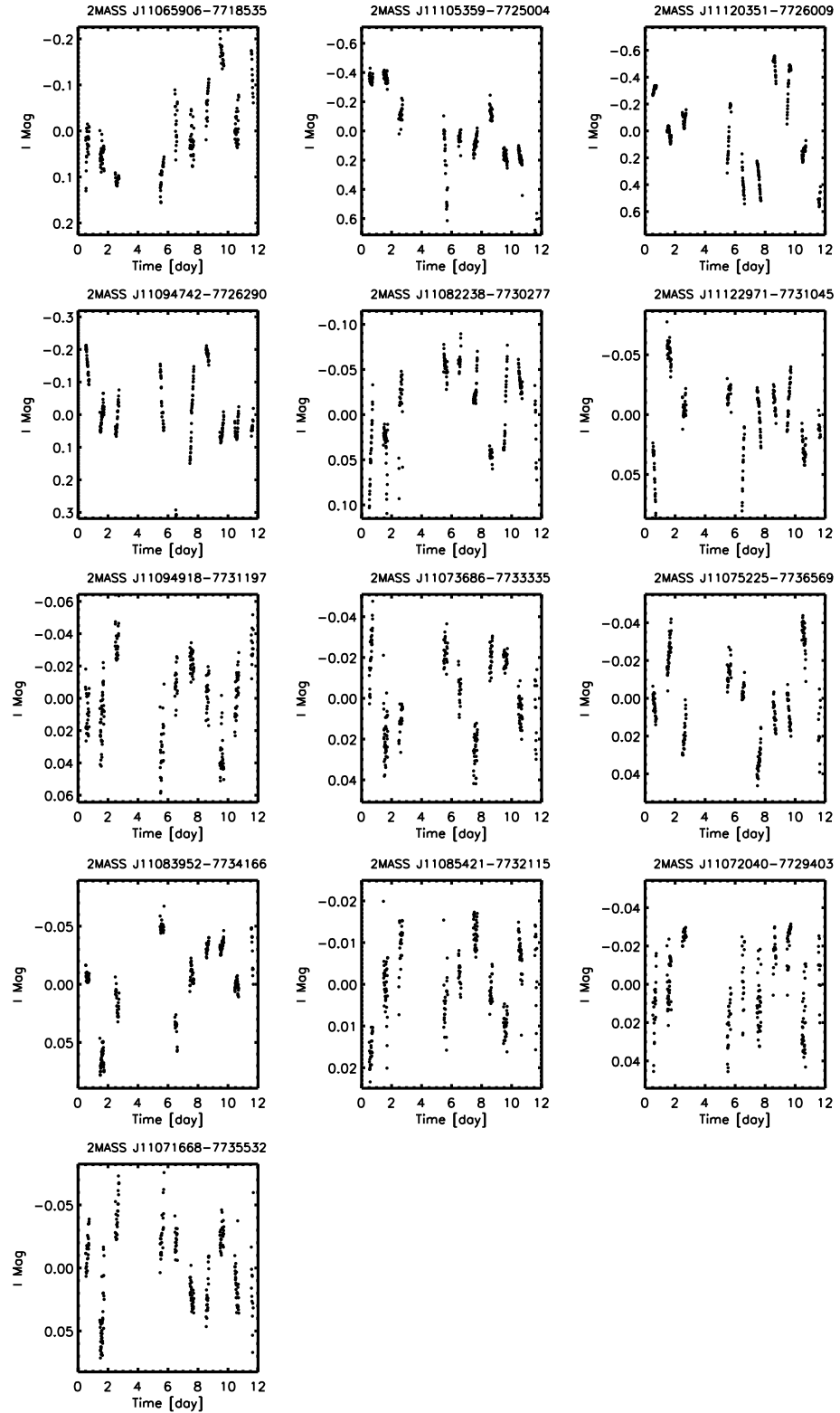
Figure 5.6 Cha I light curves selected as aperiodic based on large χ^2 values and lack of periodicities. Objects are arranged in order of right ascension, and membership information is available in Table 4.4.
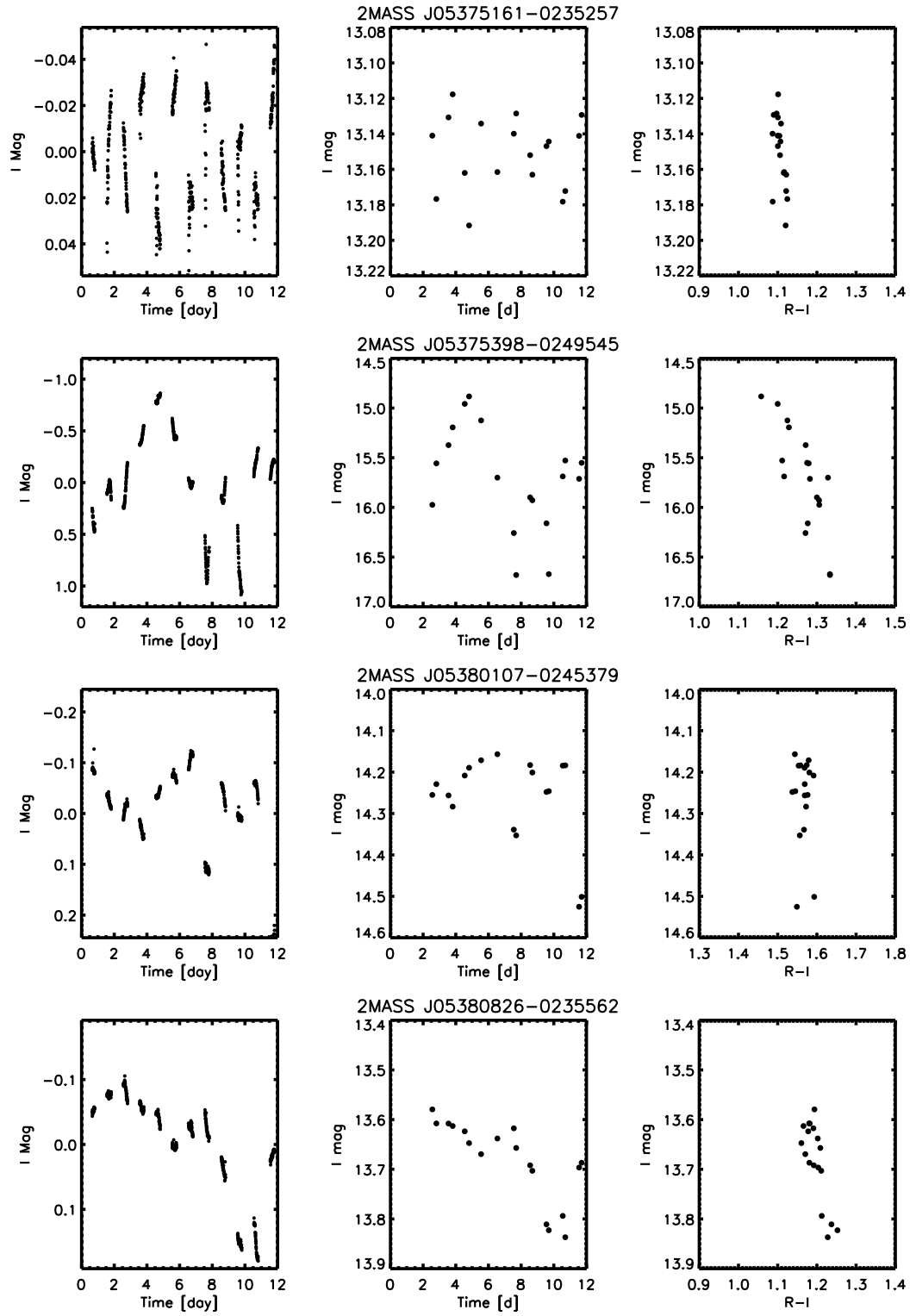
Figure 5.7 σ Ori light curves selected as aperiodic based on large χ^2 values and lack of periodicities. Objects are arranged in order of right ascension, and membership information is available in Table 4.1. The left column displays the full I-band light curves, while the middle shows the same data at the reduced cadence corresponding to the R-band observations. The right column shows R-I color trends.
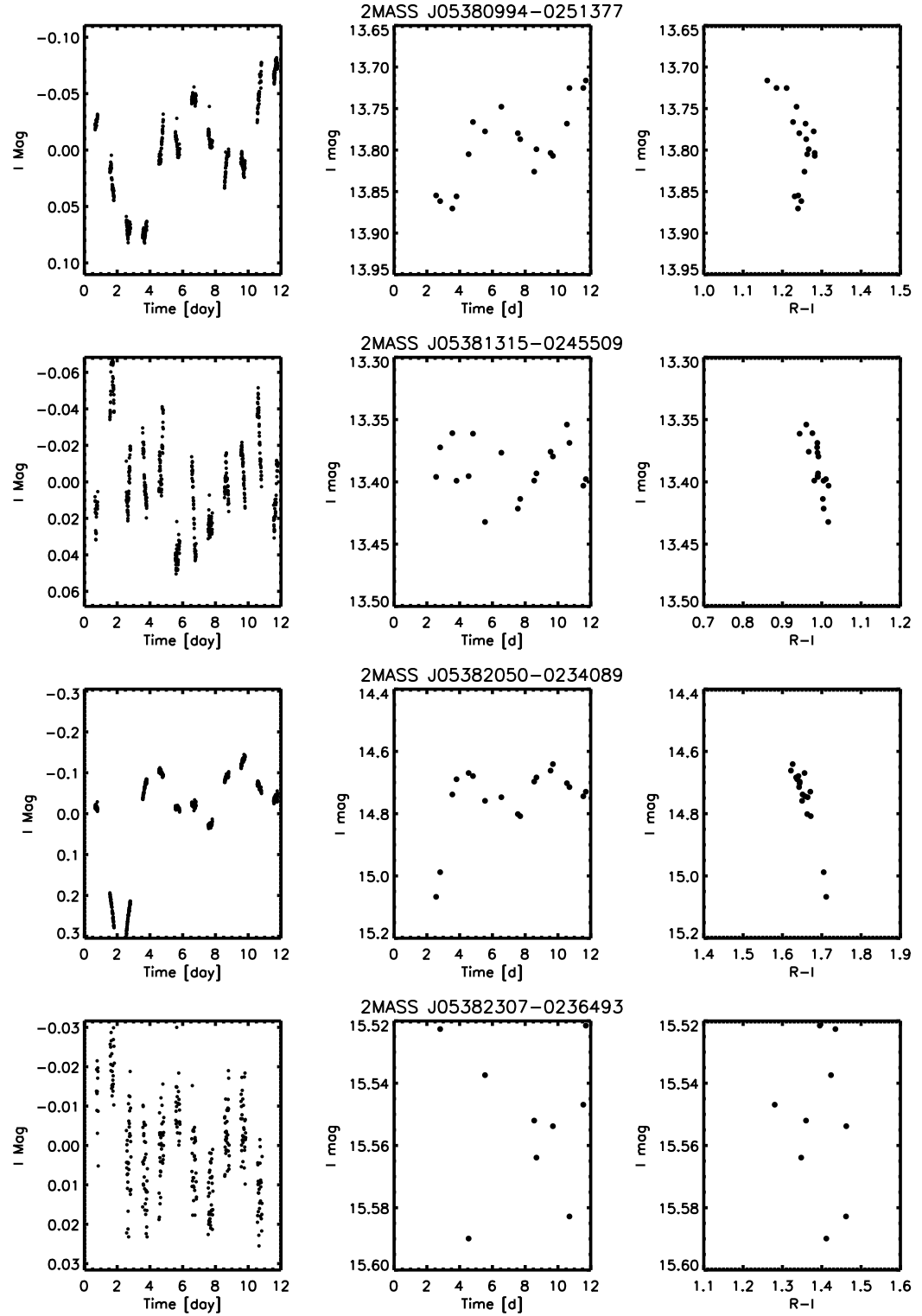
Figure 5.7 –Continued
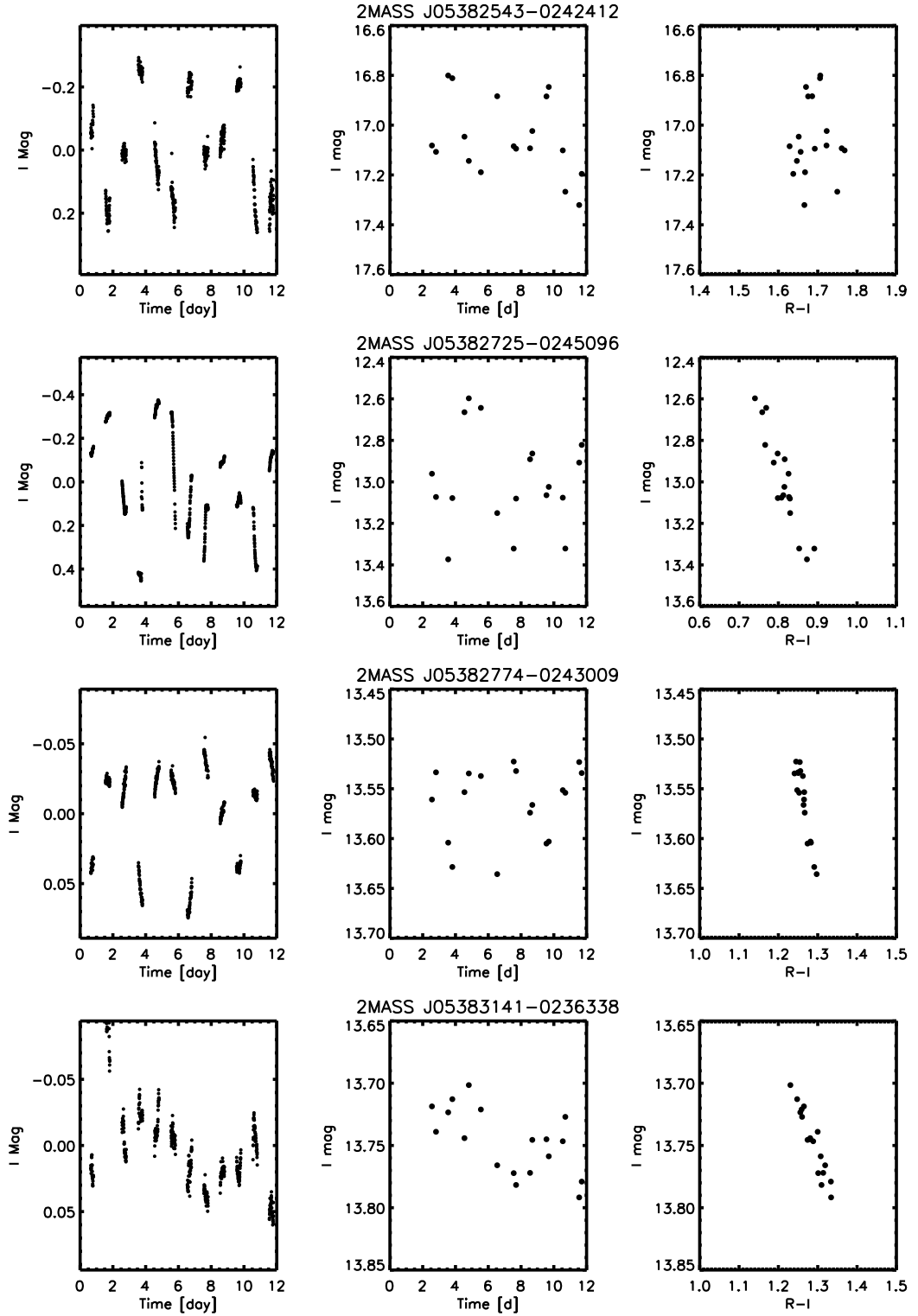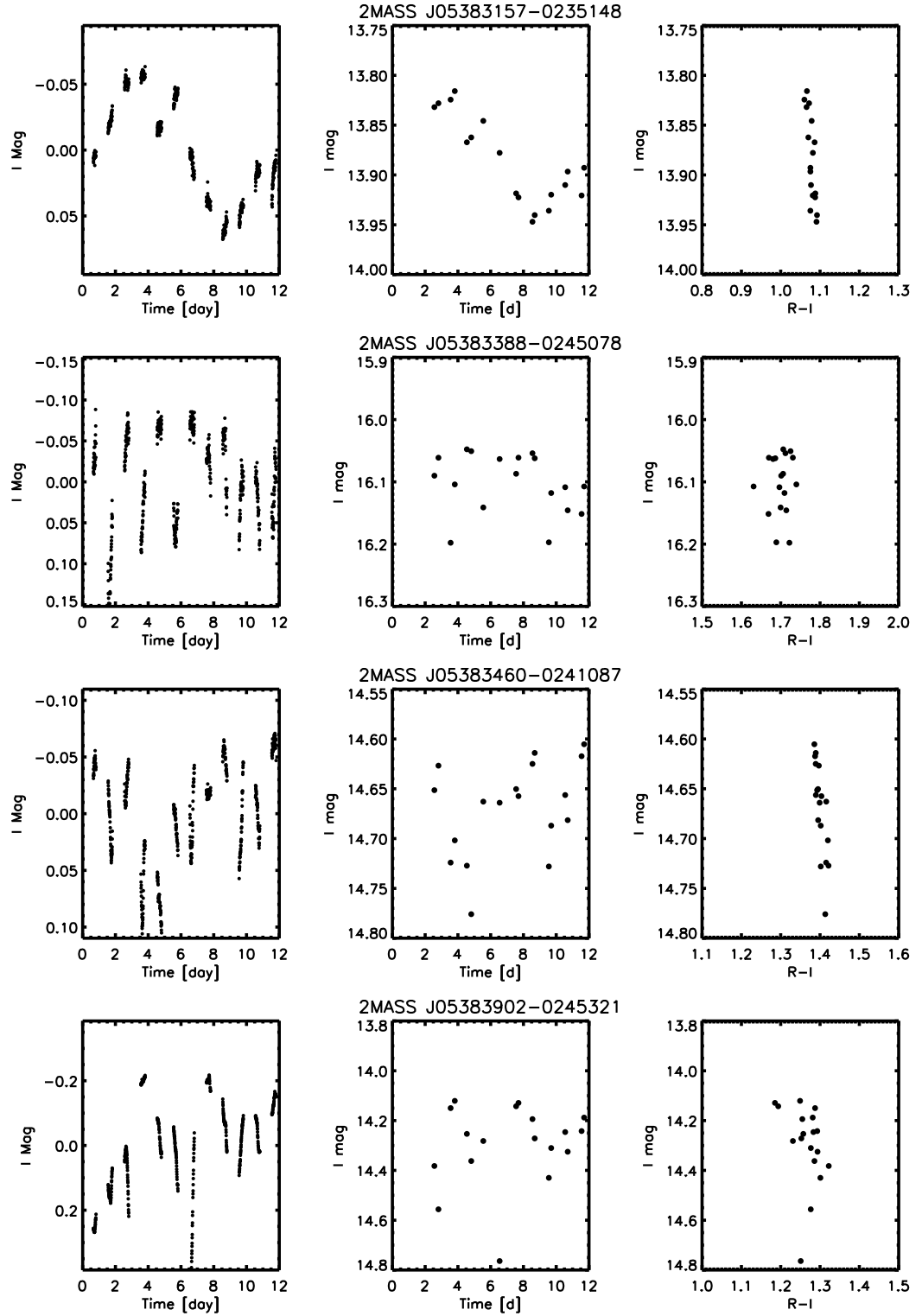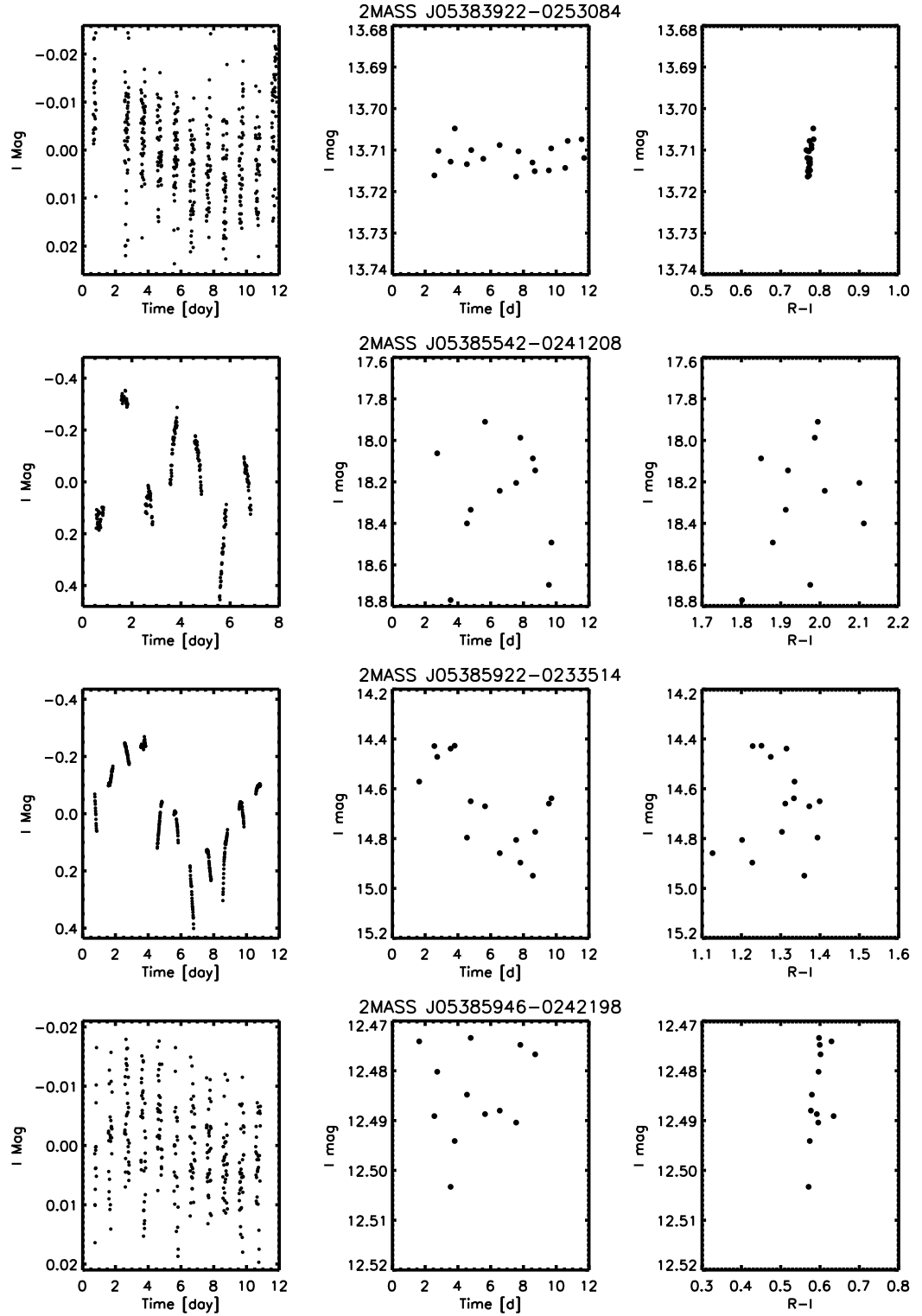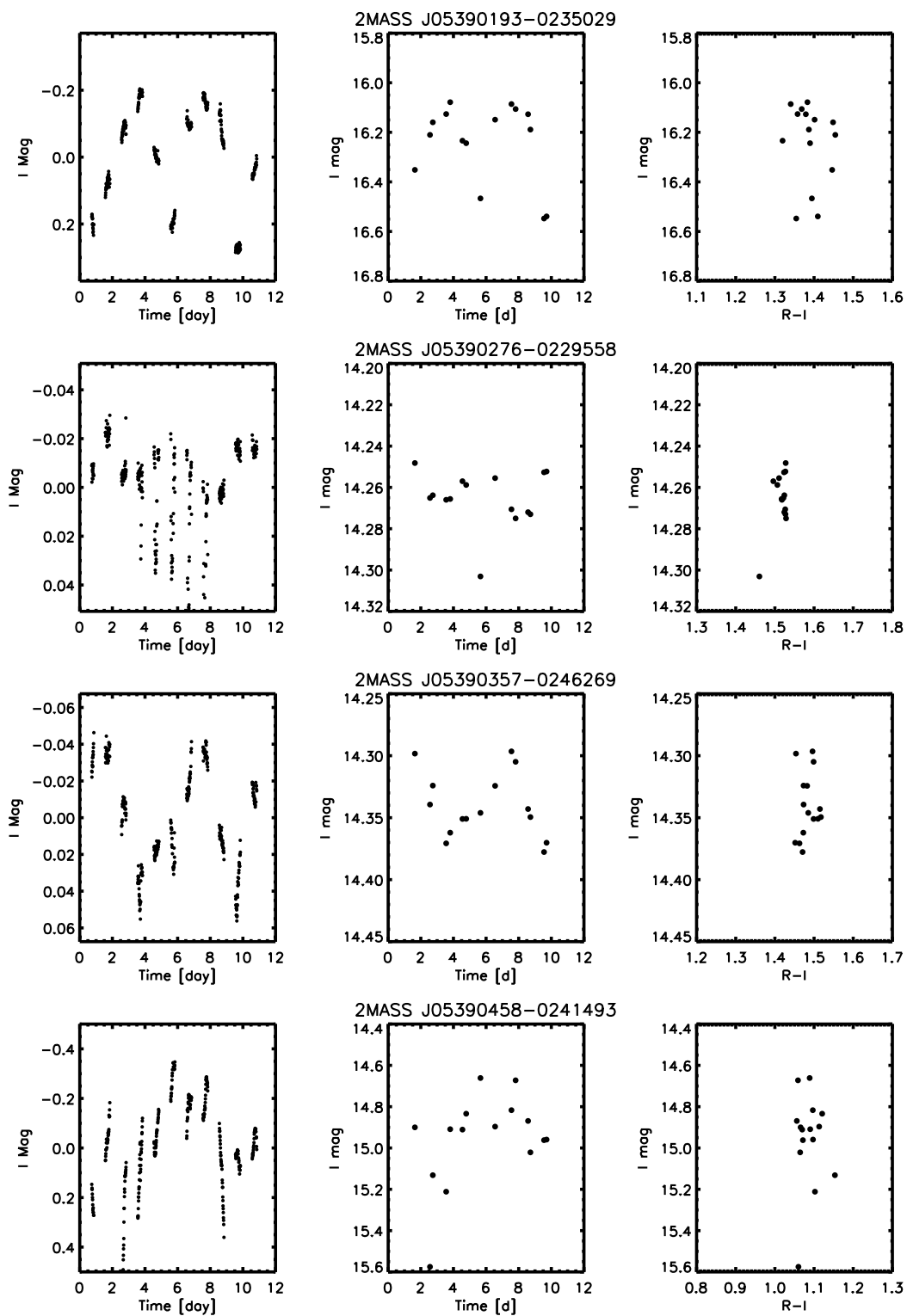
197

Figure 5.7 –Continued

Figure 5.7 –Continued

Figure 5.7 –Continued

200

2MASS J05390193−0235029

2MASS J05390276−0229558

2MASS J05390357−0246269

2MASS J05390458−0241493

Figure 5.7 –Continued

Figure 5.7 –Continued

2MASS J05392307−0228112

2MASS J05392519−0238220

2MASS J05392677−0242583

2MASS J05393982−0231217

Figure 5.7 –Continued

203
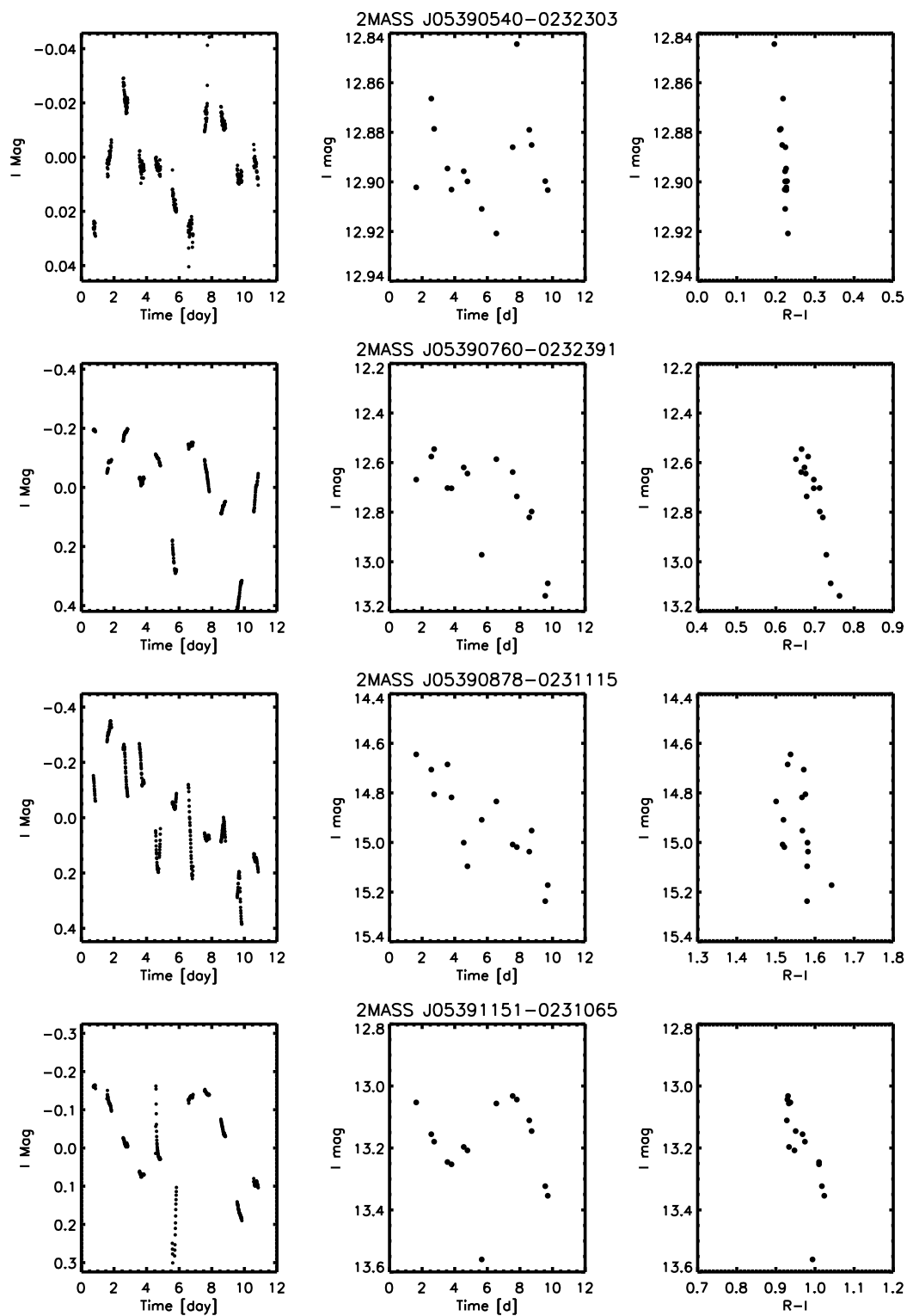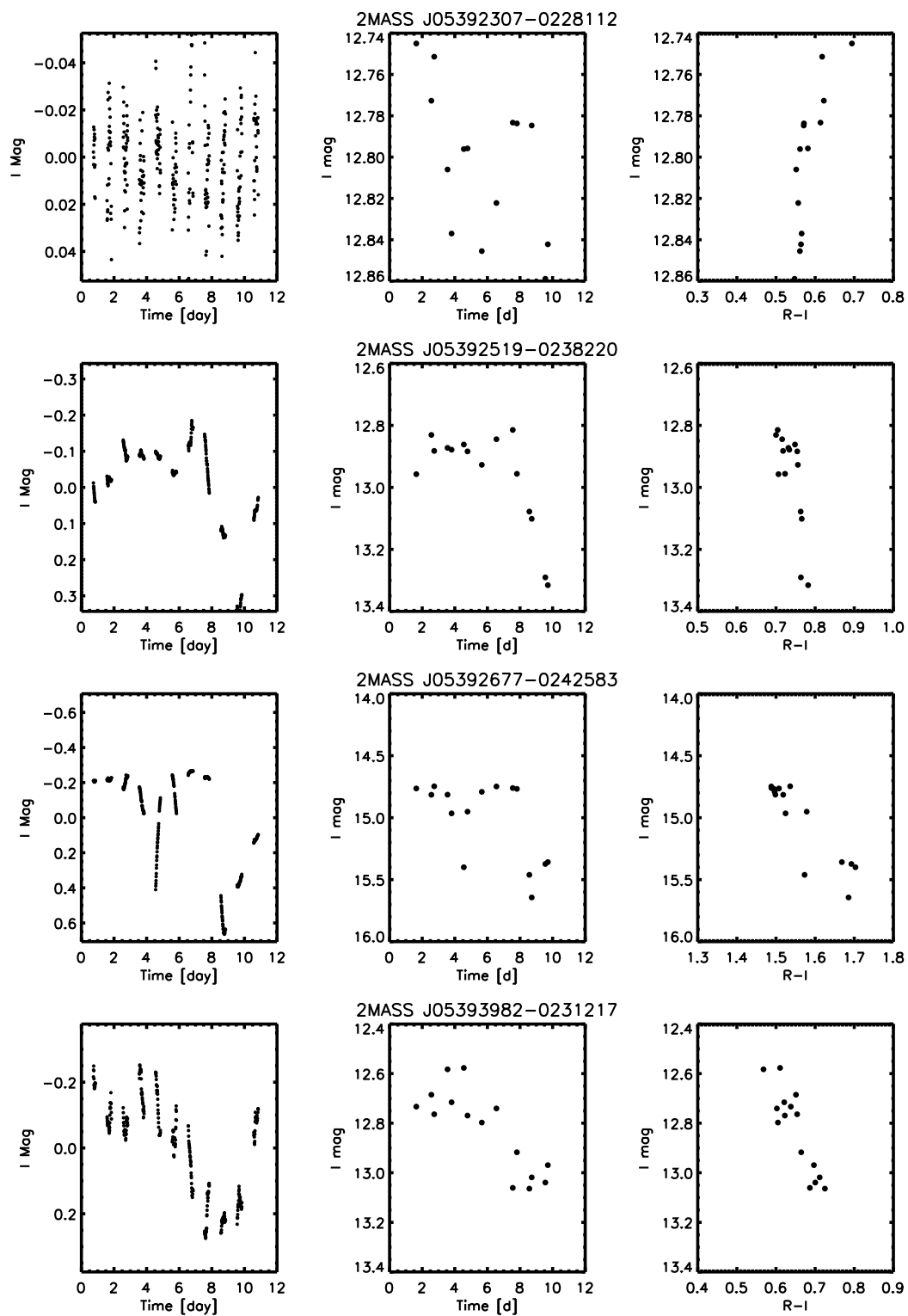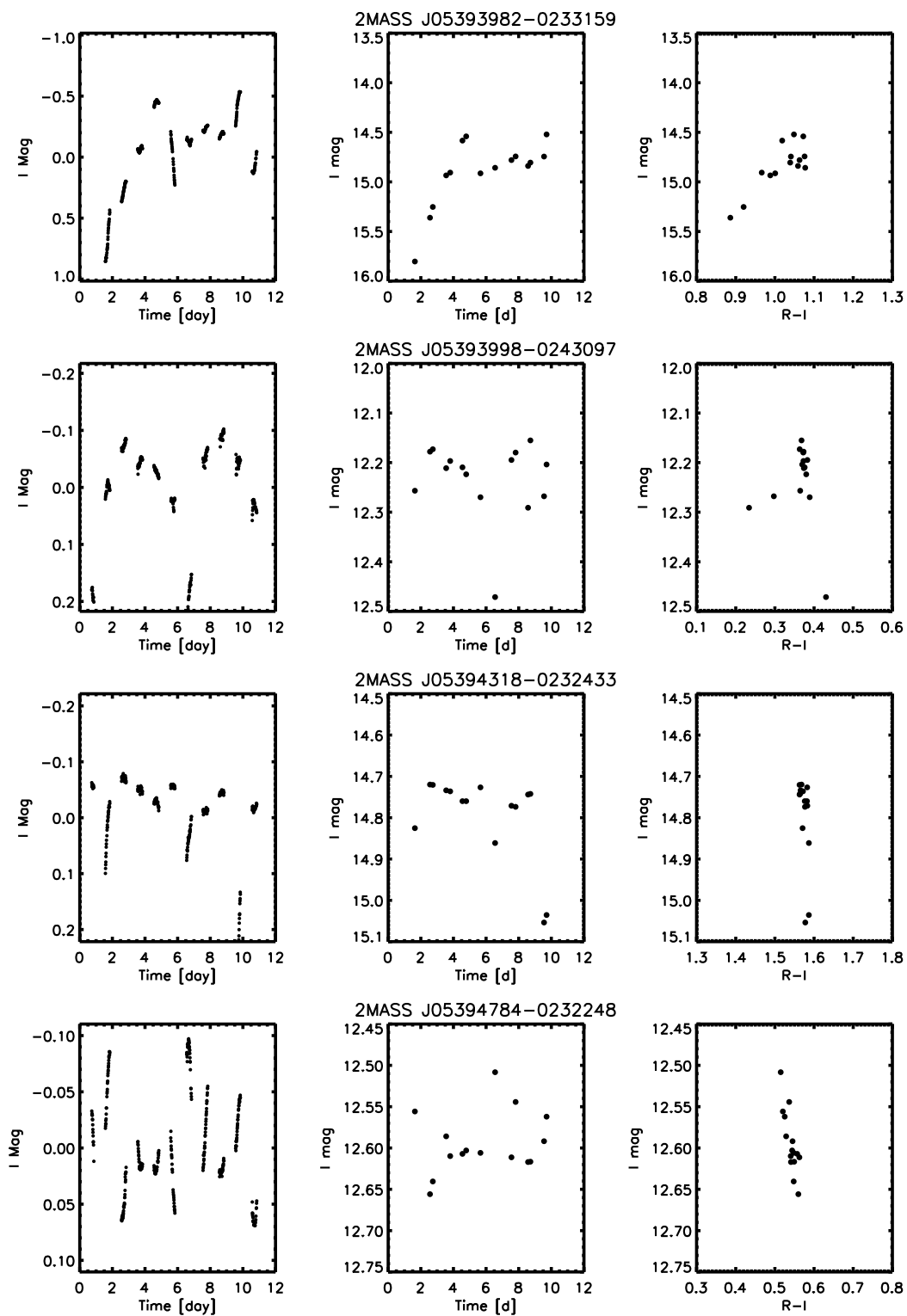
Figure 5.7 –Continued
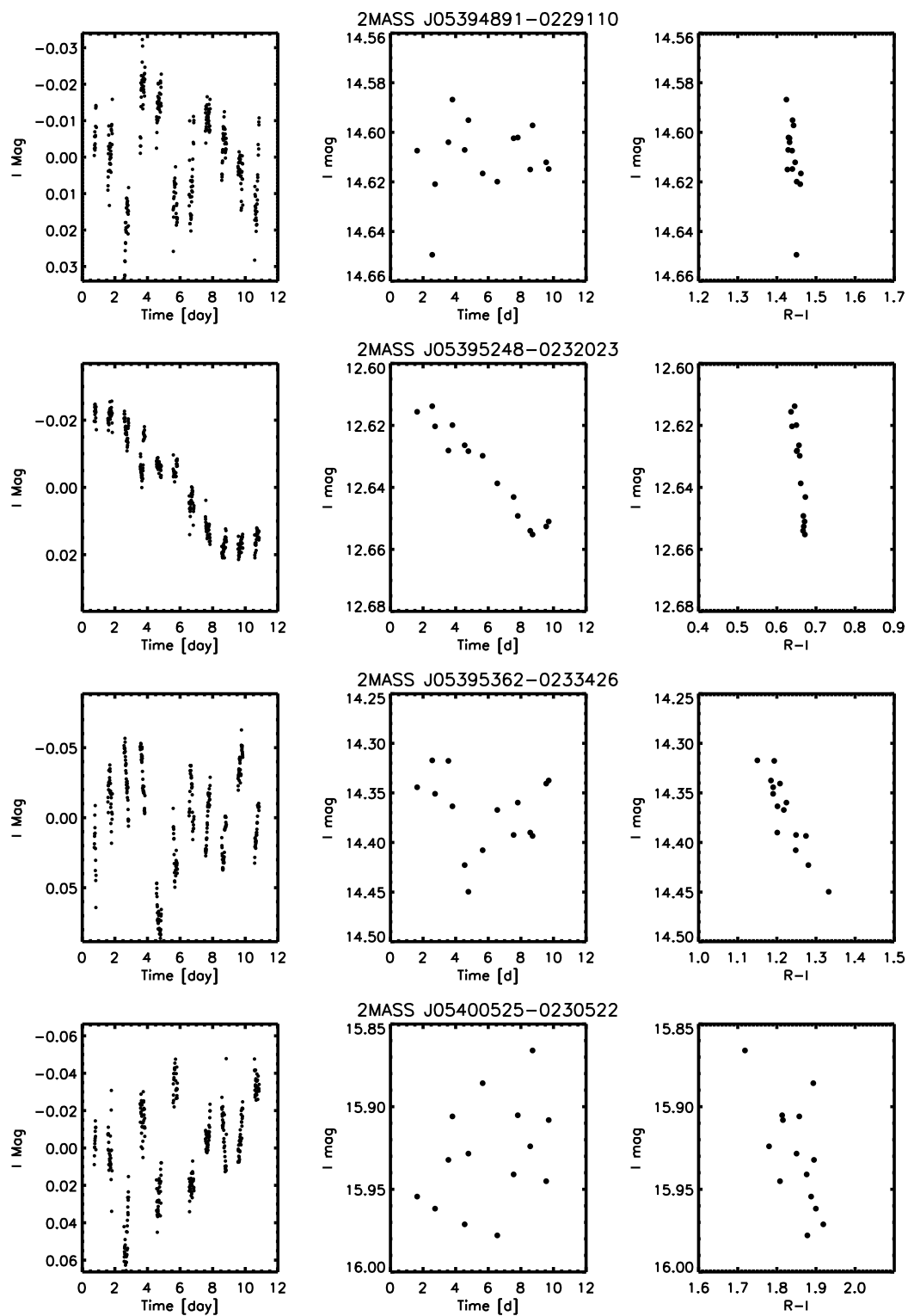
Figure 5.7 –Continued
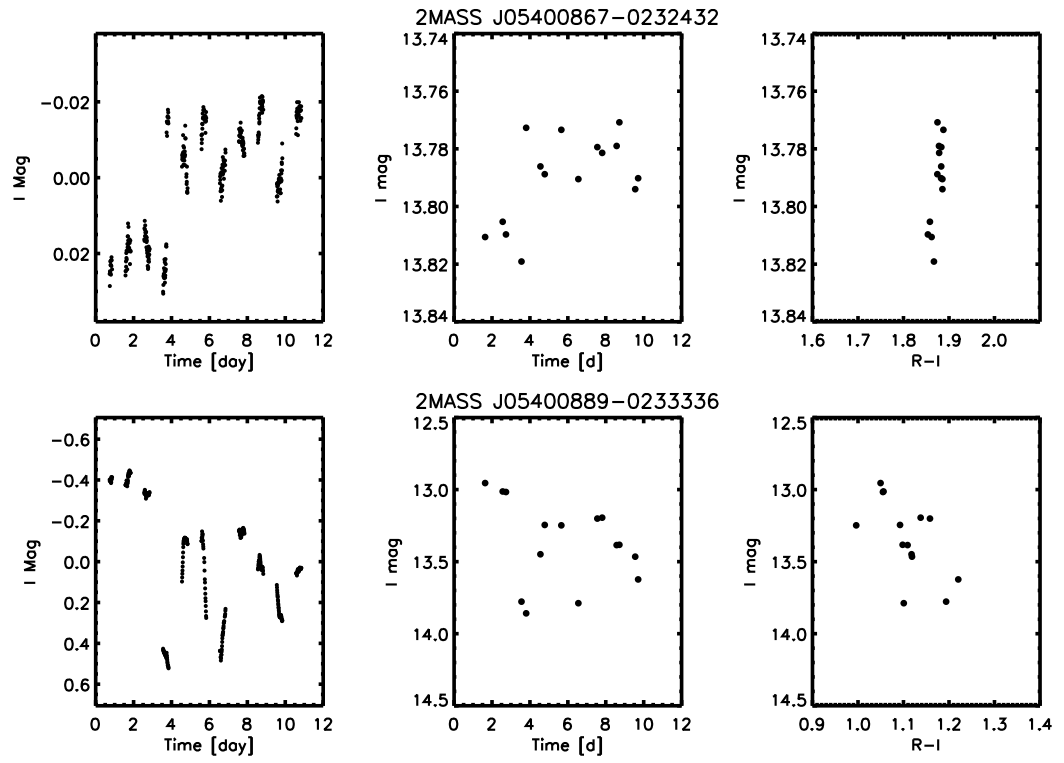
Figure 5.7 –Continued

Table 5.2.   Key features of σ Ori objects with detected I-band aperiodic variability

Object	Peak-to-peak amplitude [mag]	RMS [mag]	Member?	pEW Hα [Å]
2MASS J05375161-0235257	0.10	0.02	Y	-4.5±0.5[1]
2MASS J05375398-0249545	1.95	0.48	Y	-
2MASS J05380107-0245379	0.41	0.10	Y	-
2MASS J05380826-0235562	0.29	0.08	Y	-27.43±2.36[2]
2MASS J05380994-0251377	0.16	0.04	Y	-
2MASS J05381315-0245509	0.13	0.03	Y	-
2MASS J05382050-0234089	0.61	0.12	Y	-28.0±4.0[3]
2MASS J05382307-0236493	0.07	0.01	M	-
2MASS J05382543-0242412	0.55	0.16	Y	-260±30[4]
2MASS J05382725-0245096	0.83	0.23	Y	-53.5±9.0[3]
2MASS J05382774-0243009	0.13	0.04	Y	-5.02±0.30[2]
2MASS J05383141-0236338	0.19	0.04	Y	-197.57±11.64[2]
2MASS J05383157-0235148	0.13	0.04	Y	-10.18±0.92[2]
2MASS J05383388-0245078	0.29	0.06	M	-
2MASS J05383460-0241087	0.18	0.04	Y	-
2MASS J05383902-0245321	0.64	0.15	Y	-10.63±0.65[2]
2MASS J05383922-0253084	0.06	0.01	M	-
2MASS J05385542-0241208	0.87	0.19	Y	-190±20[1]
2MASS J05385922-0233514	0.82	0.17	Y	-
2MASS J05385946-0242198	0.05	0.01	M[a]	-
2MASS J05390193-0235029	0.93	0.28	Y	-72±4[1]
2MASS J05390276-0229558	0.10	0.02	Y	-4.45±0.27[2]
2MASS J05390357-0246269	0.10	0.03	Y	-
2MASS J05390458-0241493	1.00	0.20	Y	-
2MASS J05390540-0232303	0.10	0.02	Y	-0.94±0.05[2]
2MASS J05390760-0232391	0.61	0.17	Y	-13.19±1.38[2]
2MASS J05390878-0231115	0.73	0.18	Y	-
2MASS J05391151-0231065	0.55	0.13	Y	-25.76±0.79[2]
2MASS J05392307-0228112	0.12	0.02	M[b]	-
2MASS J05392519-0238220	0.55	0.14	Y	-40.03±2.80[2]
2MASS J05392677-0242583	0.93	0.28	Y	-
2MASS J05393982-0231217	0.53	0.15	Y	-
2MASS J05393982-0233159	1.72	0.41	Y	-
2MASS J05393998-0243097	0.34	0.09	Y	-
2MASS J05394318-0232433	0.38	0.09	Y	-
2MASS J05394784-0232248	0.17	0.04	M	-
2MASS J05394891-0229110	0.08	0.01	M	-
2MASS J05395248-0232023	0.05	0.01	M	-

Table 5.2—Continued

Object	Peak-to-peak amplitude [mag]	RMS [mag]	Member?	pEW Hα [Å]
2MASS J05395362-0233426	0.17	0.04	Y	-
2MASS J05400525-0230522	0.16	0.03	Y	-20.5±6.0[3]
2MASS J05400867-0232432	0.05	0.02	M	-
2MASS J05400889-0233336	0.97	0.28	M	-

Note. — Membership and Hα values were determined by other groups; thus Hα measurements are *not* simultaneous with our photometric data. Membership criteria are the same as in Table 5.1 , with "Y" for definitive σ Ori members and "M" for possible members (no non-members exhibited high-RMS light curve fluctuations). The two objects with numbered notes represent new candidate cluster members based on their position in the color-magnitude diagram and light curve RMS indicative of variability. Their magnitudes are [a]$I \sim 12.6$ (2MASS J05385946-0242198) and [b]$I \sim 12.9$ (2MASS J05392307-0228112). References are as follows: [1]Caballero et al. (2008), [2]Sacco et al. (2008), [3]Zapatero Osorio et al. (2002), [4]Caballero et al. (2007).

Table 5.3. Cha I objects with detected variability

Object	Variability type	Variability parameters	Disk?	Member?
2MASS J11065906-7718535	A	0.405 0.090	Y	Y
2MASS J11071668-7735532	A	0.405 0.090	Y	Y
2MASS J11072040-7729403	A	0.105 0.022	N	Y
2MASS J11072988-7725017	P	2.28d, 0.25	-	N
2MASS J11073302-7728277	P	0.67d 0.0197	N	M
2MASS J11073519-7734493	P	4.74d 0.0478	N	Y
2MASS J11073686-7733335	A	0.098 0.020	N	Y
2MASS J11074245-7733593	P	1.52d 0.0138	-	N
2MASS J11075225-7736569	A	0.090 0.022	N	Y
2MASS J11082238-7730277	A	0.229 0.046	Y	Y
2MASS J11083952-7734166	A	0.145 0.036	Y	Y
2MASS J11085421-7732115	A	0.043 0.010	N	Y
CTIO J11093360-7731113	P	0.46d 0.1271	-	N
2MASS J11094742-7726290	A	0.571 0.128	Y	Y
2MASS J11094918-7731197	A	0.128 0.026	N	Y
2MASS J11101153-7733521	P	2.354d 0.0152	N	Y
2MASS J11103481-7722053	P	0.5229 0.0137	N	Y
2MASS J11105076-7718031	P	1.91d 0.0286	N	Y
2MASS J11105359-7725004	A	1.431 0.285	Y	Y
2MASS J11105665-7733557	P	0.14d 0.1244	-	N
CTIO J11111463-7737020	P	0.59d 0.1827	-	N
2MASS J11120288-7722483	P	1.52d 0.0169	N	Y
2MASS J11120351-7726009	A	1.122 0.309	Y	Y
2MASS J11122675-7735183	P	3.52d, 0.0129	N	M
2MASS J11122971-7731045	A	0.171 0.035	-	M

Note. — We list objects in the Cha I field with detected variability. "A" corresponds to aperiodic variability, while "P" is for periodic variability. The values listed in column 3 are either the peak-to-peak and RMS light curve spreads in I-band magnitudes (A) or the period in days and amplitude in I-band magnitudes (P). Determination of disk presence was based on the criteria presented in §5.5.1; "-" indicates a lack of *Spitzer* photometry. Membership is based on previous censuses of Cha I; non-members ("N") have colors that are inconsistent with a position above the main sequence. "M" indicates a possible new cluster member based on the detected variability.

5.1.2.2   Sensitivity to combined aperiodic and periodic variability

In §5.1.1.1 we simulated our sensitivity to photometric periodicities at different frequencies by assuming that the underlying light curves are well represented by a combination of simple noise sources (white and red) and a single sinusoidal signal. However, the large number of aperiodic variables detected via the χ^2 test indicates that many light curves are in fact dominated by other types of variability, such as that associated with accretion. In these cases, we may not be able to detect periodicities superimposed on the larger-amplitude erratic fluctuations. We have investigated this reduction in sensitivity by injecting sinusoids of various frequency and amplitude into the light curves of a large subset of our aperiodic variables. The sample includes objects with RMS ranging from 0.01 to 0.3 magnitudes and I-band brightnesses from 12.0 to 17.5 magnitudes. We then attempted to recover the injected signals in the periodograms. The erratic nature of these light curves produces a steep trend in the frequency domain similar to the red noise from correlated photometric errors, but reaching higher amplitudes.

Since detection of periodic variability is frequency dependent, we have performed signal recovery tests in three regimes: frequencies less than 1 cd^{-1} (e.g., periods greater than 1 day), frequencies between 1 and 3 cd^{-1}, and frequencies greater than 3 cd^{-1}. These domains were chosen based on the typical exponential shape that we find for periodograms in our aperiodic variable sample. Our tests indicate that the periodogram noise levels for these objects are well correlated with the RMS spread in their light curves, regardless of brightness. This RMS ranges from 0.01 to 0.4 (see Tables 5.2 and 5.3) and should not be confused with the photometric noise level, which is typically much smaller. Amplitudes of the injected signals ranged from 25–400% of the RMS for the two lower-frequency regimes and 5–50% of the RMS for the high-frequency regime.

Most of the injected signals appeared clearly in the periodogram, but the decision as to whether they were "detectable" depended on the surrounding noise level. For frequencies less than 1 cd^{-1}, the mean periodogram noise is approximately the light curve RMS divided by 2.2 (e.g., $\sim$0.45$\times$RMS), whereas for frequencies from 1 to 3 cd^{-1}, this decreases to the RMS divided by 2.9 (e.g., $\sim$0.34$\times$RMS). Noise in the periodograms of aperiodic variables decreases drastically toward higher frequencies or short periods, and consequently for frequencies beyond 3 cd^{-1}, the mean periodogram noise level decreases to RMS/23 (e.g.,

~0.04×RMS). Detectability of a periodic signal requires an amplitude of at least 4.0 times the periodogram noise level. Therefore, our ability to detect periodic signals superimposed on aperiodic variability requires periodic amplitudes larger than ~1.8×RMS, ~1.36×RMS, and ~0.16×RMS in the three respective frequency ranges. Based on a median *periodic* variability amplitude of 0.02 magnitudes, we then expect to detect both aperiodic and periodic variability in cases where the period is less than eight hours (e.g., frequency >3 cd^{-1}) and the RMS of aperiodic variability is less than 0.13 magnitudes. It may also be possible to detect periodicities with longer periods, but only if the RMS of aperiodic variability is near 0.01–an uncommon occurrence, according to Table 5.2. We conclude that it is a challenge to identify both periodic and aperiodic variability in individual objects because of the different characteristic amplitudes of these phenomena.

5.2 Overall variability properties

We have identified 126 variables in our σ Orionis fields, including at least 107 suspected σ Ori members (101 of these are previously proposed members and six are candidate members newly identified here). We found an additional 25 variables in the Cha I field, including 20 confirmed and candidated cluster members, 3 of which we identify for the first time here. The majority of objects in our cluster sample were also detected in the 2MASS survey, which provides J, H, and K_s-band data. We cross-referenced the positions of likely cluster members to identify all 2MASS sources in our sample. Since young VLMSs and BDs have very red colors, all but the faintest (e.g., $I > 20$) have $J/H/K_s$ detections. Table 4.2 contains a compilation of our own absolute photometry of confirmed and candidate σ Orionis members, along with the corresponding 2MASS magnitudes. In Fig. 5.9 we present R-I versus I optical color-magnitude diagrams derived from our σ Ori photometric data and overplotted with 3 Myr theoretical isochrones from Baraffe et al. (1998) and D'Antona & Mazzitelli (1997), incorporating a conversion to photospheric colors using color-temperature and bolometric-correction-temperature relationships, along with a distance of 440 pc (Sherry et al. 2008).

The vast majority of the variables in each case fall above the main sequence and along a possible young cluster sequence. This finding confirms that single-band photometric monitoring is an efficient way to identify pre-main-sequence low-mass stars and brown
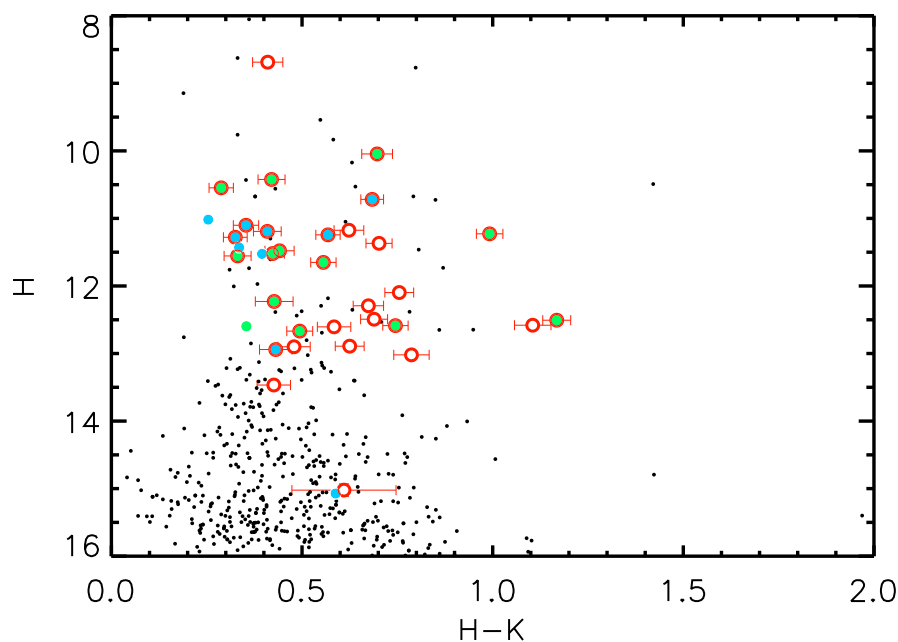
Figure 5.8 H and K color-magnitude diagram for all objects with 2MASS photometry (black dots) in our Cha I field. Red circles are confirmed Cha I members, while cyan filled circles are detected periodic variables and green filled circles are aperiodic variables.

dwarfs, and thus an effective technique in fields where the pre-main-sequence stars do not stand out in color-magnitude diagrams as distinct from the field stars.

The light curves and their temporal properties offer insights into the origin and prevalence of brightness variations, which we discuss in §5.2.1 and §5.2.2. Yet we can also make use of the rich array of data from previous spectroscopic studies (e.g., Table 4.1) as well as the *Spitzer* mission to analyze variability from several additional angles. In the forthcoming sections, we assess the correlations of variability with stellar and circumstellar properties. The *R-I* photometry available from our σ Ori work provides not only information on the relationship between brightness and color changes (§5.4), but also a means to investigate the mass-dependent properties of young stars and brown dwarfs (§5.3). In addition, we employ mid-infrared data to connect variability with the presence of disks around these objects (§5.5).
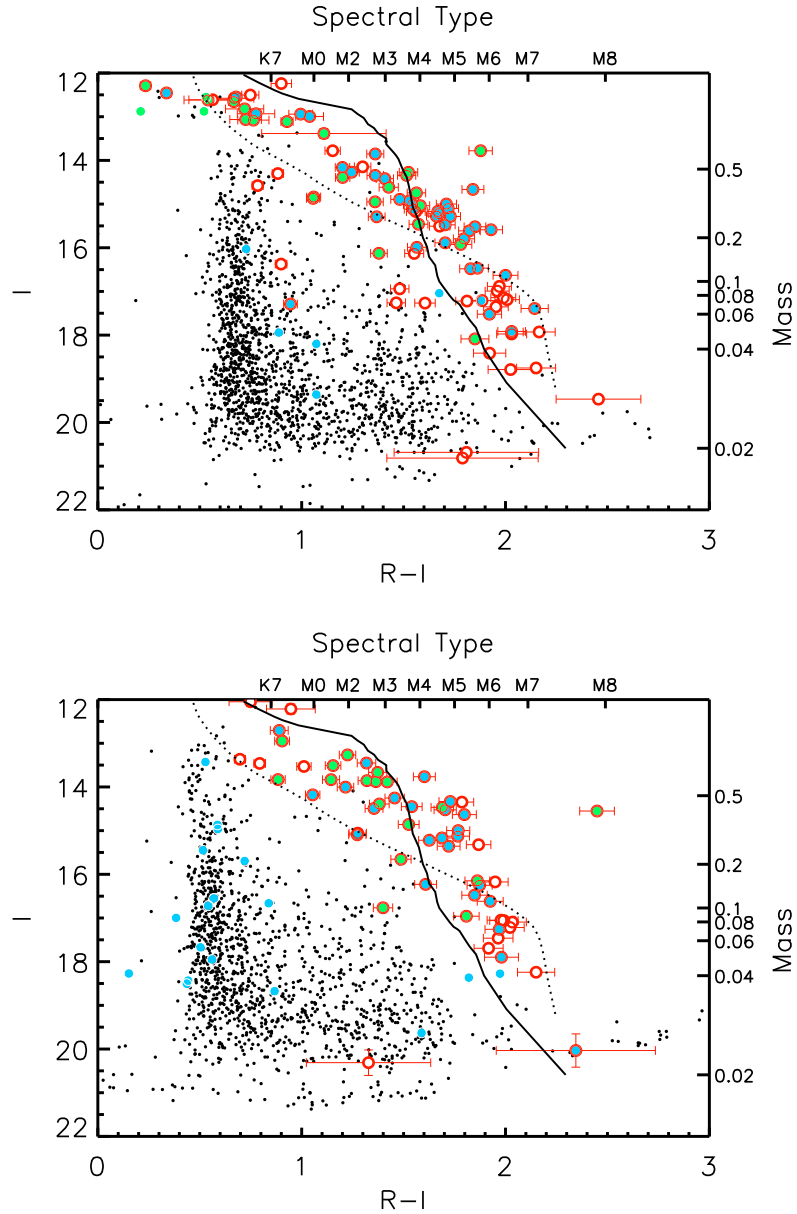
Figure 5.9 R and I color-magnitude diagrams for all objects with photometry (black dots) derived from our σ Ori fields (top: 2008; bottom: 2007). Red circles are confirmed and candidate σ Ori cluster members, while cyan filled circles are detected periodic variables and green filled circles are aperiodic variables. We have overplotted 3-Myr isochrones from Baraffe et al. (1998) (solid curve) and D'Antona & Mazzitelli (1997) (dotted curve) to illustrate the theoretically predicted sequence for young cluster members. Masses are from Baraffe et al. (1998), but those from D'Antona & Mazzitelli (1997) are similar. Spectral types shown were derived from the empirical relationship between R-I and spectral type among objects in our data and a few from σ Ori datasets in the literature. The two fields exhibit different average reddening due to spatial variations in extinction.

5.2.1 Variability classification and persistence

Characterization of variability can illuminate our understanding of the physical processes that take place on and around few-Myr-old low-mass stars. We have identified several types of variability among our sample of 151 variables, including irregular variability and various forms of periodic variability such as spot modulated stellar rotation, pulsations, and full or partial eclipse signatures, as listed in Table 5.1. Among 147 previously known or suspected σ Ori cluster members included in our photometry, the overall variability fraction is 69%, with irregulars (27%) and periodic objects (42%) comprising this cluster sample. Furthermore, we uncovered 25 variables with no prior membership information, most of whose light curves resemble eclipsing binaries or short-period pulsators. However, six have colors consistent with membership in σ Ori and light curves consistent with either spot modulation or accretion. Since these six objects encompass a range of brightnesses, it is not clear as to why they they were missed in previous surveys. The new candidates are included in Table 4.1 and noted in Tables 5.1 and 5.2 as possible members. Just under half (44%) of objects in the remaining 31% of our sample for which no variability is detected have strong evidence for σ Ori membership based on Table 4.1. Hence we conclude that at least 15% of young cluster members may not display obvious brightness fluctuations on timescales up to two weeks.

In the Cha I sample, the variability fraction is between 53 and 69%, depending on the membership status of several newly identified variable objects. The variability classification is divided into roughly equal proportions of periodic and aperiodic objects. Among the 8 variables with no prior membership information, three have light curves and colors characteristic of field eclipsing binaries or pulsators. Five may be new members, and we note these in Table 5.3.

Few Cha I members have been photometrically monitored previously, apart from a sample of 10 BDs and VLMSs presented by Joergens et al. (2003). Of the five with reported periods, *none* are redetected as periodic variables here. However, three (CHXR 78C, Cha Hα 3, and Cha Hα 6) appear to be aperiodic by our criteria. Among the 41 σ Ori members in our fields previously identified as variable objects (35 aperiodic and 6 periodic; see Appendix A), we confirm variability in 33 (30 aperiodic and 3 periodic); this suggests that the variability mechanisms are long-term rather than sporadic phenomena. In the subset for which

we do not redetect variability, there are no particular biases toward long or short timescale. We suspect that the combination of low numbers of data points, uneven time sampling, and underestimated uncertainties could have contributed to previous false detections in some cases. However, it is also possible that the variability mechanism itself turned off during the time of our observations.

In addition to comparing our variability detections with those of other works, we can use our own repeat observations of the CTIO 2007 field to glean further information about the timescales on which various types of variability operate. While the small number of data points per light curve (23, or two per night taken in 2008) precludes detailed comparison of variability properties from one year to the next, we can nevertheless identify objects with high-amplitude variability persisting on this longer timescale. Of the 17 aperiodic variables found in our 2007 field, we re-detect *all* of them again in 2008, based on the χ^2 analysis described in §5.1.2.1. In addition, 22, or over 80%, of our 27 periodic variables identified as likely σ Ori members in the 2007 field display significant variability at a similar period (the majority agreed to within 5%) in 2008.

We can estimate a minimum characteristic timescale, T, on which the various types of variability operate, by considering the set of all objects with repeat observations separated by at least one year. In total, there are 52 aperiodic variables that were either observed in both 2007 and 2008 by us, or identified by another group and observed later by us. Of these, 47 displayed aperiodic variability during both sets of observations. We suppose that for a typical duration of accretion (or other source of aperiodic variability) T, the probability that variability will persist one year after its initial detection is $p \sim e^{-1/T}$. Taking this probability to equal 47/52, we find the typical characteristic timescale for aperiodic variability to be $T \sim 10$ years. A similar result is obtained using a binomial distribution to describe the probabilities for the outcomes of measuring variability. Since this is much shorter than the cluster age timescale, the result may offer insights for models of unsteady accretion.

Likewise, we can perform the same analysis for the periodic variables. In this case, 25 of 33 objects exhibited variability at roughly the same period during repeat observations over one year apart. The corresponding timescale for persistence of periodic variability is then at least $\sim$4 years. Based on these results, we conclude that the types of variability present among these young cluster sources are long-lived in comparison to the objects' rotation periods ($\sim$1–10 days) as well as the intra-night time scale of abrupt light variations seen in

aperiodic objects.

5.2.2 Variability demographics across timescale and brightness

In addition to visual classification of light curves, we can also consider variability properties in the time and magnitude domains. In doing so, it is important to understand any selection or other effects that may mask certain kinds of variability from being observed. The observing setup imposes practical constraints on variability detection through photometric cadence, precision, interruptions, and total duration. These details translate into a maximum detectable amplitude for periodic variables and sets the range of detectable periods. The demographics of variability present additional considerations for our ability to classify light curve behavior. Some fraction of young stars and brown dwarfs may not have magnetic spots, or their surface features may be too small to induce observable variability and potentially infer a rotation period. Other objects may have multiple sources of variability (e.g., spots, accretion, circumstellar variability) that are difficult to separate from each other. In what follows, we carefully consider the connection between these effects and the variability trends that we have uncovered.

In the time domain, our ground-based observations are sensitive to photometric periods between $\sim$20 minutes and $\sim$12 days, as discussed in §5.1.1. While we do encounter periodic variability close to the longest possible timescales, we detect no periodicities on the shortest timescales–less than 7 hours (e.g., Fig. 5.12). If this effect is the result of our photometric sensitivity, then it should be explained by the detection limits determined in (§5.1.1.1 and §5.1.2.2). Instead, we find (Fig. 5.1) that we are *more* sensitive to short periods and could recover signals down to 0.001 magnitude amplitudes for objects brighter than $I = 16$, or signals with 0.01 magnitude amplitudes out to $I \sim 19$ or 20. Another possibility is that we are somehow missing periodic variability in cases where the light curves are dominated by aperiodic behavior. In §5.1.2.2 we concluded that we are likely to identify both types of variability in a single object only if the timescale for the periodic component is less than 8 hours and the light curve RMS is below $\sim$0.13 magnitudes. A number of the detected aperiodic variables do indeed have RMS values that satisfy this criterion (Table 5.2). Hence while detection limits may explain our failure to identify combinations of aperiodic variability and longer timescale periodicity in single targets, they do not account for the dearth of short-period variables. We conclude that the lack of periodic variability

on timescales under 7 hours is a real physical effect.

Changes in variability properties as a function of magnitude can also shed light on the properties of young stars and brown dwarfs. To estimate the correspondence between mass, I-band magnitude, and R-I color in σ Ori, we have overlaid 3 Myr theoretical isochrones from Baraffe et al. (1998) and D'Antona & Mazzitelli (1997) on our data in Fig. 5.9. Since reddening is low in this cluster, the observed R-I values are close to the intrinsic photospheric colors. Although mass predictions are fairly uncertain at these ages (Baraffe et al. 2002), the two models agree well with each other and we have adopted the mass values of Baraffe et al. (1998). These estimates indicate that our dataset encompasses objects with masses from approximately 0.02 to 1.0 $M_\odot$. The substellar limit, at $\sim$0.08 $M_\odot$, lies near $I = 17$ or spectral type M6. The spectral types shown in Fig. 5.9 were adopted directly from the objects in our σ Orionis sample with available spectroscopy at the time of the observations (Table 4.1).

We find variables of all types spanning the entire range of magnitudes, but Fig. 5.9 displays a subtle decrease in variable cluster members at the faint end, which might be explained by the decline in photometric sensitivity. For the subclass of variables identified as aperiodic, we note that the brightest objects have light curve RMS values from 0.03 to 0.2. Based on the detection limits described in §5.1.2.2, we lose sensitivity to this type of variability around an I magnitude of 18.0. For objects brighter than this limit, we find that aperiodic variables seem to populate the entire range of magnitudes, including a portion of the brown dwarf regime. Attributing aperiodic variability to accretion and its associated hot spots or fluctuating dust extinction levels, we do not find significant evidence for physical changes in these effects across the substellar boundary. Indeed, one of the faintest IC 348 cluster BDs observed with *HST* (L1434) displays substantial variability at the 15% level, as shown in Fig. 5.10.

Magnitude trends in *periodic* objects are slightly more difficult to determine, as they are dependent on period as well as the potential presence of aperiodic variability at larger amplitude. The σ Ori dataset was the only one large enough to investigate this issue. Our detection limits (Fig. 5.1) indicate that we are sensitive to amplitudes of $\sim$0.01 magnitudes out to $I \sim 18.5 - -19.5$, depending on period. Thus we should be able to detect whether the properties of periodic variability are similar from the stellar through the brown dwarf regime. If we divide our σ Ori sample into "bright" ($I < 17$) and "faint" ($I > 17$) groups,
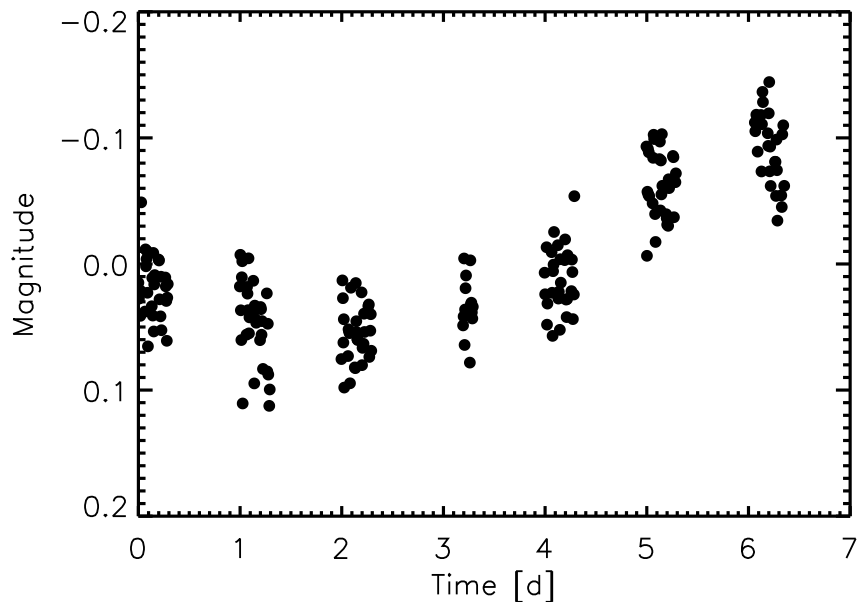
Figure 5.10 Light curve of the IC 348 object L1434, observed with *HST*/WFC3. This BD displays significant variability over the 7 days that it was monitored.

we find the fraction of periodically variable faint objects to be 34±10%. Compared to the number of targets that are periodically variable at brighter magnitudes (46±6%), there appears to be a reduction in the fraction of variable members for faint magnitudes and thus lower mass. An exception to this trend is the IC 348 BD L761, which is periodically variable, as shown in Fig. 5.11. The period of either 0.6 or 1.4 days is consistent with rotational modulation of a spot (§5.3).

The significance level of this finding is difficult to assess since cluster membership status is not secure for many of the fainter objects. However, if we restrict our estimate to *confirmed* (e.g., via spectroscopy or infrared excess) cluster members, the periodic variability fractions are similar to those of uncertain cluster members: 45±7% for objects with $I < 17$, and 26±12% for those with $I > 17$. The majority of periodically variable cluster members display roughly sinusoidal light curves consistent with rotational modulation of stellar spots. Therefore the apparent reduction in periodic variables toward fainter magnitudes suggests a difference in the photospheric properties of young brown dwarfs, as compared to the higher mass stars.
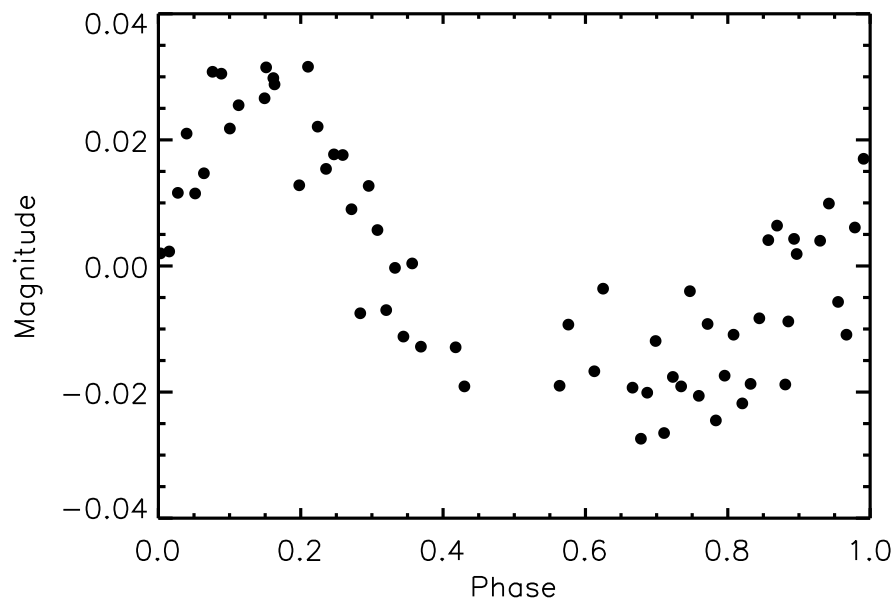
Figure 5.11 Phased light curve of the IC 348 object L761, observed with *HST*/WFC3. This BD displays significant periodic variability on a timescale of 0.6 days.

5.2.3   Comparison of optical and infrared data

Assessment of the wavelength dependence of variabiity is also instructive for our understanding of its mechanisms. Our high-cadence CTIO 1.0 m telescope observations included both Spitzer fields. Although the overall time baseline of the *Spitzer* observations is short compared to that of the ground-based campaign, we have searched for common variability in the two datasets.

A total of seven variable σ Ori cluster members from the ground-based campaign fall in the fields of the *Spitzer* observations, as noted in Table 4.3. In the 4.5 μm field, S Ori J053833.9-024508 and 4771-41 were identified as aperiodic variables in the ground-based photometry. In addition, the BD S Ori 45 was identified as being periodic in the *I*-band, with a period of 7.2 hours and amplitude 0.034 magnitudes, whereas VLMS SWW40 was found to have a period of 4.47 days and amplitude 0.013 magnitudes. In the 3.6 μm field, the BD S Ori J053825.4-024241 was identified as an aperiodic variable. Two additional variables were found be periodic in the *I* band: S Ori J053823.6 ($P = 1.7$d; $A = 0.017$ mag) and S Ori J053817.8-024050 ($P = 2.4$d; $A = 0.008$ mag).

For those ground-based variables with brightness fluctuations on timescales longer than a day, we do not necessarily expect to observe variability in our shorter *Spitzer* dataset. Indeed, we do not recover periodic variability at greater than the 1% level in any of the ground-based periodic variables. In addition to the shorter time baseline, it is possible that the non-simultaneity of observations and the different wavelengths make rotational spot modulation–the primary explanation for periodic variability in young VLMSs and BDs–unobservable in our light curves.

Several of the previously identified aperiodic variables, on the other hand, do appear to be variable at infrared wavelengths. The BD S Ori J053825.4-024241 displays relatively high amplitude erratic fluctuations (see §5.4.1). Object 4771-41 shows residual variability after correction for the pixel-phase effect (light curve RMS of ~0.01 versus ~0.001 magnitudes), and S Ori J053833.9-024508 also displays variability at a significantly higher level than predicted by signal-to-noise estimates (light curve RMS of ~0.05 versus <0.01 magnitudes). The RMS values in the *Spitzer* bands are similar to those found in the optical for S Ori J053825.4-024241 and S Ori J053833.9-024508, whereas they are roughly an order of magnitude lower for 4771-41. Thus the light curve of this latter object may exhibit residual pixel-phase effects, as opposed to real variability. However, for the other two aperiodic variables, the rough correspondence of RMS amplitudes in both the optical and infrared suggests that the variability mechanism may be relatively insensitive to wavelength.

Interestingly, object S Ori J053829.0-024847 displays substantial variability at 4.5 μm (a 0.06 magnitude drift over 24 hours), whereas it did not appear variable in our ground-based dataset. We suspect that the variability mechanism in this case was dormant during the optical observations, although its photometry could have been affected by a nearby neighbor on the array. Since this object exhibits an infrared excess (Hernández et al. 2007; Caballero et al. 2007), there is an additional possibility that the variability is associated with the disk and thus only visible in the near-infrared and at longer wavelengths.

In addition to the recovery of aperiodic variability in our σ Ori cluster sample, we also re-identify a number of eclipsing binaries; further details on these field objects are provided in the appendix.

5.3 Rotational modulation of spots

5.3.1 Origin of periodic variability

Since the periodic variability in our cluster sample does not occur on the timescales appropriated for deuterium-burning pulsation, it is instead most likely due to spot modulation of the light curves. On timescales of 0.3–12 days and with amplitudes of 0.003–0.12 mag, the periods of the brightness changes among known and suspected cluster members are too long to be explained by the pulsation theory (Palla & Baraffe 2005). We would have detected the shorter periods predicted by the theory if they had amplitudes of $\sim$0.001 (bright sample; $I < 16$) to 0.01 magnitudes (faint sample; $I \sim 20$). Further, the roughly sinusoidal shapes of the periodic variables are not consistent with other varieties of pulsators or a population of eclipsing systems, apart from the 22 field objects listed in Tables 5.1 and 5.3. Instead, the time scales and amplitudes are compatible with modulation of spots that may be either cooler than the photosphere, as in active chromosphere models, or hotter than the photosphere, as in accretion column models (Carpenter et al. 2001; Scholz et al. 2009b). Comparison of theoretical spot models with multi-color photometric data has shown that both scenarios can produce larger amplitude light curves at shorter wavelength (e.g., Frasca et al. 2009). Although we have a small sample of R-band data points for each target, the color data are not extensive enough to allow for detailed modeling. In either case we assume that the periodicities extracted from our analysis can be attributed to rotational modulation of surface inhomogeneities and directly adopted as rotation periods.

5.3.2 Distribution of rotation rates with color/mass

For "higher"-mass ($>$0.3–0.4 $M_\odot$) stars in the ONC, NGC 2264, and IC 348 clusters, derived periods have in some cases revealed double-peaked distributions, with two groups clustered near 1–2 and 8–10 days (Herbst et al. 2002; Lamm et al. 2005; Cieza & Baliber 2006). For other young cluster datasets, the distribution is not bimodal but peaks near 3–5 days (Cieza & Baliber 2007; Irwin et al. 2008). In contrast, our σ Ori sample extends well into the brown dwarf regime and the corresponding periods cluster at short timescales, 1–2 days, with a uniform or exponentially decreasing tail extending out to and perhaps beyond 10 days. Only a few objects in the sample have periods in the 8–10 day range. Since the dataset includes a representative sampling of the σ Ori IMF between $\sim$0.02 and 1.0 $M_\odot$,

it is possible to search for trends in the period distribution along the color and magnitude axes.

In Figs. 5.12 and 5.13, we present the period as a function of R-I and I, both of which serve as a proxy for mass since extinction is low. Included are only those periodically variable objects with solid or likely cluster membership status based on colors and spectroscopic data available in the literature (Tables 4.1 and 5.1). In this way, contamination by periodicities of field variables should be negligible. Apart from one or two outliers, there is a significant decrease in period with progressively redder color or fainter magnitude, implying that within this mass range, lower mass objects rotate faster than the higher mass ones. Taking the substellar boundary to be near spectral type M6 or R-$I \sim 1.9$ and $I \sim 16.5$ (see Fig. 5.9), there are nine brown dwarfs in the rotation sample with periods ranging from ~ 7 hours to ~ 3 days. On the other hand, the higher mass stars with R-$I < 1.3$ or $I < 14.3$ and $M \gtrsim 0.45 M_\odot$ have periods larger than 4.5 days, with the exception of one object. The correlation of period with mass is statistically significant at the 10^{-6}–10^{-5} level, depending on whether the test is run on period and color or period and magnitude. Masses estimated from photometry are dependent on the theoretical model used, and the values presented here are derived from Baraffe et al. (1998), based on I-band magnitude and an age of 3 Myr. Previous works have used cut-offs between young "low" and "high" mass stars of spectral type M2.5 and masses of either 0.25 or 0.4 $M_\odot$ depending on the theoretical model (e.g., Herbst et al. 2007). We adopt a slightly higher value of 0.45 $M_\odot$ corresponding to $I = 14.3$ and find that 78% of our sample falls in the low-mass end.

An intriguing aspect of our data is that several regions of the color-period and magnitude-period diagrams are nearly devoid of data points. Only one σ Ori cluster member appears with a rotation period less than 14 hours. This finding cannot be a result of our detection limits, as our sensitivity *increases* on shorter timescales (§5.2). To test whether a short-period cut-off might be explained by the maximum allowed rotational velocities, we have estimated the periods required for break-up as a function of mass, using masses and radii from the 3 Myr models of Baraffe et al. (1998) and D'Antona & Mazzitelli (1997). Break-up is assumed to occur when the centrifugal force from rotation exceeds self gravity; the results of these computations are shown in Figs. 5.12 and 5.13. The break-up periods increase slowly with mass and range from 2 to 7 hours, and thus there is a significant gap between the break-up curve and the observed rotation data. Consequently, some physical
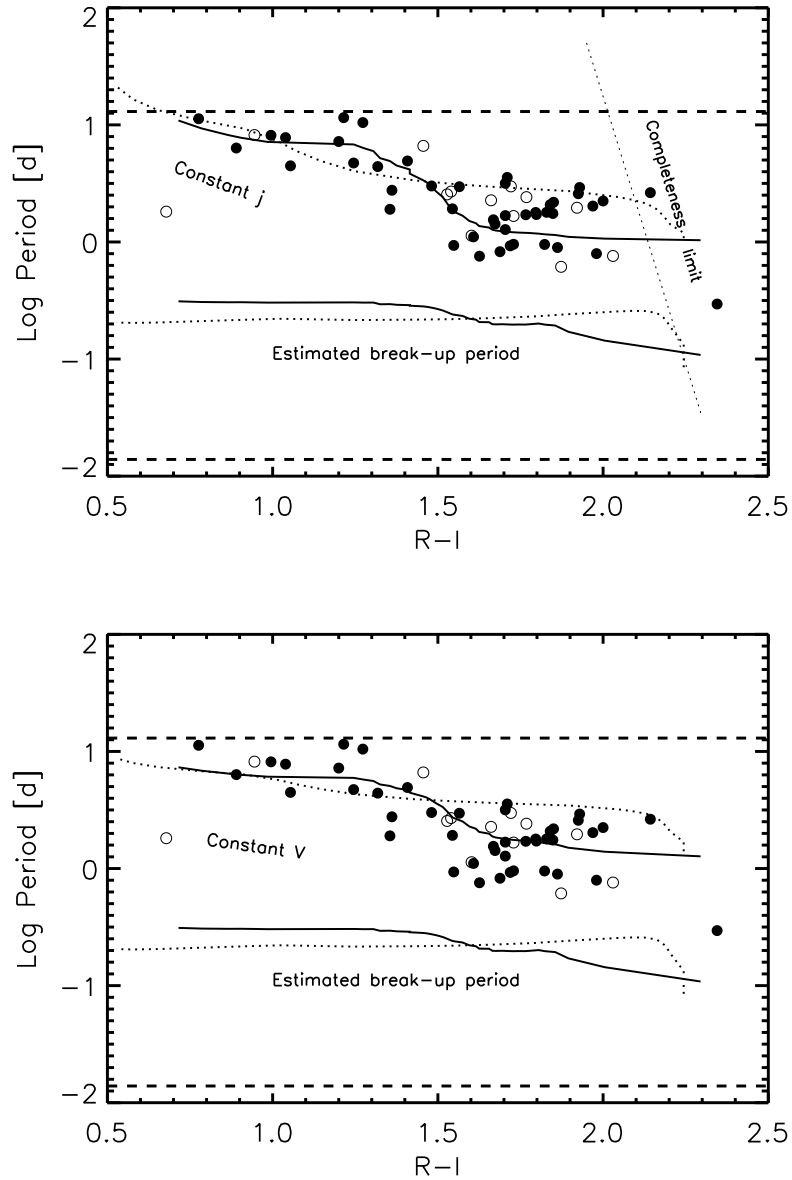
Figure 5.12 Period of σ Ori variables versus their $R - I$ color. Variables without obvious periods are not included, nor are those periodic variables having colors inconsistent with cluster membership. Objects with infrared excesses indicative of disks (§5.5.1) are marked as open circles, whereas objects without evidence of a disk are filled circles. In the top diagram, we have overplotted models of constant specific angular momentum (j) derived from radii provided by the 3 Myr isochrones of Baraffe et al. (1998) (solid curve) and D'Antona & Mazzitelli (1997) (dotted). The dotted line at the right side represents the completion limit redward of which we cannot detect periodic signals of amplitude less than 0.007 magnitudes. In the bottom diagram, we overplot models of constant angular velocity from the same isochrones. In both plots, we show estimated break-up periods derived from mass and radii predicted by the same theoretical models.
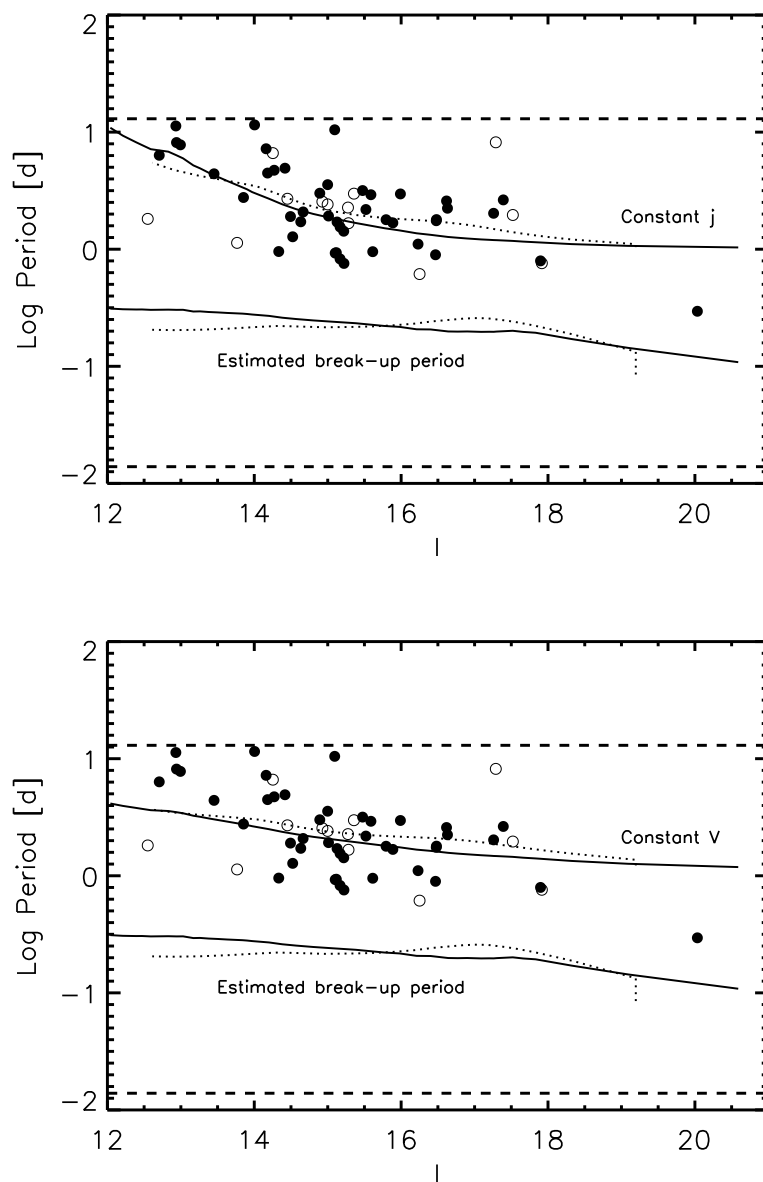
Figure 5.13 Period of σ Ori variables versus their I-band magnitude. The sample, as well as the symbols and curves, are the same as in Fig. 5.12. Likewise in the bottom diagram, we show models of constant angular velocity.

mechanism seems to limit the rotation speed of most low-mass objects to at most 40% of break-up, and even slower speeds at higher mass.

In addition to a lack of variability on few-hour timescales, we also find a dearth of periodic variables in two other regions of the period-color and period-magnitude diagrams: from Figs. 5.12 and 5.13, we see that only two blue objects (e.g., $R\text{-}I \lesssim 1.3$, $I \lesssim 14.3$, or spectral type earlier than M2.5) rotate with periods faster than 3 days, and only one of the redder objects (e.g., $R\text{-}I > 1.5$, $I \gtrsim 15$, or spectral types later than M3.5) rotates with a period greater than 3.2 days. It is these two largely empty regions that conspire to create the pattern of increasing period with mass. To confirm that this trend is not a data selection effect, we have explored several scenarios that might prevent detection of rotation periods in the two regions.

As emphasized previously, our sensitivity to periodic signals increases on shorter timescales down to 20 minutes; hence this does not explain the gap in period detections at the bright end. However, detection also depends on variability amplitude. In Fig. 5.1, we have shown that we are sensitive to amplitudes of $\gtrsim 0.001$ magnitudes for the brightest ($I < 16$) and bluest objects. The entire sample of periodic variables associated with rotation has a mean amplitude of 0.02 magnitudes, with a standard deviation of 0.013 magnitudes. Thus we expect only a small fraction of periodic variables to display amplitudes less than 0.007 magnitudes. To determine whether a population of "missing" blue objects with such low amplitudes could explain the deficit of data points in the lower left portion of the color-period diagram, we examined the periodograms of all cluster members with $R\text{-}I < 1.3$ and no detected variability. In the majority of these objects, we are able to rule out the presence of periodicities with amplitudes greater than 0.007 magnitudes. For those members that display aperiodic variability, identification of underlying periodicities is nearly impossible (see §6.2). However, we see no reason that the light curves of aperiodic objects would contain periodic variability with preferentially short period, unless there is some additional spin-up due to ongoing accretion. Thus we tentatively conclude that there is a real deficit of σ Ori members blueward of $R\text{-}I = 1.3$ and $I = 14.3$ with periods less than 3 days.

The second empty region of the color-period diagram, where $R\text{-}I \gtrsim 1.5$ or $I \gtrsim 15$, displays an apparent boundary at periods over $\sim$4 days. It is tempting to identify this as a physical trend, but not immediately clear whether it could simply reflect our diminished sensitivity to longer periods at faint magnitudes. To find the locus of colors, magnitudes, and

periods for which we could detect periodic variability amplitudes as low as 0.007 magnitudes, we averaged all periodograms of non-variable field objects in 0.5 magnitude bins. For each bin, we fit an exponential curve to the mean periodogram, as in Fig. 2.10. To detect a signal of amplitude 0.007, the noise level must be approximately 1/4 of this, or 0.0018 magnitudes. The point at which the exponential fit reaches this value was then taken to be the minimum frequency required for a detection. We then converted this frequency to period, and employed an empirical isochrone fit to Fig. 5.9 to translate the I-band magnitude of each bin to an R-I value. The resulting set of data points from all magnitude bins forms a locus on the color-period diagram which declines steeply with color, as shown by the completeness limit line in Fig. 5.12. Redward of this relation, we cannot uncover signals of amplitude less than 0.007 magnitudes, and thus the periodic sample may not be complete. The locus crosses our maximum detectable period, $\sim$12 days, at R-$I \sim 2.0$ and reaches a period of 1 day between R-$I = 2.1$ and 2.15. While several data points fall redward of this line (these detections had higher amplitudes), a large swath of the empty region still lies on the blue side and cannot be explained by the completeness limit. As with the other gap in the color-period and magnitude-period diagrams, a survey of the periodograms of non-variable objects shows no evidence of overlooked periodicities with amplitudes greater than 0.007 magnitudes. It is once again possible that we may be missing periods in objects that are accreting and display high-amplitude erratic variability or have very small surface spots, but we cannot explain why these effects would only occur for certain combinations of colors and periods. Consequently, the trend of increasing period with decreasing color seen in Figs. 5.12 and 5.13 appear to reflect a physical correlation between rotation and mass.

To explore whether the gaps found in our period-color and period-magnitude diagrams are a general feature of young star and brown dwarf rotation, we have compared our data to the period-mass distributions of the similar age clusters NGC 2264 ($\sim$2 Myr; Lamm et al. 2005; Irwin & Bouvier 2009) and NGC 2362 ($\sim$5 Myr; Irwin et al. 2008). We in fact find quite a few objects with periods from 1–3 days across all masses. Nevertheless, there does appear to be a relative deficit of fast rotators at higher mass, as well as slow rotators at lower mass, similar to σ Orionis. To compare rotation data from the three clusters more quantitatively, we have plotted them together in Fig. 5.14. I-band magnitudes from each set have been transformed to masses using the models of Baraffe et al. (1998), as well as cluster distances and I-band extinctions. Although there are inherent uncertainties to the

theoretical models at this age, the systematic errors should be similar for each cluster. Superimposed on the data in Fig. 5.14 are median fits to each set of periods and masses, which are remarkably similar for each of the three clusters, particularly for masses below 0.4 $M_\odot$. In addition, the rotation distributions in all three clusters appear to transition to longer periods above this mass (which is model dependent and corresponds roughly to $I \sim 14.5$ for σ Orionis). A Kolmogorov-Smirnov test reveals no significant differences between the three period distributions from the brown dwarf regime up to 0.5 $M_\odot$ where our own data peter out.
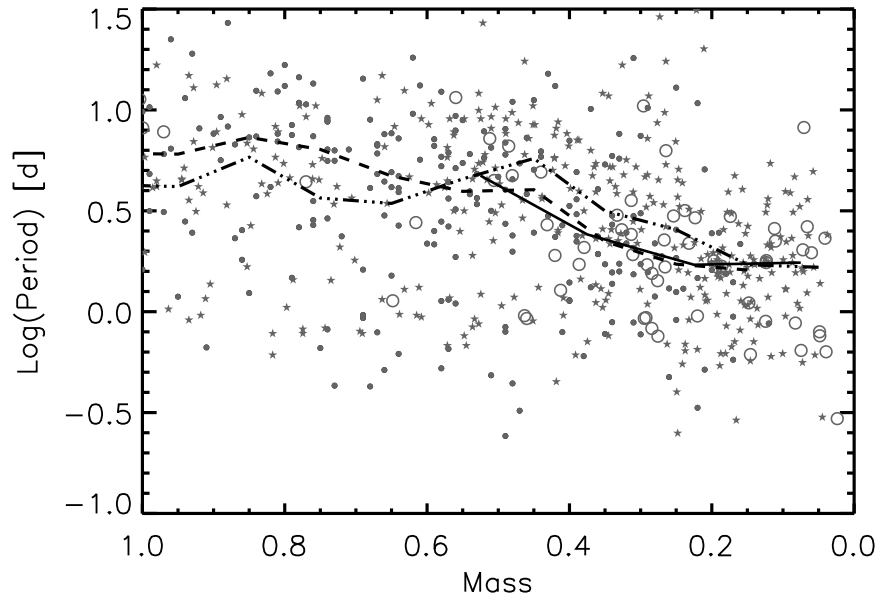
Figure 5.14 Period of variables in our σ Orionis sample (open circles), NGC 2264 (stars; Lamm et al. 2005), and NGC 2362 (small circles; Irwin et al. 2008) versus estimated mass in solar units, based on I-band magnitude and the theoretical models of Baraffe et al. (1998). Curves show the the median period in 0.1 $M_\odot$ bins (or 0.15 $M_\odot$ for our sparser data): a dash-dotted line for Lamm et al. (2005), dashed line for Irwin et al. (2008), and a solid line for our own data, which stops at $\sim$0.55 $M_\odot$.

5.3.3 Connection to internal structure and surface physics

The measured periods and amplitudes can inform us about the angular momentum and magnetic field properties of very low mass stars and brown dwarfs. The fact that rotation period seems to be connected with color or magnitude, and hence mass, implies that a

physical conservation law may be at work.

Light curve period, P, is related to specific angular momentum, j, via $j \propto R^2/P$. If specific angular momentum from the natal cluster gas is conserved among σ Ori members, then we expect periods to scale as R^2. The actual radii of our sample objects are unknown, but theoretical models predict their values with significant uncertainty due to lack of information about initial conditions, opacity, and treatment of convection (Baraffe et al. 2002). We have used the 3 Myr isochrones of Baraffe et al. (1998) and D'Antona & Mazzitelli (1997) to estimate R^2 as a function of mass. Converting masses to R-I and I as in Fig. 5.9, determination of a relationship between period and color requires the selection of a scaling constant to represent fixed specific angular momentum. Since the moments of inertia of young, low-mass objects are not well known, we have simply used one end of the *observed* color-period relation to anchor the calculated constant angular momentum function. We present the results in Figs. 5.12 and 5.13 (top panels) for data from both Baraffe et al. (1998) and D'Antona & Mazzitelli (1997); both curves fit the color-period data surprisingly well. In particular, the model derived from the Baraffe et al. (1998) isochrone can be adjusted so as to pass through the center of the data, reproducing the "gaps" seen in the lower-left and upper-right quadrants of the color-period diagram.

If young ($\sim$3–5 Myr) stars maintain constant angular velocity rather than angular momentum, we would expect periods to scale as R instead of R^2. Although there is reason to believe that individual stars may *evolve* at constant angular momentum (Rebull et al. 2004, e.g.,), we have adopted this model primarily to illustrate how much freedom there is in fitting the data. We generated a constant angular velocity curve in the same way as we did for specific angular momentum and once again anchored one end to the observational data. As shown at the bottom of Figs. 5.12 and 5.13, this function fits the observed periods and colors almost as well as the R^2 model, although two curves derived from the D'Antona & Mazzitelli (1997) isochrone are a bit flatter than the data. So while there certainly seems to be a trend in periods with color and magnitude, it is not tight enough to conclusively determine its cause. In addition, a single outlier (2MASS J05391883-0230531) at R-$I = 0.7$ and a clear period of 1.8 days confounds the idea.

While observed period may tell us something about physical properties of the variability mechanisms in the very-low-mass regime, light curve amplitude can also offer valuable information. This parameter is related to surface spot coverage and contrast. In Fig. 5.15,
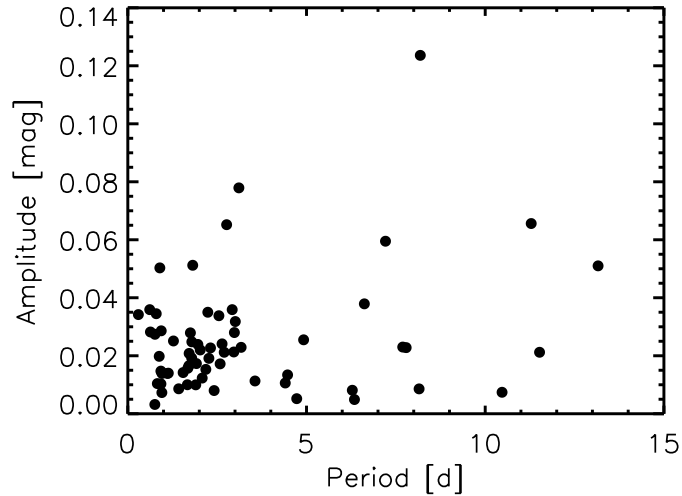
Figure 5.15 Periods and amplitudes of variable σ Orionis members. Most error bars are smaller than the size of the points.

we show amplitude as a function of period for the sample of variables with good σ Ori membership information. Short-period rotators appear slightly more likely to have amplitudes below 0.04 magnitudes than those with periods greater than 5 days, but it is difficult to sort out observational biases from this effect. Although different spot configurations may produce the same brightness patterns, we estimate a typical spot coverage of at least $\sim$2% based on the median 0.02 magnitude light curve amplitudes, assuming black spots. If, on the other hand, the temperature contrast between spots and the surrounding photosphere is closer to 80% (e.g., $T_{\text{spot}}/T_{\text{phot}}$), then coverage increases to $\sim$10%. Such contrasts and amplitudes are characteristic of either cool or hot spot covering fractions in young star samples (Frasca et al. 2009). Since amplitude does not appear to be correlated with period or color, we suggest that the mechanism producing the spots does not vary appreciably with rotation and possibly mass. Furthermore, because the majority of our objects are expected to be fully convective, the lack of correlation between spot coverage and other parameters may be indicative of uniform magnetic properties across the low-mass regime.

5.4 "Peculiar" variables

While over 40% of our detected variables are clearly periodic (Tables 5.1 and 5.3; Figs. 5.2 and 5.3), some 28% are highly stochastic (Tables 5.2 and 5.3; Figs. 5.7 and 5.6). As

discussed above, the former are associated with stellar rotation and the latter with processes associated with disk accretion. A number of intriguing objects among the stochastic class in σ Ori appear to have repeating patterns that are not, however, identified as periodic, the most prominent eight of which are shown in Fig. 5.16. They tend to display large-amplitude ($\sim$0.2–0.5 mag) dips of short duration (less than one day to a few days) in their light curves, preceded and followed by lower amplitude and longer timescale fluctuations. In some cases the fading can take up to a week. A few objects (2MASS J05382050-0234089 and 2MASS J05390276-0229558) display brightness dips with symmetric ingress and egress suggestive of some sort of occulting body; other brightness dips are rapid enough that we have only observed a portion of the event. Among all of the aperiodic σ Ori light curves we identify approximately 20% of the sample that undergo fading events. We do not identify this phenomenon in the Cha I dataset, but this may be because of the somewhat sparser time sampling.

Stars displaying such distinct fading episodes may represent a low-mass analog of the UX Ori class (UXORs), in which brightness decreases of up to several magnitudes appear and persist for up to tens of days. The phenomenon has also been referred to as "Type III" pre-main-sequence variability (Herbst 1994). While it is typically associated with objects of spectral type K0 and earlier, it has been identified in the form of quasi-periodic, deep (i.e., on the order of a magnitude) brightness dips in a few T Tauri stars, notably AA Tau (Bouvier et al. 1999). Among the several theories that have been suggested to explain the prominent dips seen in these variables, the most common invokes extinction events, in which clumpy material in a surrounding disk occults the central object from time to time. As the opacity increases the star becomes fainter and redder until scattering dominates and the object becomes bluer as it continues to fade. Bertout (2000) accounted for the recurrence of brightness dips with a model in which the occulting region is a high-latitude "warp" that periodically obscures the star above the extinction of a flared disk that is typical over the rest of the orbit. For the more sporadic fading, another theory is that the behavior may be due to variable accretion (Herbst 1994).

The diversity of light curve properties for the "peculiar" variables discussed here hints at multiple origins for the fading events, some of which may be well described by the periodic disk occultation model. While all of these objects have been classified as aperiodic based on the lack of one or more discrete peaks in the periodogram, most do display signal patterns in
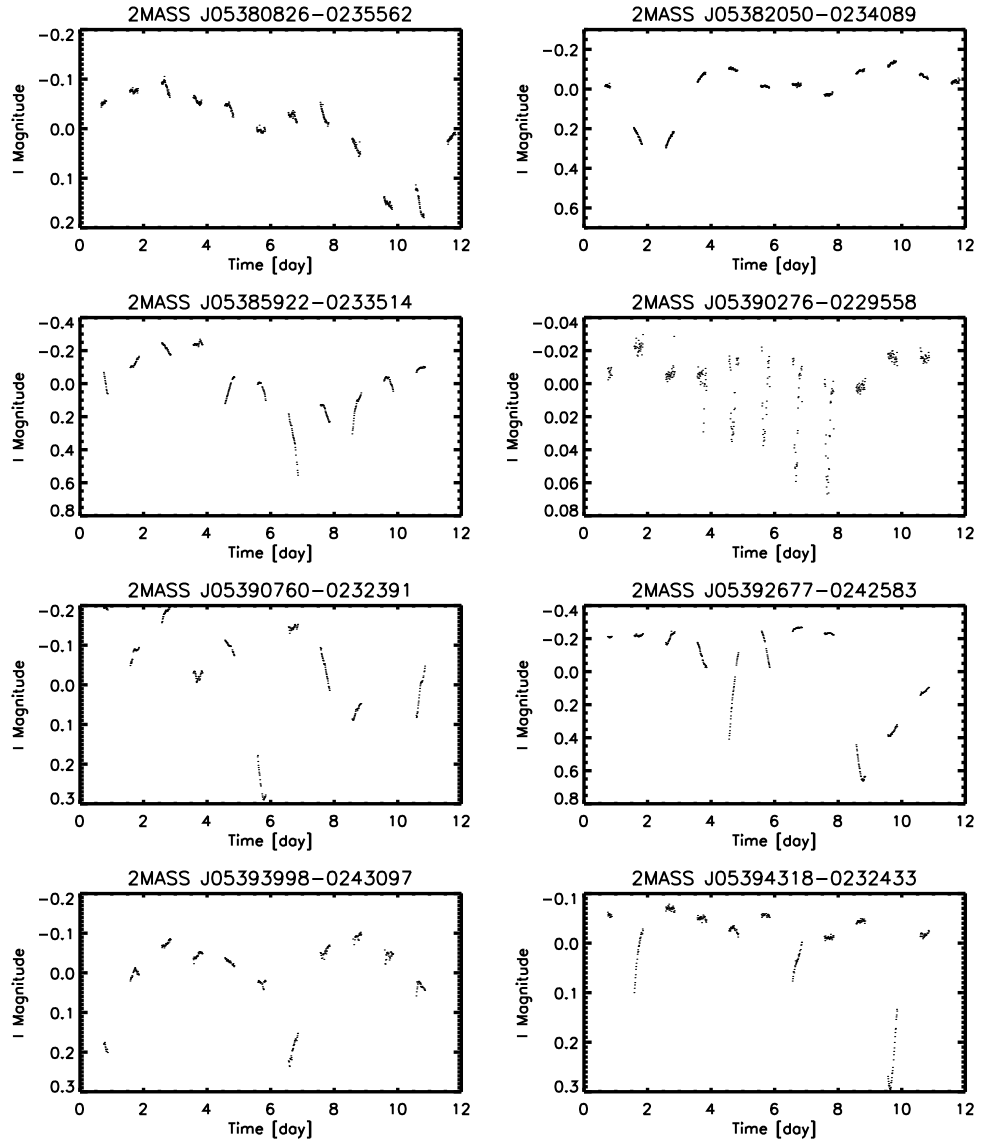
Figure 5.16 Aperiodic light curves with one or more unusually pronounced brightness dips

the frequency domain that are not consistent with either white or red noise. These include five or more peaks or clusters of peaks in the periodogram, indicating semi-periodic light curve behavior. We find that two or three objects, or ∼25–40% of this sample of eight, are quasi-periodic in their short duration fading behavior. This fraction is similar to the 28% estimated by Alencar et al. (2010) for periodic "AA Tau like" behavior in a comparable set of young stars in NGC 2264 determined from consideration of optical wavelength CoRoT data. Examining in detail the light curves of 2MASS J05390276-0229558 and 2MASS J05394318-0232433, we can estimate eclipse durations, depths and frequencies, assuming that the same "blob" of material is responsible for each fading event. For 2MASS J05390276-0229558, we estimate an eclipse repeat period of ∼1 day and duration of ∼0.2 day, while the light curve of 2MASS J05394318-0232433 displays dips of period ∼4 days and duration of ∼0.85 day. The stars, which are of similar I-band magnitude, have masses of ∼0.4 $M_\odot$ and radii ∼1.2 $R_\odot$, as estimated from the 3 Myr models of Baraffe et al. (1998). If the material is in a circular orbit, then its distance from the star can be deduced based on these stellar parameters along with the ratio of the eclipse duration to the repeat period. This rough estimate reveals that the occulting material must be extremely close to the star–within a stellar radius in both cases. In this scenario, the light curves may actually be displaying an impending accretion event, in which migrating material merges with the central star. If, on the other hand, the fading events are caused by distinct blobs of material, then their locations may be much farther out. The depths of the fading events (∼4% and ∼15%, respectively) imply sizes for the material of 0.2–0.4 stellar radii.

The presence of disks around our peculiar variables also sheds light on the origin of brightness fluctuations. Based on Spitzer photometry (§5.5.1) and the analysis of Hernández et al. (2007), we find that five of the eight peculiar variables shown in Fig. 5.16 are Class II type young stellar objects, surrounded by a thick disk but beyond the stage with significant high latitude (envelope) material. A further two objects (2MASS J05392677-0242583 and 2MASS J05390760-0232391) have weak $Spitzer$ infrared excesses ([3.6]-[8.0] color between 0.3 and 0.7). 2MASS J05392677-0242583 is probably an "anemic" disk (Lada et al. 2006), while 2MASS J05390760-0232391 was classified as a transition disk by Hernández et al. (2007) based on its large 24 μm excess. The data suggest that both have optically thin inner regions. 2MASS J05390276-0229558, on the other hand, does not appear to have either a disk or any signs of strong Hα emission. The fact that the intriguing eclipse-like variations

seen in its light curve are much lower in amplitude than the other peculiar variables may indicate the presence of more consolidated disk material unobservable at $Spitzer$/IRAC wavelengths. For the majority of objects mentioned here, we believe the variability can be plausibly interpreted as extinction by "clouds" or geometric warps of relatively higher opacity than the disk atmosphere which produce fading events as the feature passes through our line of sight to the star while the disk rotates.

Color data can help further illuminate the source of peculiar variability, since we have not ruled out accretion effects. Different trends in color are expected depending on whether the variations are caused by extinction, disk scattering, or stellar spots, as explained by Carpenter et al. (2001) and Scholz et al. (2009b). Since we have acquired R-band data twice per night for all targets, we can examine R-I as a function of brightness for all aperiodic variables, and check whether any particular pattern stands out for the eight selected peculiar variables. We present in the right panel of Fig. 5.7 the available colors and magnitudes. Notably, with only lower cadence data (as represented in the middle panel) the richness and coherence of the light curve forms would be hidden. In many cases the fading events observed among our aperiodic variables are relatively colorless although both significant reddening and significant blueing is observed among the sample. We have measured the slope of reddening for all aperiodic variables in Fig. 5.7 by fitting a linear trend to the I-band magnitude as a function of R-I. We then negate the result so that slopes less than zero represent reddening as an object becomes fainter. The distribution of values is presented in Fig. 5.17. Although the color light curves do not have enough points to enable a detailed fit to the various variability models, we note that the vast majority of aperiodic variables show either negative or zero slope. For comparison, we have also plotted the value expected for pure interstellar extinction. Since the material in disks may be substantially different, we do not necessarily expect it to follow the same extinction law. Indeed, several of the peculiar variables display much more reddening during their fading episodes. The modeling by Carpenter et al. (2001) and Scholz et al. (2009b) showed that hot spots from accretion can in fact exhibit steeper reddening slopes than extinction, at least in the near-infrared. This is certainly a possible explanation for some of our own sources. Only two objects in our sample, however, exhibit variability that may be accounted for by emission or scattering by the circumstellar disk, which is predicted to produce relatively *blue* fading events (Carpenter et al. 2001). Intriguingly, 2MASS J05390276-0229558, the only peculiar
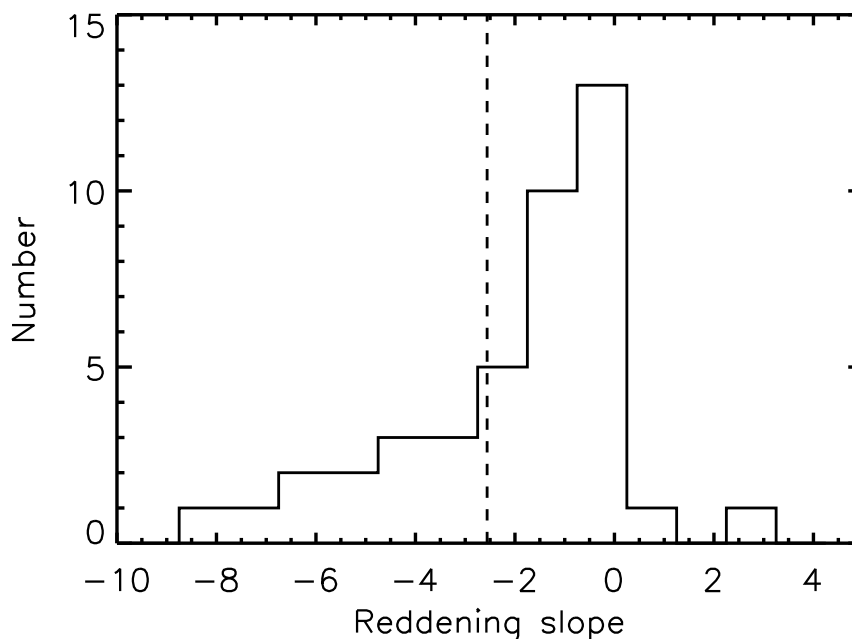
Figure 5.17 Histogram of reddening values derived from the slopes of the I versus R-I trends displayed in Fig. 5.7. Negative values correspond to increased reddening with decreasing brightness. The dashed line marks the value for interstellar extinction, -E(R-I)/A_I.

variable with no infrared excess, is one example. The single data point caught while this object was at its faint limit shows substantially bluer color than the rest of the light curve. We envision a scenario in which material temporarily occulting the star also scatters light toward us.

Although we cannot rule out the presence of accretion effects, we conclude that the hypothesis of occultation by disk material is qualitatively consistent with both the duration and the color-magnitude behavior of the brief fading events seen in the set of eight peculiar variables presented here. Further, as some of the events are periodic or semi-periodic, we note that the derived periods are consistent with those expected from an inner disk region in co-rotation with a star having typical spin for a Class II T Tauri star (2–10 days). Similar features located further out in the disk could be responsible for the non-repeating and/or broader fading events.

5.4.1 SOriJ053825.4-024241: a high-amplitude variable brown dwarf

Among our sample, the substellar σ Ori member SOriJ053825.4-024241 stands out as the lone target highly variable on timescales less than 24 hours. With a 3.6-μm-band RMS of 0.035 magnitudes, this object has a peak-to-peak amplitude of 0.15 magnitudes. It displays variations about four times as large in the I-band, based on our longer timescale ground-based dataset (Cody & Hillenbrand 2010). Other studies (Caballero et al. 2006) have indicated that SOriJ053825.4-024241 is actively accreting and has a disk (Hernández et al. 2007).

No previous infrared studies of brown dwarfs have uncovered aperiodic variability on such short timescales. However, variability of young stars at Spitzer wavelengths or of brown dwarfs in general with these amplitudes and on longer timescales is not unprecedented. The Young Stellar Object Variability (YSOVAR) project (Morales-Calderón et al. 2011) campaign on young Orion Nebula Cluster stars (masses $\gtrsim 0.1$ $M_\odot$) has also found substantial erratic variability in the 3.6 and 4.5 μm bands. Assessment of their data has shown that the aperiodic variables among the sample known to harbor disks display a range of variability RMS values centered on ~ 0.03 magnitudes in the 3.6 μm band (Morales-Calderón 2011, private communication). Similar amplitude distributions were obtained using existing multi-epoch data with limited cadence in Taurus and Chamaeleon I by Luhman et al. (2008a) and Luhman et al. (2010). The typical RMS of a few hundredths of a magnitude is quite consistent with the value that we have measured for S Ori J053825.4-024241. Morales-Calderón et al. (2011) discuss the possible causes of the mid-infrared variability and surmise that many of their variables may be explained by variable obscuration by overdense regions in the inner disk, while others are caused by intrinsic changes in the inner disk emission itself. Either of these scenarios may apply to SOriJ053825.4-024241. In any case, hot accretion gas is likely too faint at infrared wavelengths to serve as the source of variability for this object.

To further explore the behavior of this BD on different timescales, we have performed an autocorrelation analysis. In addition to displaying quasi-periodicity patterns not picked up by the periodogram, it is useful in assessing the timescale on which the variability mechanism remains coherent. We have calculated an autocorrelation function based on the S Ori J053825.4-024241 light curve using both a standard, "biased" formula, as well as one
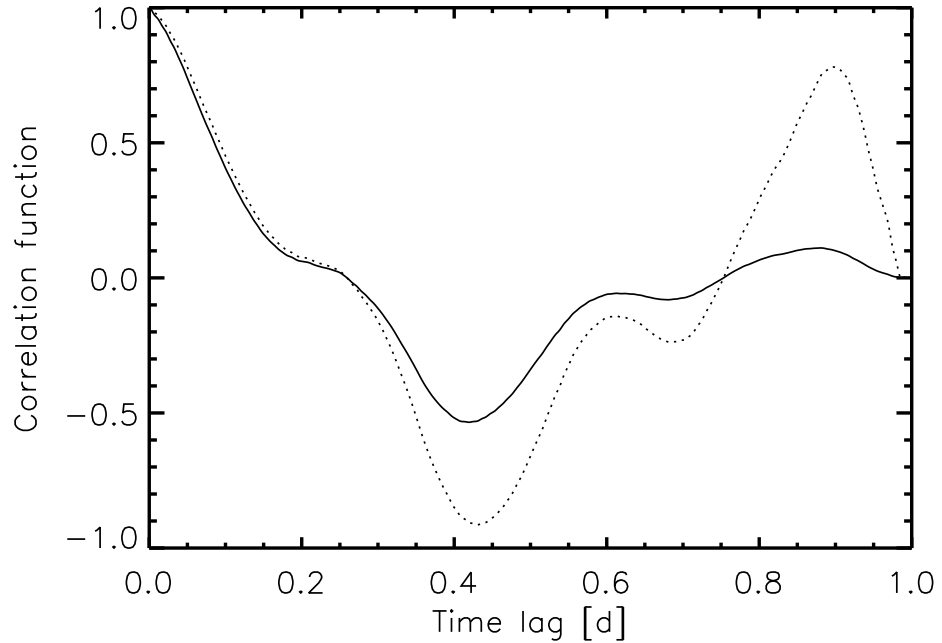
Figure 5.18 Autocorrelation functions for SOriJ053825.4-024241. The solid line is the standard ACF, whereas the dashed line is the version that has been corrected for finite data length.

that corrects for the finite data length. The standard autocorrelation function (ACF) is given by:

$$A(t) = \frac{1}{A(0)} \sum_{j=1}^{N-t/\Delta t} L(j)L(j + t/\Delta t),$$

where $L(j)$ are the light curve points, Δt is the time spacing between data points (which must be uniform), N is the total number of points, and the $A(0)$ factor in front is included so that at a time lag of zero, the ACF is completely correlated ($A(0) = 1$).

To account for the fact that fewer points are available to calculate the ACF at longer lag times ($t > 0.5$), we have produced another version–the "unbiased" ACF–in which the this roughly linear effect ($\sim N - t/\Delta t$)) has been divided out. In both cases, we have computed the autocorrelation via Fourier transform of the power spectrum (as specified by the Wiener-Khinchin theorem; Wiener 1930; Khinchin 1934), since this is both faster and less prone to numerical inaccuracies.

Both versions of the ACF are plotted in Fig. 5.18. We find that the light curve is well correlated up to timescales of $\sim$0.15 d, or 3.6 h. At longer timescales, it also shows significant correlation due to the overall trend seen in the light curve; this is illustrated

by the two peaks at $\sim$0.43 d and $\sim$0.9 d (the latter primarily in the unbiased ACF). We conclude that the variability mechanism is physically coherent on timescales of at least a few hours. The hypothesis of variable obscuration in association with the disk is qualitatively consistent if the scale of clumpiness and location of dust is such that fluctuations would pass by the face of the BD in several hours.

5.5 The relationship between variability and circumstellar disks

Disks around young stars can be readily identified through thermal emission from circumstellar dust, manifest as infrared excess, or from gaseous emission lines attributed to accretion and outflow processes close to the star and seen spectroscopically. In this section we investigate the correlation between optical photometric variability and the evidence for circumstellar dust and gas.

We cross-referenced our photometric samples in σ Ori and Cha I with those of Luhman et al. (2008b), Luhman et al. (2008a), and Luhman & Muench (2008), which provide *Spitzer* Infrared Array Camera (IRAC; 3.6–8.0 μm) and in some cases Multiband Imaging Photometer for Spitzer (MIPS; 24 μm) photometry. In σ Ori, we find that 133 of 153 confirmed or candidate members in our time series dataset have *Spitzer* photometry, including 57 of 65 cluster periodic variables. For the Cha I sample, all 37 cluster members monitored in the i band have available IRAC measurements, and in many cases, MIPS data in addition. While there is *Spitzer* data available for the IC 348 cluster as well, we have not included it in the analysis here since extensive comparison of photometric periods with infrared excess was already carried out by Cieza & Baliber (2006). Furthermore, our own IC 348 photometry is difficult to cleanly separate into the periodic and aperiodic categories due to systematics resulting from the lack of tracking on the P60 telescope.

Mid-infrared photometry enables nearly unambiguous identification of unevolved disks in young clusters, as noted by Luhman et al. (2008b). The σ Orionis observations are unique among nearby young cluster observations with *Spitzer* in that they were designed to search for disks around low-mass brown dwarfs and even planetary-mass objects; hence they are particularly deep. This additional data gives us an unprecedented opportunity to study the relationship between variability, rotation, and presence of disks in the very low mass

regime, potentially illuminating the reason why young cluster rotation period distributions have been reported to change around $\sim$0.25 or 0.4 $M_\odot$ (Rebull et al. 2006; Cieza & Baliber 2007), and why the rotation periods in our own dataset appear to undergo a transition near R-$I = 1.3$ ($\sim$0.45 $M_\odot$; as discussed in §7.3.1).

5.5.1 Disk selection criteria

We display in Figs. 5.19 the distribution of $Spitzer$/IRAC 3.6–8.0 μm colors for all objects in our σ Ori and Cha I datasets with available infrared photometry. As seen in the figures, the samples split relatively cleanly into two groups, with the narrower blue sequence near [3.6]-[8.0] $= 0$ representing bare photosphere colors. The cloud of objects with [3.6]-[8.0] colors between 1 and 2 is indicative of infrared excesses signifying the presence of a dusty disk. While the sequence of *photospheric* colors is fairly well defined, several ambiguous objects lie between 0.3 and 0.7 magnitudes. We have therefore chosen a somewhat conservative disk selection criteria of [3.6]-[8.0] > 0.7 (e.g., Cieza & Baliber 2007) so as to omit these objects from the disk sample.

In total, we identify 47 likely σ Ori members with both photometry from our campaign and $Spitzer$ colors indicative of disks, along with 21 disk-bearing Cha I members. The resulting disk fractions in our samples are roughly 35±5% and 57±9%, respectively. We find that our disk identification is entirely consistent with that of Hernández et al. (2007), Caballero et al. (2007), Luhman et al. (2008a), and Luhman & Muench (2008) (based on the same $Spitzer$ data), apart from one newly-identified disk-bearing object in σ Ori, 2MASS J05375398-0249545, which has a [3.6]-[8.0] color of 1.3. The full listings of disk classifications are provided in Tables 4.1 and 5.3.

Previous works exploring connections between variability and the presence of disks often have relied on colors at shorter wavelengths to infer the presence of circumstellar dust. To test the suitability of this method, we produced another color-magnitude diagram for σ Ori objects using R-J and H-K colors, as seen in Fig. 5.20. Here the $Spitzer$-identified disk-bearing objects in σ Ori are highlighted by red squares. While there are a number of targets with sufficiently large H-K to confirm a dust excess, many others that *do* have disks based on the $Spitzer$ data cannot be distinguished from the sequence of photospheric colors with H-K ranging from 0.2 to 0.4.

238
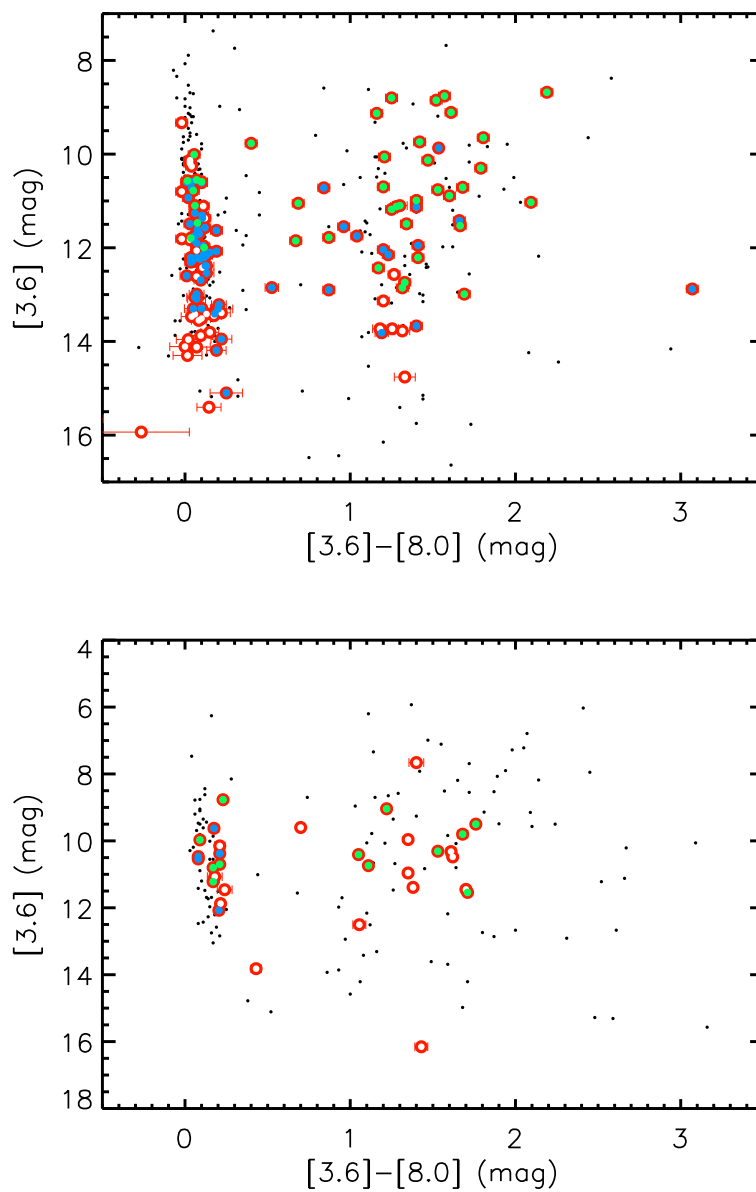
Figure 5.19 *Spitzer* photometry of likely σ Ori members (*top*) and Cha I members (*bottom*). Objects found in our photometric sample are marked with red circles, while those out of the fields are left as dots. Error bars are included but in many cases too small to see. Aperiodic variables detected in our photometry are overplotted as filled green circles, while periodic variables in our sample are marked by filled blue circles. The nearly vertical cluster of objects near [3.6]-[8.0] = 0 is the sequence of colors and magnitudes pertaining to bare photospheres.
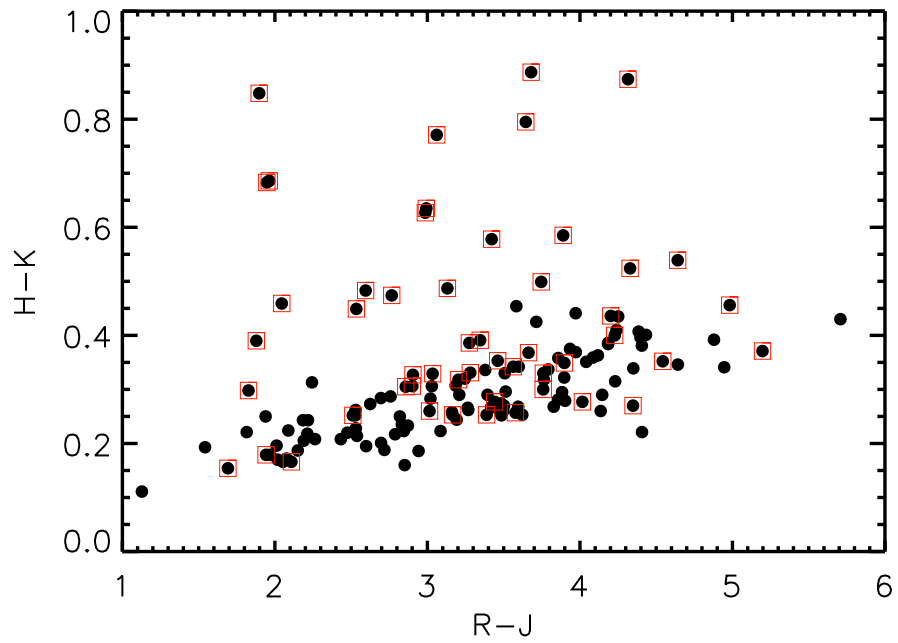
Figure 5.20 *R-J* and *H-K* colors for σ Ori cluster members in our sample. Disk identification at these wavelengths is possible for objects whose *H-K* colors significantly exceed the trend in photospheric colors visible along thee bottom of the diagram. Targets for which *Spitzer* infrared data implies the presence of a disk are surrounded by red squares. Fewer than half of disk-bearing members would have been selected based on the near-infrared method.

5.5.2   Variability-disk connection

In Fig. 5.19 we have distinguished variable objects from the non-variables in the *Spitzer*/IRAC color-magnitude diagram. Not all of our photometric targets in σ Ori are included in the *Spitzer* sample due to varying spatial coverage. Of the 133 that are, we identified 97 as variables (e.g., Tables 5.1 and 5.2). The majority of objects with clear periodicities have no evidence for a disk (43 of 57), while a subset of 13 do show clear infrared excess. The disk fraction among periodic variables in this cluster is thus $\sim$23$\pm$6%, somewhat lower than the overall disk fraction. However, this measurement may be biased by the fact that we cannot measure periods in disk-bearing objects that are undergoing relatively high amplitude accretion events. Four objects fall in the ambiguous category with [3.6]-[8.0] colors between 0.3 and 0.7. One of these (2MASS J05390808-0228447; [3.6]-[8.0] = 0.53) has a clear periodicity with period 1.7 days and amplitude 0.02 magnitudes, similar to other variables that lack infrared excesses. The remaining three (2MASS J05390760-0232391, 2MASS J05390878-0231115, 2MASS J05392677-0242583) exhibit much more erratic and higher amplitude (RMS$\sim$ 0.2–0.3 magnitudes) variability. In the smaller Cha I sample, on the other hand, none of the periodic variables has an infrared excess suggestive of a disk.

For both clusters, we can associate disks with the majority of aperiodic variables in our sample and lack of a disk with most of the periodic variables. This outcome is no surprise, since the aperiodic variability is likely due to accretion, which requires a disk. Likewise, since the variability in most of these disk-bearing objects is relatively high amplitude ($\sim$0.1 magnitudes RMS on average), we do not expect to detect many periodic variables among this sample, for the reasons outlined in §5.1.2.2.

But a number of objects do not fit these scenarios. Nine σ Ori members and five Cha I members display aperiodic variability but no sign of infrared excess in the *Spitzer* data; the additional three σ Ori objects highlighted above have only weak signs of an excess. In addition, 13 σ Ori members with clear-cut infrared excesses display periodic variability with only low-level erratic behavior suggestive of accretion. In a few cases where signal-to-noise is particularly high (e.g., 2MASS J05391883-0230531 and 2MASS J05381866-0251388), it is possible to see that the phased light curve is a combination of a nearly perfect sinusoid and a small additional "blip" that may be ascribed to transitory accretion.

Since the *Spitzer* data enables us to conclude only that an object is surrounded by

warm *dust*, the association between an infrared excess and accretion (i.e., infall of *gas*), is imperfect. This may explain why a number of objects identified as having disks do not exhibit aperiodic variability, if the gas supply in these systems has already diminished. Likewise, we conjecture that those targets displaying aperiodic variability but no infrared excess probably still have a gas component of a disk, whereas the dust is reduced or changed to the point of being undetectable at 8.0 μm and shortward. In the following sections, we explore in more detail the connections between each type of variability and the presence or absence of a disk.

5.5.3 Relationship between disks and periodic variability due to rotation

The connection between stellar rotation period and disk presence has long been a subject of speculation. Disks have been invoked as a mechanism to remove angular momentum from young stars, in order to explain the slow rotation rates seen at older ages, as compared to models of spin-up associated with radial contraction (Bouvier 2007). But while some studies have claimed a correlation between rotation rate and disk presence (e.g., Rebull et al. 2006; Cieza & Baliber 2007), others have refuted the so-called disk-locking theory (Koenigl 1991; Makidon et al. 2004), particularly in the low-mass regime. Our σ Ori dataset provides an opportunity to retest this paradigm at very low masses, and in a new cluster. The other clusters involved in the campaign had either too small a sample of rotation periods (USco, Cha I), or *Spitzer* data that was fairly shallow and has already been analyzed with respect to rotation rate (IC 348; Cieza & Baliber 2006).

To investigate the disk-rotation connection with our own data, we have examined the subset of 57 objects in σ Ori identified with both periodic variability and *Spitzer* [3.6]-[8.0] data. Among these periodic variables, only 13 fall in the disk sample with infrared color excesses. Unfortunately for the majority of disk-bearing objects, we cannot photometrically measure most of their rotation rates because of the prominent high-amplitude aperiodic variability. But we can nevertheless plot the periodic sample against *Spitzer* [3.6]-[8.0] color to discern any large differences between the rotation rates of objects with and without disks, as shown in Fig. 5.21. The sequence of likely diskless objects at [3.6]-[8.0] $\sim$ 0.0 contains a large spread of photometric periods from 8 hours to over 10 days. The objects with disks do have a slightly lower mean period, but this could be a selection effect. If there is a mass dependence for rotation or accretion properties, then this diagram may not
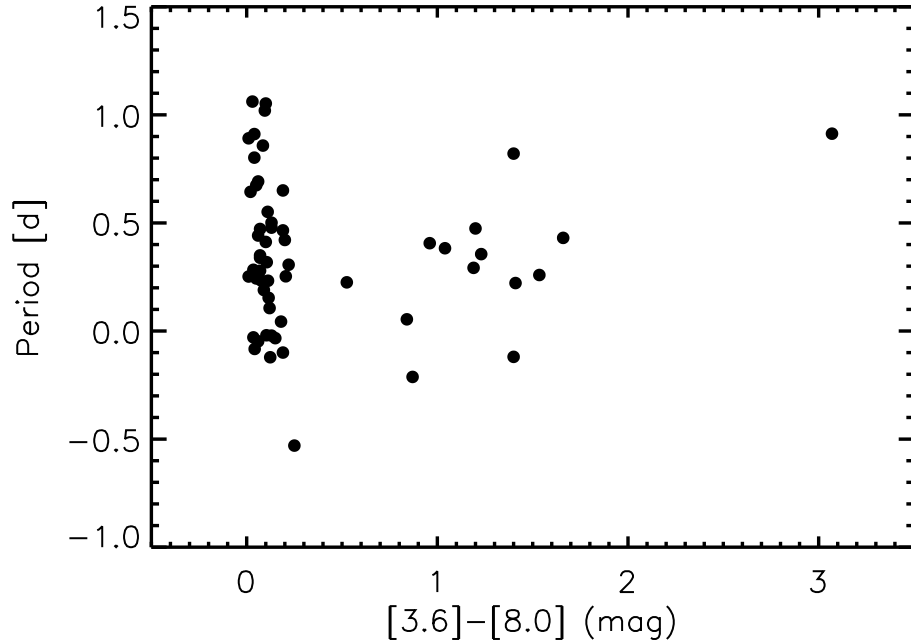
Figure 5.21 *Spitzer* [3.6]-[8.0] color versus rotation period for our periodic σ Ori members.

indicate the true distribution of rotation periods. For example, if low-mass stars rotate faster but accrete for longer, then we may not be detecting a number of short rotation periods through the larger-amplitude fluctuations due to accretion in the light curves. In addition, the fraction of disk-bearing objects appears to increase from $\sim40\%$ of low-mass stars (0.1–0.5 $M_\odot$) to $\sim60\%$ of brown dwarfs in σ Ori (Luhman et al. 2008b).

To circumvent the possible mass biases from our data, we have highlighted the disk-bearing objects among the rotation sample in Figs. 5.12 and 5.13; these are indicated by open circles. The inclusion of color information in addition to periods and disk presence enables us to examine the effect of the mass distribution underlying our sample. We have seen from this diagram that the rotation periods have a marked and significant trend toward longer timescale at bluer color (and hence higher mass), as discussed in §5.3.2. This correlation appears relatively independent of whether an object possesses a disk. To statistically test for differences between the rotation periods of objects with disks and without disks, we have plotted histograms of each distribution. We restrict both samples to $R\text{-}I > 1.3$ since there are only two disk-bearing stars blueward of this boundary, and rotation rates of the diskless

stars might be biased by mass. Using a two-sided Kolmogorov-Smirnov test (Press et al. 1992), we find that any differences between the rotation rate distributions of disk-bearing and diskless objects are not statistically significant, at the 7% level (i.e., $p = 0.93$). Even if we expand the analysis to include stars with R-$I < 1.3$, there remain no differences, at the 35% level $p = 0.65$). With the caveat that the statistics are based on small numbers, we conclude that the disk-locking paradigm is largely inconsistent with our observations. The distribution of rotation periods instead appears to be set primarily by mass and additionally by a possible a third parameter.

5.5.4 Relationship between disks and aperiodic variability

In this section, we explore more directly a linkage between aperiodic variability, accretion, and disks. Erratic light curve variations in young stars have long been tied to spectroscopic signatures of accretion (Joy 1942), although they can have several origins (Herbst 1994). In particular, classical T Tauri stars, classified by their broad Hα emission lines, undergo larger brightness fluctuations than the periodic variations more often seen in weak-lined stars Herbst (1994). The fact that most of our disk-bearing objects display variability that is both higher amplitude and more erratic supports this picture.

We can study the relationship between accretion and disk presence more directly by examining the available spectroscopy for our detected aperiodic variables in σ Ori. We have listed in Table 5.2 the Hα pseudo-equivalent widths (pEW) where available from previous work. The value of this parameter is typically used to distinguish between Hα emission that is chromospheric in nature, as compared to emission created in an accretion column and hence indicative of a disk. An equivalent width greater than 5–15 $\mathring{A}$ is typically chosen to identify accretors. We adopt here the criteria of Barrado y Navascués et al. (2003), in which the Hα pEW boundary between accretors and chromospheric emitters varies with spectral type. The value varies from 7 to 11 $\mathring{A}$ across the M spectral type range typical of our sample. We find that 13 of our 17 aperiodic variables with Hα pEW measurements from the literature have values consistent with accretion. The remaining four objects have fairly low RMS spread in their light curves that may indicate a different source for the variability.

Two of our σ Ori targets with the largest Hα pEW values are brown dwarfs, based on their faint I-band magnitudes: 2MASS J05382543-0242412 and 2MASS J05385542-0241208. The photometric data alone suggests that they are substellar accretors, because of the high-

amplitude variability and lack of detectable periodicities. The former object was studied in detail by Caballero et al. (2006, see note in Appendix A), but the latter was heretofore unknown as a variable, although it was noted as having a broad Hα emission line with an equivalent width of 190$\mathring{A}$ and other T Tauri-like spectroscopic features by Caballero et al. (2008).

To tie together the variability features, accretion indicators, and disk presence, we have compared the values of light curve RMS, Hα pEW, and *Spitzer* [3.6]-[8.0] color for our aperiodic variables in σ Ori and Cha I. We detect no correlation between RMS and Hα pEW in the former cluster, suggesting that the mechanism producing variability is somehow decorrelated with the strength of accretion. However, it must be noted that our photometry was taken well after (years, in many cases) the spectroscopic data. If either light curve amplitude or Hα emission is highly time-variable, non-simultaneity of the observations may explain this finding. In addition, we have examined the relationship between these parameters and the infrared excess. Large Hα pEW (> 10 Å) compares well with infrared excess as a predictor of disk presence in that all but one target with values greater than 10 Åalso have [3.6]-[8.0] > 1.0. But once again, we do not see any noteworthy trends in RMS or Hα with [3.6]-[8.0] color among targets identified as having disks.

There is a curious small population of objects, though, with RMS values ($\sim$0.01–0.03 magnitudes) much lower than the other aperiodic variables and whose Hα pEW and [3.6]-[8.0] values suggest *absence* of accretion or an associated disk. In addition to having light curves in which variability is clearly obvious by eye, these objects have χ^2 values high enough that their status as variables is not in doubt. All but one have $\chi^2 > 4.5$, or less than 10^{-5} probability that the light curve trends arose by chance; the remaining object (2MASS J05383922-0253084) has a χ^2 value of 2.85, or an estimated 0.4% probability that its light curve behavior is explained by noise. We show in Fig. 5.22 the RMS and infrared colors for σ Ori and Cha I members. The subset of nine low-RMS objects is seen as a cluster in the lower left corners and is clearly differentiated from the larger cloud of points with colors indicative of disks. Not all of these objects have available Hα pEW values, but for those that do we find they are all low, between 0 and 10 Å.

In summary, both Hα emission and [3.6]-[8.0] color are good indicators of disk presence. Light 'curve RMS is only a moderate indicator, since we encounter a number of disk-bearing objects with only low-level or periodic photometric variability. Of 47 σ Ori targets identified
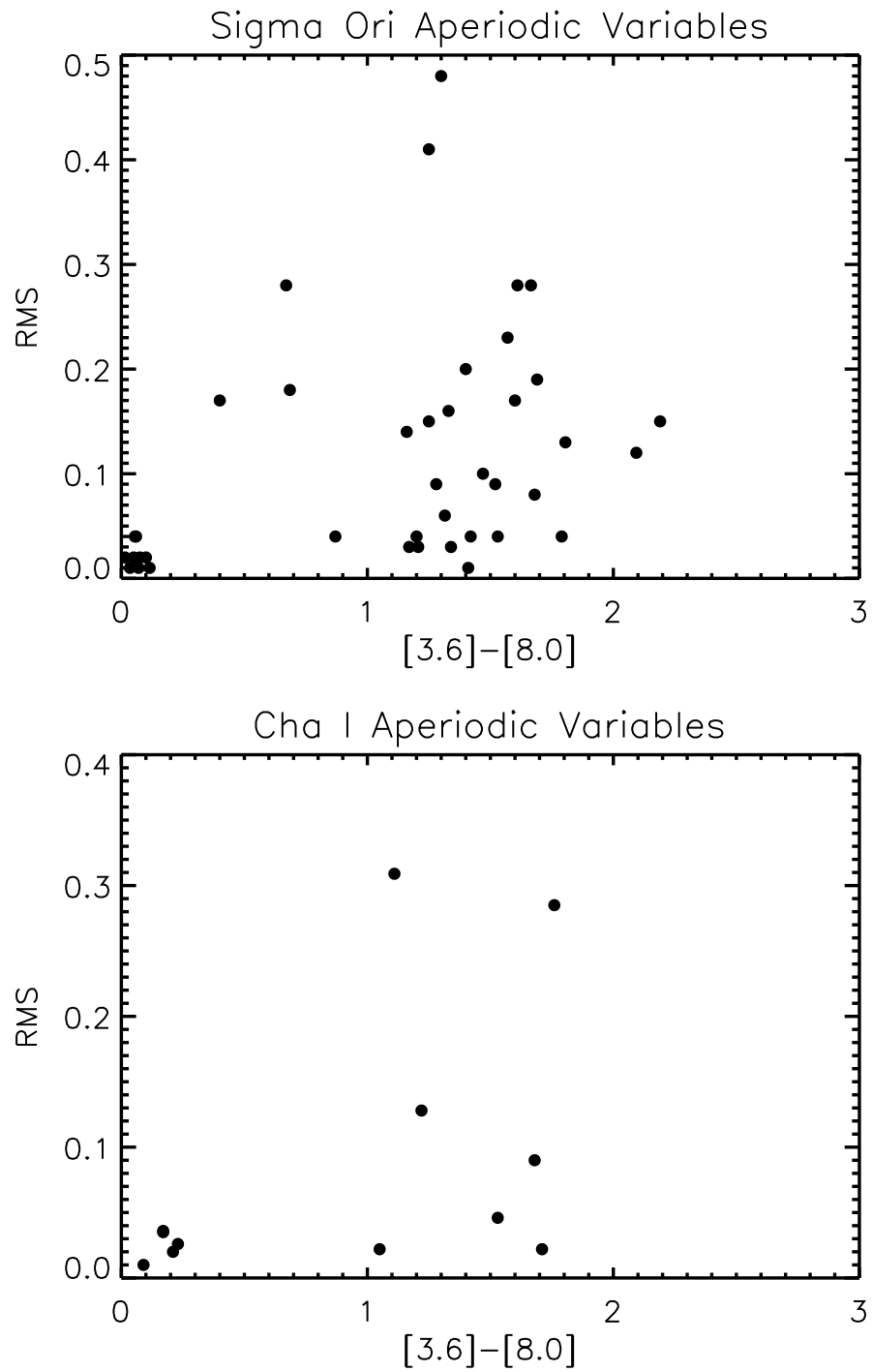
Figure 5.22 *Spitzer* [3.6]-[8.0] color versus light curve RMS value for our aperiodic variables in σ Ori (*top*) and Cha I (*bottom*)

with disks via *Spitzer* data, we find 19 (40%) have aperiodic variability with RMS values above 0.05 magnitudes. The distinct advantage of photometric monitoring thus appears to be the ability to identify aperiodic variables for which the other indicators do *not* suggest a disk or accretion. The variability in these cases is difficult to reproduce without invoking some sort of circumstellar material, since its erratic and short-time-scale nature suggests a dynamic process as opposed to thermal or magnetic phenomena associated with the stellar surface. We suggest that this small population of objects does in fact have residual disks undetectable at *Spitzer*/IRAC wavelengths, with possible accretion or dust occultation as the source of low-level variability. An alternate explanation is that we are witnessing rapidly changing surface spot features.

Chapter 6

Low-resolution spectroscopy of σ Orionis cluster candidates

6.1 The need for spectroscopic follow-up in σ Orionis

With our extensive photometric monitoring campaign on yong BDs and VLMSs, we have acquired high precision time series to identify variability on 10 minute to two-week timescales. The resulting light curves have revealed signs of numerous physical phenomena, producing variability down to the millimagnitude level, including periodic modulation by rotating stellar spots, accretion-related brightness fluctuations, and eclipses by companions. We have also identified several new candidate cluster members, based on variability alone.

To take full advantage of the wealth of photometric information, it is crucial to correlate the observed variability properties with more detailed spectroscopic measurements. Multicolor photometry offers an initial method to separate young cluster members from field objects but does not distinguish them well from foreground dwarfs and background giants of similar spectral type; a subset of our CTIO data illustrates this problem in Figs. 5.9 and 5.8. Low-resolution spectra, on the other hand, enable confirmation of youth via gravity-sensitive features and accretion indicators such as Hα. Spectroscopy also affords a determination of spectral type and hence inference of effective temperature and mass via well-calibrated models. The addition of spectroscopic membership confirmation and spectral types to photometric rotation datasets is also vital to placing low-mass pulsation candidates on the the H-R diagram for comparison with the theoretical deuterium-burning instability strip.

Fortunately most of the monitored objects have been extensively vetted for youth and hence cluster membership. The exception is our σ Orionis sample. For 91 objects in

cluster with photometry but no prior spectral types, we obtained low-resolution ($R \sim 1400$) spectra from the Double Spectrograph ("DBSP") on the 200-inch Hale Telescope at Palomar Observatory ("P200"). The relatively high spatial density and low extinction of this cluster make it one of the more attractive areas for comprehensive studies of young stars and BDs. While color magnitude diagrams based on photometric surveys (Wolk 1996; Sherry et al. 2004) have identified several hundred candidate cluster members in the vicinity of σ Orionis, the most recent compilation of confirmed members Caballero (2008) is relatively incomplete at low masses (<0.3 M$_\odot$) and largely devoid of spectral types. Spectral types tied to the effective temperature scale for particular theoretical models (e.g., Luhman et al. 2003b) permit a mass estimate, which is in turn important to our study of the angular momentum trends at young ages as well as the selection of pulsation candidates. We have therefore begun to extend the cluster membership census by obtaining spectra for a set of $\sim$100 candidate low-mass σ Ori members monitored with our photometric campaign. Of particular interest is the subset of targets that displayed variability during our monitoring survey.

6.2 Target list and observations

Our primary target list is drawn from a set of $\sim$120 variable objects detected at R-band magnitudes 14–20 in our photometric studies with the CTIO 1.0 m telescope. Much of the background work to pinpoint likely cluster members via two-color photometry and theoretical isochrones has already been carried out by, e.g., Béjar et al. (2004), Sherry et al. (2004), Kenyon et al. (2005), Hernández et al. (2007), and Caballero (2008). We cross-correlated these lists to assemble a set of very low mass stars and brown dwarfs with high probability of youth (i.e., ages 1–10 Myr), and ultimately observed 91 of them. The majority of these suspected cluster members lie within 0.5 degrees of the star σ Orionis. Additional targets on the list included several spectrophotometric standards, as well as a grid of K- and M-type spectral standards including field dwarfs and young stars and BDs in IC 348 previously classified by Luhman et al. (2003b).

Observations took place during two runs in 2009 from January 18 through January 21 and 2009 December 19 through December 21. Conditions were not photometric, so interruptions to observation were frequent and sky lines were prominent in many spectra.

We primarily used a $2''$ slit. The Double Spectrograph is so named because of its two CCDs, one of which operates at predominantly blue wavelengths (e.g., $\lambda < 7000$ Å), and the other in the red ($\lambda > 6000$ Å). The red CCD is significantly more sensitive than the blue, but exposures times for both sides are usually the same since data is acquired simultaneously. Most of the spectral lines of interest to young cluster members lie at 6563 Å (Hα) and redward. Therefore, in the interest of observing as many targets as possible, we optimized exposures to the red CCD and accepted lower signal-to-noise spectra in the blue.

For the first of the two runs, we used a 6800 Å dichroic with a 316 lines mm^{-1} grating blazed at 7500 Å on the red side, for a total wavelength coverage of 6875–9400 Å. On the blue end, the grating was 1200 lines mm^{-1} blazed at 7100 Å, resulting in data from 5600–6620 Å. The corresponding spectral resolutions for this setup were approximately 1500 and 4200, respectively. On the second run, we instead employed a 5500 Å dichroic with a 316 lines mm^{-1} grating blazed at 7500 Å on the red side, and a 1200 lines mm^{-1} grating blazed at 5000 Å on the blue side. The respective wavelength ranges were 6300–8900 Å and 4190–5300 Å, and the resolutions were 1450 and 3300. With exposure times from 200–600 seconds we obtained spectra with typical signal-to-noise values near 30 per pixel in the red and much poorer in the blue ($\sim$5–10). Some targets required multiple exposures to obtain adequate signal, and 12 spectra had to be discarded because of severe sky line contamination.

6.3   Data reduction procedures

Basic reduction of the spectroscopic data was carried out[1] separately for the red and blue exposures, using standard IRAF procedures in the *ccdproc* package. These included subtraction of the bias, trimming the overscan, and normalizing the sensitivity via dome flatfields. Extraction of the signal was straightforward, except in a few cases for which the signal-to-noise ratio was poor. For these, we used a lower degree polynomial for the spatial trace, and sky subtraction was sub-par, imprinting some atmospheric absorption lines in the spectra.

We performed the dispersion correction based on the identification of arc lines from a combination of He, Ne, Ar, and FeAr lamps. Finally, flux calibration was carried out based on comparison with the spectra of the four spectrophotometric standard stars Feige 34, Hiltner 600, HD 19445, and G191B2B from Massey & Gronwall (1990) and Fukugita

---

[1]We acknowledge J. Robaszewski for performing most of these procedures.

et al. (1996). We estimated the signal-to-noise ratio of the flux-calibrated spectra within the ranges 7445–7515 Å (red) and 5985–6015 Å (blue). The set of red spectra from each run is presented in Figs. 6.1 and 6.2.

6.4 Emission line features

Young stars and brown dwarfs tend to display several prominent emission features, including Hα (6563 Å), He (5876 Å), and calcium II (8542 Å). While some of these are chromospheric in origin, very broad lines are associated with accretion. We measured the equivalent widths of these three lines where present and tabulate the values ("EW" or "W"), in Angstroms, in Table 6.1. As expected for actively accreting young stars, broad Hα emission is found in nearly every spectrum. Helium and calcium emission also appear but are somewhat less common. For some objects with spectra from both observing runs, we note substantial variability in the Hα equivalent width.

The Hα lines, if broad enough, provides strong evidence of an object's youth. A typical cutoff for the equivalent width (W_λ) used to distinguish chromospheric and accretion-related emission is W_λ=15 Å, a value typical of field dwarfs. However, since the level of chromospheric activity varies as a function of mass, Barrado y Navascués et al. (2003) have suggested an alternative trend for the cutoff that varies with spectral type. We take this into consideration when determining the membership status of the targets (§6.6).

6.5 Spectral Types

We have derived spectral types through a combination of quantitative and visual methods. Within the optical band are a number of temperature-sensitive molecular absorption regions such as TiO (7140, 8165Å). Measurement of spectral indices and calibration against standards can provide spectral type to half a subclass and temperature to approximately 100 K (e.g., Reid et al. 1995; Slesnick et al. 2006a). We adopted the indices suggested by Slesnick et al. (2008), which are denoted TiO-7140 and TiO-8465. These represent the flux ratios of TiO absorption as compared to surrounding continuum bands. Our measurements are listed in Table 6.1, and we used them to estimate spectral types based on the calibration by Slesnick et al. (2008).

We visually confirmed spectral types by comparison with data taken with the same

251
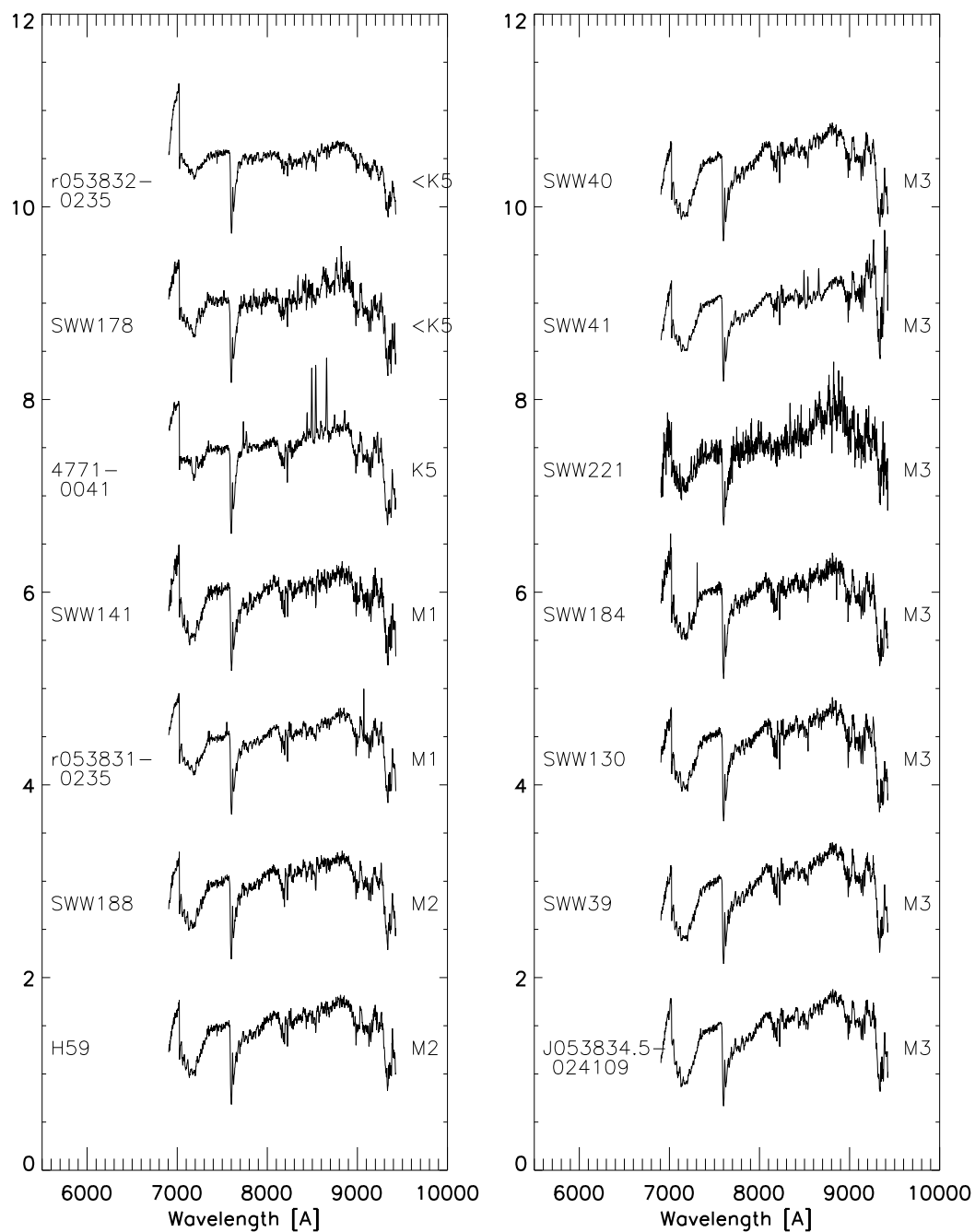
Figure 6.1 Red channel spectra of σ Ori candidates from the January 2009 Palomar 200-inch/DBSP observing run. Spectra are normalized to their median flux value and shifted for clarity.
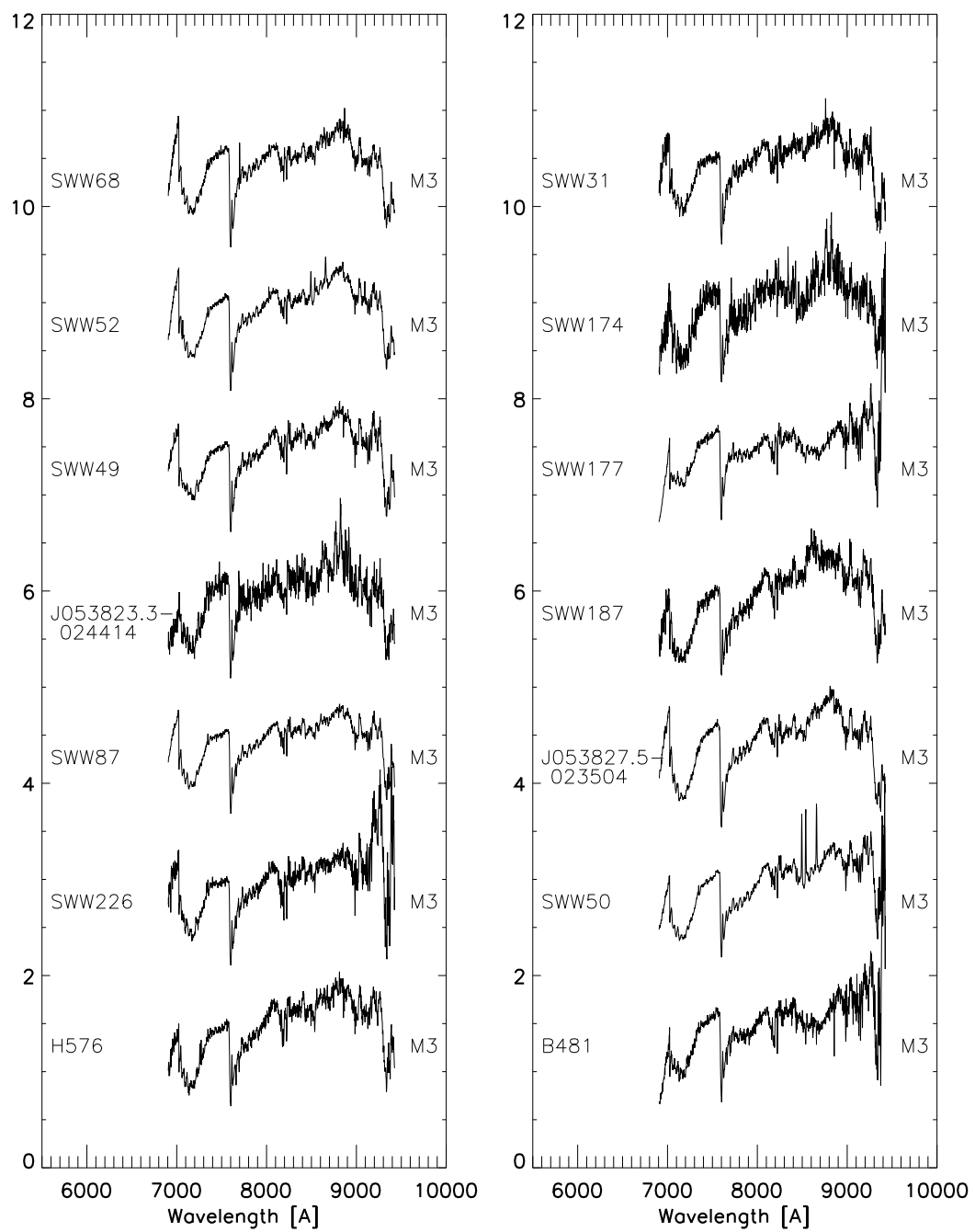
Figure 6.1 –Continued
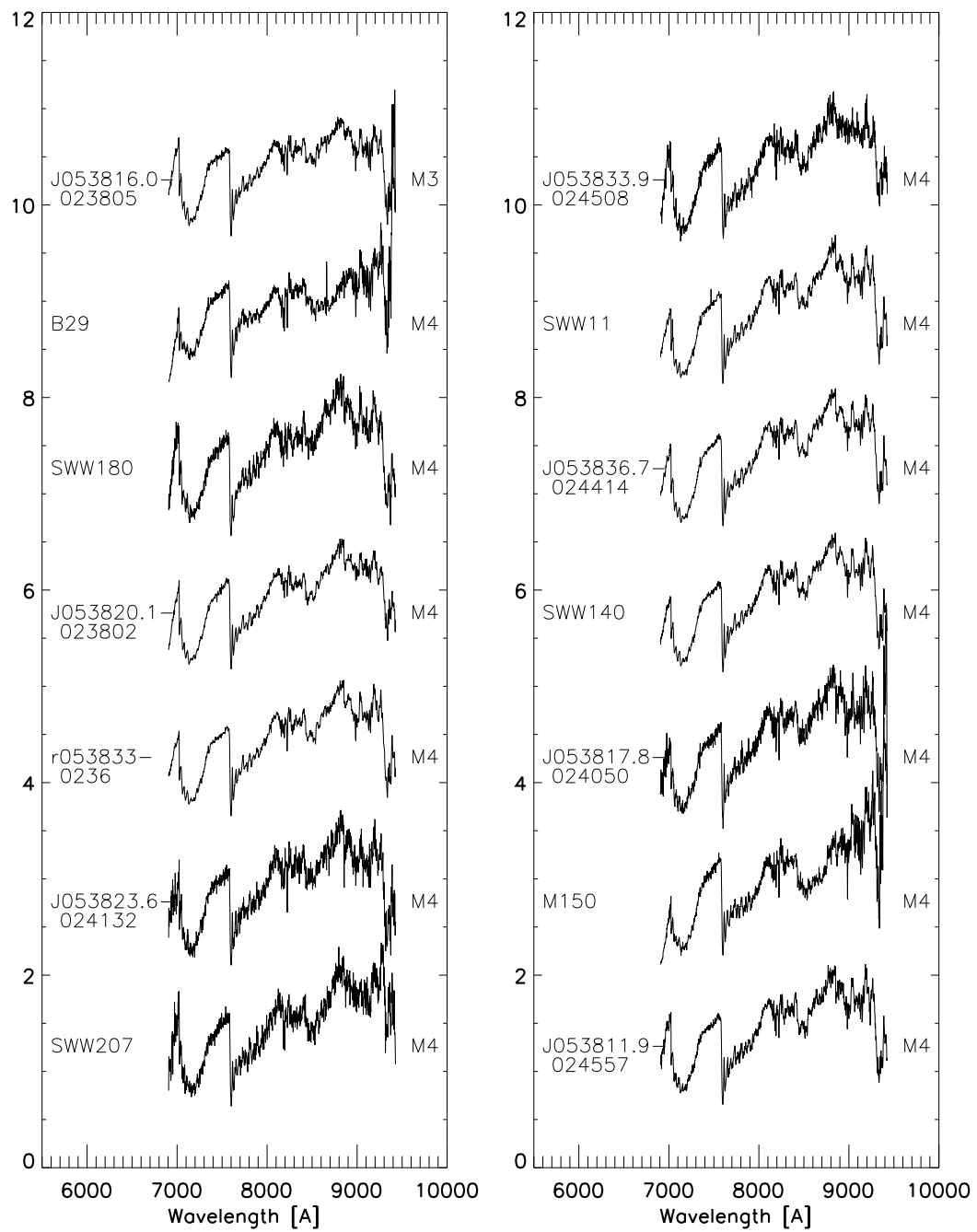
Figure 6.1 –Continued
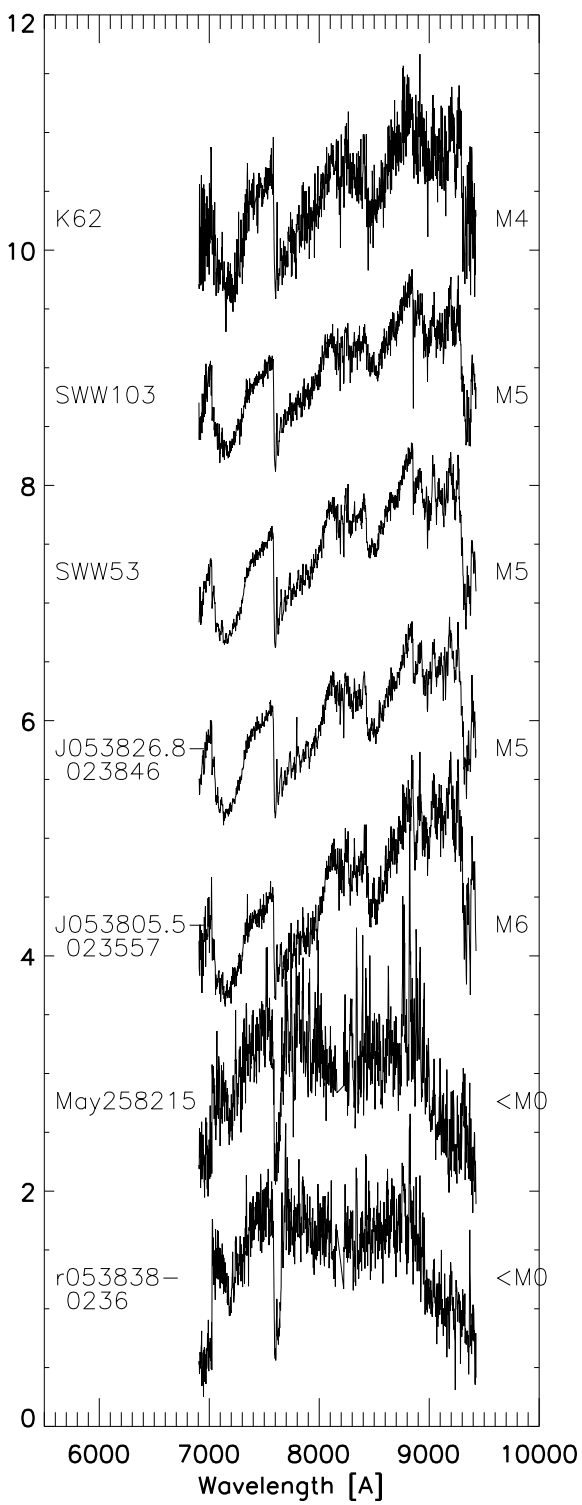
Figure 6.1 –Continued
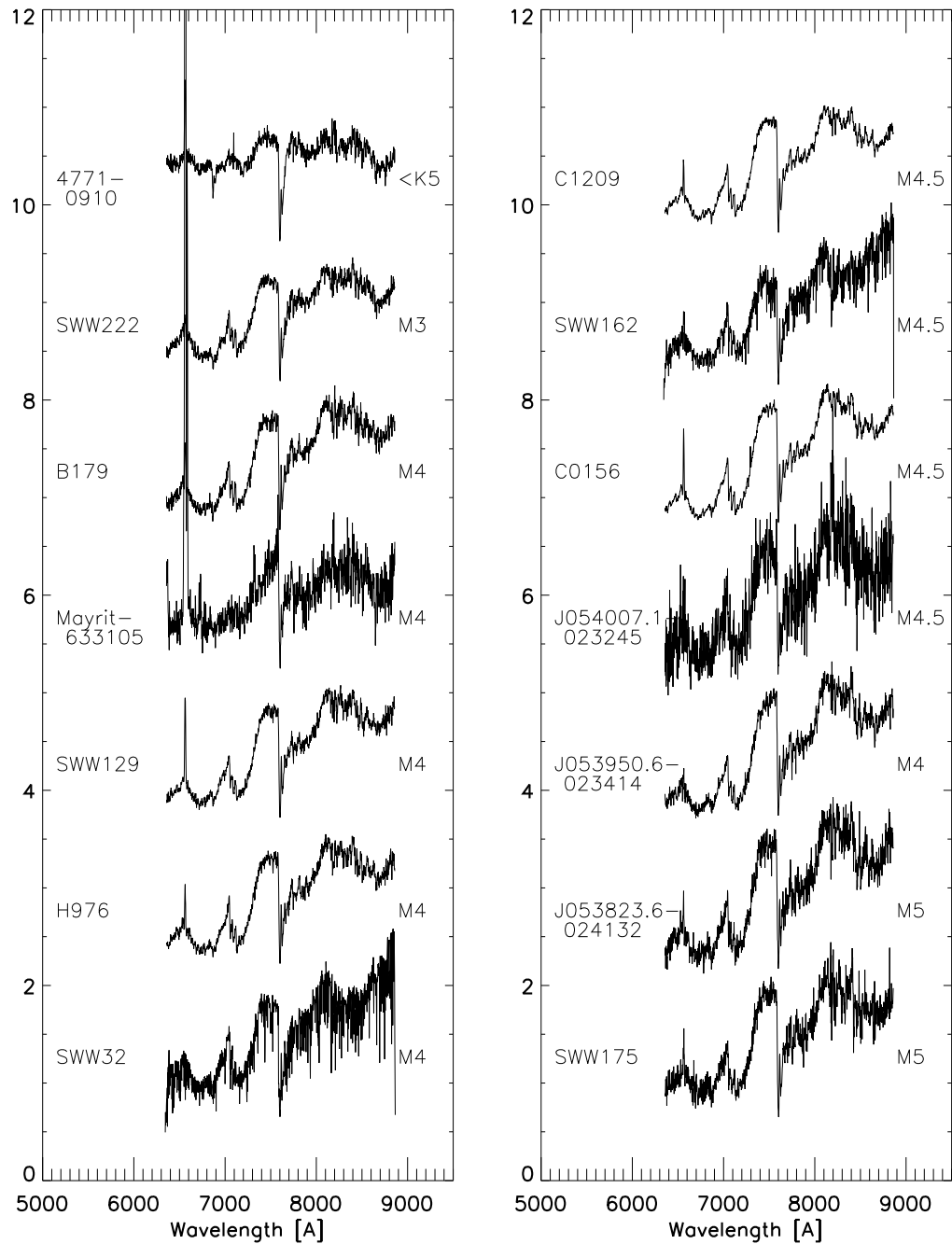
Figure 6.2 Red channel spectra of σ Ori candidates from the December 2009 Palomar 200-inch/DBSP observing run. Spectra are normalized to their median flux value and shifted for clarity. Objects with "C" identifications are variables discovered in our photometric program. Hα emission at 6563Å is seen in many targets.
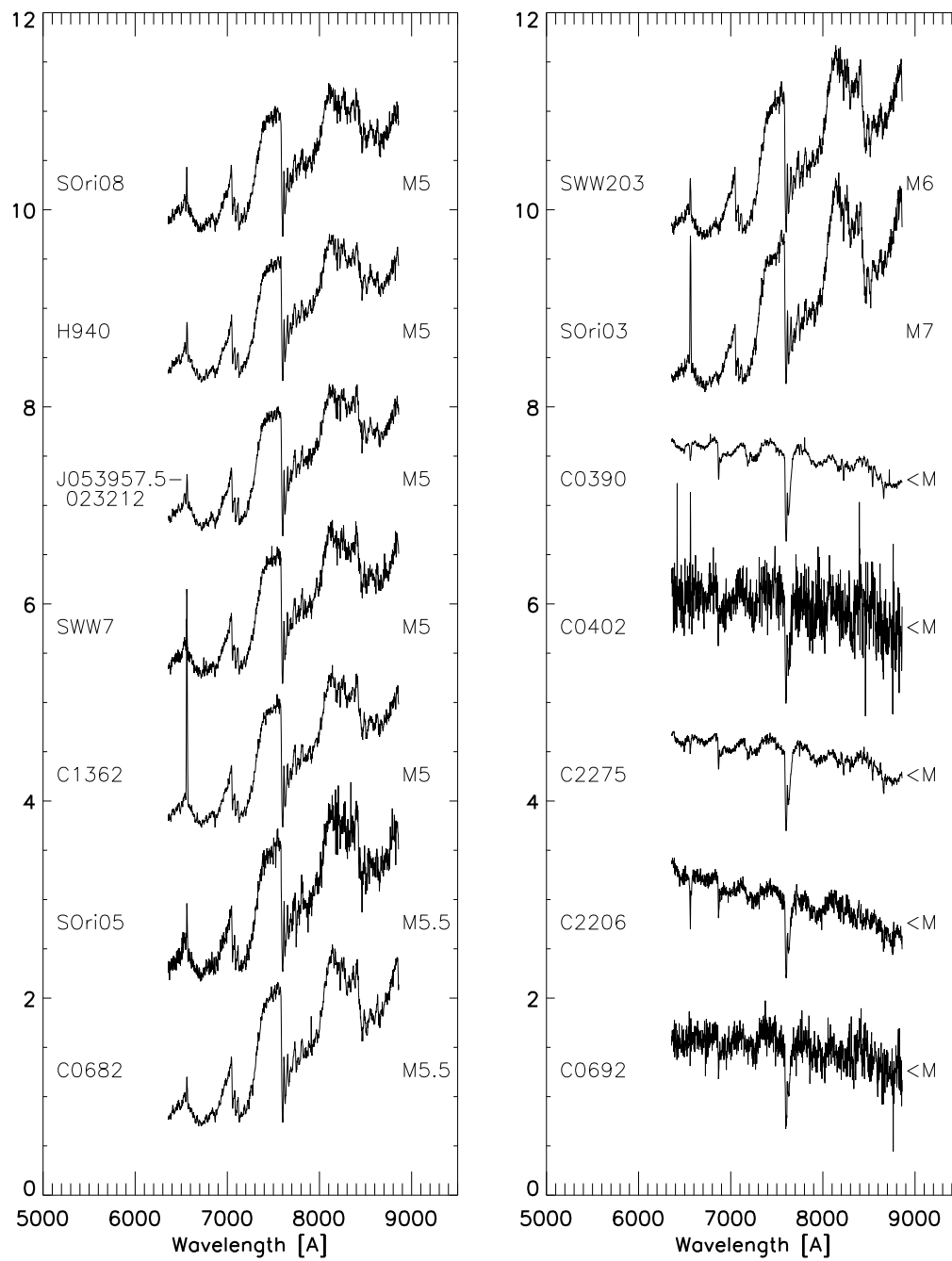
Figure 6.2 –Continued

setup for ∼3 Myr low-mass IC 348 members previously classified by Luhman et al. (2003b), as well as ∼1 Myr Taurus and ∼5 Myr Upper Scorpius members observed by Slesnick et al. (2006a,b). The typical adopted uncertainties are 100 K, equivalent to just under one spectral subclass. Since extinction is very low in this region, it is expected to have a negligible effect on the classifications. Not surprisingly, the majority of the stars appear to be M dwarfs.

Table 6.1.   Spectroscopic data for σ Orionis candidates from P200/DBSP

2MASS ID	Alternate ID	Spectral type	$W(\mathrm{H}\alpha)$	EW He 5876	EW Ca 5842	TiO-7140 index	TiO-8465 index	Na-8190 index	Youth?
05383284-0235392	r053832-0235	<K5	-1.7	-	-	1.3776	0.990235	0.942339	-
05383160-0251268	SWW178	<K5	-1.6	-	-	2.00917	1.09173	0.939814	-
05382725-0245096	4771-0041	K5	-40.7	-2.0	-6.0	1.05266	1.07862	1.16256	Y
05373666-0234003	SWW141	M1	-	-	-	0.938477	1.0337	1.00053	-
05383157-0235148	r053831-0235	M1	-17.5	-	-	1.45092	1.04852	0.951124	Y
05382848-0246170	SWW188	M2	-	-	-	1.61465	1.00743	0.933542	-
05372806-0236065	H59	M2	-1.9	-	-	1.64146	1.0196	0.940673	-
05381824-0248143	SWW40	M3	-2.3	-	-	1.862	1.05962	0.976234	-
05380826-0235562	SWW41	M3	-35.6	-	-4.3	0.746287	1.08284	-	Y
05375398-0249545	SWW221	M3	-11.7	-	-	1.64098	0.990403	0.936656	-
05373784-0245442	SWW184	M3	-3.1	-	-	1.69962	1.03683	0.947668	-
05383335-0236176	SWW130	M3	-2.3	-	-	1.7244	1.04779	0.974716	-
05381886-0251388	SWW39	M3	-6.9	-	-	1.84441	1.07732	0.967212	-
05383460-0241087	S Ori J053834.5-024109	M3	-6.3	-	-	3.03352	1.05647	0.969124	-
05375404-0244407	SWW68	M3	-4.4	-	-	1.99172	1.0626	0.947734	-
05380994-0251377	SWW52	M3	-27.9	-	-	1.9579	1.06449	0.95181	Y
05383157-0235148	SWW49	M3	-21.8	-	-	1.41126	1.01431	0.980663	Y
05382332-0244142	S Ori J053823.3-024414	M3	-8.5	-	-	0.88294	1.12831	-	-
05382774-0243009	SWW87	M3	-5.4	-	-	1.76398	1.08237	0.93015	-
05383460-0241087	S Ori J053834.5-024109	M3	-4.2	-	-	1.92835	1.11705	0.946446	-
05381816-0243349	SWW226	M3	-	-	-	1.8371	1.09361	0.923098	-
05383302-0239279	H576	M3	-	-	-	1.94961	1.11644	0.849016	N
05383902-0245321	SWW31	M3	-37.8	-	-	1.70111	1.03811	1.02354	Y
05375486-0241092	SWW174	M3	-7.1	-	-	1.00298	0.925105	-	-

Table 6.1—Continued

2MASS ID	Alternate ID	Spectral type	$W(\mathrm{H}\alpha)$	EW He 5876	EW Ca 5842	TiO-7140 index	TiO-8465 index	Na-8190 index	Youth?
05382911-0236026	SWW177	M3	-3.3	-	-	1.19786	1.06698	0.985021	-
05372912-0240200	SWW187	M3	-	-	-	2.23572	1.11412	0.889896	-
05382750-0235041	S Ori J053827.5-023504	M3	-15.7	-	-	2.38396	1.10881	0.983942	Y
05383141-0236338	SWW50	M3	-127.3	-	-6.5	1.91833	1.14382	0.959225	Y
05383638-0247082	B481	M3	-0.7	-	-	1.33418	1.09322	0.935698	-
05381610-0238049	S Ori J053816.0-023805	M3	-4.2	-	-	2.31973	1.165	0.953301	Y
05382283-0245304	B29	M4	-	-	-	1.50329	1.14133	0.887283	-
05380107-0245379	SWW180	M4	-43.6	-	-	2.50899	1.2524	0.968704	Y
05382021-0238016	S Ori J053820.1-023802	M4	-12.1	-	-	2.60935	1.22149	0.911306	-
05383405-0236375	r053833-0236	M4	-15.9	-	-	2.18148	1.23013	0.977892	-
05382354-0241317	S Ori J053823.6-024132	M4	-	-	-	2.53881	1.17932	0.942519	-
05382307-0236493	SWW207	M4	-67.0	-	-	2.66926	1.31897	0.836855	Y
05383388-0245078	S Ori J053833.9-024508	M4	-19.8	-	-	2.98282	1.28914	0.90611	-
05383745-0250236	SWW11	M4	-9.9	-	-	2.50642	1.26418	0.964807	-
05383669-0244136	S Ori J053836.7-024414	M4	-4.8	-	-	2.66424	1.2832	0.971008	-
05380055-0245097	SWW140	M4	-	-	-	2.454	1.23687	0.956115	-
05381778-0240500	S Ori J053817.8-024050	M4	-11.5	-	-	2.50759	1.28049	0.9326	-
-	M150	M4	-6.8	-	-	1.89854	1.27048	0.995857	-
05381189-0245568	S Ori J053811.9-024557	M4	-6.1	-	-	2.22747	1.30288	0.939655	-
05375206-0236046	K62	M4	-	-	-	3.35359	1.53711	0.55325	N
05382307-0236493	SWW103	M5	-84.2	-3.9	-	1.97696	1.26176	0.976552	Y
05375840-0241262	SWW53	M5	-	-	-	2.8226	1.41888	0.923966	-
05382684-0238460	S Ori J053826.8-023846	M5	-10.4	-	-	3.07123	1.48324	0.968521	-
05380552-0235571	S Ori J053805.5-023557	M6	-	-	-	2.84612	1.55805	0.939039	-

Table 6.1—Continued

2MASS ID	Alternate ID	Spectral type	$W(\mathrm{H}\alpha)$	EW He 5876	EW Ca 5842	TiO-7140 index	TiO-8465 index	Na-8190 index	Youth?
05383479-0239300	Mayrit 258215	<M0	-	-	-	0.835932	0.981671	-	-
05383822-0236384	r053838-0236	<M0	-	-	-	0.883651	1.16224	-	Y
05381315-0245509	SWW98	<M0	-59.1	-	-	0.812804	1.04603	-	Y
05391883-0230531	4771-0910	<K5	-10.5	-	-	1.05266	1.07862	1.16256	Y
05381816-0243349	SWW222	M3	-2.9	-	-	1.41272	1.13783	0.980245	Y
05394770-0236230	B179	M4	-10.2	-	-	1.62677	1.21981	0.92991	Y
05392560-0238436	Mayrit 633105	M4	-73.4	-	-	1.08363	1.13146	1.04465	Y
05390878-0231115	SWW129	M4	-19.6	-	-	1.62208	1.2132	0.922211	Y
05391699-0241171	H976	M4	-6.8	-	-	1.66902	1.17099	0.889596	-
05394799-0240320	SWW32	M4	-2.7	-	-	1.61829	0.996142	0.724122	-
05391582-0236507	C1209	M4.5	-6.5	-	-	1.69356	1.20679	0.939776	Y
05392633-0228376	C0156	M4.5	-12.2	-	-	1.90648	1.2703	0.928713	Y
05400708-0232446	S Ori J054007.1-023245	M4.5	-	-	-	1.94079	1.56767	1.48325	Y
05395056-0234137	S Ori J053950.6-023414	M5	-0.9	-	-	1.93968	1.37424	0.94973	Y
05390524-0233005	SWW175	M5	-5.7	-	-	1.7951	1.37902	0.959283	Y
05390808-0228447	SOri08	M5	-5.8	-	-	1.95515	1.32563	0.93774	Y
05391346-0237391	H940	M5	-7.4	-	-	1.94475	1.30981	0.918821	Y
05395753-0232120	S Ori J053957.5-023212	M5	-6.3	-	-	1.97482	1.34063	0.908849	Y
05392561-0234042	SWW7	M5	-6.1	-	-	1.38666	0.947397	1.41272	-
05395645-0238034	C1362	M5	-46.9	-	-	1.95064	1.39392	0.91234	Y
05392023-0238258	SOri05	M5.5	-8.4	-	-	2.2766	1.56131	1.02787	Y
05393931-0232252	C0682	M5.5	-7.0	-	-	2.34866	1.52411	0.955509	Y
05391232-0230064	SWW203	M6	-8.6	-	-	2.28808	1.62537	0.983395	Y
05392097-0230334	SOri03	M7	-32.7	-	-	2.29697	1.7271	0.942205	Y

6.6 Membership confirmation

Objects in σ Ori are not particularly reddened, and their proper motions are not significantly different from those of field stars. Therefore, alternative methods must be applied to confirm membership for objects whose colors lie redward of the main sequence in a color-magnitude diagram.

Spectral types provide a straightforward method to distinguish low-mass cluster members from higher mass field stars. But to separate young cluster objects and old field dwarfs or giants of *similar* spectral type, a further indicator is needed. Lithium absorption is one such method, but unfortunately the resolution of the spectra acquired is not high enough to definitively detect this since the 6708 Å line is diluted by TiO features in late-type objects. We instead determine which of our targets are sufficiently youthful to be bona fide σ Orionis members by relying on the fact that pre-main-sequence objects have larger radii and thus lower surface gravity than their more evolved counterparts. Thus the measurement of gravity-sensitive spectral features can effectively sort the sample by age. In our selected wavelength range, indices around Na I, K I, and CaH are suitable for this task (Slesnick et al. 2006). We have used the equivalent width of Hα emission as a secondary diagnostic of youth (e.g., as a sign of active accretion) but cannot depend on it completely since it is also present, albeit at lower strength in some field M dwarfs.

The Na I doublet at 8183 and 8195 Å is sensitive to gravity in objects with spectral types later than about M1 (Slesnick et al. 2008), in that it becomes stronger with age. For objects earlier than M1, we cannot unambiguously determine σ Ori membership status and must continue to rely on the H-R diagram colors. Although the K I features at 7665 and 7699 Å, as well as CaH absorption at 6975 Å are also gravity indicators, we have chosen to evaluate youth mainly on the prominent Na I doublet.

We used the Na-8190 index defined by Slesnick et al. (2008), which is the ratio of the strength of absorption at 8189 Å compared to the surrounding pseudocontinuum, both measured in 30-Å-wide bands. Their analysis has shown that values greater than $\sim$0.9 are indicative of low gravity. Taking the Na-8190 values in Table 6.1 into account, we have determined the membership status for many of the observed σ Ori candidates. In the youth column we indicate whether the spectrum shows broad Hα emission or weak Na absorption typical of a young cluster member ("Y"). Objects marked "N" can be definitively ruled out

as σ Ori members, while those with a "-" do not have enough information. We confirmed membership for 32 objects including two brown dwarfs and reject it for another two. This contribution to the low-mass census in σ Ori enlarges the known population by about 15%, providing many additional targets for future studies of the cluster and its environment.

Chapter 7

Conclusions

7.1 The lack of short-timescale periodicities in young BDs and VLMSs

We uncovered many cases of periodic variability in the collected time series, over a wide range of timescales. Our detection of both rotation on $\sim$1–3 day timescales in young cluster members and on hour timescales in background field pulsators and eclipsing binaries shows that our period detection algorithms are robust. Yet in the search for deuterium-burning pulsation, the data unanimously point to one conclusion: this instability is not present in young BDs and VLMSs above an amplitude of several millimagnitudes in the I band.

One might argue that that objects in our dataset simply do not exhibit pulsation because they are not situated on the H-R diagram instability strip. However, the large sample size makes this possibility highly unlikely. To show how improbable the chances are that *none* of our sample have H-R diagram positions overlapping the instability strip, we consider temperature-luminosity probability distributions for each object. We take these to be two-dimensional asymmetric Gaussians, normalized and centered at the adopted luminosities and temperatures. The Gaussian widths are given by the associated 1-σ uncertainties, which are shown in the H-R diagrams in Chapter 4. The position of each target then corresponds to a probability that it is susceptible to pulsation, which we determine by integrating its distribution over the entire region of the instability strip. For objects on or very close to the strip, this value is at least $\sim$20–25%, whereas for the higher mass stars far from the strip it is close to zero. The probability that the position of a given object does *not* overlap with the instability strip is then 1.0 minus this quantity. The product of these values over

all targets provides an estimate of the chance that no pulsators would be present in our sample.

We have performed this exercise for each of the clusters observed, and for alternate distances in cases where there is more than one possible value (IC 348 and σ Ori). In Cha I, we determined an expectation value of 3–4 objects on the strip and find a probability of 0.015 that *no* object positions actually overlap it. Turning this number around, there is a nearly 99% chance that at least one object should exhibit pulsation based on its position within the instability strip, assuming that the theoretical calculations underpinning it (PB05) do not suffer from gross systematic errors.

USco does not have many targets overlapping the instability strip, and therefore the expectation is for only 1 or 2 objects to lie directly on it. In this region, we find a non-negligible probability of 0.22 that our sample did not include any pulsation candidates. For IC 348, on the other hand, we expect $\sim$11 objects on the strip and find a probability of 4×10^{-6} that none are actually on it. If we instead assume the lower distance of 260 pc, then the expectation is similar: nine objects on the strip and a probability of 5×10^{-5} that none are on it. Finally, we have computed probabilities for σ Ori assuming a cluster distance of 440 pc and find that at least 4 targets are expected to be on the strip, with at most a 0.02 chance that none are. Substituting the alternate distance of 350 pc, we find nearly the same values (3, 0.06). The probabilities are upper limits since we do not have spectral types for part of the σ Ori sample and hence cannot reliably place these objects on the H-R diagram.

In conclusion, we expect with high confidence to have observed deuterium-burning oscillations if it is present at observable amplitudes. We now quantify the overall detection limits by considering the power-law to the periodograms of each observed young cluster member. These curves, of form $A/(f + B) + C$ for frequency f and constants A, B, and C, trace out the noise level as a function of frequency (see Figs. 4.4, 4.8, and 4.12). For each object analyzed, we take the fit values at 5 cd^{-1} ($\sim$5 hours) and 25 cd^{-1} ($\sim$1 hour) as representative of the 1–σ level above which no pulsation is observed. We display these values as a function of object magnitude in Fig. 7.1 to illustrate the collective limit imposed by our entire dataset.

The median amplitude limit is several millimagnitudes. Objects with high-amplitude aperiodic variability are exceptions, as they have excess periodogram noise which is intrinsic. The rest of our targets, however, have maximum amplitudes in the periodogram of at

most 0.002 to 0.004 magnitudes. This represents the threshold above which we detect no periodicities. We conclude that if deuterium-burning pulsation is present in any of our sources, then its amplitude must be below this level.

In addition, we present the infrared limits from *Spitzer* separately in Fig. 7.2. Here we plot direcctly the fits as a function of frequency. For the majority of objects, we have detected no periodicities in the pulsation frequency range with amplitudes greater than several millimagnitudes. Brown dwarfs S Ori 45 and S Ori 53 stand out, as they have higher limits (0.005 and 0.04 magnitudes respectively in the 4.5 μm band) owing to their faintness and correspondingly high noise levels in both the light curves and periodograms. In addition, brown dwarf S Ori J053825.4-024241 has a higher limit for pulsation (0.004–0.007 magnitudes in the 3.6 μm band, depending on frequency) since it displays substantial intrinsic variability. The rest of our targets have maximum amplitudes in the periodogram of at most 0.002 to 0.003 magnitudes. This represents the threshold above which we detect no periodicities. Once again, there is no evidence that deuterium-burning pulsation is present above this level in any of our sources.

7.1.1 Implications

Despite exquisite photometric sensitivity, we have not detected signs of short-period variations in any of our young BD and VLMS targets. Although the theory of PB05 does not preclude very low amplitudes, we suspect that the failure to find pulsation is indicative of a physical damping mechanism operating within these objects. The convective timescale is over two orders of magnitude longer than the pulsation timescale, but it becomes quite short near the (sub)stellar surface layers. Neglect of the energy exchange between pulsation and convection may have led to overly optimistic predictions of mode amplitude growth. Indeed, models of this interaction in other types of stars have recently shown that convection can quench pulsation under some circumstances (Gastine & Dintrans 2011).

To continue the search for pulsation and probe to lower amplitudes, future campaigns will need to produce extraordinarily high precision photometry. Data of this quality is currently available through the Kepler and CoRoT missions, but only for stars brighter than ~12th magnitude in the optical, and primarily on field stars, as opposed to young clusters. Therefore, the results presented here are likely to stand for quite a long time to come.
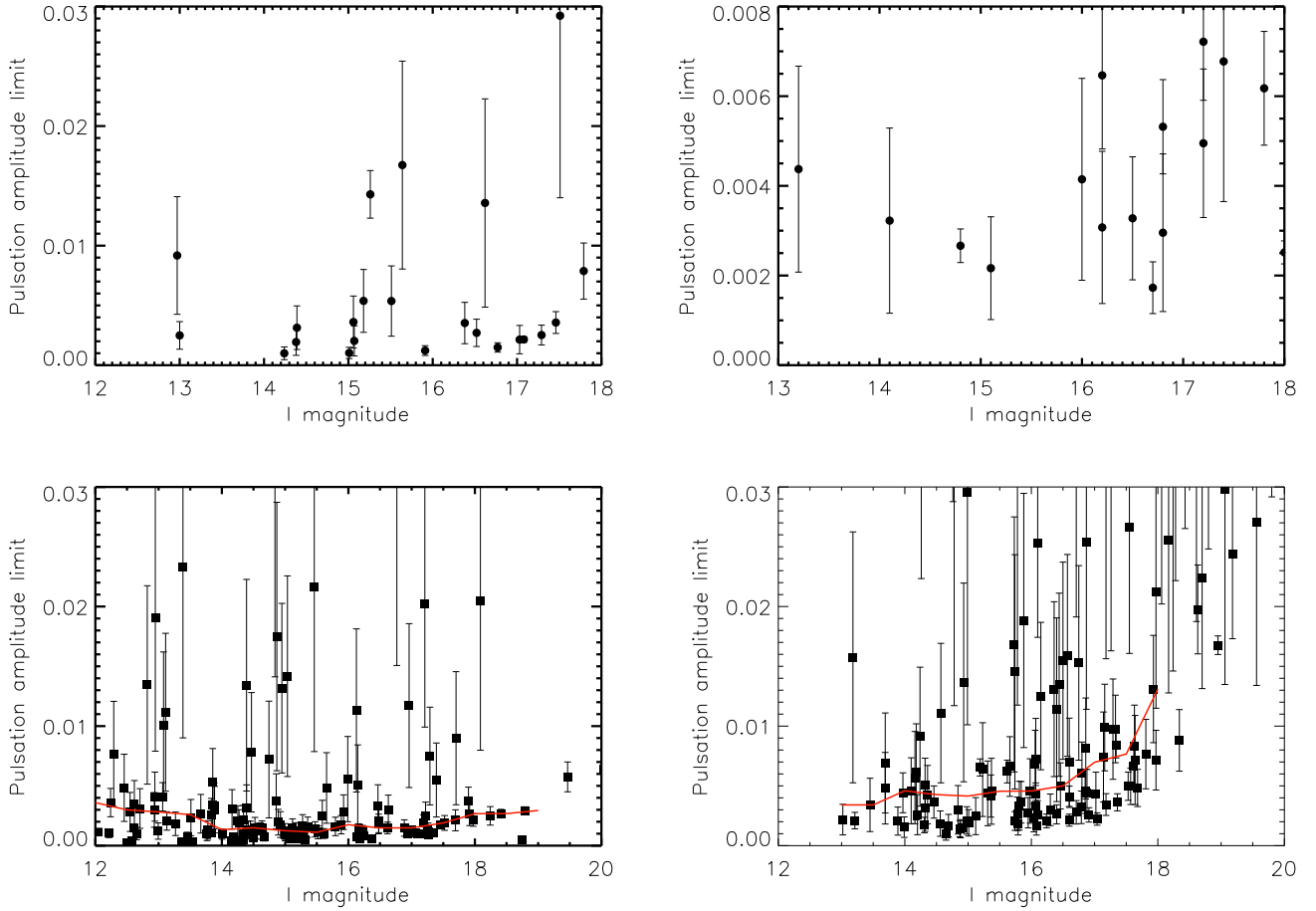
Figure 7.1 Pulsation detection limits for individual objects versus their magnitudes. The clusters represented, from clockwise top left: Chamaeleon I, Upper Scorpius, IC 348, and σ Ori. For the latter two, we have drawn a binned median curve in red. Based on the position of the instability strip, we would expect pulsating objects to have magnitudes of ~14 and fainter. While in general the limits are quite low–in the millimagnitude range– there is a large population of outliers in which high-amplitude intrinsic aperiodic introduced significant power into the higher frequency regions of the periodogram.
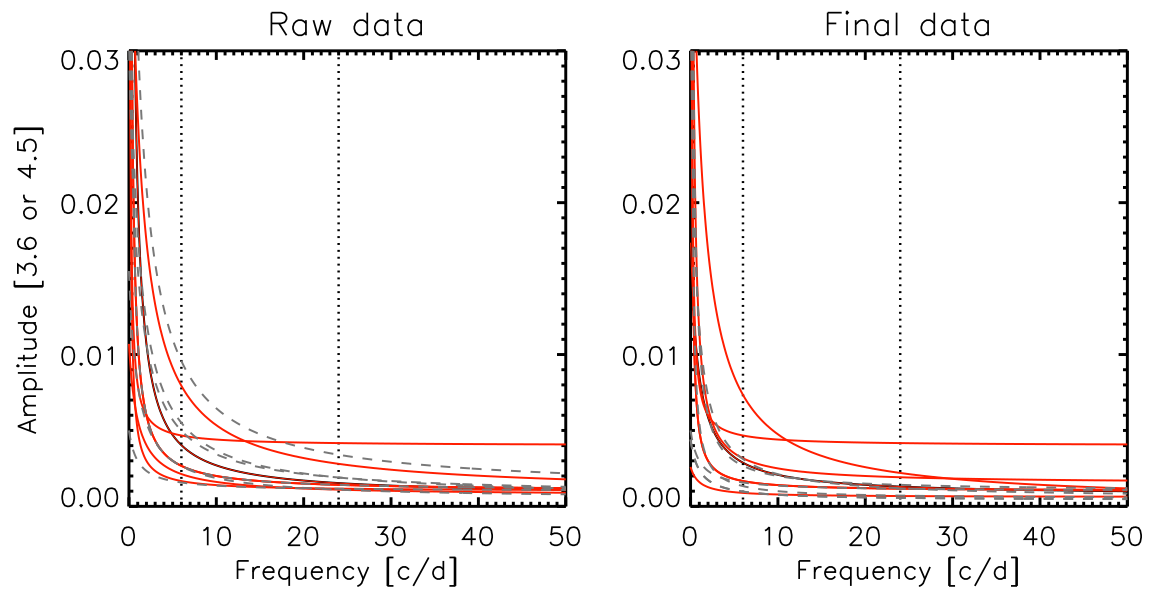
Figure 7.2 Limits on pulsation detection in the mid-infrared periodograms based on *Spitzer* light curves. Solid red curves show the limits for objects on or near the instability strip, whereas grey dashed curves are for objects not expected to exhibit pulsation. The curve for S Ori 53 is off the chart at a uniform amplitude of 0.04 magnitudes. The dotted lines indicate the region of frequency space where we expect pulsation to occur (i.e., 1–4 hour periods). The left panel displays data before pixel-phase correction, and the right shows the final data after removal of pixel-phase oscillation trends. For the few objects that did not require these corrections, the curves derived directly from raw data are repeated.

What are the future prospects for employing time series analysis to study the interiors and evolution of young, very low mass objects? We propose that the general lack of short-timescale variability among young, low-mass cluster members may be in fact useful for future studies at infrared wavelengths, such as searches for planets around young BDs and VLMSs. Models have begun to predict the formation of such exotic systems (e.g., Pascucci et al. 2011), and both transit searches and radial velocity measurements benefit from low levels of activity on short timescales. For objects that exhibit more erratic variability related to accretion and dust obscuration, further high-precision, high-cadence analyses of their light curves has begun to reveal the dynamic structure of their inner disks.

7.2 Summary

While the photometric monitoring survey may not have uncovered pulsation, it did reveal other potentially fundamental features of young cluster members. We summarize here the campaign and its main findings.

Central to the search for pulsation in young BDs and VLMSs was a high-cadence photometric monitoring campaign on four stellar clusters and associations in the 1 Myr range where the deuterium-burning instability is predicted to be prominent: IC 348, σ Orionis, Chamaeleon I, and Upper Scorpius. These regions were chosen for their substantial populations of spectroscopically confirmed members. Because the expectation for pulsation is a sinusoidal flux modulation with periods of 1–4 hours, we carried out 1–10 minute exposures (depending on the instrument and aperture size) continuously for up two weeks at a time on a set of several hundred young cluster members, including some 85 VLMSs and 65 BDs. The two-week time baseline was chosen not only to gather a substantial number of data points for statistical purposes, but also to assess longer timescale variability that is frequently associated with young stars.

Over the course of this work, we have relied on a number of observational facilities, including the robotic Palomar 60-inch telescope, the CTIO 1.0 m telescope, the *Spitzer Space Telescope* (24 hours continuous monitoring at 3.6 and 4.5 μm with the Warm mission IRAC instrument), and the *Hubble Space Telescope* (35 orbits with the WFC3 camera in the F814W filter). In addition, follow-up spectroscopy was obtained with the Palomar 200-inch Double Spectrograph to determine the spectral types and determine cluster membership of

targets for which this information was previously unavailable.

We have presented photometric monitoring on a collection of low-mass stars and brown dwarfs in σ Orionis. Extensive vetting of membership via prior spectroscopic information and the relative spatial compactness of our fields has ensured that the cluster samples are relatively homogeneous in terms of age and initial conditions. In addition, the selection of $\sim$10 minute cadence and time baseline of nearly two weeks for ground-based runs, along with excellent photometric precision has enabled us to carry out an unprecedented analysis of variability in young stars and brown dwarfs, complete to amplitudes below the 1% level for most sources. This combination of cadence and precision has allowed us to probe new areas of variability parameter space: those pertaining to short timescale and low-amplitude fluctuations. In the preceding sections, we have explored the general properties of variability in very low mass σ Orionis members and their connections to other stellar parameters. In putting the pieces together, we will now highlight the analysis tools developed, the various phenomena encountered and possible connections to physical properties.

7.2.1 Precision photometry techniques

Since the initial goal of the campaign was to identify or place stringent amplitude limits on the presence of pulsation, we placed special emphasis on the development of high-precision photometric extraction routines. The new variable-aperture image subtraction technique accounted for systematic effects such as background gradients and stellar crowding in ground-based photometry and produced best photometric precisions of several millimagnitudes over the entire duration of each two-week run.

To achieve similar precisions in the mid-infrared with IRAC required careful accounting of the pixel-phase and other detector effects that plague Warm *Spitzer* data. When these systematics are folded into a light curve that is intrinsically variable, they are a challenge to model and extract. We established a novel approach to remove the effect of varying detector sensitivity as target positions oscillate within individual pixels. The algorithm reduced systematic variation within IRAC light curves from as much as 10% to less than 0.5%. For future high-precision photometric time series work, we recommend further exploration of the sensitivity distribution within individual pixels, perhaps through even higher cadences that might provide more data points over a given time and thus greater spatial coverage within individual pixels. We expect that these new photometry methods will be useful to

future high-precision time-series monitoring programs.

7.2.2 Variability in young stars and brown dwarfs is persistent–in time and mass

In addition to achieving an unprecedented combination of photometric precision and cadence on young cluster members, the campaign comprised a comprehensive sample and, perhaps most importantly, very low mass targets. The sensitivity of our photometric monitoring has provided opportunity to probe for variability and explore its trends well into the brown dwarf regime. We have detected variability of various forms in nearly 70% of our sample, including 80% of stars with strong evidence for cluster membership. The $\sim$20% of likely cluster members with *no* evidence for variability do not appear to have any distinguishing characteristics, such as belonging to a particular mass range or possession of disks. This fraction is similar to the proportion of σ Ori variables identified as periodic in 2007 but not in 2008. Using the 2007 field as well as data from other studies, we have also found (§5.2.1) that the observed periodic and aperiodic variability is persistent on typical timescales of at least 5–10-years. This finding is consistent with studies of other clusters such as IC 348, in which analysis of data acquired by different groups retrieve largely the same photometric periods for objects in common (e.g., Cieza & Baliber 2006). Scholz & Eislöffel (2004) also carried out two photometry monitoring campaigns in another region of σ Ori and identified a number of objects with persistent variablity across both datasets. Nevertheless they also suggest evidence for spot evolution based on a subset of targets displaying periodicities during only one campaign. While our analysis in §5.2.1 points to long-lived accretion and magnetic activity on young, low-mass stars (in comparison to, e.g., the rotation period timescale), it is not sensitive to light curve amplitude or phase changes. Thus magnetic spots may come and go, but the typical young low-mass star or brown dwarf has one or more spots large enough to be detected in photometry at the 0.5% level for time spans of multiple years.

Also intriguing are variability trends (or lack thereof) with mass, particularly across the substellar boundary. Reiners et al. (2009) have observed that magnetic field strengths on young brown dwarfs are substantially weaker than those in higher mass young stars. As a result, we might expect accretion and spot properties to change with mass. We have concluded (§5.2.2) that there is no such evidence for a trend in *aperiodic* variability. Like

several other studies of σ Ori (Caballero et al. 2006; Scholz & Eislöffel 2004) we identify several accreting brown dwarfs based on their high-level erratic light curve behavior. The persistence of T-Tauri-like variability to very low masses may reflect more so the presence of disks than the surface magnetic field properties of these objects. The fraction of *periodic* variables, on the other hand, does seem to decrease into the brown dwarf regime (§5.2.2) to an extent not accounted for by our photometric sensitivity. This result is consistent with decreasing magnetic field strength in that a lack of spots or decreased coverage would be expected. Alternatively, spots may still be present but at much lower temperature contrast.

7.2.3   New young cluster members identified

The ubiquity of variability in young cluster members has also led to the discovery of a handful of new candidate young BDs and VLMSs in σ Ori and Cha I (listed in Tables 5.1, 5.2, and 5.3, even though the regions in question had already been thoroughly searched with photometric and spectroscopic surveys. In cases where extinction or disks distort a cluster member's colors, variability may be a more efficient way to select members.

Our follow-up spectroscopy program in σ Ori also confirmed membership for dozens of very low mass objects in this cluster. In doing so, we nearly doubled the number of objects with spectral types. The greatly expanded census will be useful for future work requiring estimates of mass and spectral line indicators for a large number of members.

7.2.4   A correlation of rotation period with color and magnitude at low mass

Several previous studies have examined the distribution of rotation periods among stars in a number of young clusters. Initially, many of the stellar samples did not include stars with masses less than $\sim$0.2 $M_\odot$, and the resulting rotation period exhibited two peaks near 2 and 8 days (e.g., Herbst et al. 2002). However, extension of rotation studies to lower mass has failed to retrieve such a bimodal distribution. Lamm et al. (2005) and later Cieza & Baliber (2007) indeed observed a change in rotation properties near R-$I = 1.3$ or spectral type M2–M3, with the redder objects rotating faster on average. The disappearance of the long period peak in the rotation distribution when a low-mass (or equivalently, red color) cut is applied to the distribution implies that a mass-dependent effect is at work. Additional rotational studies incorporating components of the low-mass star population in the IC 348

cluster (Cieza & Baliber 2006), the northern portion of σ Orionis (Scholz & Eislöffel 2004), and the ONC (Stassun et al. 1999; Rodríguez-Ledesma et al. 2009) have confirmed a trend of increasingly rapid rotation toward lower mass.

Although our data includes few periodic objects more massive than $\sim$0.5 $M_\odot$, they support the conclusion that low-mass stars and brown dwarfs have a different period distribution from higher mass but similarly aged young stars. The distribution of rotation periods uncovered in our analysis of σ Ori data contains few objects with 8–10 day periods, but a steady increase in number of objects up to a peak near 1 day. We have further explored this phenomenon by plotting periods for σ Ori members as a function of photospheric color as well as I-band magnitude, both of which serve as proxies for mass. The results (Figs. 5.12 and 5.13) and statistical tests confirm that there does indeed appear to be a strong trend in rotation with mass. We have ruled out (e.g., §5.3.2) the possibility that biases in our photometric sensitivity and signal detection algorithm could produce such a strong correlation of period with color or magnitude.

In general, we find no periodic variability at periods less than 7 hours. The cut-off in rotation periods around 7–10 hours is abrupt and significant, considering that we are fully able to detect periods down to $\sim$15 minutes. This result suggests some sort of physical mechanism which limits rotation rates. In §5.3.2 we estimated that the break-up period for objects from 0.02 to 0.1 $M_\odot$ lies near 2–7 hours, although there are substantial uncertainties in radius, and hence velocity, at these ages. Based on these values, it appears that young BDs rotate at up to, but not beyond, $\sim$40% of their break-up velocity. This result stands in contrast to the observations of Stassun et al. (1999) in the younger Orion Nebula Cluster, for which a number of low-mass objects were found to rotate at 60–100% percent of break-up speed.

In σ Ori, we also observe a transition in rotation periods near $R\text{-}I = 1.3$ (spectral type M2.5), similar to that reported by Lamm et al. (2005) and Cieza & Baliber (2007), which they attributed to a possible shift in magnetic field properties at low mass. However, we are at a loss to explain such a transition, since low-mass stars and brown dwarfs at the age of σ Ori should all be fully convective. We have attempted to explain the trend of rotation with color (and hence mass) with a much simpler hypothesis of constant angular momentum. We consider this to be a "toy" model since in reality angular momentum likely adheres to a distribution rather than a single value (e.g., Rebull 2001). The internal structure models

from Baraffe et al. (1998) and D'Antona & Mazzitelli (1997) do provide a reasonable fit to the data, with the exception of one prominent outlier at R-$I = 0.6$. Thus we conclude that it is possible to account for the spins of σ Ori members with models for mass and radius currently in use, which invoke formation of H_2 in the atmosphere and increasing importance of electron degeneracy at low mass but do not incorporate magnetic fields (Baraffe et al. 1998). Nevertheless, larger numbers of rotation data points and additional data incorporating higher mass cluster members is likely required to reach a definitive conclusion on the origin of the rotation trend uncovered in our study.

7.2.5 A surprisingly weak connection variability properties and the presence of a disk

Perhaps the most surprising finding to arise from our data is the apparent lack of correlation between the derived rotation periods and presence of a circumstellar disk around low-mass stars and brown dwarfs (e.g., $M \lesssim 0.5\ M_\odot$) in σ Ori. This is one of the few clusters for which *Spitzer*/IRAC data is available and deep enough to identify disks around even the lowest mass members. Likewise, our photometric monitoring is sensitive enough to permit the derivation of rotation periods in all non-accreting objects with spots producing brightness deviations greater than 0.007 magnitudes (e.g., §5.3.2). Much attention has been paid in previous works to the role of disks in regulating the angular momentum evolution of young stars, and in particular the role of disk locking (Koenigl 1991) in limiting rotation rates. Many measurements of rotation periods for stars with and without disks have produced discrepant results in that some studies show slower rotation on average for disk-bearing stars and others do not; Cieza & Baliber (2006) provide an excellent overview. One issue has been the actual selection of disk candidates. The process has recently become much more clear-cut with the advent of *Spitzer* data, but previous reliance on mainly near-infrared data may have muddled the samples, as illustrated in Fig. 5.20.

Fortunately we have access to excellent *Spitzer* data for many of our targets in σ Ori and Cha I, presenting the opportunity to examine for the first time correlations between rotation period and disk presence among low-mass members. At the same time, our conclusions are limited by the fact that we have measured rotation periods for only 13 (28%) of the disk-bearing objects in σ Ori and none of those in Cha I. But the spread in rotation periods among objects in the former cluster (as shown in Fig. 5.12) is nevertheless quite wide,

encompassing roughly the same range as the diskless objects. Rebull et al. (2006)'s study of ONC members with *Spitzer* data revealed significantly slower rotation among their disk sample even to low masses, although this result may have been biased by the detection limits of their *Spitzer* data. In contrast, the median rotation periods for both disk-bearing and diskless periodic variables in our sample do not differ significantly for either the entire sample or the large subsample of objects with $M \lesssim 0.45\ M_\odot$ (§5.5.3), leading us to conclude that any disk-locking phenomenon is not prominent in the low-mass regime at the age of σ Ori. Since we are concerned about mass-dependent effects, we have also highlighted the disk-bearing objects in the period-color diagram (Fig. 5.12). Once again, it is clear that these targets do not occupy a region of preferentially long or short period, regardless of mass. Instead, we find a substantial spread in rotation periods for the disk-bearing sample, independent of both disk presence and other properties. These results suggest that the disk may not in fact play the lead role in determining the angular momentum of rates of young, very low mass stars. They are also consistent with a recent theoretical study by Matt et al. (2010) which concluded that other processes like stellar winds must be invoked to explain the observed spread in rotation rates.

7.2.6   New classes of low-mass star variability

The sensitivity and cadence of our photometric observations have led to the discovery of several novel types of variability among the low-mass young cluster members. We discussed the details (§5.4) of a small set of "peculiar" variables in σ Orionis, whose abrupt dips in brightness mirror those of the higher mass UX Ori stars, but on much shorter timescales. With the recent identification of "AA-Tau-like" variables in NGC 2264 (Alencar et al. 2010), this is not an entirely new finding, but it does suggest that the eclipse-like brightness dip phenomenon is somewhat common in young clusters. Such variables may have been overlooked in previous photometric studies since the fading events only become obvious when data are taken at the appropriate fast cadence. Indeed, we are unable to definitively identify this phenomenon in our more irregularly sampled Cha I and IC 348 time series. Additional multicolor studies should allow for further evaluation of its origin.

We also highlight the subsample of aperiodic variables in our sample whose light curve RMS values are particularly low and whose *Spitzer* infrared data shows no indication of a disk (Fig. 5.22). Although the objects also do not have strong Hα emission, the erratic

nature of the light curves is strongly suggestive of accretion, but perhaps at a lower level than the variables with obvious disks. A similar phenomenon was observed in the IC 348 cluster, in which a number of weak T Tauri stars (i.e., weak Hα) were found to be erratic variables by Littlefair et al. (2005). These results bring into question our ability to determine which cluster members are truly surrounded by disk material, which ultimately affects the analysis of rotation and possible disk locking. It appears from these light curves that a percentage of young objects retain enough gas and/or dust beyond the time that we would expect their disks to be fully cleared based on infrared observations. Alternatively, we may be viewing rapid evolution of magnetic spot features on the stellar surface.

7.2.7 Future directions

While the initial goal of discovering pulsation among young BDs and VLMSs remains to be realized, we have begun to uncover some of the fundamental properties of these objects in unexpected ways. In addition to putting strong limits–several millimagnitudes–on the amplitude of this phenomenon, we have used the phenomenal precision and cadence of the dataset to investigate the hitherto unexplored variability properties of the very low mass regime. The trends in rotation rate, as well as relationship of variability to accretion and disk properties, will certainly be the subject of further exploration. We suggest that future work in high-precision photometry of young cluster members will benefit particularly from a multiwavelength approach, as well as the addition of simultaneous high-resolution spectroscopic monitoring to better probe fundamental disk and accretion properties at very low mass.

Appendix A

Objects with Previous Reports of Variability

We report on follow-up of objects in σ Orionis that were previously identified as variables. Since it is is a well-studied cluster, several monitoring programs have targeted its brown dwarf and low-mass star population. Despite different cadences and sensitivities, we can use prior data to assess variability patterns over timescales much longer than the duration of our observing runs. Repeat detection of a periodicity not only confirms the accuracy of the measurement but also attests to the long-term stability of the mechanism behind it. However, non-detection of variability can also offer insights into the physical processes affecting young VLMSs and BDs on relatively short astronomical timescales. We detail results here on a number of targets in our sample that were put forth as variables by other authors.

r053820/SWW124/Mayrit 380287 = 2MASS J05382050-0234089 Lodieu et al. (2009) report variability in this object in the J, H, and K bands. The difference in magnitudes over several years is 1.0, 0.67, and 0.28 magnitudes, respectively. Hernández et al. (2007) also identified it as a variable (see below). In this study, we find significant undulations in the I-band light curve (RMS $\sim$ 0.1 magnitudes), including a $\sim$0.4 magnitude eclipse-like drop over several days (see §7.5).

SWW221/Mayrit 1129222 = 2MASS J05375398-0249545 Lodieu et al. (2009) detect variability of this object at J, H, and K bands. The brightness in each band differ by 0.4–0.5 magnitudes over a baseline of several years. During our shorter campaign we find that the object has an rms variation of 1.95 magnitudes in the I band–the largest change among all of our variables.

Mayrit 458140 = 2MASS J05390458-0241493 Lodieu et al. (2009) inferred variability in this source in the J, H, and K bands. The change in brightness on timescales of several years is ∼0.2 magnitudes. We also find up to one magnitude in erratic variations on the two-week timescale in the I-band, suggesting ongoing accretion.

S Ori J053855.4-0241208= 2MASS J05385542-0241208 Lodieu et al. (2009) report changes of 0.29 and 0.23 magnitudes in the J and H bands, respectively, over several years. We also detect variability of aperiodic nature, at an RMS of 0.19 magnitudes in the I band.

S Ori 2 = 2MASS J05392633-0228376 Scholz & Eislöffel (2004) report this object as variable, with an RMS of 0.038 magnitudes. Likewise, we detect it as periodic with amplitude 0.019 magnitudes and period 2.3 days. After subtracting this signal from the data, we also note slightly non-Gaussian residuals possibly indicative of additional low-level variability.

SE77 = 2MASS J05385492-0228583 Scholz & Eislöffel (2004) report this object as variable, with an RMS of 0.028 magnitudes. We do not detect any variability, down to less than 0.001 magnitudes.

S Ori J053826.1-024041 = 2MASS J05382623-0240413 Caballero et al. (2004) detected variability on minute-to-hour timescales with amplitude less than 0.04 magnitudes. We see hints of a potential periodicity at amplitude 0.006 magnitudes and period 4.8 days, but it is too weak to confirm (S/N ∼ 4 in the periodogram). The RMS spread in our light curve is 0.01 magnitudes.

S Ori 25 = 2MASS J05390894-0239579 Caballero et al. (2004) detected periodic variability with a period of 40±8 hours (1.7±0.3 days) and amplitude 0.15±0.02 magnitudes. We also find variability, but with a period of ∼2.6 days, and amplitude ∼0.025. The periods could be consistent with each other if one of the detections selected an alias of the true value. However, the 0.046 magnitude RMS of our light curve implies strong disagreement between the amplitudes.

S Ori 42 = 2MASS J05392341-0240575 Caballero et al. (2004) detected a brightness change of 0.11±0.03 from one set of photometry to the next, on a timescale of ∼2 years. We cannot probe variability on such long timescales but find an RMS spread of 0.056, in line with uncertainties expected for field objects of similar magnitude. We also fail to detect any periodicities down to the 0.02 magnitude level.

S Ori J054004.5-023642 = 2MASS J05400453-0236421 Caballero et al. (2004) found variability on night-to-night timescales and amplitude 0.073 magnitudes. Likewise, we detect this object as a variable with period ~18 hours and amplitude 0.03 magnitudes.

S Ori J053948.1-022914 = 2MASS J05394826-0229144 Scholz & Eislöffel (2004) noted this object (their #108) as a variable (although not periodic) with an I-band RMS spread of 0.139, as compared to a median noise level of ~0.08 magnitudes. We do not detect any such variability, down to our noise floor of ~0.04 magnitudes.

S Ori J053825.4-024241 = 2MASS J05382543-0242412 This brown dwarf and was highlighted by Caballero et al. (2006) as a substellar accretor, as indicated by strong Hα and other spectroscopic emission line features. They observed its I-band light curve undergo day-to-day variability of ~0.25 magnitudes, with smaller variations on shorter timescales. We redetect high-amplitude non-periodic variability with I-band RMS 0.55 magnitudes and peak-to-peak amplitude 0.16 magnitudes, confirming that this object likely continues to accrete.

S Ori 27 = 2MASS J05381741-0240242 Variability was previously reported by Caballero et al. (2004), with a period of 2.8±0.4 hours. However, the source appears to be constant to within the photometric errors of our data; we find no evidence of periodic signals with amplitudes greater than several millimagnitudes.

S Ori 28 = 2MASS J05392319-0246557 Variablity was previously detected by Caballero et al. (2004), with a period of 3.3±0.6 hours but is not re-detected in this data. For this source, we are sensitive to periodic signals down to 0.004 magnitudes at periods less than 8 hours and ~0.01 magnitudes for longer timescales.

S Ori 31 = 2MASS J05382088-0246132 Variability was previously detected by Bailer-Jones & Mundt (2001), with potential periods of 1.75±0.13 and 7.5±0.6 hours. We do not detect variability on any timescale, but are sensitive down to an amplitude level of ~0.004 magnitudes.

S Ori 45 = 2MASS J05382557-0248370 Variability was previously detected by Zapatero Osorio et al. (2003), with possible periods of 46.4±1.5 minutes, 2.56±0.10 hours, and 3.6±1.2 hours. Bailer-Jones & Mundt (2001) also reported a tentative detection of periodicity at 0.50±0.13 hours. We detect variability at a longer period of ~7 hours and amplitude 0.03 magnitudes.

Hernández et al. (2007) have extracted a number of objects from the CIDA Equatorial Variability Survey (Vivas et al. 2004). Twenty-five of these are in our fields, and we redetect variability in all but one of them (2MASS J05385317-0243528). These objects, all but five of which display aperiodic variability, have the following identification numbers from Hernández et al. (2007) and 2MASS: SO848 (2MASS J05390193-0235029), SO1154 (2MASS J05393982-0233159), SO1235 (2MASS J05395038-0243307), SO1260 (2MASS J05395362-0233426), SO1361 (2MASS J05400889-0233336), SO362 (2MASS J05380826-0235562), SO300 (2MASS J05380107-0245379), SO123 (2MASS J05373784-0245442), SO374 (2MASS J05380994-0251377), SO396 (2MASS J05381315-0245509), SO435 (2MASS J05381778-0240500), SO462 (2MASS J05382050-0234089), SO482 (2MASS J05382307-0236493), SO598 (2MASS J05383460-0241087), SO646 (2MASS J05383902-0245321), SO827 (2MASS J05385922-0233514), SO865 (2MASS J05390357-0246269), SO879 (2MASS J05390540-0232303), SO976 (2MASS J05391699-0241171), SO1017 (2MASS J05392286-0233330), SO1036 (2MASS J05392519-0238220), SO1057 (2MASS J05392677-0242583), SO1153 (2MASS J05393982-0231217), SO1182 (2MASS J05394318-0232433).

Appendix B

Infrared Eclipsing Binary Systems

In addition to examining the *Spitzer*/IRAC light curves of the 14 σ Ori cluster member targets, we also searched the entire 3.6 and 4.5 μm fields for serendipitous foreground and background variables. After producing light curves for all point sources with magnitudes less than $\sim$ 19.0, we assessed their RMS spread as a function of brightness. Objects lying more than three standard deviations above the median trend were flagged as possible variables. We visually examined their light curves and disregarded those whose brightness fluctuations were clearly caused by pixel sensitivity effects. Four objects (other than BD 053825.4-024241; §5.2) displayed conspicuous variability by these criteria; their light curves are presented in Fig. B.1. For consistency with the other presented light curves, we show both the time series and their periodograms. We list the estimated period, which often does not correspond to the largest periodogram peak since this analysis method is relatively insensitive to the presence of secondary eclipses.

All four stars were also identified as variables in our I-band ground-based dataset; therefore, we refer to them by the same nomenclature. We have not rigorously fit eclipse profiles or other models to the data but present estimates ($\sim$10–20% accuracy) of their main parameters here:

CTIO J05381870-0246582 is an eclipsing binary system with an I-band depth of $\sim$0.45 magnitudes, and 4.5 μm depth of at least 1.2 magnitudes. The most likely period is $\sim$11.8 hours, or 5.9 hours if all of the eclipses are primary (the data are too noisy to to distinguish different depths in subsequent eclipses).

CTIO J05382129-0240318 also appears to be an eclipsing binary, with period $\sim$9.6 hours. This period is fully consistent with our ground-based data, for which we unfortu-

nately reported an erroneous value (4.6 days instead of 9.5 hours). The 3.6 μm depth ($\gtrsim 1.3$ magnitudes) is significantly deeper than the I-band depth ($\sim$0.35 magnitudes).

2MASS J05382188-0241039 exhibits a slightly asymmetric periodic profile, reminiscent of an RR Lyrae star. Its period of 11.8 h is also consistent with this type of pulsator. Since the timescale is so close to half a day, aliasing caused us to misidentify and report a 1.0d period for the ground-based data. The 3.6 μm peak-to-peak amplitude is $\sim$0.25 magnitudes, whereas the value at I band is just over 0.6 magnitudes.

2MASS J05381949-0241224 also displays the characteristic shape of a close eclipsing binary, although there is slight decrease in its peak amplitude over 24 hours which may be attributed to systematic pixel sensitivity effects. The period is 2.8 or 5.6 hours, depending on whether alternating brightness dips are secondary eclipses. At $\sim$0.5 magnitudes, the peak-to-peak amplitude at 3.6 μm is about 20% smaller than that in the I band.
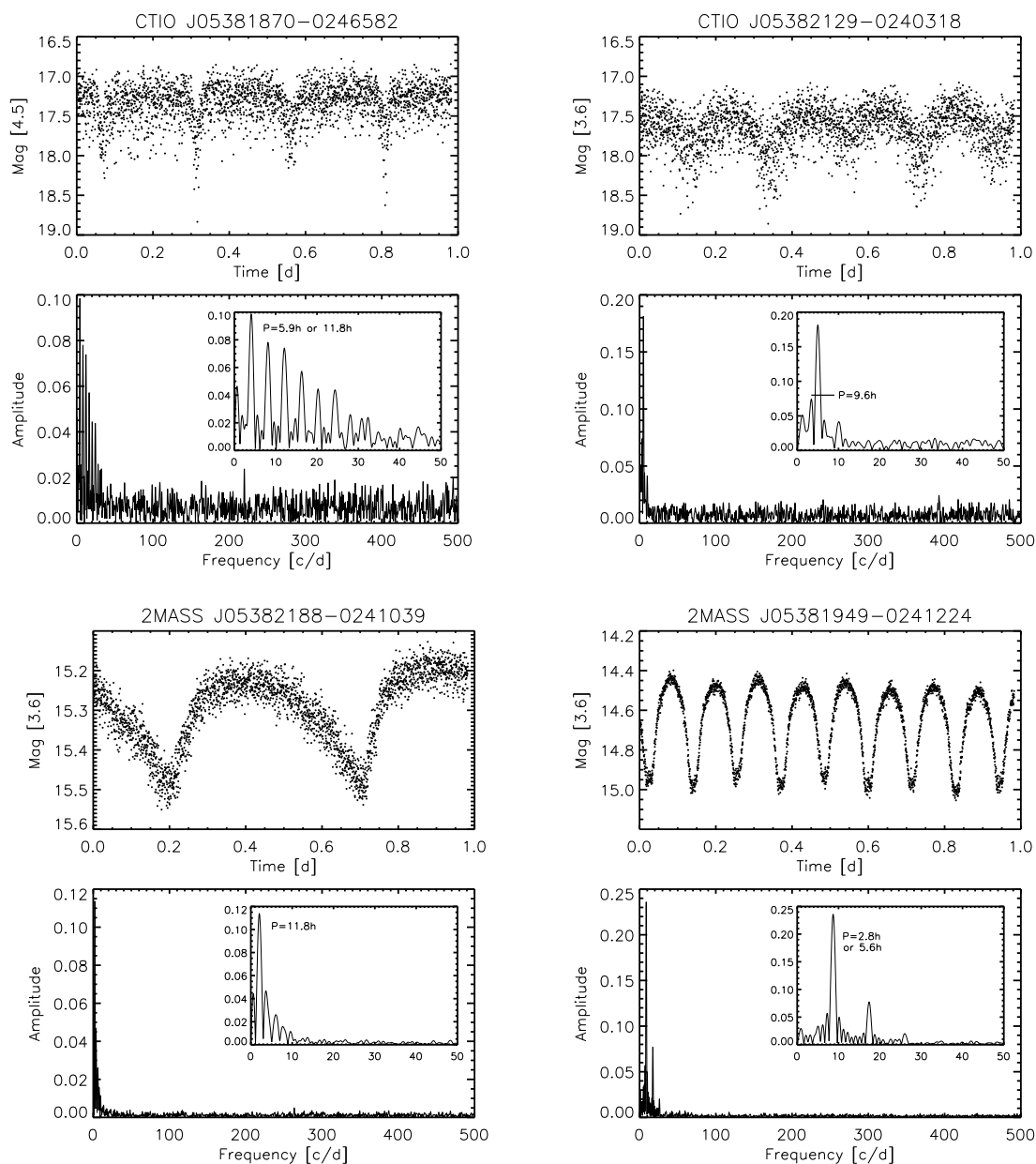
Figure B.1 Field variable stars. Light curves (top) and periodograms (bottom) are as in Fig. 4.3; estimated periods are marked near the corresponding frequency peaks.

Bibliography

Alard, C. & Lupton, R. H. 1998, ApJ, 503, 325

Alencar, S. H. P., Teixeira, P. S., Guimarães, M. M., McGinnis, P. T., Gameiro, J. F., Bouvier, J., Aigrain, S., Flaccomio, E., & Favata, F. 2010, A&A, 519, 88

Allard, F., Hauschildt, P. H., Alexander, D. R., & Starrfield, S. 1997, A&A Rev., 35, 137

Allen, P. R., Luhman, K. L., Myers, P. C., Megeath, S. T., Allen, L. E., Hartmann, L., & Fazio, G. G. 2007, ApJ, 655, 1095

Andrews, S. M., Reipurth, B., Bally, J., & Heathcote, S. R. 2004, ApJ, 606, 353

Anthony-Twarog, B. J. 1982, AJ, 87, 1213

Apai, D. 2005, Science, 310, 834

Ardila, D., Martín, E., & Basri, G. 2000, AJ, 120, 479

Bailer-Jones, C. A. L. & Mundt, R. 2001, A&A, 367, 218

Ballard, S., Charbonneau, D., Deming, D., Knutson, H. A., Christiansen, J. L., Holman, M. J., Fabrycky, D., Seager, S., & A'Hearn, M. F. 2010, PASP, 122, 1341

Baraffe, I. & Chabrier, G. 2000, in Very Low-Mass Stars and Brown Dwarfs, ed. R. Rebolo & M. R. Zapatero-Osorio, 186

Baraffe, I., Chabrier, G., Allard, F., & Hauschildt, P. H. 1998, A&A, 337, 403

—. 2002, A&A, 382, 563

Baraffe, I., Chabrier, G., Allard, F., & Hauschildt, P. H. 2002, A&A, 382, 563

Baraffe, I., Chabrier, G., Barman, T. S., Allard, F., & Hauschildt, P. H. 2003, A&A, 402, 701

Baraffe, I., Chabrier, G., & Gallardo, J. 2009, ApJ, 702, L27

Barrado y Navascués, D., Béjar, V. J. S., Mundt, R., Martín, E. L., Rebolo, R., Zapatero Osorio, M. R., & Bailer-Jones, C. A. L. 2003, A&A, 404, 171

Barrado y Navascués, D., Stauffer, J. R., Bouvier, J., Jayawardhana, R., & Cuillandre, J.-C. 2004, ApJ, 610, 1064

Barrado y Navascués, D., Stauffer, J. R., Morales-Calderón, M., Bayo, A., Fazzio, G., Megeath, T., Allen, L., Hartmann, L. W., & Calvet, N. 2007, ApJ, 664, 481

Barrado y Navascués, D., Zapatero Osorio, M. R., Béjar, V. J. S., Rebolo, R., Martín, E. L., Mundt, R., & Bailer-Jones, C. A. L. 2001, A&A, 377, L9

Bate, M. R., Bonnell, I. A., & Bromm, V. 2003, Monthly Notice of the Royal Astronomical Society, 339, 577

Baud, B., Beintema, D. A., Wesselius, P. R., Young, E., Beichman, C. A., Emerson, J. P., Harris, S., Habing, H. J., Jennings, R. E., & Marsden, P. L. 1984, ApJ, 278, L53

Becker, A. C., Wittman, D. M., Boeshaar, P. C., Clocchiatti, A., Dell'Antonio, I. P., Frail, D. A., Halpern, J., Margoniner, V. E., Norman, D., Tyson, J. A., & Schommer, R. A. 2004, ApJ, 611, 418

Béjar, V. J. S., Martín, E. L., Zapatero Osorio, M. R., Rebolo, R., Barrado y Navascués, D., Bailer-Jones, C. A. L., Mundt, R., Baraffe, I., Chabrier, C., & Allard, F. 2001, ApJ, 556, 830

Béjar, V. J. S., Osorio, M. R. Z., & Rebolo, R. 2004, Astronomische Nachrichten, 325, 705

Béjar, V. J. S., Zapatero Osorio, M. R., & Rebolo, R. 1999, ApJ, 521, 671

—. 2004, Astronomische Nachrichten, 325, 705

Bertout, C. 2000, A&A, 363, 984

Bertout, C., Robichon, N., & Arenou, F. 1999, A&A, 352, 574

Bevington, P. R. & Robinson, D. K. 1992, Data reduction and error analysis for the physical sciences (New York: McGraw-Hill)

Bouabid, M.-P., Montalbán, J., Miglio, A., Dupret, M.-A., Grigahcène, A., & Noels, A. 2011, Astronomy & Astrophysics, 531, 145

Bouvier, J. 2007, in IAU Symposium, ed. J. Bouvier & I. Appenzeller, Vol. 243, 231

Bouvier, J. & Bertout, C. 1989, A&A, 211, 99

Bouvier, J., Chelli, A., Allain, S., Carrasco, L., Costero, R., Cruz-Gonzalez, I., Dougados, C., Fernández, M., Martín, E. L., Ménard, F., Mennessier, C., Mujica, R., Recillas, E., Salas, L., Schmidt, G., & Wichmann, R. 1999, A&A, 349, 619

Breger, M. 2000, Delta Scuti and Related Stars, 210, 3

Breger, M., Balona, L., Lenz, P., Hollek, J. K., Kurtz, D. W., Catanzaro, G., Marconi, M., Pamyatnykh, A. A., Smalley, B., Suárez, J. C., Szabo, R., Uytterhoeven, K., Ripepi, V., Christensen-Dalsgaard, J., Kjeldsen, H., Fanelli, M. N., Ibrahim, K. A., & Uddin, K. 2011, MNRAS, 414, 1721

Breger, M., Handler, G., Garrido, R., Audard, N., Zima, W., Paparó, M., Beichbuchner, F., Zhi-Ping, L., Shi-Yang, J., Zong-Li, L., Ai-Ying, Z., Pikall, H., Stankov, A., Guzik, J. A., Sperl, M., Krzesinski, J., Ogloza, W., Pajdosz, G., Zola, S., Thomassen, T., Solheim, J., Serkowitsch, E., Reegen, P., Rumpf, T., Schmalwieser, A., & Montgomery, M. H. 1999, A&A, 349, 225

Breger, M., Stich, J., Garrido, R., Martin, B., Jiang, S. Y., Li, Z. P., Hube, D. P., Oster-mann, W., Paparo, M., & Scheck, M. 1993, A&A, 271, 482

Briceño, C., Hartmann, L., Hernández, J., Calvet, N., Vivas, A. K., Furesz, G., & Szentgy-orgyi, A. 2007, ApJ, 661, 1119

Briceño, C., Hartmann, L., Stauffer, J., & Martín, E. 1998, AJ, 115, 2074

Briceño, C., Luhman, K. L., Hartmann, L., Stauffer, J. R., & Kirkpatrick, J. D. 2002, ApJ, 580, 317

Burningham, B., Naylor, T., Littlefair, S. P., & Jeffries, R. D. 2005, MNRAS, 356, 1583

Burrows, A., Hubbard, W. B., Lunine, J. I., & Liebert, J. 2001, Reviews of Modern Physics, 73, 719

Burrows, A., Marley, M., Hubbard, W. B., Lunine, J. I., Guillot, T., Saumon, D., Freedman, R., Sudarsky, D., & Sharp, C. 1997, ApJ, 491, 856

Burrows, A., Marley, M., Hubbard, W. B., Lunine, J. I., Guillot, T., Saumon, D., Freedman, R., Sudarsky, D., & Sharp, C. 1997, ApJ, 491, 856

Burrows, A., Sudarsky, D., & Lunine, J. I. 2003, ApJ, 596, 587

Caballero, J. A. 2008, A&A, 478, 667

Caballero, J. A., Béjar, V. J. S., Rebolo, R., Eislöffel, J., Zapatero Osorio, M. R., Mundt, R., Barrado Y Navascués, D., Bihain, G., Bailer-Jones, C. A. L., Forveille, T., & Martín, E. L. 2007, A&A, 470, 903

Caballero, J. A., Béjar, V. J. S., Rebolo, R., & Zapatero Osorio, M. R. 2004, A&A, 424, 857

Caballero, J. A., Martín, E. L., Zapatero Osorio, M. R., Béjar, V. J. S., Rebolo, R., Pavlenko, Y., & Wainscoat, R. 2006, A&A, 445, 143

Caballero, J. A., Valdivielso, L., Martín, E. L., Montes, D., Pascual, S., & Pérez-González, P. G. 2008, A&A, 491, 515

Carpenter, J. M., Hillenbrand, L. A., & Skrutskie, M. F. 2001, AJ, 121, 3160

Carpenter, J. M., Hillenbrand, L. A., Skrutskie, M. F., & Meyer, M. R. 2002, AJ, 124, 1001

Cenko, S. et al. 2006, PASP, 118, 1396

Chabrier, G., Baraffe, I., Allard, F., & Hauschildt, P. 2000, ApJ, 542, L119

Chabrier, G., Baraffe, I., & Plez, B. 1996, ApJ, 459, L91

Chabrier, G., Gallardo, J., & Baraffe, I. 2007, A&A, 472, L17

Christensen-Dalsgaard, J. 2008, Ap&SS, 316, 113

—. 2011, eprint arXiv, 1110, 5012

Cieza, L. & Baliber, N. 2006, ApJ, 649, 862

Cieza, L. & Baliber, N. 2007, ApJ, 671, 605

Cody, A. M. & Hillenbrand, L. A. 2010, ApJS, 191, 389

Cohen, R. E., Herbst, W., & Williams, E. C. 2004, AJ, 127, 1602

Comerón, F. 2008, Handbook of Star Forming Regions, 295

Comerón, F., Fernández, M., Baraffe, I., Neuhäuser, R., & Kaas, A. A. 2003, A&A, 406, 1001

Comerón, F., Neuhäuser, R., & Kaas, A. A. 2000, A&A, 359, 269

Comerón, F., Reipurth, B., Henry, A., & Fernández, M. 2004, A&A, 417, 583

Comerón, F., Rieke, G. H., & Neuhäuser, R. 1999, A&A, 343, 477

Córsico, A. H., Althaus, L. G., Kawaler, S. D., Bertolami, M. M. M., García-Berro, E., & Kepler, S. O. 2011, MNRAS, 418, 2519

Cushing, M. C., Tokunaga, A. T., & Kobayashi, N. 2000, AJ, 119, 3019

Damjanov, I., Jayawardhana, R., Scholz, A., Ahmic, M., Nguyen, D. C., Brandeker, A., & van Kerkwijk, M. H. 2007, ApJ, 670, 1337

Dantona, F. & Mazzitelli, I. 1985, ApJ, 296, 502

D'Antona, F. & Mazzitelli, I. 1997, Memorie della Società Astronomia Italiana, 68, 807

D'Antona, F., Ventura, P., & Mazzitelli, I. 2000, ApJ, 543, L77

Dawson, P., Scholz, A., & Ray, T. P. 2011, MNRAS, 1553

de Zeeuw, P. T., Hoogerwerf, R., de Bruijne, J. H. J., Brown, A. G. A., & Blaauw, A. 1999, AJ, 117, 354

Deeg, H. J. & Doyle, L. R. 2001, in Third Workshop on Photometry, p. 85, ed. W. J. Borucki & L. E. Lasher, 85

Deming, D., Knutson, H., Agol, E., Desert, J., Burrows, A., Fortney, J. J., Charbonneau, D., Cowan, N. B., Laughlin, G., Langton, J., Showman, A. P., & Lewis, N. K. 2011, ApJ, 726, 95

Demory, B.-O., Ségransan, D., Forveille, T., Queloz, D., Beuzit, J.-L., Delfosse, X., di Folco, E., Kervella, P., Bouquin, J.-B. L., Perrier, C., Benisty, M., Duvert, G., Hofmann, K.-H., Lopez, B., & Petrov, R. 2009, A&A, 505, 205

Dolan, C. J. & Mathieu, R. D. 2001, AJ, 121, 2124

Dullemond, C. P., van den Ancker, M. E., Acke, B., & van Boekel, R. 2003, ApJ, 594, L47

Dunham, M. M., Crapsi, A., Evans, N. J., Bourke, T. L., Huard, T. L., Myers, P. C., & Kauffmann, J. 2008, ApJS, 179, 249

Eiroa, C., Djukvip, A. A., & Casali, M. M. 2006, Astronomische Nachrichten, 327, 14

Eiroa, C. et al. 2002, A&A, 384, 1038

Espaillat, C., Furlan, E., D'Alessio, P., Sargent, B., Nagel, E., Calvet, N., Watson, D. M., & Muzerolle, J. 2011, ApJ, 728, 49

Everett, M. E. & Howell, S. B. 2001, PASP, 113, 1428

Fazio, G. G. et al. 2004, ApJS, 154, 10

Fernández, M. & Comerón, F. 2001, A&A, 380, 264

Fernandez, M. & Eiroa, C. 1996, A&A, 310, 143

Flaherty, K. M. & Muzerolle, J. 2010, ApJ, 719, 1733

Franciosini, E., Pallavicini, R., & Sanz-Forcada, J. 2006, A&A, 446, 501

Frasca, A., Covino, E., Spezzi, L., Alcalá, J. M., Marilli, E., Fżrész, G., & Gandolfi, D. 2009, A&A, 508, 1313

Fukugita, M., Ichikawa, T., Gunn, J., Doi, M., Shimasaku, K., & Schneider, D. 1996, AJ, 111, 1748

Gabriel, M. 1964, Annales d'Astrophysique, 27, 141

—. 1967, Annales d'Astrophysique, 30, 745

Gahm, G. F., Fischerstrom, C., Lindroos, K. P., & Liseau, R. 1989, A&A, 211, 115

Gastine, T. & Dintrans, B. 2011, A&A, 528, A6

Gauvin, L. S. & Strom, K. M. 1992, ApJ, 385, 217

Gennaro, M., Prada Moroni, P. G., & Tognelli, E. 2012, MNRAS, 420, 986

Gilliland, R. et al. 2010, PASP, 122, 131

Gilliland, R. L., Brown, T. M., Kjeldsen, H., McCarthy, J. K., Peri, M. L., Belmonte, J. A., Vidal, I., Cram, L. E., Palmer, J., Frandsen, S., Parthasarathy, M., Petro, L., Schneider, H., Stetson, P. B., & Weiss, W. W. 1993, AJ, 106, 2441

Glass, I. 1979, MNRAS, 187, 305

Gómez, M. & Mardones, D. 2003, AJ, 125, 2134

González Hernández, J. I., Caballero, J. A., Rebolo, R., Béjar, V. J. S., Barrado Y Navascués, D., Martín, E. L., & Zapatero Osorio, M. R. 2008, A&A, 490, 1135

Greissl, J., Meyer, M. R., Wilking, B. A., Fanetti, T., Schneider, G., Greene, T. P., & Young, E. 2007, AJ, 133, 1321

Grossman, A. S. & Graboske, H. C. 1973, ApJ, 180, 195

Guieu, S., Monin, J.-L., Dougados, C., Magnier, E., & Martín, E. L. 2005, Astronomische Nachrichten, 326, 1068

Hartman, J. D., Stanek, K. Z., Gaudi, B. S., Holman, M. J., & McLeod, B. A. 2005, AJ, 130, 2241

Hayashi, C. & Nakano, T. 1963, Progress of Theoretical Physics, 30, 460

Henize, K. G. 1963, AJ, 68, 280

Henize, K. G. & v, E. E. M. 1973, ApJ, 180, 115

Hennebelle, P. & Chabrier, G. 2008, ApJ, 684, 395

Herbig, G. 1998, ApJ, 497, 736

Herbig, G. H. 1954, PASP, 66, 19

Herbst, W. 1994, in Astronomical Society of the Pacific Conference Series, Vol. 62, The Nature and Evolutionary Status of Herbig Ae/Be Stars, ed. P. S. The, M. R. Perez, & E. P. J. van den Heuvel, 35

Herbst, W., Bailer-Jones, C. A. L., & Mundt, R. 2001, ApJ, 554, L197

Herbst, W., Bailer-Jones, C. A. L., Mundt, R., Meisenheimer, K., & Wackermann, R. 2002, A&A, 396, 513

Herbst, W., Eislöffel, J., Mundt, R., & Scholz, A. 2007, in Protostars and Planets V, ed. B. Reipurth, D. Jewitt, & K. Keil, 297

Herbst, W., Herbst, D. K., Grossman, E. J., & Weinstein, D. 1994, AJ, 108, 1906

Hernández, J., Hartmann, L., Megeath, T., Gutermuth, R., Muzerolle, J., Calvet, N., Vivas, A. K., Briceño, C., Allen, L., Stauffer, J., Young, E., & Fazio, G. 2007, ApJ, 662, 1067

Hillenbrand, L. A. 1997, AJ, 113, 1733

—. 2009, The Ages of Stars, 258, 81

Hillenbrand, L. A. & Carpenter, J. M. 2000, ApJ, 540, 236

Hoffmeister, C. 1963, Veroeff. Sternwarte Sonneberg, 6, 1

Horne, J. H. & Baliunas, S. L. 1986, ApJ, 302, 757

Hosokawa, T., Offner, S. S. R., & Krumholz, M. R. 2011, ApJ, 738, 140

Houdek, G. & Gough, D. O. 2011, MNRAS, 418, 1217

Hyland, A. R., Jones, T. J., & Mitchell, R. M. 1982, Royal Astronomical Society, 201, 1095

Irwin, J. & Bouvier, J. 2009, in IAU Symposium, ed. E. E. Mamajek, D. R. Soderblom, & R. F. G. Wyse, Vol. 258, 363

Irwin, J., Hodgkin, S., Aigrain, S., Bouvier, J., Hebb, L., Irwin, M., & Moraux, E. 2008, MNRAS, 384, 675

Irwin, J., Irwin, M., Aigrain, S., Hodgkin, S., Hebb, L., & Moraux, E. 2007, MNRAS, 375, 1449

Jackson, R. J., Jeffries, R. D., & Maxted, P. F. L. 2009, MNRAS: Letters, 399, L89

Jeans, J. H. 1902, Philosophical Transactions of the Royal Society of London. Series A, 199, 1

Jeffries, R. D., Maxted, P. F. L., Oliveira, J. M., & Naylor, T. 2006, MNRAS, 371, L6

Joergens, V., Fernández, M., Carpenter, J. M., & Neuhäuser, R. 2003, ApJ, 594, 971

Joy, A. H. 1942, PASP, 54, 15

—. 1949, ApJ, 110, 424

Kenyon, M. J., Jeffries, R. D., Naylor, T., Oliveira, J. M., & Maxted, P. F. L. 2005, MNRAS, 356, 89

Kenyon, S. J. & Hartmann, L. 1995, ApJS, 101, 117

Kenyon, S. J. & Hartmann, L. W. 1990, ApJ, 349, 197

Khinchin, A. Y. 1934, Mathematische Annelen, 109, 604

Kjeldsen, H., Bedding, T. R., & Christensen-Dalsgaard, J. 2008, Exploring the Solar System and the Universe. AIP Conference Proceedings, 1043, 365

Kjeldsen, H. & Frandsen, S. 1992, Astronomical Society of the Pacific, 104, 413

Klotz, A., Caux, E., Monin, J.-L., & Lodieu, N. 2004, A&A, 425, 927

Koenigl, A. 1991, ApJ, 370, L39

Kraus, A. L. & Hillenbrand, L. A. 2007, ApJ, 662, 413

Kraus, A. L. & Hillenbrand, L. A. 2007, AJ, 134, 2340

Kraus, A. L., Tucker, R. A., Thompson, M. I., Craine, E. R., & Hillenbrand, L. A. 2011, ApJ, 728, 48

Kumar, S. S. 1963, ApJ, 137, 1121

—. 2003, Brown Dwarfs (Proceedings of IAU Symposium #211), ed. E. Martín (San Francisco, CA: ASP), 3

Kunkel, M. 1999, PhD thesis, Julius-Maximilians-Univ., Wurzburg

Kuschnig, R., Weiss, W. W., Gruber, R., Bely, P. Y., & Jenkner, H. 1997, A&A, 328, 544

Lada, C. J., Muench, A. A., Luhman, K. L., Allen, L., Hartmann, L., Megeath, T., Myers, P., Fazio, G., Wood, K., Muzerolle, J., Rieke, G., Siegler, N., & Young, E. 2006, AJ, 131, 1574

Lada, E. A. & Lada, C. J. 1995, AJ, 109, 1682

Lamm, M. H., Mundt, R., Bailer-Jones, C. A. L., & Herbst, W. 2005, A&A, 430, 1005

Lee, T. A. 1968, ApJ, 152, 913

Lenz, P. & Breger, M. 2005, Communications in Asteroseismology, 146, 53

Levine, J. L., Steinhauer, A., Elston, R. J., & Lada, E. A. 2006, ApJ, 646, 1215

Littlefair, S. P., Naylor, T., Burningham, B., & Jeffries, R. D. 2005, MNRAS, 358, 341

Littlefair, S. P., Naylor, T., Mayne, N. J., Saunders, E., & Jeffries, R. D. 2011, MNRAS, 413, L56

Lodieu, N., Caux, E., Monin, J.-L., & Klotz, A. 2002, A&A, 383, L15

Lodieu, N., Dobbie, P. D., & Hambly, N. C. 2011, Astronomy & Astrophysics, 527, 24

Lodieu, N., Hambly, N. C., & Jameson, R. F. 2006, MNRAS, 373, 95

Lodieu, N., Zapatero Osorio, M. R., Rebolo, R., Martín, E. L., & Hambly, N. C. 2009, A&A, 505, 1115

Lomb, N. R. 1976, Ap&SS, 39, 447

López-Morales, M. 2006, PASP, 118, 716

Luhman, K., Rieke, G., Lada, C., & Lada, E. 1998, ApJ, 508, 347

Luhman, K. L. 1999, ApJ, 525, 466

—. 2004a, ApJ, 602, 816

—. 2004b, ApJ, 617, 1216

—. 2006, ApJ, 645, 676

—. 2007, ApJS, 173, 104

Luhman, K. L., Allen, L. E., Allen, P. R., Gutermuth, R. A., Hartmann, L., Mamajek, E. E., Megeath, S. T., Myers, P. C., & Fazio, G. G. 2008a, ApJ, 675, 1375

Luhman, K. L., Allen, P. R., Espaillat, C., Hartmann, L., & Calvet, N. 2010, ApJS, 186, 111

Luhman, K. L., Briceño, C., Stauffer, J. R., Hartmann, L., y Navascués, D. B., & Caldwell, N. 2003a, ApJ, 590, 348

Luhman, K. L., Hernández, J., Downes, J. J., Hartmann, L., & Briceño, C. 2008b, ApJ, 688, 362

Luhman, K. L., Lada, C. J., Hartmann, L., Muench, A. A., Megeath, S. T., Allen, L. E., Myers, P. C., Muzerolle, J., Young, E., & Fazio, G. G. 2005a, ApJ, 631, L69

Luhman, K. L., Lada, E. A., Muench, A. A., & Elston, R. J. 2005b, ApJ, 618, 810

Luhman, K. L., Liebert, J., & Rieke, G. H. 1997, ApJ, 489, L165

Luhman, K. L., Mamajek, E. E., Allen, P. R., Muench, A. A., & Finkbeiner, D. P. 2009, ApJ, 691, 1265

Luhman, K. L. & Muench, A. A. 2008, ApJ, 684, 654

Luhman, K. L., Stauffer, J. R., Muench, A. A., Rieke, G. H., Lada, E. A., Bouvier, J., & Lada, C. J. 2003b, ApJ, 593, 1093

Mainzer, A. K. & McLean, I. S. 2003, ApJ, 597, 555

Maiti, M. 2007, AJ, 133, 1633

Makidon, R. B., Rebull, L. M., Strom, S. E., Adams, M. T., & Patten, B. M. 2004, AJ, 127, 2228

Marconi, M. & Palla, F. 2003, Ap&SS, 284, 245

Martí, B. L., Eislöffel, J., & Mundt, R. 2005, A&A, 440, 139

Martí, B. L., Eislöffel, J., Scholz, A., & Mundt, R. 2004, A&A, 416, 555

Martín, E. L., Delfosse, X., & Guieu, S. 2004, AJ, 127, 449

Martín, E. L., Dougados, C., Magnier, E., Ménard, F., Magazzù, A., Cuillandre, J.-C., & Delfosse, X. 2001, ApJ, 561, L195

Massey, P. & Gronwall, C. 1990, ApJ, 358, 344

Mathieu, R. D. 2008, Handbook of Star Forming Regions, 757

Matt, S. P., Pinzón, G., de la Reza, R., & Greene, T. P. 2010, ApJ, 714, 989

Maxted, P. F. L., Jeffries, R. D., Oliveira, J. M., Naylor, T., & Jackson, R. J. 2008, MNRAS, 385, 2210

Mendoza, E. E. 1972, PASP, 84, 641

Menten, K., Reid, M., Forbrich, J., & Brunthaler, A. 2007, A&A, 474, 515

Mochejska, B. J., Stanek, K. Z., Sasselov, D. D., & Szentgyorgyi, A. H. 2002, AJ, 123, 3460

Mohanty, S., Basri, G., & Jayawardhana, R. 2005, Astronomische Nachrichten, 326, 891

Morales-Calderón, M., Stauffer, J. R., Kirkpatrick, J. D., Carey, S., Gelino, C. R., Barrado y Navascués, D., Rebull, L., Lowrance, P., Marley, M. S., Charbonneau, D., Patten, B. M., Megeath, S. T., & Buzasi, D. 2006, ApJ, 653, 1454

Morales-Calderón, M. et al. 2011, ApJ, 733, 50

Muench, A. A., Lada, C. J., Luhman, K. L., Muzerolle, J., & Young, E. 2007, AJ, 134, 411

Muench, A. A., Lada, E. A., Lada, C. J., Elston, R. J., Alves, J. F., Horrobin, M., Huard, T. H., Levine, J. L., Raines, S. N., & Román-Zúñiga, C. 2003, AJ, 125, 2029

Muzerolle, J., Flaherty, K., Balog, Z., Furlan, E., Smith, P. S., Allen, L., Calvet, N., D'Alessio, P., Megeath, S. T., Muench, A., Rieke, G. H., & Sherry, W. H. 2009, ApJ, 704, L15

Muzerolle, J., Hillenbrand, L., Calvet, N., Briceño, C., & Hartmann, L. 2003, ApJ, 592, 266

Muzić, K., Scholz, A., Geers, V., Fissel, L., & Jayawardhana, R. 2011, ApJ, 732, 86

Najita, J. R., Tiede, G. P., & Carr, J. S. 2000, ApJ, 541, 977

Neuhauser, R. & Comeron, F. 1998, Science, 282, 83

Nguyen, D. C., Jayawardhana, R., van Kerkwijk, M. H., Brandeker, A., Scholz, A., & Damjanov, I. 2009, ApJ, 695, 1648

Osorio, M. R. Z., Caballero, J. A., Béjar, V. J. S., & Rebolo, R. 2003, A&A, 408, 663

Padoan, P. & Nordlund, Å. 2002, ApJ, 576, 870

Palla, F. & Baraffe, I. 2005, A&A, 432, L57

Pascucci, I., Laughlin, G., Gaudi, B. S., Kennedy, G., Luhman, K., Mohanty, S., Birkby, J., Ercolano, B., Plavchan, P., & Skemer, A. 2011, eprint arXiv, 1101, 1913

Percy, J. R., Wilson, J. B., & Henry, G. W. 2001, PASP, 113, 983

Pickett, B. K., Durisen, R. H., Cassen, P., & Mejia, A. C. 2000, ApJ, 540, L95

Porras, A., Christopher, M., Allen, L., Francesco, J. D., Megeath, S. T., & Myers, P. C. 2003, AJ, 126, 1916

Preibisch, T., Brown, A. G. A., Bridges, T., Guenther, E., & Zinnecker, H. 2002, AJ, 124, 404

Preibisch, T., Guenther, E., & Zinnecker, H. 2001, AJ, 121, 1040

Preibisch, T., Guenther, E., Zinnecker, H., Sterzik, M., Frink, S., & Roeser, S. 1998, A&A, 333, 619

Preibisch, T. & Zinnecker, H. 1999, AJ, 117, 2381

—. 2001, AJ, 122, 866

—. 2004, A&A, 422, 1001

Press, W. H. 1978, Comments on Astrophysics, 7, 103

Press, W. H., Teukolsky, S. A., Vetterling, W. T., & Flannery, B. P. 1992, Numerical recipes: The art of scientific computing (Cambridge: Cambridge University Press)

Rebull, L. M. 2001, AJ, 121, 1676

Rebull, L. M., Stauffer, J. R., Megeath, S. T., Hora, J. L., & Hartmann, L. 2006, ApJ, 646, 297

Rebull, L. M., Wolff, S. C., & Strom, S. E. 2004, AJ, 127, 1029

Reegen, P. 2007, A&A, 467, 1353

Reggiani, M., Robberto, M., Rio, N. D., Meyer, M. R., Soderblom, D. R., & Ricci, L. 2011, Astronomy & Astrophysics, 534, 83

Reid, I. N. & Hawley, S. L. 1999, AJ, 117, 343

Reid, I. N., Hawley, S. L., & Gizis, J. E. 1995, AJ, 110, 1838

Reiners, A., Basri, G., & Christensen, U. R. 2009, ApJ, 697, 373

Reipurth, B. & Clarke, C. 2001, AJ, 122, 432

Riaz, B. & Gizis, J. E. 2008, ApJ, 681, 1584

Riaz, B., Lodieu, N., & Gizis, J. E. 2009, ApJ, 705, 1173

Ribas, I., Morales, J. C., Jordi, C., Baraffe, I., Chabrier, G., & Gallardo, J. 2008, Memorie della Società Astronomica Italiana, 79, 562

Rio, N. D., Robberto, M., Soderblom, D., Panagia, N., Hillenbrand, L., Palla, F., & Stassun, K. 2009, ApJS, 183, 261

Ripepi, V., Palla, F., Marconi, M., Bernabei, S., Ferro, A. A., Terranegra, L., & Alcalá, J. M. 2002, A&A, 391, 587

Rodríguez-Ledesma, M. V., Mundt, R., & Eislöffel, J. 2009, A&A, 502, 883

Rodríguez-López, C., MacDonald, J., & Moya, A. 2012, MNRAS, 419, L44

Romanova, M. M., Ustyugova, G. V., Koldoba, A. V., & Lovelace, R. V. E. 2011, MNRAS, 416, 416

Ryan, P. & Sandler, D. 1998, PASP, 110, 1235

Sacco, G. G., Franciosini, E., Randich, S., & Pallavicini, R. 2008, A&A, 488, 167

Saumon, D., Bergeron, P., Lunine, J. I., Hubbard, W. B., & Burrows, A. 1994, ApJ, 424, 333

Scargle, J. D. 1982, ApJ, 263, 835

Scholz, A. 2009, in American Institute of Physics Conference Series, Vol. 1094, Proceedings of the 15th Cambridge Workshop on Cool Stars, Stellar Systems and the Sun, ed. E. Stempels, 61

Scholz, A. & Eislöffel, J. 2004, A&A, 419, 249

Scholz, A. & Eislöffel, J. 2005, A&A, 429, 1007

Scholz, A. & Jayawardhana, R. 2008, ApJ, 672, L49

Scholz, A., Jayawardhana, R., Wood, K., Meeus, G., Stelzer, B., Walker, C., & O'Sullivan, M. 2007, ApJ, 660, 1517

Scholz, A., Xu, X., Jayawardhana, R., Wood, K., Eislöffel, J., & Quinn, C. 2009a, MNRAS, 398, 873

—. 2009b, MNRAS, 398, 873

Scholz, R.-D., Brunzendorf, J., Ivanov, G., Kharchenko, N., Lasker, B., Meusinger, H., Preibisch, T., Schilbach, E., & Zinnecker, H. 1999, A&AS, 137, 305

Schwarzenberg-Czerny, A. 1989, MNRAS, 241, 153

—. 1996, ApJ, 460, L107

Sherry, W. H., Walter, F. M., & Wolk, S. J. 2004, AJ, 128, 2316

Sherry, W. H., Walter, F. M., Wolk, S. J., & Adams, N. R. 2008, AJ, 135, 1616

Siess, L., Dufour, E., & Forestini, M. 2000, A&A, 358, 593

Slesnick, C. L., Carpenter, J. M., & Hillenbrand, L. A. 2006a, AJ, 131, 3016

Slesnick, C. L., Carpenter, J. M., Hillenbrand, L. A., & Mamajek, E. E. 2006b, AJ, 132, 2665

Slesnick, C. L., Hillenbrand, L. A., & Carpenter, J. M. 2004, ApJ, 610, 1045

—. 2008, ApJ, 688, 377

Sokoloski, J. L., Bildsten, L., & Ho, W. C. G. 2001, MNRAS, 326, 553

298

Sperl, M. 1998, Communications in Asteroseismology, 111, 1

Spezzi, L., Alcalá, J., Covino, E., Frasca, A., Gandolfi, D., Oliveira, I., Chapman, N., Evans, N., Huard, T., Jørgensen, J., Merín, B., & Stapelfeldt, K. 2008, ApJ, 680, 1295

Spezzi, L., Alcalá, J. M., Frasca, A., Covino, E., & Gandolfi, D. 2007, A&A, 470, 281

Stamatellos, D. & Whitworth, A. 2011, EPJ Web of Conferences, 16, 05001

Stassun, K. G., Mathieu, R. D., Mazeh, T., & Vrba, F. J. 1999, AJ, 117, 2941

Stassun, K. G., Mathieu, R. D., & Valenti, J. A. 2006, Nature, 440, 311

Stellingwerf, R. 1978, ApJ, 224, 953

Stetson, P. B. 1996, PASP, 108, 851

—. 2000, PASP, 112, 925

Strom, K. M. & Strom, S. E. 1994, ApJ, 424, 237

Strom, S. E., Strom, K. A., & Carrasco, L. 1974, PASP 86, 86, 798

Szűcs, L., Apai, D., Pascucci, I., & Dullemond, C. 2010, ApJ, 720, 1668

Tognelli, E., Moroni, P. G. P., & Degl'Innocenti, S. 2011, Astronomy & Astrophysics, 533, 109

Toma, E. 1972, A&A, 19, 76

Torres-Lopez, R. M., Mioduszewski, A. J., Loinard, L. R., & Rodriguez, L. F. 2007, American Astronomical Society, 211, 999

Trullols, E. & Jordi, C. 1997, A&A, 324, 549

van Saders, J. L. & Pinsonneault, M. H. 2012, ApJ, 746, 16

Vivas, A. K. et al. 2004, AJ, 127, 1158

Vorobyov, E. & Basu, S. 2009, ApJ, 703, 922

Walter, F., Vrba, F., Mathieu, R., Brown, A., & Myers, P. 2, AJ, 107, 692

Walter, F. M., Wolk, S. J., Freyberg, M., & Schmitt, J. H. M. M. 1997, Memorie della Societa Astronomica Italiana, 68, 1081

Werner, M. W., Roellig, T. L., Low, F. J., Rieke, G. H., Rieke, M., Hoffmann, W. F., Young, E., Houck, J. R., Brandl, B., Fazio, G. G., Hora, J. L., Gehrz, R. D., Helou, G., Soifer, B. T., Stauffer, J., Keene, J., Eisenhardt, P., Gallagher, D., Gautier, T. N., Irace, W., Lawrence, C. R., Simmons, L., Cleve, J. E. V., Jura, M., Wright, E. L., & Cruikshank, D. P. 2004, ApJS, 154, 1

Whelan, E. T., Ray, T. P., Bacciotti, F., Natta, A., Testi, L., & Randich, S. 2005, Nature, 435, 652

Whelan, E. T., Ray, T. P., Podio, L., Bacciotti, F., & Randich, S. 2009, ApJ, 706, 1054

Whittet, D. C. B., Prusti, T., Franco, G. A. P., Gerakines, P. A., Kilkenny, D., Larson, K. A., & Wesselius, P. R. 1997, A&A, 327, 1194

Whitworth, A. P. & Stamatellos, D. 2006, A&A, 458, 817

Whitworth, A. P. & Zinnecker, H. 2004, A&A, 427, 299

Wiener, N. 1930, Acta Mathematica, 55, 117

Wilking, B. A., Greene, T. P., & Meyer, M. R. 1999, AJ, 117, 469

Wilking, B. A., McCaughrean, M. J., Burton, M. G., Giblin, T., Rayner, J. T., & Zinnecker, H. 1997, AJ, 114, 2029

Wilking, B. A., Meyer, M. R., Greene, T. P., Mikhail, A., & Carlson, G. 2004, AJ, 127, 1131

Wolk, S. J. 1996, PhD thesis, State Univ. New York, Stony Brook

Young, A. T. 1967, AJ, 72, 747

Young, A. T., Genet, R. M., Boyd, L. J., Borucki, W. J., Lockwood, G. W., Henry, G. W., Hall, D. S., Smith, D. P., Baliumas, S. L., Donahue, R., & Epand, D. H. 1991, PASP, 103, 221

Zapatero Osorio, M. R., Béjar, V. J. S., Martín, E. L., Rebolo, R., Barrado y Navascués, D., Bailer-Jones, C. A. L., & Mundt, R. 2000, Science, 290, 103

Zapatero Osorio, M. R., Béjar, V. J. S., Pavlenko, Y., Rebolo, R., Allende Prieto, C., Martín, E. L., & García López, R. J. 2002, A&A, 384, 937

Zapatero Osorio, M. R., Caballero, J. A., Béjar, V. J. S., & Rebolo, R. 2003, A&A, 408, 663